Spectroscopic Study of the Organic Conductors: Charge-transfer Salts of BDT-TTP and DMTSA

Jianyong Ouyang

Doctor of Philosophy

Department of Structural Molecular Science
School of Mathematical and Physical Science
The Graduate University for Advanced Studies

1999

Acknowledgements

I would like to express my cordial gratitude to my supervisor, Prof. Kyuya Yakushi, for his continuous interest, constant encouragement and enlightening guidance and discussion throughout the course of my doctoral program. What I have learned from the research under the supervision of Prof. Yakushi will certainly benefit me greatly for my upcoming work.

I am deeply grateful to Prof. Yoji Misaki of Kyoto University for providing us their results and many samples of BDT-TTP, its analogues and their salts. I would like to express my sincere gratitude to Prof. Tetsuo Otsubo and Dr. Kazuo Takimiya of Hiroshima University for providing us DMTSA and DMTTA. I would like to thank Prof. Hiroyuki Tajima of the University of Tokyo for his cooperation in the interpretation of the optical transition of DMTSA-BF_4. I am indebted to Prof. Yongfang Li of the Institute of Chemistry, Chinese Academy of Science for his generous help and constant encouragement.

I am deeply grateful to Mr. Mikio Uruichi for teaching and assisting me in conductivity and X-ray diffraction measurement. I would like to express my gratitude to Dr. Chikako Nakano for teaching and assisting me to take oscillator and Weissenberg photograph of X-ray diffraction and to calculate the transfer integrals of DMTSA-ClO_4. I am indebted to Dr. Jian Dong for assisting me in the measurement of the polarized reflection spectrum and telling me his know-how of the crystal growth. I wish to thank Dr. Mkhital Simonyan for teaching and assisting me in ESR measurement. I am grateful to Dr. Yukako Yonehara for her help in some experiments. I would like to acknowledge the other members at Yakushi's group: Prof. Jacek Ulanski, Dr. Kaoru Yamamoto, Dr. Mikhail Maksimuk, and Mrs. Yuqin Ding, for their generous help and useful discussion. Thanks go to all members of the Institute for Molecular Science for various contribution and kindness.

Finally, I would like to express my sincere gratitude to my parents, my wife and my sisters for their support, understanding and encouragement.

Abbreviation

BDT-TTP	2,5-bis(1,3-dithiol-2-ylidene)-1,3,4,6-tetrathiapentalene
ST-TTP	2-(1,3-diselenol-2-ylidene)-5-(1,3-dithiol-2-ylidene)-1,3,4,6-tetrathiopentalene
BDS-TTP	2,5-bis(1,3-diselenol-2-ylidene)-1,3,4,6-tetrathiapentalene
TTM-TTP	2,5-bis[4,5-bis(methylthio)-1,3-dithiol-2-ylidene]-1,3,4,6-tetrathiapentalene
BEDT-TTF	bis(ethylenedithio)tetrathiafulvalene
BMDT-TTF	bis(methylenedithio)tetrathiapulvalene
TMTSF	tetramethyltetraselenafulvalene
TMTTA	tetramethyltetrathiafulvalene
TTF	tetrathiafulvalene
TSF	tetraselenafulvalene
DMET	Dimethyl(ethylenedithio)-diselenadithiafulvalene
MDT-TTF	methylenedithiotetrathiafulvalene
DMTSA	2,3-dimethyltetraselenoanthracene
DMTTA	2,3-dimethyltetrathioanthracene
TSeT	tetraselenotetracene
TTT	tetrathiotetracene
NMP	N-methylphenazinium
TCNQ	Tetracyanoquinodimethane
dmit	1,3-dithiol-2-thione-4,5-dithiolate

Contents

Chapter 1

General Introduction

1.1 Development of organic conductors

Great progress has been made in the field of the organic conductors after the appearance of the acceptor TCNQ and the donor TTF. Since then, many organic molecules, which are good acceptors or donors to form charge-transfer (CT) organic crystals, were synthesized. The members of this family are still expanding at a certain acceleration. The development of new organic conductors is toward two directions: one is to decrease on-site Coulomb repulsion U of the molecule; another is to increase the dimensionality of the crystal. Some compounds played very important roles in the development of this field, including TCNQ, TTF, TMTSF and BEDT-TTF.

TCNQ was synthesized in 1960[1], which is a very good acceptor to form CT salts[2] and is still extensively used today. Many TCNQ analogues are good acceptors as well. Some TCNQ salts exhibit a remarkably high conductivity[3, 4], such as NMP-TCNQ with a conductivity of 10^2 S cm^{-1}. However, the conductive behavior of the early TCNQ salts is non-metallic.

TTF was synthesized about a decade later than TCNQ[5], which is a very good donor molecule to form organic CT salts. Many TTF salts were prepared with organic or inorganic acceptor. Up to date, many organic donors base on TTF and TSF.

A breakthrough in this field is the obtainment of TTF-TCNQ in 1973[6]. TTF-TCNQ is the first organic CT salt which exhibits metallic behavior down to 58K[6, 7], this metallic behavior is also confirmed by the polarized reflection spectroscopy[8,9]. Many TTF analogue salts, such as TSF-TCNQ[10] and HMTSF-TCNQ[11], and some TTF salts[12,13] of inorganic anions are metallic in a limited temperature range as well. The inter-chain transfer integral of these salts is negligible, so that they are quasi-one-dimensional metals along the stacking direction. They suffer a Peierls transition turning into charge-density wave (CDW) insulator at low temperature. Extremely high conductivity was observed at low temperature, which is comparable with the good metal conductors. However, no superconductivity was observed on these one-dimensional organic conductors.

A striking finding in this field is the observation of superconductivity on TMTSA salts. $(TMTSF)_2PF_6$ is the first organic conductor observed superconductive behavior below 0.9 K under a pressure of 12 kbar[14)]. Subsequently superconductivity was observed on many TMTSA salts as well, such as AsF_6, SbF_6, TaF_6 and ReO_4 salts[15-18)]. $(TMTSF)_2ClO_4$ is the first organic conductor exhibiting superconductivity below 1.3 K under ambient pressure[22)]. Despite the inter-chain transfer integral studied by both the theoretical calculation[23)] and the optical measurement[24,25)] is not negligible, which is about one-tenth of the intra-chain transfer integral, the electronic structure of TMTSA salts is still quasi-one-dimensional. Owning to the nature of one-dimensional structure, they can not escape the metal-insulator transition at low temperature under ambient pressure[19)]. But the metal-insulator transition temperature is lower than TTF-TCNQ. It is believed that the inter-chain transfer integral contributes greatly to the very low metal-insulator transition temperature and the appearance of the superconductivity. The insulator is in spin-density wave (SDW) state[20,21)], this SDW state is suppressed while the superconductive state appears at lower temperature when a high pressure is applied on the crystal. The critical superconductivity transition temperature T_c is 1-2 K for TMTSA salts under relatively strict conditions. The research on TMTSA salts is almost exhaust, it seems impossible to get a superconductor at a high temperature. In contrast to $(TMTSF)_2PF_6$, the sulphur analogue $(TMTTF)_2PF_6$ is an insulator at room temperature and does not exhibit a superconductive behavior at low temperature[26,27)].

$(BEDT\text{-}TTF)_2ReO_4$ is the first sulphur-containing organic-salt superconductor found below 2K under the pressure of 4kbar[28)]. Superconductive behavior has been observed on many BEDT-TTF salts at low temperature under high or ambient pressure as well[29)]. Even today the study on BEDT-TTF salts is still a highlighted subject in the field of organic conductors and superconductors. The highest critical temperature T_c of organic superconductors has been observed on BEDT-TTF salts except C_{60}. Three κ-type BEDT-TTF salts show transition temperature T_c higher than 10K: κ-(BEDT-TTF)$_2$Cu(NCS)$_2$ (T_c=10.4K)[30,31], κ-(BEDT-TTF)$_2$Cu[N(CN)$_2$]Br (T_c=11.6K)[32] and κ-(BEDT-TTF)$_2$Cu[N(CN)$_2$]Cl (T_c=12.8K)[33]. The appearance of the superconductivity strongly depends on the species of the anions and the crystal phase. Diverse crystal phases which are more than ten have been observed. Sometimes several crystal phases exist for the BEDT-TTF salt with the same stoichiometry. The inter-chain transfer integral is very large in some BEDT-TTF salts, even isotropic two-dimensional structure have been observed on many BEDT-TTF salts[34-37], especially the α-, θ-, and κ-salts.

Superconductivity has been observed on many other organic CT salts. Many BEDT-TTF analogue salts show superconductive behavior as well, such as (BEDO-TTF)$_3$Cu(NCS)$_3$ (T_c=1K)[38], κ-(BEDSe-TTF)$_2$Cu[N(CN)$_2$]Br (T_c=7.5K)[39] and λ-(BEDT-TSF)$_2$GaX$_z$Y$_{4-z}$ (X, Y, Z = F, Cl, Br, T_c=8K when $0<Z<1.5$)[40,41]. Superconductivity has also observed on the salts of non-symmetrical donor DMET[42-45] and MDT-TTF[46]. The salts of the acceptor M(dmit)$_2$ (M=Ni, Pd) also show superconductivity at low temperature[47].

As mentioned above, all organic salts except M(dmit)$_2$ salts exhibiting the superconductivity have donor molecules containing the TTF or TSF structure. On the other hand, all of them have somewhat two-dimensional structure. These indicate the dimensionality plays an important role for superconductive behavior together with many other factors. Though superconductivity has been observed in many organic salts, the transition temperature T_c remains very low, which is much lower than many inorganic superconductors. Consequently, organic superconductors are still very far from the practical application. To explore the organic superconductors of high T_c is a very important task. Organic conductors show some peculiar physical properties which are different from the conventional conductors, the understanding of these properties enriches the knowledge of the solid state physics. Many physical properties of organic conductors and superconductors can not be understood very well yet. There are still much work waiting for chemist, physicist and material scientist.

1.2 Electronic structure of organic charge transfer salts

The electronic structure of organic conductors is determined by the packing form of the molecules in the crystal. The organic molecules in the crystal usually form a layer, which is separated by the inorganic ion layers. The overlap of the HOMOs of the organic molecules occurs between the organic molecules in the same column or neighboring column, when the distance between two atoms in the neighboring molecules is shorter than the sum of their van der Waals radii. Hence, the charge carriers are localized in the organic layer. Whether the electronic structure is one- or two-dimensional depends on the ratio of the inter-chain transfer integral to the intra-chain transfer integral. The overlap of the HOMO, of which the value depends on both the species and the arrangement of the molecules, forms the energy band. Usually, the bandwidth of the organic conductor is very narrow about 1eV, thus the behavior of the conduction electron is different from the conventional inorganic conductors. The good description for the energy band of the organic conductors is given by the tight-binding approximation.

For simplicity, the electronic structure of one-dimension conductor along the stacking direction is presented. The wavefunction ψ of the conduction electron is the linear combination of the molecule wavefunction ϕ48). When one carrier is at one site, the wavefunction is

$$\psi_k(r) = \sum_i \phi_i(r - R_i)e^{ik \cdot R_i} , \tag{1.1}$$

where k stands for the vector in the reciprocal space, $-\pi/a < k < \pi/a$ with a denoting the lattice spacing along the chain, and R_i represents the position vector of i-th unit cell in the real space. The electronic energy corresponding to the state $\psi(k)$ is

$$E(k) = 2t\cos(ka) \tag{1.2}$$

with $t = <\phi_i|H|\phi_{i+1}>$ as the transfer integral between the neighboring molecules. Admittedly, the bandwidth is $4t$.

The Fermi surface is two parallel planes in the first Brillouin zone for the complete one-dimensional conductor with the neglect of the inter-chain transfer integrals. It becomes warping when the inter-chain transfer integral is considered. Jacobsen pointed out that the Fermi surface becomes closed in the first Brillouin zone when the inter-chain transfer integral is larger than one-third of the intra-chain transfer integral in orthorhombic crystal49). The one-dimensional Fermi surface is nested if one piece can be transferred to other piece with respect to a vector q. A one-dimensional metal with nested Fermi surface is unstable at low temperature50).

A characteristic feature for one-dimensional conductors is the Peierls metal-insulator transition at low temperature ($2k_F$ transition). This transition is caused by the electron-phonon interaction. The Peierls instability can be understood by the polarization function $\chi(q)$. For one-dimensional conductor51), it is:

$$\chi(q) = \frac{2m}{\pi n\hbar q}\ln\left|\frac{q+2k_F}{q-2k_F}\right|, \tag{1.3}$$

where m is the mass of free electron, n the density of the states and q the wavenumber of the lattice. Apparently, $\chi(q)$ is divergent at $q=2k_F$ (Fig. 2). This divergence becomes a jump for two- or three-dimensional conductor. A precursor before the Peierls transition is the Kohn anomaly, namely the $2k_F$ lattice vibration increases its amplitude and decreases its frequency on lowering temperature toward to the Peierls temperature. By the jellium model, the phonon frequency Ω_q by the electron-phonon interaction is52):

$$\Omega_q^2 = \omega_q^2 - \frac{2|g_q^2|\omega_q n}{\hbar}\chi(q), \tag{1.4}$$

where ω_q is the bare phonon frequency, and g_q the electron-phonon coupling constant.

Apparently, the frequency Ω_q is lower than the bare phonon frequency ω_q. The Kohn anomaly becomes more and more remarkable on lowering temperature before the Peierls transition (Fig. 3(a)). As illustrated in Fig. 3(b), the softening of the $2k_F$ lattice vibration is not remarkable for two-dimensional conductor and disappears for three-dimensional conductor. Hence, the Peierls instability becomes suppressed when the dimensionality increases. A rough gauge $\eta = t_\perp / t_{//}$ ($t_\perp$ and $t_{//}$ are the transverse and the longitudinal transfer integral, respectively) has been proposed by Jérome and Schulz to estimate the Peierls transition temperature48), the extreme limit is $\eta_c = 3(T_p^0 / T_F)^{1/2}$, where T_p^0 is the mean-field transition temperature of an isolated chain and T_F is the Peierls transition temperature. The Peierls instability is suppressed through the temperature when $\eta = t_\perp / t_{//} > 1/5$.

The above electronic picture is based on the one-electron model without the consideration of the electron-electron correlation. The electron-electron correlation sometime plays a very important role, especially in SDW insulator. The Hubbard model is a suitable model to describe the tight-binding electronic behavior after the consideration of the transfer integral t and on-site Coulomb repulsion U53):

$$H = -t \sum C_{i\sigma}^{+} C_{j\sigma} + U \sum n_{i\uparrow} n_{j\downarrow} \tag{1.5}$$

where C_i^+ and C_j denotes the creation and annihilation operators, respectively, σ stands for the spin, and n represents the number operator $n \equiv C_{i\sigma}^{+} C_{i\sigma}$. The relation between the electronic structure and U, t is illustrated in Fig. 4 for a dimer A^-A^-54). Two extreme limits are proposed: the Heitler-London Limit and the Molecular Orbital Limit. In the former limit, $U >> t$, the ground state A^-A^- is lower by U than the excited state A^0A^{2-}. In the latter limit, $U << t$, the electrons are regarded as free particles without electron-electron correlation. The actual electronic structure of the organic CT salts is the case between the two limits.

The conductive properties are determined by the competition of U and t. Evidently, large t and small U favor the metallic state. When an insulator is derived from the electron-electron correlation, it is called a Mott insulator. Half-filled organic salts usually are Mott insulators. Besides the Peierls transition caused by the electron-phonon coupling, another important metal-insulator transition is frequently observed resulting from the electron-electron correlation. The insulator state after the former transition usually is in CDW state while after the latter transition is in SDW state. CDW and SDW are two main insulator states for organic CT salts.

1.3 Optical spectroscopic study on the organic conductors

The optical spectroscopic methods are very powerful tools to study the electronic structure of the organic conductors. Among these methods, the polarized reflection spectroscopy and the Raman spectroscopy may be most important. They are extensively exploited.

The polarized reflection spectroscopy is a very powerful to probe the dimensionality, energy band, and electron-phonon interaction. Some insight can also be gained into the electron-electron correlation.

The reflectivity R is the result of the interaction between the incident light and the matter, which is related to the complex dielectric constant ε of the matter[55]:

$$R(\omega)=\left|\frac{\sqrt{\varepsilon}-1}{\sqrt{\varepsilon}+1}\right|^2, \tag{1.6}$$

and

$$\varepsilon=\varepsilon_1+i\varepsilon_2 \tag{1.7}$$

ε_1 and ε_2 are the real and the imaginary parts of ε, respectively. In one electron model, both the intra-band transition and the inter-band transition contribute to the total dielectric constant:

$$\varepsilon(\omega)=1+\varepsilon_{\mathrm{intraband}}+\varepsilon_{\mathrm{interband}}, \tag{1.8}$$

$$\varepsilon_{intraband} \cong -\frac{e^2}{\varepsilon_0\omega^2}\left(\sum_k \frac{1}{\hbar^2}\frac{\partial^2 E_k}{\partial k^2} f(E_k)\right), \tag{1.9}$$

$$\varepsilon_{interband} \cong -\frac{2e^2}{\varepsilon_0 m}\left(\sum_{k,n,n'} \frac{\left|P_{n'n}^k\right|^2 f(E_k)}{\hbar\omega_{nn'}(k)\left[\omega_{n'n}^2(k)-\omega^2\right]}\right), \tag{1.10}$$

$$P_{n'n}^k = \frac{1}{V}\int_{unit\ cell} u_{k,n'}^* (e\cdot P) u_{k,n} d^3r, \tag{1.11}$$

where n', n are the band indices, $f(E_k)$ represents the Fermi-Dirac distribution, $\hbar\omega_{n'n} = (E_{k,n'} - E_{k,n})$, $e \cdot P$ is the momentum operator along the field, and V is the unit cell volume.

For a metal, the intra-band transition is described by the Drude model:

$$\varepsilon(\omega) = \varepsilon_c - \frac{\omega_p^2}{\omega(\omega + i\gamma)}, \tag{1.12}$$

where ε_c, ω_p and γ are the residual dielectric constant, plasma frequency and the scattering constant, respectively. The generalized Drude model is the modification of the simple Drude model by introducing the frequency dependence of the plasma frequency and the scattering constant. The generalized Drude model is useful to investigate the conductive mechanism, which is frequently employed for the transition metal oxide conductors with a strong electron-electron correlation[56, 57].

The reflection spectrum can be transformed into the spectrum of the dielectric constant or the conductivity spectrum by the Krames-Kronig transformation:

$$\theta(\omega) = \frac{\omega}{\pi} P\int_0^{\infty} \frac{\ln[R(\omega')]}{\omega^2 - \omega'^2} d\omega, \tag{1.13}$$

and the relations between the optical constants:

$$n = \frac{1-R}{1+R-2\sqrt{R}\cos\theta}, \tag{1.14}$$

$$k = \frac{2\sqrt{R}\sin\theta}{1+R-2\sqrt{R}\cos\theta}, \tag{1.15}$$

$$\varepsilon_1 = n^2 - k^2,\ \ \varepsilon_2 = 2nk\,, \tag{1.16}$$

$$\sigma = \varepsilon_0 \varepsilon_2 \omega\,. \tag{1.17}$$

The anisotropy of the organic conductors can be observed very explicitly by the polarized reflection spectroscopy. The appearance of the CT band reflects the charge transfer in that direction. Hence, it appears only in one direction for one-dimensional conductors while in two directions for two-dimensional conductors. The CT band may be Drude-like when the crystal is metallic in this direction.

The polarized reflection spectrum can be fitted by the Drude model when the crystal is metallic in that direction, to obtain the three Drude parameters. The Drude plasma frequency is related to the electronic energy in the metal:

$$\omega_{pi}^2 = \frac{e^2}{\pi^2 \hbar^2} \frac{\iiint f(E) \frac{\partial^2 E}{\partial k_i^2} dk_a dk_b dk_c}{\iiint f(E) dk_a dk_b dk_c} \tag{1.18}$$

where i denotes the direction, e is the static charge of the electron, E is the energy dispersion in three dimension, and $f(E)$ the Fermi-Dirac function. This is the theoretical basis to estimate the energy band according to the Drude plasma frequency. Besides this Drude plasma frequency ω_p, another plasma frequency ω_p' can be obtained by integrating the conductivity of the CT band in the real conductivity spectrum[55]:

$$\omega'^2_p = \frac{2}{\varepsilon_0 \pi} \int_0^\infty \sigma_1(\omega) d\omega \tag{1.19}$$

It is often found for organic metals that the ω_p' value is smaller than ω_p. This discrepancy is considered as the short-range effect by the electron-electron correlation. It has been proposed that the Hubbard U of one-dimensional organic metal can be estimated from this discrepancy[58-60].

Many organic acceptor or donor molecules are planar with a center of symmetry. Hence, the totally symmetrical a_g modes should not appear in the polarized reflection spectrum.

However, some a_g modes are often observed as peaks or dips in the spectrum of many organic CT salts in the conductive direction, especially in the insulator state. The appearance of these a_g modes arises from the electron-phonon coupling. The understanding of this electron-phonon coupling is very important for the understanding of the Peierls transition and even the superconductive mechanism. Several theoretical models have been proposed to interpret these a_g modes and to estimate the electron-phonon coupling of one-dimensional semiconductors[61-63)]. Very interesting change of some phonons has also been observed through the phase transition, such as the softening of some phonons and the change of the intensity[68-70)].

The appearance of the a_g modes in the reflection spectrum is derived from the electron-phonon coupling, the positions are different from the non-interacting bare modes. The appearance of the CT band in the infrared region makes it more difficult to know the exact positions. This problem is solved by the Raman spectroscopy, which can probe the a_g modes very well. The positions are not subject to the electron-phonon coupling. On the other hand, the positions of some a_g modes are very sensitive to the charge perching on the molecule. Some modes even linearly shift with respect to the change of the charge. Such linear relation is observed for many organic salts, such as TTF[64, 65)], TCNQ[65, 66)], and BEDT-TTF[67)]. The charge transfer in TTF-TCNQ determined by the Raman spectroscopy[65, 66)] agrees with the result by other means very well. Hence, the Raman spectroscopy is very effective to probe the charge on the organic molecule of the organic conductors.

1.4 Motivation and organization of this thesis

Though a BDT-TTP derivative was early synthesized in 1980, no report was about the structure and the properties[71)]. In 1993, Misaki *et al.* found a novel way to synthesis BDT-TTP[72)]. One BDT-TTP molecule contains eight sulfur atoms like BEDT-TTF. A small U is expected in BDT-TTP and its derivatives. Since then, many salts of TTP-containing donor were found to be very stable organic metals[73,74]. BDT-TTP is the most basic molecule among the TTP derivatives. Many 2:1 CT salts, such as $(BDT\text{-}TTP)_2X$ ($X=AsF_6$, SbF_6, ClO_4, and ReO_4), exhibit metallic behavior down to liquid helium temperature[75,76]. This behavior is regarded as the result of the two-dimensional electronic structure in the crystal. The band structure of the BDT-TTP salts is very interesting, seems between the one- and two-dimensional structure. Calculated by the extended Hückel calculation, the ratio of the inter-stack transfer integral to the intra-stack transfer integral is around the critical value of a closed Fermi surface. Thereby, the Fermi surface is very sensitive to the small change of this ratio. Some salts have closed Fermi surfaces while others have open Fermi surfaces in the first Brillouin zone, despite the transfer integrals of them are very close and the physical properties are very similar. The study of the band structure will be very useful to understand the relation between the dimensionality and the physical properties. Different from many 2:1 BDT-TTP salts, $\theta\text{-}(BDT\text{-}TTP)_2Cu(NCS)_2$ is an insulator at room temperature. The study of the electronic structure of $\theta\text{-}(BDT\text{-}TTP)_2Cu(NCS)_2$ can further benefit the understanding of the conduction mechanism of the organic conductors.

As the derivatives of TSeT and TTT, which has been studied for many years[77], DMTSA and DMTTA are newly synthesized donor molecules[78]. Smaller U is expected in such large molecule. It is very surprising that the 1:1 salts $DMTSA\text{-}BF_4$ and $DMTSA\text{-}NO_3$ exhibit one-dimensional metallic behavior at room temperature[79], although the conventional 1:1 organic CT salts are regarded as Mott insulators. For elucidation of the peculiar metallic origin, it is very important to investigate the dimensionality of the conducting path, the possibility of the multiple bands, and the on-site Coulomb energy.

The format of this thesis is organized as follow. The first four chapters from Chapter 2 to Chapter 5 are concerned with the electronic structure of the CT salts of BDT-TTP and its analogues, and the last two chapters Chapter 6 and Chapter 7 deal with the electronic structure of DMTSA-BF_4. Chapter 2 presents the study of the energy band structure of β-$(BDT\text{-}TTP)_2X$ (X=SbF_6, AsF_6) by the polarized reflection spectroscopy. Two-dimensional structure is observed while the Fermi surface is open in the first Brillouin zone. The study on the Se analogue salts $(ST\text{-}TTP)_2AsF_6$ and $(BDS\text{-}TTP)_2AsF_6$ is presented in Chapter 3. The effect of the replacement of the sulfur atoms in BDT-TTP by the selenium atoms is discussed by comparing the electronic structure with the BDT-TTP salts. Chapter 4 is about the spectroscopic study of organic metals $(BDT\text{-}TTP)_2Y$ (Y=ClO_4, ReO_4). At first, the charge on the BDT-TTP molecule is studied by the Raman spectroscopy. Then the band structure is studied by the polarized reflection spectroscopy as well and compared with other BDT-TTP salts. The electronic transition of the intra-BDT-TTP^+ monocation radical is discussed in this chapter as well. Chapter 5 is the presentation of the electronic structure of semiconductors $(BDT\text{-}TTP)_2Cu(NCS)_2$. The phase transition at *ca.* 250K was investigated experimentally by the polarized reflection spectroscopy, Raman spectroscopy and ESR. Charge disproportionation is concluded during the phase transition. Chapter 6 deals with the electronic structure of 1:1 metal DMTSA-BF_4 and the iso-structural DMTTA-BF_4 which is non-metallic. Both of them show phase transition at low temperature accompanying the loss of the screw symmetry. The phase transition of DMTSA-BF_4 is concluded as Peierls transition while the phase transition of DMTTA-BF_4 is a spin-Peierls transition. In Chapter 7, an interpretation is proposed for the optical band at near infrared region of DMTSA-BF_4. This band is interpreted very well as the results of the electronic transition from the lower branch to the upper branch.

References:

1) D. S. Acker, R. J. Harder, W. R. Hertler, W. Mahler, L. R. Melby, R. E. Benson, and W. E. Mochel, *J. Am. Chem. Soc.*, **82** (1960) 6408.

2) H. Henres, in *Extended Linear Chain Compounds*, volume 3, ed. by J. S. Miller, Plenum Press, New York, (1983), p263.

3) D. S. Acker, R. J. Harder, W. R. Hertler, W. Mahler, R. E. Benson, and W. E. Mochel, *J. Am. Chem. Soc.*, **84** (1962) 3374.

4) J. B. Torrance, *Acc. Chem. Res.*, **12** (1979) 79.

5) F. Wudl, G. M. Smith, E. J. Hufnagel, *J. Chem. Soc., Chem. Commun.*, (1970) 1453.

6) J. Ferraris, D. O. Cowan, V. Walatka, Jr. Perlstein, and J. H. Perlstein, *J. Am. Chem. Soc.*, **95** (1973) 948.

7) S. Etemad, *Phys. Rev. B,* **13** (1976) 2254.

8) A. A. Bright, A. F. Garito, and A. J. Heeger, *Solid State Commun.*, **13** (1973) 943.

9) D. B. Tanner, C. S. Jacobsen, A. F. Garito, and A. J. Heeger, *Phys. Rev. B*, **13** (1976) 3381.

10) S. Etemad, T. Penney, E. M. Engler, B. A. Scott, and P. E. Seiden, *Phys. Rev. Lett.*, **34** (1975) 741.

11) A. N. Bloch, J. O. Cowan, K. Bechgaard, R. E. Pyle, R. H. Banks, and T. O. Poehler, *Phys. Rev. Lett.*, **34** (1975) 1561.

12) R. B. Somoano, A. Gupta, V. hadek, M. Nonotny, M. Jones, T. Datta, R. Deck, and A. M. Hermann, *Phys. Rev. B*, **15** (1977) 595.

13) F. Wudl, D. Wubschall, and E. J. Hufnagel, *J. Am. Chem. Soc.*, **94** (1972) 670.

14) D. Jérome, A. Mazaud, M. Ribault, and K. Bechgaard, *J. Phys. Lett.*, Paris, **41** (1980) L95.

15) R. Brusett, M. Ribault, D. Jérome, and K. Bechgaard, *J. Phys.*, Paris, **43** (1982) 801.

16) S. S. P. Parkin, D. Jérome, and K. Bechgaard, *Mol. Cryst. Liq. Cryst.*, **79** (1982) 213.

17) S. S. P. Parkin, M. Ribault, D. Jérome, and K. Bechgaard, *J. Phys. C*, **14** (1981) L445.

18) S. S. P. Parkin, M. Ribault, D. Jérome, and K. Bechgaard, *J. Phys. C*, **14** (1981) 5305.

19) K. Bechgaard, C. S. Jacobsen, K. Mortensen, H. J. Pederson, and N. Thorup, *Solid State Commun.*, **33** (1980) 1119.

20) A. Andrieux, D. Jérome, and K. Bechgaard, *J. Phys. Lett.*, Paris, **42** (1981) L87.

21) K. Mortensen, Y. Torekiewicz, T. D. Schultz, and E. M. Engler, *Phys. Rev. Lett.*, **46** (1981) 1234.

22) K. Bechgaard, K. Carneiro, M. Olsen, and F. B. Rasmussen, *Phys. Rev. Lett.*, **46** (1981) 852.

23) L. Ducasse, M. Abderrabba, J. Hoarau, M. Pesquer, B. Gallois, and J. Gaultier, *J. Phys. C*, **19** (1986) 3805.

24) C. S. Jacobsen, D. B. Tanner, and K. Bechgaard, *Phys. Rev. Lett.*, **46** (1981) 1142.

25) T. Ishiguro and K. Yamaji, *Organic Superconductor*, Springer-Verlag, Berlin, (1990) 77.

26) R. Laversanne, C. Coulon, B. Gallois, J. P. Pouget, and R. Moret, *J. Phys. Lett.*, **45** (1984) L393.

27) C. S. Jacobsen, D. B. Tanner, and K. Bechgaard, *Mol. Cryst. Liq. Cryst.*, **79** (1982) 25.

28) S. S. P. Parkin, E. M. Engler, R. R. Schumaker, R. Lagier, V. Y. Lee, J. C. Scott, and R. L. Greene, *Phys. Rev. Lett.*, **50** (1983) 270.

29) J. M. Williams, J. R. Ferraro, R. J. Thron, K. D. Carlson, U. Geiser, H. H. Wang, A. M. Kini, and M.-H. Whangbo, *Organic Superconductors: Synthesis, Structure, Properties, and Theory*, Prentice Hall, Inc., New York (1992).

30) H. Urayama, H. Yamochi, G. Saito, K. Nozawa, T. Sugano, M. Kinoshita, S. Sato, K. Oshima, A. Kawamoto, and J. Tanaka, *Chem. Lett.*, (1988) 55.

31) S. Gärtner, E. Gogu, I. Heinen, H. J. Keller, T. Klutz, D. Schweitzer, *Solid State Commun.*,

65 (1988) 1531.

32) A. M. Kini, U. Geiser, H. H. Wang, K. D. Carlson, J. M. Williams, W. K. Kwok, K. G. Vandervoort, J. E. Thompson, D. L. Stupka, D. Jung, M.-H. Wangbo, *Inorg. Chem.*, **29** (1990) 2555.

33) J. M. Williams, A. M. Kini, H. H. Wang, K. D. Carlson, U. Geiser, L. K. Montgomery, G. J. Pyrka, D. M. Watkins, J. M. Kommers, S. J. boryschuk, A. V. Strieby Crouch, W. K. Kwok, J. E. Schirber, D. L. Overmyer, D. Jung, and M.-H. Whangbo, *Inorg. Chem.*, **29** (1990) 3262.

34) H. Kuroda, K. Yakushi, and H. Tajima, *Mol. Cryst. Liq. Cryst.*, **125** (1985) 135.

35) H. Tajima, K. Yakushi, and H. Kuroda, *Solid State Commun.*, **56** (1985) 159.

36) A. Urayama, G. Ojima, K. Yakushi, and H. Kuroda, *Synth. Met.*, **27** (1988) A445.

37) M. Tamura, H. Tajima, K. Yakushi, H. Kuroda, A. Kobayashi, R. Kato, and H. Kobyashi, *J. Phys. Soc. Jpn.*, **60** (1991) 3861.

38) M. A. Beno, H. H. Wang, A. W. Kini, K. D. Carlson, U. Geiser, U. K. Kwok, J. E. Thompson, J. M. Williams, J. Ren, and M.-H. Whangbo, *Inorg. Chem.*, **29** (1990) 1599.

39) J. Sakata, H. Sato, A. Miyazaki, T. Enoki, Y. Okano, and R. Kato, *Solid State Commun.*, **108** (1998) 377.

40) L. K. Mmontgomery, T. Burgin, T. Miebach, D. Dunham, J. C. Huffman, and J. E. Schirber, *Mol. Cryst. Liq. Cryst.*, **284** (1996) 73.

41) H. Kobayashi, H. Tomita, T. Naito, A. Kobayashi, F. Sakai, T. Watanade, and P. Cassoux, *J. Am. Chem. Soc.*, **118** (1996) 368.

42) K. Kikuchi, K. Murata, Y. Honda, T. Namiki, K. Saito, H. Anzai, K. Kobayashi, T. Ishguro, and I. Ikemoto, *J. Phys. Soc. Jpn.*, **55** (1987) 4241.

43) K. Kikuchi, K. Murata, Y. Honda, T. Namiki, K. Sato, T. Ishiguro, K. Kobayashi, and I. Ikemoto, *J. Phys. Soc. Jpn.*, **55** (1987) 3435.

44) K. Kikuchi, Y. Honda, Y. Ishikawa, K. Saito, I. Ikemoto, K. Murata, A. Anzai, and T. Ishiguro, *Solid State Commun.*, **66** (1988) 405.

45) K. Murata, K, Kikuchi, T. Takahashi, K.Kobayashi, Y. Honda, K. Saito, K. Kanada, T. Toliwa, H. Anzai, and T. Ishiguro, *J. Mol. Elect.*, **4** (1988) 17.

46) G. C. Papavassilion, G. A. Mousdis, J. S. Zambounis, A. Terzis, A. Hountas, B. Hilti, C. W. Mayer, J. Pfeiffer, *Synth. Met.*, **27** (1988) B379.

47) L. Brossard, H. Hurdequint, M. Ribault, L. Valade, J. P. Legros, and P. Cassoux, *Synth, Met.*, **27** (1988) B157.

48) D. Jérome and H. J. Schulz, *Advance In Physics*, **31** (1982) 299.

49) C. S. Jacobsen, J. M. Williams, and H. H. Wang, *Solid State Commun.*, 54 (1985) 937.

50) M.-H. Whangbo, *J. Chem. Phys.*, **75** (1981) 4983.

51) S. Kagoshima, H. Nagasawa, and T. Sambongi, *One-Dimensional Conductors, Spinger-Verlag, Berlin,* (1982) P9.

52) *Ibid,* P18.

53) J. Hubbard, *Proc. R. Soc.*, London, **276** (1963) A238.

54) J. B. Torrance, in *Low-Dimensional Conductors And Superconductors*, Ed. By D. Jérome and L. G. Caron, Plenum Press, New York, (1987) P113.

55) C. S. Jacobsen, in *Low-Dimensional Conductors And Superconductors*, Ed. By D. Jérome and L. G. Caron, Plenum Press, New York, (1987) P253.

56) H. Makino, I. Inoue, M. J. Rezenberg, I. Hase, Y. Aiura, and S. Onari, *Phys. Rev. B*, **58** (1998) 4384.

57) D. A. Crandles, T. Timusk, J. D. Garrett, and J. E. Greedan, *Phys. Rev. B*, **49** (1994) 16207.

58) C. S. Jacobsen ,Ib Johannsen, and K. Bechgaard, *Phys. Rev. Lett.*, **53** (1984) 194.

59) J. Dong, K. Yakushi, K. Takimiay, aAnd T. Otsubo, *J. Phys. Soc. Jpn.*, **67** (1998) 971.

60) D. Baeriswyl, J. Carmelo, and A. Luther, *Phys. Rev. B*, **33** (1986) 7247.

61) M. J. Rice, *Solid State Commun.*, **31** (1979) 93.

62) M. J. Rice, L. Pietronero, and P. Briiesch, *Solid State Commun.*, **21** (1977) 757.

63) V. M. Yartsev, *Synth. Met.*, **83** (1996) 253.

64) A. Girlando, F. Marzola, and C. Pecile, *J. Chem. Phys.*, **79** (1983) 1075.

65) R. P. Vanduyne, T. W. Cape, M. R. Suchanski, and A. R. Siedle, *J. Phys. Chem.*, **90** (1986) 739

66) J. S. Chappell, A. N. Bloch, W. A. Bryden, M. Maxfield, T. O. Poehler, and D. O. Cowan, *J. Am. Chem. Soc.*, 103 (1981) 2442.

67) K. D. Truong, D. Achkir, S. Jandl, and M. Poirier, *Phys. Rev. B*, **51** (1995) 16168.

68) R. Bozio, M. Meneghetti, and C. Pecile, *J. Chem. Phys.*, **76** (1982) 5785.

69) R. Bozio and C. Pecile, *J. Phys, C*, **13** (1980) 6205.

70) A. D. Bandrauk, in *Low-Dimensional Conductors and Superconductors*, Ed. By D. Jérome and L. G. Caron, Plenum Press, New York, (1987) P295.

71) R. R. Schumaker and E. M. Engler, *J. Am. Chem. Soc.*, **102** (1980) 6652.

72) Y. Misaki, T. Matsui, K. Kawatami, H. Nishikawa, T. Yamabe, and M. Shiro, *Chem. Lett.*, (1993) 1337.

73) Y. Misaki and T. Mori, *Solid State Physics*, **33** (1998) 1014.

74) T. Mori, T. Kawamoto, Y. Misaki, K. Kawakami, H. Fujiwara, T. Yamabe, H. Mori, and S. Tanaka, *Mol. Cryst. Liq. Cryst.*, **284** (1996) 271.

75) Y. Misaki, T. Matsui, K. kawamoto, H. Fujiwara, T. Yamabe, T. Mori, H. Mori, S. Tanaka, and M. Shiro, *Synth. Met.*, **70** (1995) 1149.

76) Y. Misaki, H. Fujiwara, T. Yamabe, T. Mori, H. Mori, and S. Tanaka, *Chem. Lett.*, (1994) 1653.

77) I. F. Shchegolev and E. B. Yagubskii, in *Extended Linear Chain Compounds*, volume 2 ed.

by J. S. Miller, Plenum Press, New York, (1982) p385.

78) K. Takimiya, Y. Aso, T. Otsubo, and F. Ogura, *Bull. Chem. Soc. Jpn.*, **64** (1991) 2091.

79) K. Takamiya, A. Ohnishi, Y. Aso, T. Otsubo, F. Ogura, K. Kawabata, K. Tanaka, and M. Mizutani, *Bull. Chem. Soc. Jpn.*, **67** (1994) 766.

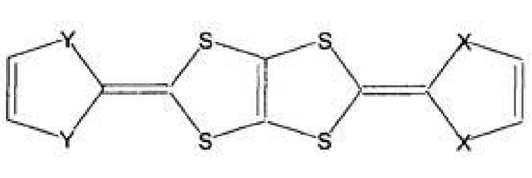

X = Y = S BDT-TTP
X = S, Y = Se ST-TTP
X = Y = Se BDS-TTP

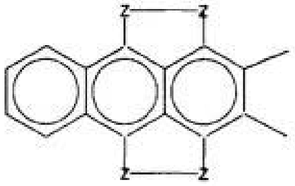

Z = Se DMTSA
Z = S DMTTA

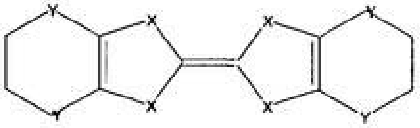

X = Y = S BEDT-TTF
X = Se, Y = S BEDT-TSF
X = S, Y = Se BEDSe-TTF

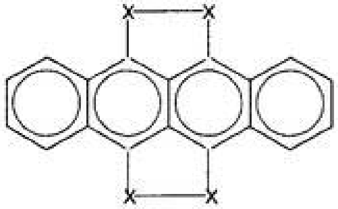

X = S TTT
X = Se TSeT

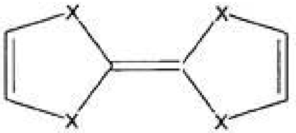

X = Se TSF
X = S TTF

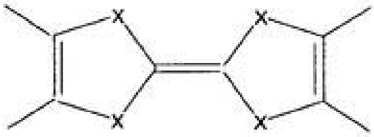

X = Se TMTSF
X = S TMTTF

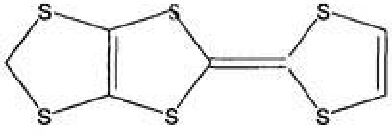

MDT-TTF

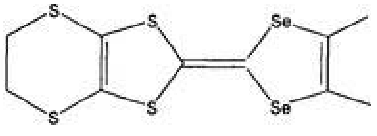

DMET

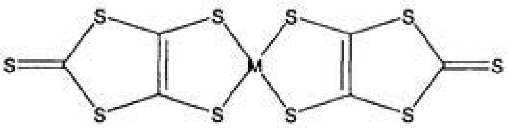

M(dmit)$_2$

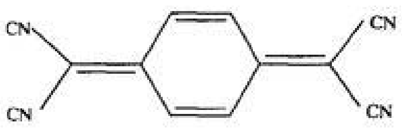

TCNQ

Fig.1 Molecular structure of some organic donors and acceptors

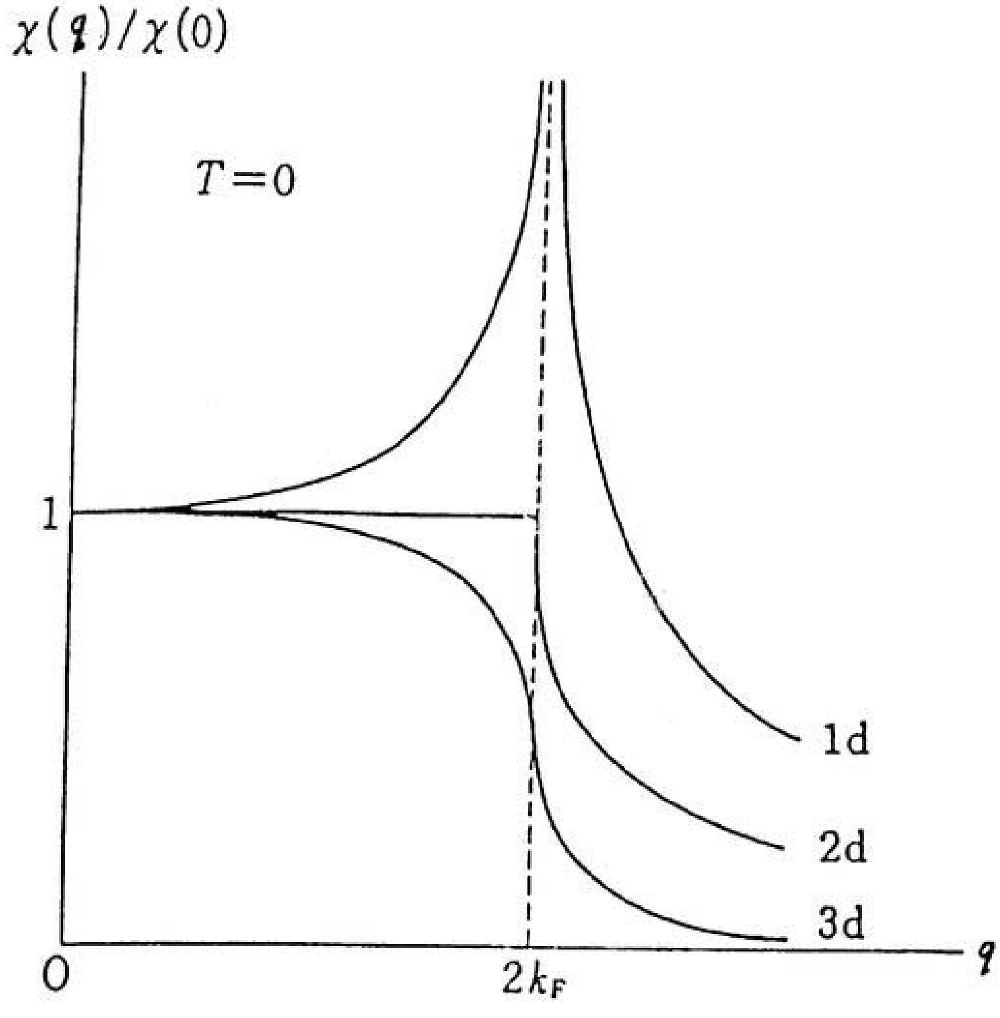

Fig. 2 Polarization function χ(Q) at absolute zero in each dimension. (from ref. 51).

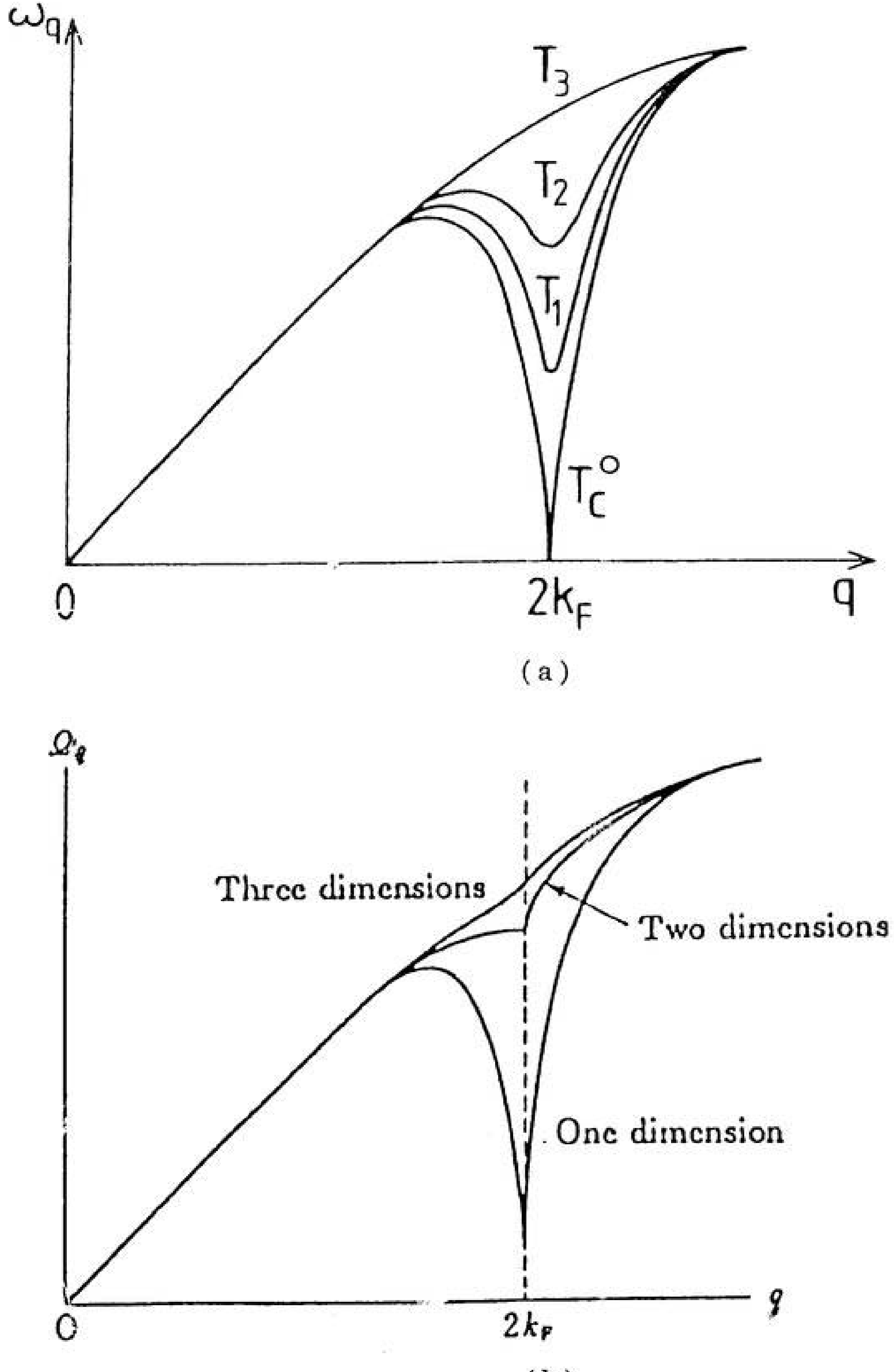

(a)

(b)

Fig. 3 (a) Development of the one-dimensional Kohn anomaly with decreasing temperature. (from ref. 48). (b) Kohn anomaly of phonons in each dimension. (from ref. 52).

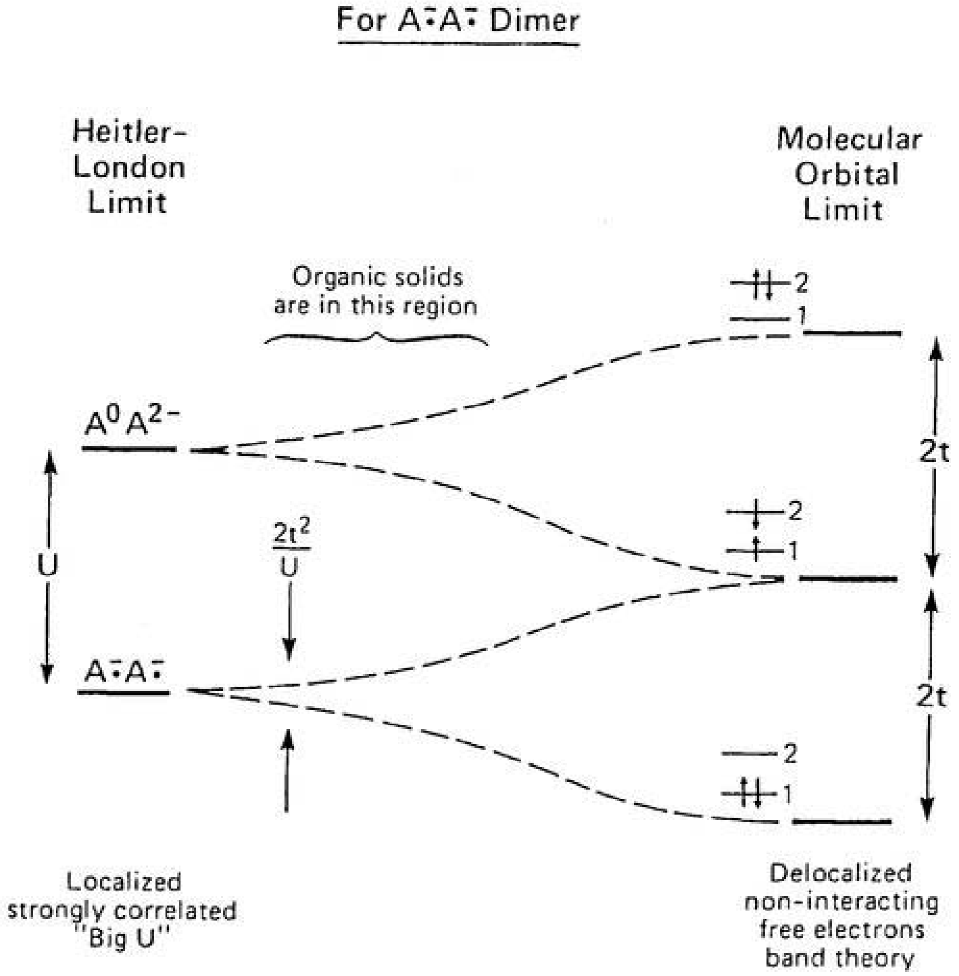

Fig. 4 Energy level for states of a A·A· dimer in the two extreme limits: Heitler-London and Molecular Orbital. Dashed lines represent schematic solution from the intermediate regime (from ref. 54).

Chapter 2

Two-Dimensional Band Structure of Organic Metals $(BDT\text{-}TTP)_2X$ ($X=SbF_6$, AsF_6) Studied by Polarized Reflection Spectroscopy

Jiangyong Ouyang, Kyuya Yakushi, Yoji Misaki, and Kazuyoshi Tanaka

Two-dimensional band structure of organic metals $(BDT\text{-}TTP)_2X$ ($X=SbF_6$, AsF_6) studied by polarized reflection spectroscopy

J. Phys. Soc. Jpn., 67 (1998) 3191.

J. Ouyang, K. Yakushi, Y. Misaki, and T. Tanaka

Band structure of $(BDT\text{-}TTP)_2X$ ($X=SbF_6$, AsF_6, ClO_4) studied by reflection spectroscopy

Synth. Met., 103 (1999) 2207

2.1. Introduction

BDT-TTP (2,5-bis(1,3-dithiol-2-ylidene)-1,3,4,6-tetrathiapentalene) and its relative molecules including TTP skeleton were found to give enormous number of metallic charge-transfer salts down to liquid helium temperature.1)-8) Among these compounds, BDT-TTP was the simplest molecule, in which two TTF skeletons were fused without loosing the π-conjugation. BDT-TTP was designed and synthesized to reduce the on-site Coulomb energy by extending the π-conjugation of the TTF skeleton. Actually the difference (E_2-E_1) between the first (E_1) and second (E_2) oxidation potentials, which was regarded as the conventional measure of the Coulomb interaction within a molecule, was significantly smaller than that of TTF.9) The stable metallic property was regarded as the result of the small on-site Coulomb energy due to this extended π-electron molecular orbital and the strong inter-chain interaction through short side-by-side S-S contacts.1,2) The electrical resistivity of $(BDT\text{-}TTP)_2AsF_6$ behaved metallic down to 2K.1) $(BDT\text{-}TTP)_2SbF_6$ showed a broad peak around 180K and then decreased again below this temperature down to 2K.1) Under high pressure, the electrical resistivity of $(BDT\text{-}TTP)_2SbF_6$ in the conducting plane (010) was metallic and showed no anomaly down to 1.5K, and the resistivity along the direction perpendicular to the conducting plane (010) is three orders magnitude larger than that of the conducting plane.10) The energy-band calculation of $(BDT\text{-}TTP)_2SbF_6$ in the framework of tight-binding approximation predicted a closed Fermi surface of a rectangular shape with round corners.1) Recently, Nakada *et al.* studied the magnetoresistance of $(BDT\text{-}TTP)_2X$ (X=SbF_6, and AsF_6) at 1.5K. The closed Fermi surface well reproduced the observed angle dependence of the low-field magnetoresistance of $(BDT\text{-}TTP)_2SbF_6$ but the very similar Fermi surface cannot reproduce the result of $(BDT\text{-}TTP)_2AsF_6$.11) In spite of the isostructure, the magnitude of the low-field magnetoresistance of AsF_6 salt is significantly larger than that of SbF_6 salt. No other studies have been conducted on these newly synthesized compounds.

The polarized reflection spectroscopy is a powerful method to probe the band structure, and the anisotropy of the plasma frequency is directly related to the transfer integrals.12) -15) The study of the band structure is the first step to understand the solid electronic properties of new materials. In this paper, we report the reflectance spectra of (BDT-TTP)$_2$X (X=SbF$_6$, AsF$_6$) single crystals, and compare the anisotropic plasma frequencies with the theoretical calculation reported by Misaki *et al.*1) Then we estimate the optimum intra- and inter-stack transfer integrals to reproduce the observed plasma frequencies. The temperature dependence of these transfer integrals is presented as well.

2.2. Experimental

Single crystals of (BDT-TTP)$_2$X (X=SbF$_6$, AsF$_6$) were grown by the electrochemical oxidation method. The crystals were black with a thin plate-like shape developing a (010) crystal face. The dimensions were $0.8\times0.35\times0.04\text{mm}^3$ for (BDT-TTP)$_2$SbF$_6$ and $0.8\times0.25\times0.04\text{mm}^3$ for (BDT-TTP)$_2$AsF$_6$. The single crystal was fixed on a copper sample holder by silicone grease. The crystal face was adjusted so as to be nearly normal to the incident light by use of a small goniometer head attached to the cold head of the cryostat, Oxford CF1104s. The sample was covered by a radiation shield and vacuum shroud with KBr window. The cryostat was evacuated below 10^{-5}Pa by turbo-molecular pump before cooling the sample. To avoid the contamination on the sample surface at low temperature, the window of the radiation shield was open only in the measurement. A microscope system, Spectra-Tech IR-Plan, was modified and inserted in the light path of the sample chamber of the FT-IR spectrometer, Nicolet Magna 760. The spectra in the region from 700 to 7000cm^{-1} were collected using a globar light, MCT detector, KBr beam splitter, and wire-grid polarizer, and those of 4000-10000cm^{-1} region were measured using a halogen lamp, MCT detector, Quartz beam splitter, and Glan-Thompson polarizer. The absolute reflectivity was obtained by comparing the reflected light from a gold mirror placed close to the sample in the cryostat, which could cancel out the spectral dependence of the transmittance of the KBr window. The reflectivity of this inner mirror was monitored at each temperature using the gold mirror outside of the cryostat. The visible region from 10000-25000cm^{-1} were measured only at room temperature using the same microscope system combined with a multi-channel detection system, Atago Macs320, using a xenon-lamp as a light source and Glan-Thompson prism as a polarizer. The reflectivity was obtained using the silicon single crystal as a standard mirror.

2.3. Results and Discussion

2.3.1 Room-temperature spectra and estimation of transfer integrals

The crystal of (BDT-TTP)$_2$SbF$_6$ belongs to triclinic system with lattice parameters of a=6.935, b=18.167, and c=6.405Å, α=98.34, β=101.11, and γ=81.50°.$^{1)}$ The BDT-TTP molecules are stacked along the a-axis aligning the long molecular axis nearly along the [$\bar{1}$20] direction. BDT-TTP makes a zigzag stack as shown in Fig. 1b. The two molecules (A and A') in a unit cell is connected with inversion symmetry, so the overlap modes A-A' and A'-A is not crystallographically equivalent. However, the above two are nearly equivalent, that is the geometrical dimerization is very weak. The crystal of (BDT-TTP)$_2$AsF$_6$ is isostructural to (BDT-TTP)$_2$SbF$_6$, the lattice parameters being a=6.940, b=17.967, c=6.397Å, α=98.88, β=100.72, γ=81.24°. The arrangement of molecules resembles those of Bechgaard salts$^{16)}$ and β-(BEDT-TTF)$_2$I$_3$$^{17)}$ except the weakly-dimerized arrangement. From these crystal structure, we can draw the following figure on the band structure: The BDT-TTP molecules make a conducting sheet in the (010) plane by fact-to-face and side-by-side hopping interactions as shown in Fig. 1c and these sheets are separated by counter anions as shown in Fig. 1b. One hole is doped in the unit cell from counter anions and a quarter-filled band is formed in these compounds. Since the hopping interaction across these BDT-TTP sheet seems to be much weaker than within the sheet, these holes are likely to be confined in this conducting sheet. As a matter of fact, the electrical resistivity of $(BDT\text{-}TTP)_2SbF_6$ along the direction perpendicular to the conducting sheet is three orders of magnitude larger than that within the conducting sheet.$^{10)}$ Therefore the two-dimensional band is a good approximation.

Figures 2a and 2b show the reflectance spectra measured with polarizations parallel ($E//a$) and perpendicular ($E\perp a$) to the stacking direction on the (010) crystal faces of $(BDT\text{-}TTP)_2SbF_6$ and $(BDT\text{-}TTP)_2AsF_6$, respectively. They are very similar to each other. Strong dispersions appear in both directions in the infrared and near-infrared regions. It should be noted that this Drude-like dispersion occurs at a slightly higher wavenumber in the $E//a$ spectrum of $(BDT\text{-}TTP)_2AsF_6$ than in $(BDT\text{-}TTP)_2SbF_6$, while it starts at a slightly lower wavenumber in the $E\perp a$ spectrum of $(BDT\text{-}TTP)_2AsF_6$ than in $(BDT\text{-}TTP)_2SbF_6$. Both of them can be satisfactorily fitted by a Drude model except the hump at $1380 cm^{-1}$ in the $E//a$ spectrum and the dispersion by phonon absorption in the $E\perp a$ spectrum. The best-fit curves of the Drude model are drawn by dotted lines in the same figures. It is rather surprising that the reflectance curve is fitted so well by such a simple Drude model, because the infrared region of the reflection spectra of organic metals such as TTF-TCNQ,$^{12)}$ $(TMTSF)_2PF_6$,$^{13)}$ and β-$(BEDT\text{-}TTF)_2I_3$ $^{14)}$ are more complicated. To the author's best knowledge, this is the first organic compound whose reflection spectrum is described by a simple Drude model.

Table I gives the Drude parameters and hole effective masses m_i^* which are calculated by the relation of $(\omega_{pi})^2=ne^2/\varepsilon_0 m_i^*$, where n is the hole density, ε_0 the dielectric constant of vacuum, i the direction of the polarization of the light. The plasma frequencies of (BDT-

TTP)$_2$SbF$_6$ in both directions are nearly the same as the corresponding ones of (BDT-TTP)$_2$AsF$_6$. The effective mass ratio $m^*_{//}/m^*_{\perp}$ is 0.11 for (BDT-TTP)$_2$SbF$_6$ and 0.08 for (BDT-TTP)$_2$AsF$_6$, which means that the latter compound is more anisotropic. The plasmon in the inter-stack direction is not over-dumped ($\gamma_{\perp}<\omega_{p\perp}$), which is different from the case of inter-stack direction of (TMTSF)$_2$PF$_6$ and β-(BEDT-TTF)$_2$I$_3$ at room temperature. This means that the inter-stack transfer integral is significantly larger than those of the above two organic metals. As predicted from the theoretical calculation of the overlap integrals between adjacent molecules, both compounds have significant inter-stack interaction. For the more quantitative comparison, the plasma frequency is calculated using the five transfer integrals given by Misaki *et al.*[1)] The plasma frequency is calculated by the following equation,[14)]

$$\omega_p^2 = \frac{ne^2}{\varepsilon_0 \hbar^2} \frac{\iint f(E(k_a k_c)) \frac{\partial^2 E(k_a k_c)}{\partial k_i^2} \mathrm{d}k_a \mathrm{d}k_c}{\iint f(E(k_a k_c)) \mathrm{d}k_a \mathrm{d}k_c} \tag{2.1}$$

where $E(k_a,k_c)$ is the two-dimensional dispersion of the energy and $f(E)$ the Fermi-Dirac function. We divided the first Brillouin zone into 200×200 meshes, and numerically integrated the second derivatives of $E(k_a,k_c)$ assuming T=0K for the distribution function. The calculated results are given in the last column of Table I. The agreement for $\omega_p(//a)$ is surprisingly good but not sufficient for $\omega_p(\perp a)$: $\omega_p(\perp a)$ is almost twice the experimental value, that is the actual material is more anisotropic.

The disagreement of the plasma frequencies is attributable to the estimation of the five transfer integrals shown in Fig. 1c. Misaki *et al.* present the transfer integrals of (BDT-TTP)$_2$SbF$_6$ as t_{a1}=-0.251, t_{a2}=-0.253, t_c=-0.008, t_{p1}=-0.079, and t_{p2}=-0.086eV.[1)] The two-dimensional energy dispersion $E(k_a,k_c)$ is expressed by the following equation,

$$E(k_a,k_c) = 2t_c \cos(k_c c) \pm |H_{12}|, \tag{2.2}$$

and

$$
\begin{aligned}
H_{12}^2 &= t_{a1}^2 + t_{a2}^2 + t_{p1}^2 + t_{p2}^2 + 2t_{a1}t_{a2}\cos(k_a a) + 2(t_{a1}t_{p1} + t_{a2}t_{p2})\cos(k_c c) \\
&+2(t_{a1}t_{p2} + t_{a2}t_{p1})\cos(k_a a + k_c c)) + 2t_{p1}t_{p2}\cos(k_u a + 2k_c c))
\end{aligned}
$$

where a and c are the lattice constant, k_i (i=a and c) is the reciprocal vector running over the first Brillouin zone. The plasma frequencies given in Table I are calculated using the equations (2.1) and (2.2). It is obvious from these equations that all the transfer integrals contribute to both the plasma frequencies $\omega_p(//a)$ and $\omega_p(\perp a)$. Due to the weakly dimerized structure, t_{a1} is nearly equals to t_{a2}, t_{p1} is also close to t_{p2}, and t_c is an order of magnitude smaller than t_{p1} and t_{p2}. Hence, it is a good approximation to assume $t_{a1}=t_{a2}=t_a$, $t_{p1}=t_{p2}=t_p$ and $t_c=0$. Under this assumption $E(k_a, k_c)$ is expressed only by two parameters t_a and t_p. To obtain t_a and t_p, we numerically solve the simultaneous equations (1) for $\omega_p(//a)$ and $\omega_p(\perp a)$ by dividing the first Brillouin zone into 200×200 meshes. The best solution is the set of t_a=-0.259 and t_p=-0.048 eV, which gives $\omega_p(//a)=9.30\times10^3\text{cm}^{-1}$ and $\omega_p(\perp a)=3.20\times10^3\text{cm}^{-1}$. The agreement of calculated plasma frequencies with the observed is quite good taking the experimental error of plasma frequencies into account. The estimated transfer integrals are listed in Table II along with those of $(\text{BDT-TTP})_2\text{AsF}_6$, $(\text{TMTSF})_2\text{PF}_6$,[18] and β-$(\text{BEDT-TTF})_2\text{I}_3$[14] for comparison. The agreement with the calculated transfer integrals along the stack (t_{a1} and t_{a2}) is surprisingly good in spite of a very simple calculation. However, the theoretical calculation overestimates the inter-stack transfer integrals (t_{p1}, t_{p2} and t_c), which is almost twice as large as the observed.

2.3.2 *Band structure*

Figures 3a and 3b show the comparison of the energy dispersion and density of state of $(\text{BDT-TTP})_2\text{SbF}_6$ which are calculated using the experimentally obtained transfer integrals and theoretically estimated transfer integrals. As it is understood from eq. (2.2), the energy band is split into upper and lower band with a very narrow gap. The energy of a special point in Brillouin zone is given by the following equations:

$$E_\Gamma = 2t_c \pm \left|t_{a1} + t_{a2} + t_{p1} + t_{p2}\right|, \tag{2.3}$$

$$E_Z = -2t_c \pm \left|t_{a1} + t_{a2} - t_{p1} - t_{p2}\right|, \tag{2.4}$$

$$E_X = 2t_c \pm \left|t_{a2} - t_{a1} + t_{p2} - t_{p1}\right|. \tag{2.5}$$

$$E_B = -2t_c \pm \left|t_{a1} - t_{a2} + t_{p2} - t_{p1}\right|. \tag{2.6}$$

The energy difference between upper and lower bands at Γ point gives the bandwidth ($W=2|t_{a1}+t_{a2}+t_{p1}+t_{p2}|$=1.22eV in (BDT-TTP)$_2SbF_6$). This bandwidth is comparable to that of (TMTSF)$_2$PF$_6$$^{13)}$ (W=1.0eV) and much wider than that of β-(BEDT-TTF)$_2$I$_3$ (W=0.5eV)$^{14)}$. The narrow gaps at X and B points are produced by the differences in t_a and t_p which come from the weak dimerization within the molecular stack. The energy on the VX line looks like crossing, but there is a very small gap at this crossing point. As shown in Figs. 4a and 4b, the Fermi surface is open in the k_c direction, which is different from the calculation by Misaki *et al.* This difference is attributable to the energy at the Z point which is determined by the difference of the intra-stack (t_a) and inter-stack (t_p) transfer integrals. Since the theoretical calculation overestimates t_{p1} and t_{p2}, the energy of the upper band at the Z point is lower than the experimentally estimated E_z, and thus it becomes slightly lower than the Fermi energy, which makes the Fermi surface closed. In this compound the energy of the upper band at Z point is close to the Fermi energy, so the small difference of the transfer integrals make a big influence on the shape of the Fermi surface near the Z point. The anisotropy of the intra- and inter-stack transfers decides whether the Fermi surface is open or closed. Under the 2-parameters approximation $t_{a1}=t_{a2}=t_a$, $t_{p1}=t_{p2}=t_p$ and $t_c=0$, E_z can be expressed as $E_Z=2t_a$(1-

t_p/t_a). If we adopt t_a=0.259eV and E_F=0.357eV, $t_p/t_a \geqq 0.31$ is the critical value to close the Fermi surface in the k_c direction. The average values of t_a and t_p obtained by theoretical calculation give t_p/t_a=0.33 just clearing this condition but the experimentally obtained ratio t_p^{opt}/t_a^{opt} (=0.19) is much lower than this critical value. Jacobsen *et al.* have proposed a simple criterion to judge whether the Fermi surface is open or closed in the orthorhombic crystal structure approximation.[19] According to their report, the Fermi surface is open, if the ratio $(\omega_{p\perp}d_{//})/(\omega_{p//}d_{\perp})$ is smaller than 0.35, where $d_{//}$ and $d_{\perp}$ are the repeating unit distance parallel and perpendicular to the stack, respectively. The ratio $(\omega_{p\perp}d_{//})/(\omega_{p//}d_{\perp})$ of (BDT-TTP)$_2$SbF$_6$ is 0.18, which is significantly smaller than the critical value. The Fermi surface of (BDT-TTP)$_2$SbF$_6$ is open according to this criterion as well. We therefore consider that the more anisotropic (BDT-TTP)$_2$AsF$_6$ also has an open Fermi surface.

Recently Nakada *et al.* studies magnetoresistance of (BDT-TTP)$_2$SbF$_6$ at 1.5K under 2.3kbar and that of (BDT-TTP)$_2$AsF$_6$ at 1.5K under 3.4kbar[11]. Let us briefly introduce their result. The behavior of the transverse magnetoresistance across the conducting sheet ($\Delta\rho\perp/\rho\perp$) is different between (BDT-TTP)$_2$SbF$_6$ and (BDT-TTP)$_2$AsF$_6$: the former shows a weak angle dependence whereas the latter shows a strong dependence. They simulate the angle dependence of the transverse magnetoresistance interpreting that the magnetoresistance in a weak magnetic field comes from the anisotropic Fermi velocity on the two-dimensional Fermi surface. According to their simulation based on the band structure given by Misaki *et al.*, the weak angle dependence of (BDT-TTP)$_2$SbF$_6$ is reproduced by the closed Fermi surface, but the strong angle dependence of (BDT-TTP)$_2$AsF$_6$ is not reproduced by the similar but slightly open Fermi surface. They suggest that this difference between SbF$_6$ and AsF$_6$ salts is ascribed to the stronger correlation effect in more anisotropic (BDT-TTP)$_2$AsF$_6$. The study of the magnetoresistance looks to be supporting the closed Fermi surface shown in Fig. 4b. On the other hand, the optical experiment indicates that the reflection spectra of (BDT-TTP)$_2$SbF$_6$ and (BDT-TTP)$_2$AsF$_6$ are very similar and even hard to be distinguished. This is reasonable since the structure of (BDT-TTP)$_2$SbF$_6$ is isostructural to that of (BDT-TTP)$_2$AsF$_6$ and the optical experiment in this spectral region is not influenced by the correlation effect. As described in the preceding paragraph, the optical spectra indicate that the Fermi surfaces of both SbF$_6$ and AsF$_6$ salts are open in the k_c direction and their shapes are almost same to each other. The Fermi surface of (BDT-TTP)$_2$SbF$_6$ at low temperature becomes more open as will be described in § 2.3.3.[20] The comparison in the same experimental condition is necessary to understand the reason of the discrepancy, since there is no structural data under high pressure which might increase the inter-stack interaction.

As described in the first paragraph of § 2.3.1, the pattern of molecular arrangement in the conducting sheet is common for (BDT-TTP)$_2$X (X=SbF$_6$, AsF$_6$), (TMTSF)$_2$PF$_6$ and β-(BEDT-TTF)$_2$I$_3$. The molecules are stacked with a ring-external bond overlap mode, making a zigzag chain. The structural features to characterize these compounds are the anisotropy of the Fermi surface and the degree of dimerization. The anisotropy is expressed by the experimentally obtained effective mass: The ratios $m_{//}^*/m_\perp^*$ are 0.11 (300K) and 0.08 (10K) for (BDT-TTP)$_2$SbF$_6$, 0.08 (300K) for (BDT-TTP)$_2$AsF$_6$, 0.04 (100K) for (TMTSF)$_2$PF$_6$[21], and 0.29 (30K) for β-(BEDT-TTF)$_2$I$_3$[22]. The anisotropy of (BDT-TTP)$_2$X is closer to (TMTSF)$_2$PF$_6$ than to β-(BEDT-TTF)$_2$I$_3$ and therefore the open Fermi surface of (BDT-TTP)$_2$X resembles (TMTSF)$_2$PF$_6$. However, the dimensionality of BDT-TTP salts is significantly higher than (TMTSF)$_2$PF$_6$. The dimerization is expressed by the ratio t_{a1}/t_{a2} shown in Table II. The strong dimerization gives rise effectively a half-filled band in 3/4-filled band, which enhances the correlation effect.[23] In this sense (BDT-TTP)$_2$X is almost free from such a dimerization effect, which may be related to the very stable metallic state of this compound.

2.3.3 Temperature dependence of the reflectance spectra of $(BDT\text{-}TTP)_2SbF_6$

Figure 5 shows the temperature dependence of *E//a* reflectance spectra of $(BDT\text{-}TTP)_2SbF_6$ from 300K to 10K. The conductivity spectra calculated by Kramers-Kronig transformation are shown in Fig. 6. The low wavenumber region ($0\text{-}700\text{cm}^{-1}$) of the reflectivity is extrapolated using a Hagen-Rubens model. The reflectivity increases on lowering the temperature, and approximately described by Drude model, although the fitting becomes more incomplete at low temperature. Since BDT-TTP is weakly dimerized along the stacking a-axis, several a_g vibronic modes usually appears in the *E//a* spectrum. However only one a_g vibronic mode is observed at 1390 cm^{-1} in this compound. This vibronic mode appears as a dip (Fano anti-resonance) in the conductivity spectra as shown in Fig. 6. The conductivity curve including the dip is well reproduced by the following function.24)

$$\sigma(\omega) = \sigma_D(\omega) + p\sigma_D(\omega)\{F(\omega) - 1\} \tag{2.7}$$

$$\sigma_D(\omega) = \frac{\varepsilon_0 \omega_p^2 \gamma_D}{\omega^2 + \gamma_D{}^2}, \text{ and } F(\omega) = \frac{\{q + (\omega - \omega_0)/\gamma\}^2}{1 + \{(\omega - \omega_0)/\gamma\}^2} \tag{2.8}$$

where $\sigma_D(\omega)$ is the real part of the conductivity of the Drude model and $F(\omega)$ is the line-shape function to describe the Fano interference effect. The parameter p represents the intensity fraction of the vibronic mode, q the inverse asymmetric parameter, ω_0 the resonance energy of the discrete state, γ the decay rate of the discrete state in the continuum state. The typical parameters for example at 10K is p=0.48, q=0.05, ω_0=1390cm^{-1}, γ=135cm^{-1}. The small q indicates that this vibronic mode is strongly coupled with the conduction electron absorption, which is consistent with the stronger intensity and much broader linewidth than the infrared active modes. This vibration is probably associated with the totally symmetric C=C stretching mode of TTF and/or TTP skeleton, which appears at 1410cm^{-1} or 1479cm^{-1} in Raman spectrum. The feature of the coupling with intra-molecular vibration (local phonon) is very different from the rich vibronic bands in (TMTSF)$_2$PF$_6$ $^{13)}$ and β-(BEDT-TTF)$_2$I$_3$$^{14)}$. It is surprising that only this mode is coupled with conduction-electron absorption band, which means that the sum of the coupling constants with local phonons is very small in (BDT-TTF)$_2$SbF$_6$.

Figures 7 and 8 show respectively the $E \perp a$ polarization of the reflectance and conductivity spectra, in which several infrared active vibrational bands are observed. Table III shows the wavenumbers and plasma frequencies of these infrared active modes at 10K. It is reasonable that no vibronic (a_g) mode is observed in this polarization, since BDT-TTP is not dimerized but regularly arranged along the *c*-axis. The strongest vibrational band at 3084cm^{-1} is assigned as the CH stretching mode. One of the reasons of this strong intensity is ascribed to the long molecular shape which is possible to induce a large transition dipole moment. In addition to this geometrical reason, the strong intensity suggests that the wave function of the conduction electron is extended over the hydrogen atom. In connection with this conjecture, we measure the absorption spectra of the powdered samples of BDT-TTP and (BDT-TTP)$_2$SbF$_6$. The CH stretching mode shifts to blue by 20-30cm^{-1} compared with that of neutral BDT-TTP. In this way the valence of molecule (0 for BDT-TTP and +0.5 in (BDT-TTP)$_2$SbF$_6$) makes an influence on the CH stretching mode. This means that HOMO of BDT-TTP is extended over the hydrogen atom. Since the conduction band is produced by HOMO of BDT-TTP, this result strongly suggests that the wave function of the conduction electron is delocalized over the hydrogen atoms as well.

Since the low-temperature reflectance spectra are approximately fitted by a Drude model, the temperature-dependent spectra are analyzed in the same way as the room-temperature using the room-temperature lattice constants and two-parameter model. The temperature dependence of the Drude parameters is listed in Table IV. $\omega_{p//}$ and $\omega_{p\perp}$ show opposite dependence upon temperature: $\omega_{p//}$ increases on lowering temperature whereas $\omega_{p\perp}$ slightly decreases, so the anisotropic ratio $\omega_{p//}/\omega_{p\perp}$ increases at low temperature. Fig.9 shows the temperature dependence of t_a, t_p and their anisotropic ratio t_a/t_p. t_a increases remarkably on lowering temperature as $\omega_{p//}$ increases, whereas t_p does not change at all, though $\omega_{p\perp}$ decreases at low temperature. This is because t_p relates not only to $\omega_{p\perp}$ but also $\omega_{p//}$. The anisotropic ratio t_a/t_p increases on lowering temperature as shown in Fig. 9. According to the equation (4), E_Z will increase at low temperatures and the Fermi surface is more open in the k_c direction at low temperature.

§2.4. Summary

Both the $E//a$ and $E\perp a$ reflectance spectra of $(BDT\text{-}TTP)_2X$ ($X=SbF_6$, AsF_6) exhibit Drude-like plasma edges in the conduction plane (010). The effective mass ratio which is obtained from the plasma frequencies shows that the anisotropy is much higher than that of two-dimensional β-$(BEDT\text{-}TTF)_2I_3$ and close to but lower than that of pseudo-one-dimensional $(TMTSF)_2PF_6$. The transfer integrals are determined to reproduce the observed plasma frequencies assuming a two-parameter model. It is concluded from this experiment that the theoretical calculation overestimates the inter-stack transfer integrals. These transfer integrals yield an open Fermi surface in the k_c direction, which is different from the closed Fermi surface predicted by the extended Hückel calculation. On lowering temperature, the transfer integrals in the parallel (t_a) and perpendicular (t_p) directions increase in $(BDT\text{-}TTP)_2SbF_6$ due to the lattice contraction, but the increase of t_p is very small, so the ratio (t_a/t_p) increases. Consequently the this compound becomes more pseudo-one-dimensional at low temperature. A strong vibronic mode is observed in the $E//a$ spectrum, the shape of which is well reproduced by the function to describe the Fano anti-resonance. A strong infrared active CH stretching mode is observed at 3084cm^{-1} in the $E\perp a$ spectrum, which suggests that the wave function of the conduction electron is extended over the hydrogen atoms of BDT-TTP molecule.

References:

1) Y. Misaki, H. Fujiwara, T. Yamabe, T. Mori, H, Mori, and S. Tanaka, *Chem. Lett.*, (1994) 1653.

2) T. Mori, Y. Misaki, H. Fujiwara, and T. Yamabe, *Bull. Chem. Soc. Jpn.*, **67** (1994) 2685.

3) T. Mori, T. Kawamoto, Y. Misaki, K. Kawakami, H. Fujiwara, T. Yamabe, H. Mori, and S. Tanaka, *Mol. Cryst. Liq. Cryst.*, **284** (1996) 271.

4) T. Mori, T. Kawamoto, Y. Misaki, K. Kawakami, H. Fujiwara, T. Yamabe, H. Mori, and S. Tanaka, *Mol. Cryst. Liq. Cryst.*, **284** (1996) 271.

5) Y. Misaki, N. Higuchi, T. Ohta, H. Fujiwara, T. Yamabe, T. Mori, H. Mori, and S. Tanaka, *Mol. Cryst. Liq. Cryst.*, **284** (1996) 27.

6) T. Mori, Y. Misaki, T. Yamabe, H. Mori, S. Tanaka, *Chem. Lett.*, **1995**, 549.

7) T. Mori, H. Inokuchi, Y. Misaki, H. Nishikawa, T. Yamabe, H. Mori, and S. Tanaka, *Chem. Lett.*, **1993**, 2085.

8) T. Mori, H. Inokuchi, Y. Misaki, H. Nishikawa, T. Yamabe, H. Mori, and S. Tanaka, *Chem. Lett.*, 1993, 733.

9) Y. Misaki, T. Matsui, K. Kawamoto, H. Nishikawa, T. Yamabe, M. Shiro, *Chem. Lett.*, (1993) 1337.

10) T. Nakada, H. Ito, T. Ishiguro, T. Miura, Y. Misaki, T. Yamabe, and T. Mori, *Synth. Met.*, **86** (1997) 2019.

11) T. Nakada, T. Ishiguro, T. Miura, Y. Misaki, T. Yamabe, and T. Mori, *J. Phys. Soc. Jpn.*, **67** (1998) 355.

12) D. B. Tanner, C. S. Jacobsen, A. F. Garito, and A. J. Heeger, *Phys. Rev. B*, **13** (1976) 3381.

13) C. S. Jacobsen, D. B. Tanner, and K. Bechgaard, *Phys. Rev. Lett.*, **46** (1981) 1142.

14) H. Tajima, K. Yakushi, H. Kuroda, G. Saito, *Solid State Commun.*, **56** (1985) 159.

15) M. Tamura, H. Tajima, K. Yakushi, H. Kuroda, A. Kobayashi, R. Kato, and H. Kobayashi, *J. Phys, Soc. Jpn.*, **11** (1991) 3861.

16) N. Thorup, G. Rindorf, H. Soling, and K. Bechgaard, *Acta Crystallogr. Sect B*, **37** (1981) 1236.

17) V. F. Kaminskii, T. G. Prokhorova, R. P. Shibaeva, E. B. Yagubskii, *JETP Letters*, **39** (1984) 17.

18) L. Ducasse, M. Abderrabba, J. Hoarau, M. Pesquer, B. Gallois, and J. Gaultier, *J. Phys. C: Solid State Phys.*, **19** (1986) 3805.

19) C. S. Jacobsen, J. M. Williams, and H. H. Wang, *Solid State Commun.*, **54** (1985) 937.

20) Using the transfer integrals of (BDT-TTP)$_2$SbF$_6$ at 10K, we conducted the same simulation of the angular dependence of the transverse magnetoresistance following the Nakada's paper. The calculated result is very similar to the angle dependence in (BDT-TTP)$_2$AsF$_6$ rather than in (BDT-TTP)$_2$SbF$_6$.

21) C. S. Jacobsen, D. B. Tanner, and K. Bechgaard, *Phys. Rev. B*, **28** (1983) 7019.

22) H. Tajima, K. Yakushi, H. Kuroda, and G. Saito, *Solid State Commun.*, **57** (1986) 911.

23) F. Mila, *Phys. Rev. B*, **52** (1995-I) 4788.

24) M. D. Sturge, H. J. Guggenheim, and M. H. L. Pryce, *Phys. Rev. B*, **2** (1970) 2459.

Table I Drude parameters at room temperature. The dielectric function of Drude model is given by $\varepsilon(\omega)=\varepsilon_c-\omega_p^2/\omega(\omega+i\gamma)$.

	ε_c	γ (10^3 cm^{-1})	$\omega_{p\,(\mathrm{obs})}$ (10^3 cm^{-1})	m^*/m_e	$\omega_{p\,(\mathrm{calc})}$ (10^3 cm^{-1})
$(\mathrm{BDT\text{-}TTP})_2\mathrm{SbF}_6$					
$E//a$ on (010)	2.88	1.04	9.32	1.3	9.36
$E\perp a$ on (010)	3.76	0.81	3.17	11.5	6.04
$(\mathrm{BDT\text{-}TTP})_2\mathrm{AsF}_6$					
$E//a$ on (010)	2.82	1.04	9.38	1.3	9.44
$E\perp a$ on (010)	3.23	0.80	2.68	16.1	5.84

Table II Intra- (t_a) and inter-stack (t_p) transfer integrals (eV) in (BDT-TTP)$_2$SbF$_6$ and (BDT-TTP)$_2$AsF$_6$ estimated from the optical spectra. The following approximation is adopted in this estimation: $t_a=t_{a1}=t_{a2}$, $t_p=t_{p1}=t_{p2}$, $t_c=0$.

	t_{a1}	t_{a2}	t_{p1}	t_{p2}	t_c
(BDT-TTP)$_2$SbF$_6$ [a]	-0.259	-0.259	-0.048	-0.048	0
(BDT-TTP)$_2$SbF$_6$ [b]	-0.251	-0.253	-0.079	-0.086	-0.008
(BDT-TTP)$_2$AsF$_6$ [a]	-0.262	-0.262	-0.041	-0.041	0
(BDT-TTP)$_2$AsF$_6$ [c]	-0.2541	-0.2545	-0.0744	-0.0860	-0.005
(TMTSF)$_2$PF$_6$ [d]	0.252	0.209	-0.0064	-0.013	0.040
β-(BEDT-TTF)$_2$I$_3$ [e]	0.064	0.245	0.064	0.034	0.025

[a] This work.

[b] calculated by Misaki *et al.*[1]

[c] calculated by Misaki, private communication.

[d] calculated by L. Ducasse *et al.*[18]

[e] estimated by optical experiment by H. Tajima *et al.*[14]

Table III Wavenumber and plasma frequency of the infrared active vibrational modes in the $E \perp a$ spectrum of $(BDT\text{-}TTP)_2SbF_6$ observed at 10K. The plasma frequency is defined as $\omega_p^2 = (2/\pi\varepsilon_0)\int\sigma(\omega)d\omega$.

wavenumber (cm^{-1})	plasma frequency (cm^{-1})	tentative assignment
806	85	CS stretch
879	16	CS stretch, CC stretch
918	40	CS stretch, CC stretch
987	5	
1022	31	
1084	25	
1238	28	CCH bend
1257	20	CCH bend
1477	80	C=C stretch
3089	150	CH stretch

Table IV Temperature dependence of the dielectric constant, plasma frequency, and relaxation rate in the *E*//*a* and *E*⊥*a* spectra of (BDT-TTP)$_2$SbF$_6$

T (K)	polarization	ε_c	γ (10^3 cm^{-1})	ω_p (10^3 cm^{-1})	m^*/m_e
295	*E*//*a*	2.88	1.04	9.32	1.33
	E⊥*a*	3.76	0.81	3.17	11.5
250	*E*//*a*	3.08	0.80	9.63	1.24
	E⊥*a*	3.76	0.64	3.15	11.6
200	*E*//*a*	3.26	0.70	9.99	1.16
	E⊥*a*	3.66	0.49	3.07	12.2
150	*E*//*a*	3.30	0.63	10.2	1.12
	E⊥*a*	3.65	0.35	3.01	12.7
50	*E*//*a*	3.36	0.59	10.3	1.08
	E⊥*a*	3.65	0.26	3.00	12.8
10	*E*//*a*	3.46	0.57	10.5	1.05
	E⊥*a*	3.65	0.25	3.00	12.8

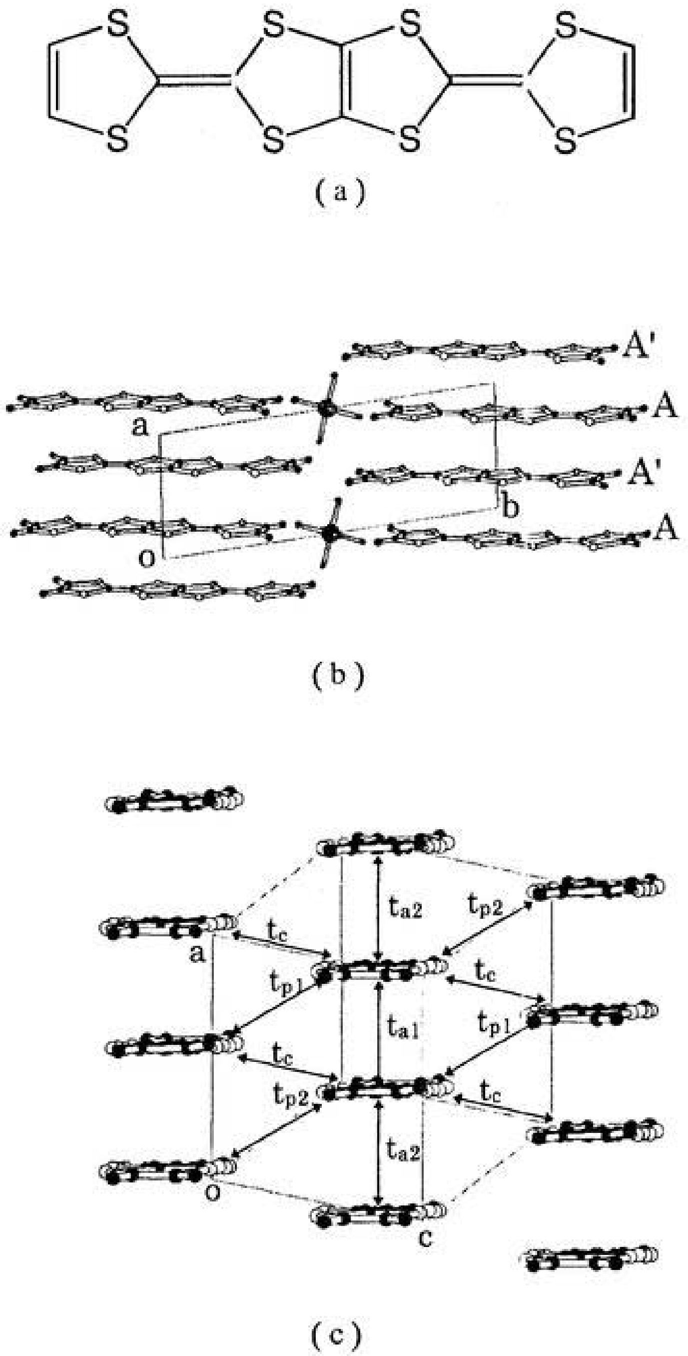

(a)

(b)

(c)

Fig 1 (a) Structural formula of BDT-TTP, (b) crystal structure of $(\text{BDT-TTP})_2\text{SbF}_6$ viewed along the *c*-axis, and (c) the conducting sheet viewed along the long molecular axis. t_{a1} and t_{a2} are the intra-stack transfer integrals and t_{p1}, t_{p2}, t_c are the inter-stack transfer integrals.

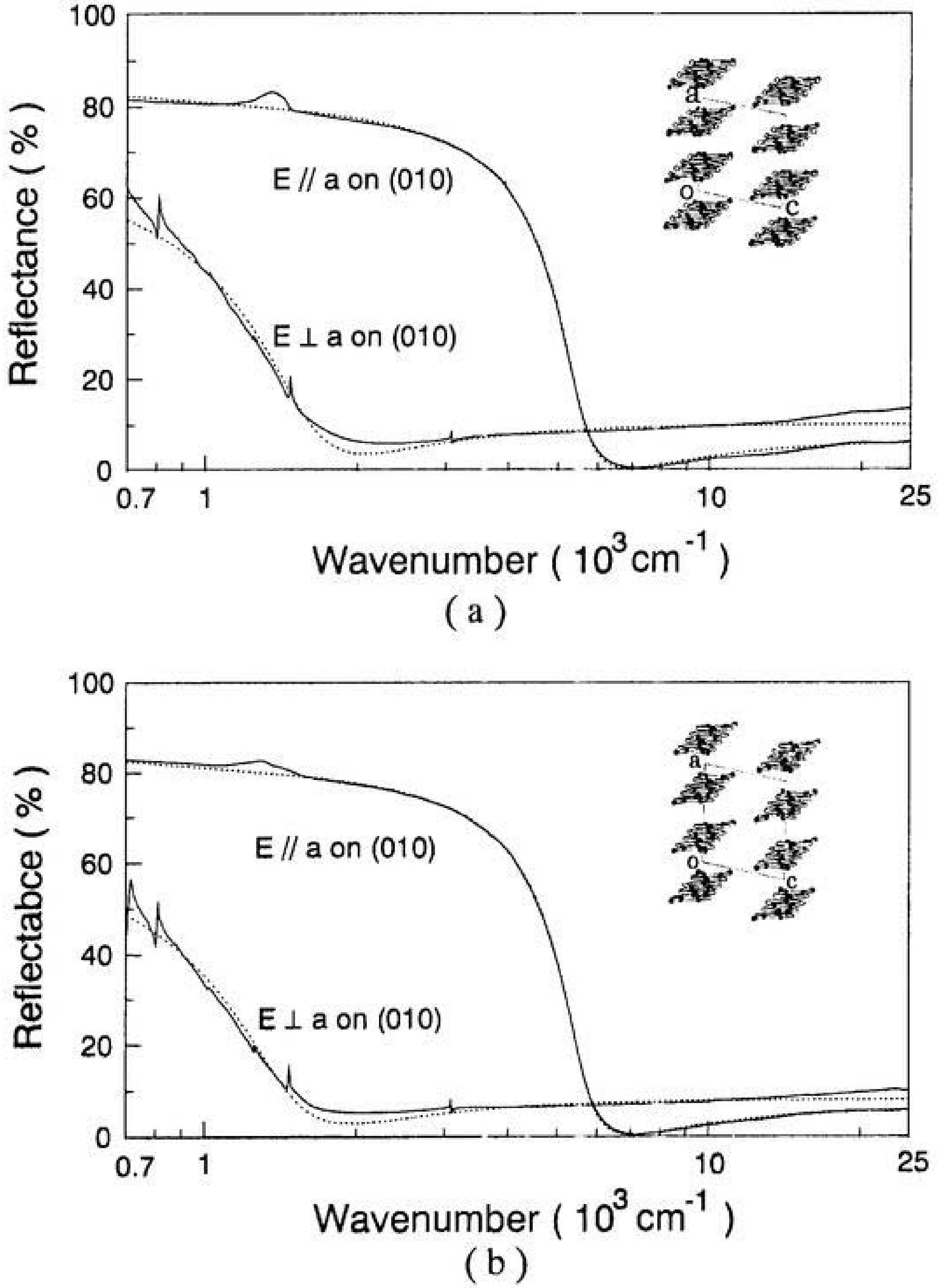

Fig. 2 Polarized reflection spectra of (a) (BDT-TTP)$_2$SbF$_6$ and (b) (BDT-TTP)$_2$AsF$_6$ at room temperature. The solid lines are the observed reflectivities and the dotted lines are the Drude-model fitting. The insert shows the arrangement of BDT-TTP molecules projected onto the (010) plane.

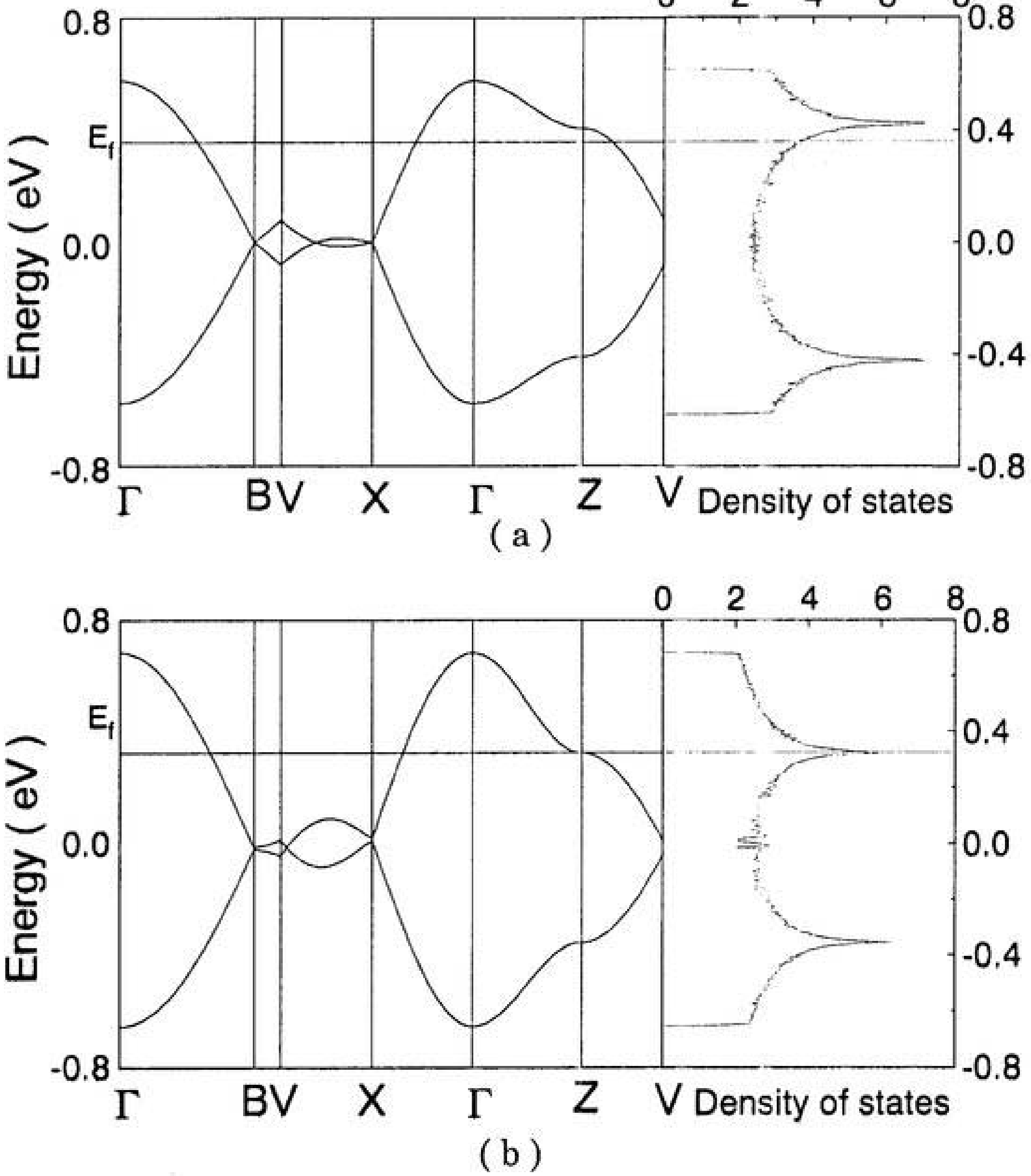

Fig. 3 Energy dispersion and density of state of the two-dimensional band of (BDT-TTP)$_2$SbF$_6$ calculated from the transfer integrals which are obtained (a) experimentally and (b) theoretically.

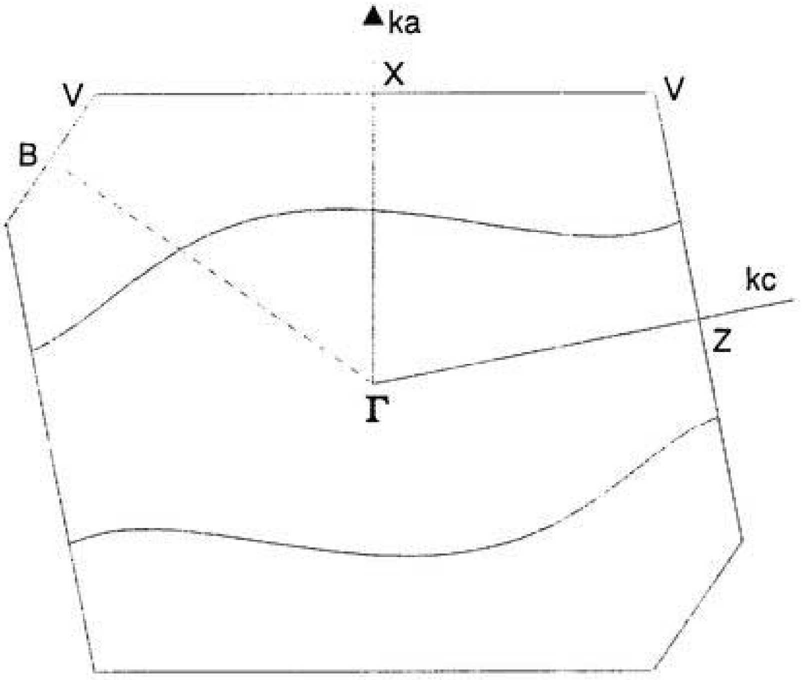

(a)

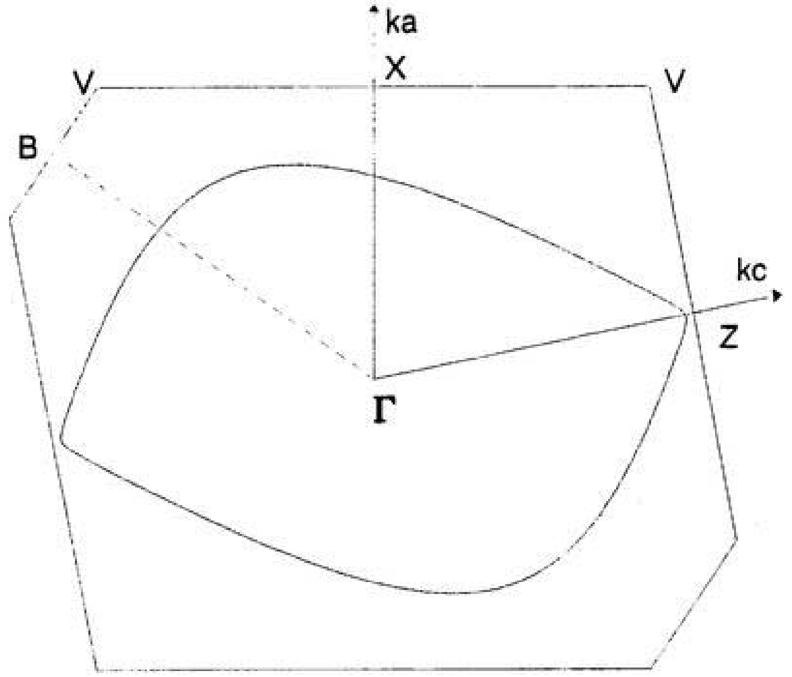

(b)

Fig. 4 Fermi surface of $(BDT\text{-}TTP)_2SbF_6$ calculated from the transfer integrals obtained by (a) the optical experiment and (b) the theoretical calculation.

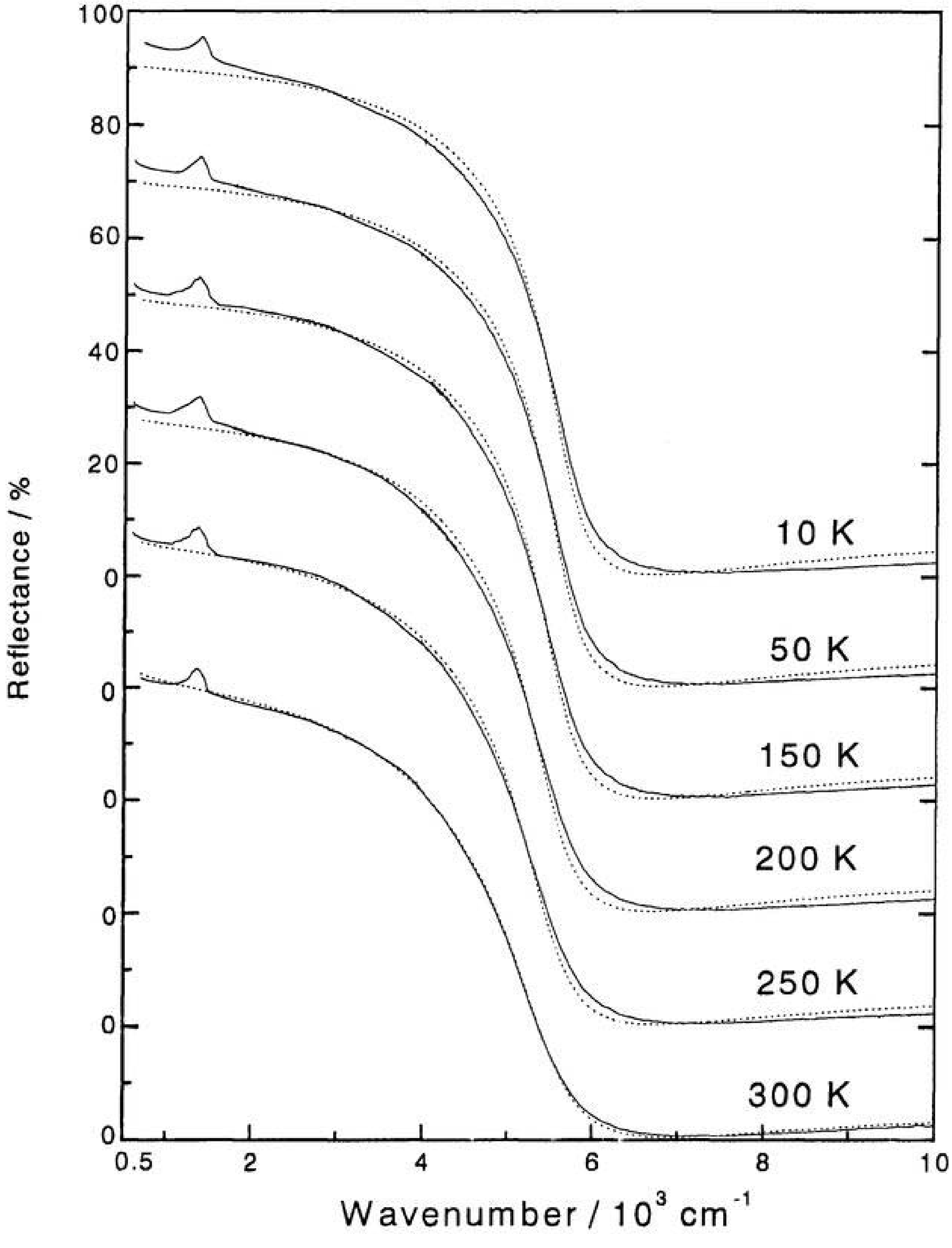

Fig. 5 *E*//*a* reflection spectra of $(BDT\text{-}TTP)_2SbF_6$ at various temperatures. The solid lines are the observed spectra and the dotted lines are the Drude-model fitting.

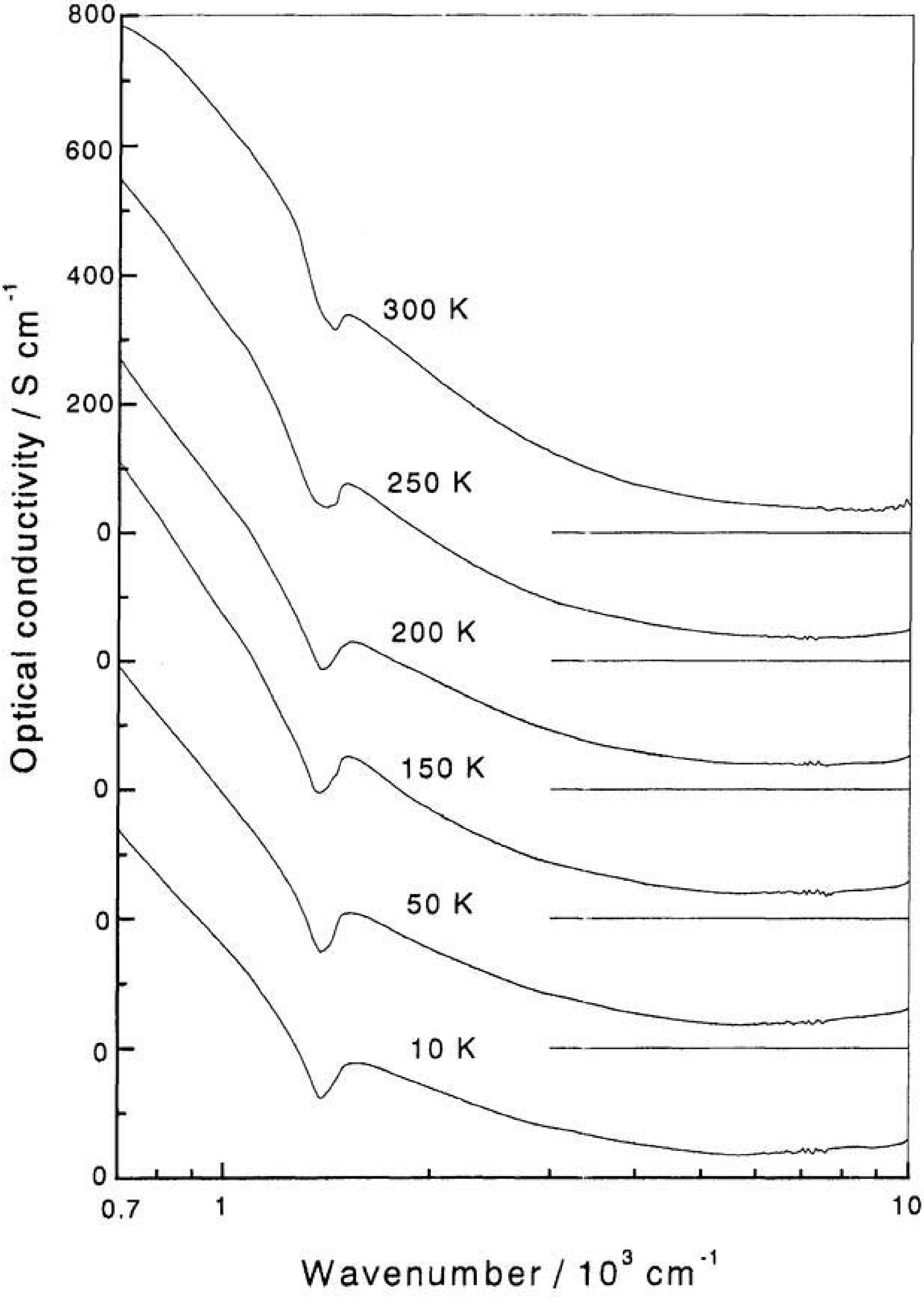

Fig. 6 *E//a* Conductivity spectra of (BDT-TTP)$_2$SbF$_6$ at various temperatures.

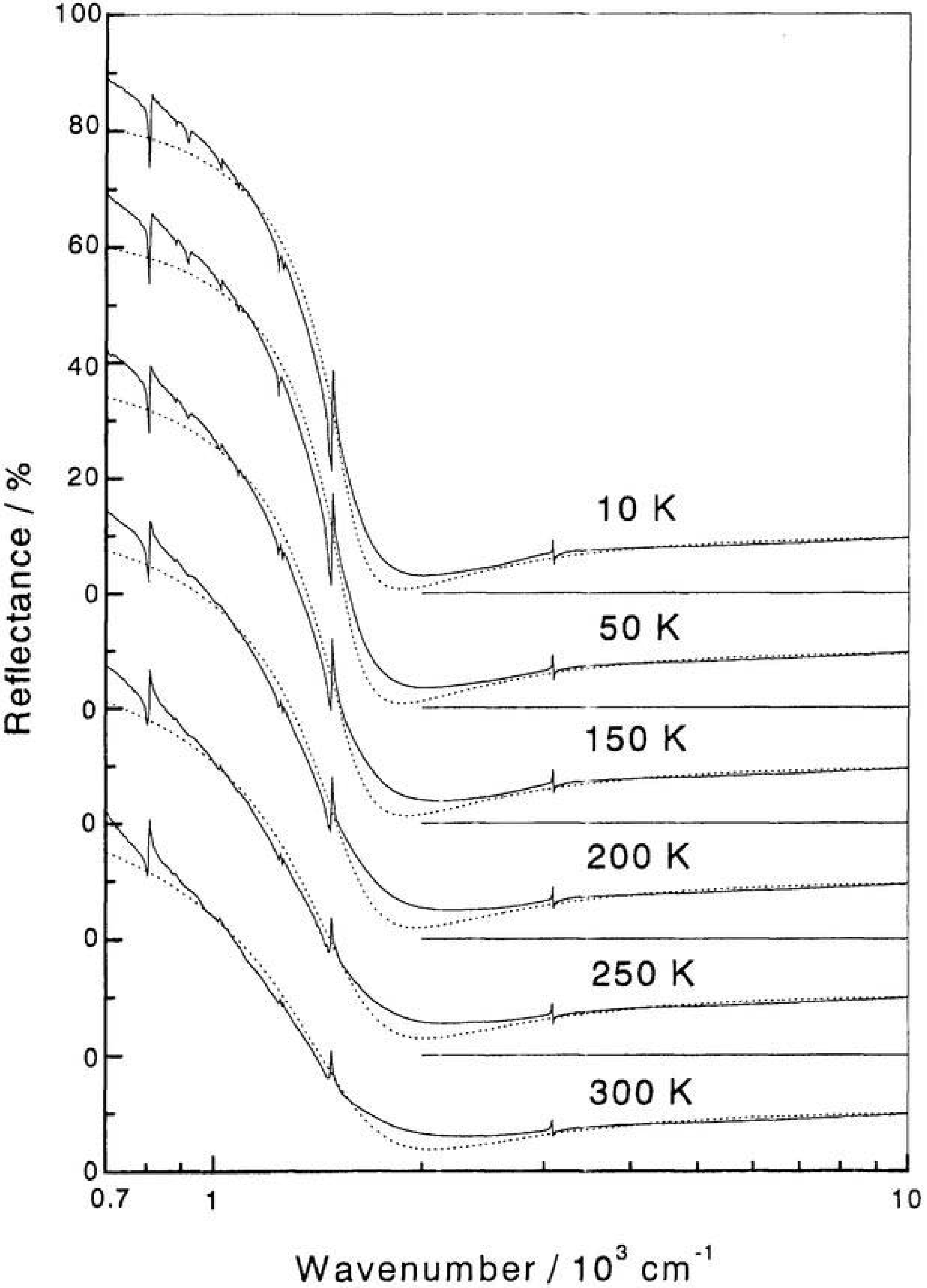

Fig. 7 $E \perp a$ Reflection spectra of $(BDT\text{-}TTP)_2SbF_6$ at various temperatures.

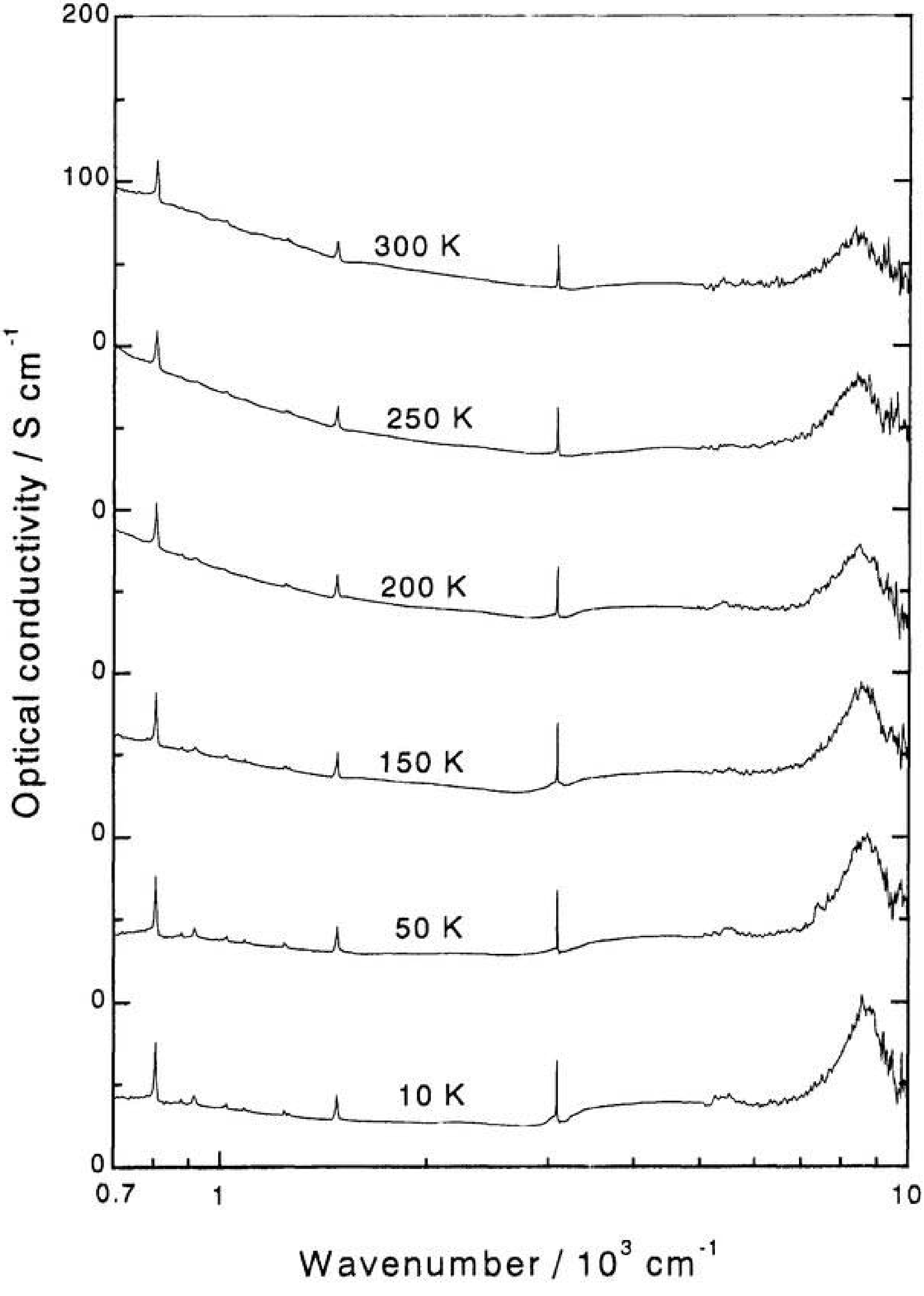

Fig. 8 *E⊥a* Conductivity spectra of (BDT-TTP)$_2$SbF$_6$ at various temperatures

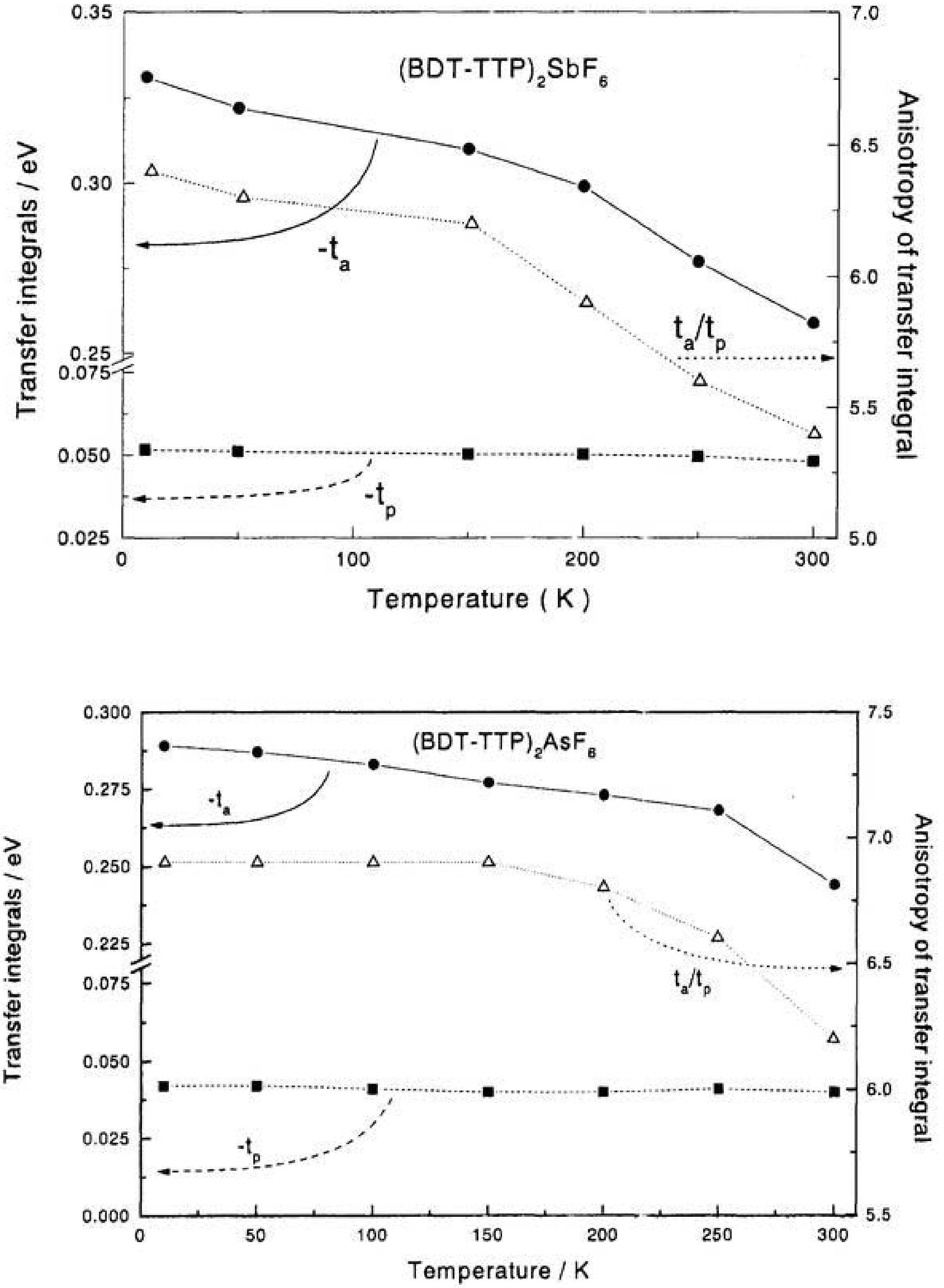

Fig. 9 Temperature dependence of the transfer integrals t_a, t_p, and t_a/t_p of (BDT-TTP)$_2$SbF$_6$ (top panel) and (BDT-TTP)$_2$AsF$_6$ (bottom).

Chapter 3

Electronic Structure of BDT-TTP analogue salts $(ST\text{-}TTP)_2AsF_6$ and $(BDS\text{-}TTP)_2AsF_6$

3.1 Introduction

Since the synthesis of TTF compounds, many organic compounds containing S atoms have been found to be good donors to form charge transfer organic salts. Two strategies are adopted to develop new organic donor molecules: one is by introducing substituents to the existing donor molecule; another is to synthesize the analogues by replacing the S atoms of the donor molecule by other atoms, such as Se, O or Te atom. The analogue salts are usually isomorphic to the parent salts while the electronic structure and the physical properties may change significantly. The replacement of S atoms by Se atoms sometimes significantly affects the dimensionality, the value of the transfer integral and the on-site Coulomb repulsion, such as TMTTF/TMTSF1-3) and DMTTA/DMTSA4, 5) salts. $(TMTSF)_2PF_6$ is a one-dimensional metal at room temperature and exhibits superconductivity at low temperature under a pressure, whereas $(TMTTF)_2PF_6$ is a one-dimensional insulator through the temperature. Two-dimensional structure has been observed on $(TMTSF)_2PF_6$ at low temperature6), whereas no such report is about $(TMTTF)_2PF_6$. DMTSA-BF_4 is a 1:1 one-dimensional metal at room temperature, in contrast to DMTTA-BF_4 being a Mott insulator.

No superconductivity has been observed on the BDT-TTP salts yet under ambient or high pressure, though many of them exhibit metallic conductivity down to liquid helium temperature7,8). Such metallic behavior without the appearance of the superconductivity has been observed on the many salts of BDT-TTP derivatives as well9,10). Many metallic BDT-TTP salts have two-dimensional electronic structure with a significant anisotropy, the Fermi surfaces are open in the first Brillouin zone11). ST-TTP and BDS-TTP are the analogues to BDT-TTP with the replacement of part or all S atoms in the outer rings by the Se atoms (Fig. 1). Their salts are isomorphic to BDT-TTP salts and exhibits similar metallic behavior through the temperature range9,12). It is expected that the replacement of S atoms by Se atoms will give an effect on the electronic structure.

Up to date, no experiment has been conducted to investigate the electronic structure of (ST-TTP)$_2$AsF$_6$ and (BDS-TTP)$_2$AsF$_6$. Here, we report our study on the electronic structure of (ST-TTP)$_2$AsF$_6$ and (BDS-TTP)$_2$AsF$_6$ by the polarized reflection spectroscopy and the Raman spectroscopy.

3.2 Experimental

(ST-TTP)$_2$AsF$_6$ and (BDS-TTP)$_2$AsF$_6$ single crystals were grown by the electrochemical oxidation method. The crystals were black with needle-like shape. The well-developed surface is the (010) crystal face. The dimensions were 0.80×0.32×0.04mm^3 for (ST-TTP)$_2$AsF$_6$ and 0.60×0.10×0.03mm^3 for (BDS-TTP)$_2$AsF$_6$, respectively. The crystals with smooth and shining surface are chosen for the measurement of the polarized reflection spectrum and the Raman spectrum. The polarized reflection spectrum was measured on the (010) face of the single crystal with the polarization along or perpendicular to the crystallographic *a*-axis. The approach to measure the polarized reflection spectrum is the same as that for (BDT-TTP)$_2$X (X=SbF$_6$, AsF$_6$)$^{11)}$. The Raman scattering spectrum was taken in back-scattering geometry by a Renishaw Ramanscope System-1000 excited by a He-Ne laser with a wavelength of 632.8 nm. The laser power was decreased by a neutral filter down to 0.05-0.1 mW and was focused on the 5 μmϕ area of the single crystal. The incident light is polarized perpendicular to the *a*-axis.

3.3 Results and discussion

3.3.1 Polarized reflection spectra

ST-TTP is an analogue of BDT-TTP with the replacement of two S atoms in one outer ring by two Se atoms, and BDS-TTP is the analogue with the replacement of all four S atoms in the two outer rings by four Se atoms. The monocations of them are almost planar, thus BDT-TTP and BDS-TTP monocation have a center of symmetry whereas ST-TTP monocation has not. The $(ST\text{-}TTP)_2AsF_6$ and $(BDS\text{-}TTP)_2AsF_6$ single crystals are isostructural to $(BDT\text{-}TTP)_2X$ ($X=AsF_6$, SbF_6) with space symmetry $P\bar{1}$ (Fig. 1). Both the donor molecules and the AsF_6 anions locate at the center of symmetry in the crystal. The Se atoms of $(ST\text{-}TTP)_2AsF_6$ are disordered in the crystal[12)]. The lattice parameters are listed in Table Ⅰ. For the AsF_6 salts, the lattice parameters *a*, *b*, *c* and the unit cell volume increase with the increase of the Se atoms in the donor molecules, due to the larger size of Se atom than S atom like DMTTA/DMTSA[4)]. The scheme of the transfer integrals for $(ST\text{-}TTP)_2AsF_6$ and $(BDS\text{-}TTP)_2AsF_6$ resembles that of $(BDT\text{-}TTP)_2X$ ($X=AsF_6$, SbF_6).

The resistance of the $(ST\text{-}TTP)_2AsF_6$ single crystals was measured along the *a*-axis by cooling the single crystal from 300K to 5K then heating to 300K. The resistance in Fig. 2 is the record during the cooling run. The resistance decreases on lowering temperature from 300K to 50K. The conductivity at 50K is almost six times as at 300K. Then several jumps occur below 50K, but the resistance still decreases on lowering temperature after every jump. A big hump appears during the heating run. The jumps during the cooling run and the hump during the heating run are sample-dependent, so they may be not intrinsic. Such behaviors have also observed on $(BDT\text{-}TTP)_2Y$ ($Y=ClO_4$, BF_4, and ReO_4)[7,13)]. The jumps and the hump of BDT-TTP salts disappear when a pressure is applied[14,15)]. Likewise, $(ST\text{-}TTP)_2AsF_6$ is regarded as a metal down to liquid helium temperature. Such jumps and hump have not been observed for $(BDT\text{-}TTP)_2AsF_6$[7)]. The effect of the replacement of S atoms by Se atoms on the conductive properties is like BEDT-TTF/BEDSe-TTF/BEDT-TSF salts rather than TMTTF/TMTSF salts and DMTTA/TMTSA salts.

The polarized reflection spectra were measured on the (010) face of $(ST\text{-}TTP)_2AsF_6$ and $(BDS\text{-}TTP)_2AsF_6$ single crystals at room temperature, with the polarization along and perpendicular to the *a*-axis (Fig. 3). The reflection spectra of both compounds resemble those of (BDT-TTP)$_2$X (X=AsF$_6$, SbF$_6$)11). High dispersions appear in both directions with a significant anisotropy. The CT bands in both directions are superimposed by some phonons. A hump is observed at *ca.* 1,400cm^{-1} in the $E//a$ reflection spectrum. The hump seems stronger in the spectrum of (BDS-TTP)$_2$AsF$_6$ than (ST-TTP)$_2$AsF$_6$. The spectra in both directions except some phonons can be fitted by the Drude model very well. The fitting Drude parameters are listed in Table Ⅱ. The ε_c value of the $E//a$ spectrum of (ST-TTP)$_2$AsF$_6$ is somewhat less than that of (BDS-TTP)$_2$AsF$_6$, though the reflectivity in the visible region of them is very close. The plasma frequencies of (ST-TTP)$_2$AsF$_6$ in both directions are less than those of (BDS-TTP)$_2$AsF$_6$. The $\omega_{p//a}$s of both (BDS-TTP)$_2$AsF$_6$ and (ST-TTP)$_2$AsF$_6$ are smaller while $\omega_{p\perp a}$s are larger that those of (BDT-TTP)$_2$AsF$_6$. This suggests that the anisotropy decrease with the increase of the Se atoms in the donor molecules since the crystals of them are isostructure.

The effective masses of both compounds are comparable with (BDT-TTP)$_2$X (X=AsF$_6$, SbF$_6$). The anisotropy of the effective masses of (BDS-TTP)$_2$AsF$_6$ ($m_{//}^*/m_{\perp}^*$=0.10) is slightly higher than (ST-TTP)$_2$AsF$_6$, and both are between (BDT-TTP)$_2$AsF$_6$ ($m_{//}^*/m_{\perp}^*$=0.08) and (BDT-TTP)$_2$SbF$_6$ ($m_{//}^*/m_{\perp}^*$=0.11). Evidently, the effect of the Se replacement on the dimensionality is not very significant.

The relation of the electronic energy to the transfer integrals for (BDS-TTP)$_2$AsF$_6$ and (ST-TTP)$_2$AsF$_6$ is the same as that of (BDT-TTP)$_2$X (X=AsF$_6$, SbF$_6$). The plasma frequencies of (ST-TTP)$_2$AsF$_6$ are calculated by using the five transfer integrals obtained theoretically by Misaki *et al.*12) t_{a1}=-0.212, t_{a2}=-0.210, t_{p1}=-0.075, t_{p2}=-0.058, and t_c=0.0099eV. As listed in Table Ⅱ, the calculated $\omega_{p//a}$ is not very different from the experimental result, while the calculated $\omega_{p\perp a}$ is almost twice as the experimental one. This agreement between the experimental results and the theoretical calculation is similar to (BDT-TTP)$_2$X (X=AsF$_6$, SbF$_6$,

ClO_4). These suggest that the inter-stack transfer integral of (ST-TTP)$_2$AsF$_6$ may be over-estimated by Misaki *et al.*

According to the transfer integrals calculated by Misaki *et al.* t_{a1}=-0.212, t_{a2}=-0.210, t_{p1}=-0.075, t_{p2}=-0.058, and t_c=0.0099eV, it is reasonable to make the same approximation of $t_{a1}=t_{a2}=t_a$, $t_{p1}=t_{p2}=t_p$, and $t_{p3}=0$ for (ST-TTP)$_2$AsF$_6$ as for (BDT-TTP)$_2$X (X=AsF$_6$, SbF$_6$). Same approximation is adopted for (BDS-TTP)$_2$AsF$_6$ as well. Thereby, the two transfer integrals t_a and t_p of (ST-TTP)$_2$AsF$_6$ and (BDS-TTP)$_2$AsF$_6$ can be estimated from the two plasma frequencies. The estimation process is the same as for (BDT-TTP)$_2$X (X=AsF$_6$, SbF$_6$), and the estimated results are listed in Table Ⅲ. The estimated t_a of (ST-TTP)$_2$AsF$_6$ is almost 15% higher than the calculated. The agreement is well but worse than that for (BDT-TTP)$_2$X (X= AsF$_6$, SbF$_6$), presumably due to both the disordered structure of Se atoms in the (ST-TTP)$_2$AsF$_6$ single crystal and the inaccuracy of the parameters about the 4p orbits of Se atoms. The estimated inter-stack transfer integral t_p is almost half of the calculated t_{p1} and about one fifth lower than t_{p2}, the agreement along this direction is similar to that of (BDT-TTP)$_2$X (X=SbF$_6$, AsF$_6$, and ClO$_4$). The estimated intra-stack transfer integral t_a is: (BDT-TTP)$_2$AsF$_6$> (BDS-TTP)$_2$AsF$_6$>(ST-TTP)$_2$AsF$_6$. This sequence is understandable by considering the crystal structure. It is clear that both the inter-molecule distance along the stack and the intra-stack transfer integral increase when all S atoms are replaced by Se atoms, such as DMTSA/DMTTA salts$^{5)}$. This is because the 4p orbits of Se atom can extend to a larger space. This may be also the reason that (BDS-TTP)$_2$AsF$_6$ has larger intra-stack transfer integral than (ST-TTP)$_2$AsF$_6$. Since only part S atoms of BDT-TTP are replaced by Se atoms and the inter-molecular distance is larger in (ST-TTP)$_2$AsF$_6$ and (BDS-TTP)$_2$AsF$_6$ than in (BDT-TTP)$_2$AsF$_6$, the overlap between the S atoms loses very much and the loss can not be compensate by the gain of the overlap between the Se atoms. Consequently, (ST-TTP)$_2$AsF$_6$ has a larger transfer integral than (BDS-TTP)$_2$AsF$_6$ and (BDT-TTP)$_2$AsF$_6$

The bandwidths $W=4|t_a+t_p|$ are 1.13 and 1.20eV for (ST-TTP)$_2$AsF$_6$ and (BDS-TTP)$_2$AsF$_6$ according to the experimental estimation, respectively. The bandwidths of both compounds are a little narrower than those of (BDT-TTP)$_2$X (X=AsF$_6$, SbF$_6$). The energy band and the density of states of (ST-TTP)$_2$AsF$_6$ are calculated by the use of the transfer integrals obtained by the optical experiments and by the theoretical calculation, as shown in Fig. 4. According to the experimental estimation, the energy of the upper band at the point *Z* and the energy of the upper maximum DOS are explicitly higher than the Fermi energy. These are remarkably different from the results by the theoretical calculation, of which both energies are a little lower than the Fermi energy. Hence, the Fermi surfaces by both methods are significantly different. It is open in the first Brillouin zone by the optical experiments while close by the theoretical calculation (Fig. 5). The band structure and the Fermi surface of (BDS-TTP)$_2$AsF$_6$ by the optical experiments resemble those of (ST-TTP)$_2$AsF$_6$. The band structures of both compounds resemble those of (BDT-TTP)$_2$X (X=AsF$_6$, SbF$_6$).

The polarized reflection spectra of the (ST-TTP)$_2$AsF$_6$ single crystal were measured from room temperature down to 16K. Fig. 6 and Fig. 7 are the temperature dependence of the $E//a$ and $E\perp a$ spectra, respectively. Th change of the spectra on lowering temperature resemble that of (BDT-TTP)$_2$X (X=AsF$_6$, SbF$_6$). The reflectivity at low wavenumber region increases and the phonon modes do not change significantly. The spectrum at low temperature can be fitted relatively well by the simple Drude model. The plasma frequencies in both directions are plotted against the temperatures from 300K to 16K (Fig. 8). $\omega_{p//a}$ increases whereas $\omega_{p\perp a}$ decreases on lowering temperatures. $\omega_{p//a}$ shows stronger temperature dependence than $\omega_{p\perp a}$. The intra-stack (t_a) and the inter-stack transfer integrals (t_p) are estimated according to the plasma frequencies at various temperatures, by adopting the crystal parameters at room temperature. Fig. 9 is the temperature dependence of t_a, t_p and their ratio t_a/t_p. The absolute value t_a increases on lowering temperature, whereas t_p is insensitive to the temperature. The ratio t_a/t_p increases on lowering temperature, suggesting the electronic structure of (ST-TTP)$_2$AsF$_6$ becomes more anisotropic at low temperature. This temperature dependence of the electronic structure is analogous to that of the BDT-TTP metallic salts.

3.3.2 Analysis of the reflection spectra by generalized Drude model

As mentioned in § 3.3.1 and in Chapter 2, the reflection spectra of BDT-TTP, ST-TTP and BDS-TTP can be fitted by the simple Drude model relatively well, but some deviation can also be observed in the very low wavenumber region. It is frequently observed that the reflection spectrum of the organic conductor deviates from the simple Drude model, especially in the low energy range. The non-Drude conductivity results from the short-range effect, such as the electron-electron correlation. Non-Drude behavior is also observed for transition metal oxide conductor of strong electron-electron correlation, and the generalized Drude mode is frequently adopted instead of the simple Drude model to analyze the polarized reflection spectrum[16-18]. The generalized Drude model is the modification of the simple Drude model by introducing the frequency dependence of the effective mass and the scattering rate:

$$\varepsilon(\omega) = \varepsilon_1 + i\varepsilon_2 = \varepsilon_c - \frac{4\pi\tilde{\sigma}(\omega)}{i\omega}, \tag{3.1}$$

$$\omega_p^2(\omega) = \frac{ne^2}{\varepsilon_0 m^*(\omega)}, \tag{3.2}$$

$$\gamma(\omega) = \frac{\omega\varepsilon_2(\omega)}{\varepsilon_c - \varepsilon_1(\omega)}, \tag{3.3}$$

$$m^*(\omega) = \frac{ne^2}{\varepsilon_0\omega^2}\,\mathrm{Re}\left[\frac{1}{\varepsilon_c - \varepsilon(\omega)}\right]. \tag{3.4}$$

Some insight into the conduction mechanism can be gained from the frequency dependence of the scattering constant and the effective mass.

The polarized reflection spectra of (ST-TTP)$_2$AsF$_6$ at 300K and 16K are analyzed by the generalized Drude model. The process is the same as in reference 18). The ε_c values obtained by the simple Drude model are adopted for the generalized Drude model analysis. The weak band in the NIR region of $E\perp a$, which is assigned to the intra-ST-TTP$^+$ transition in § 3.3.3, is far away from the IR region of interest, it is not eliminated during the analysis. The phonons in the IR region only give a very small effect on the result so that they are remained during the analysis. Fig. 10 are the frequency dependence of the scattering constant $\gamma(\omega)$ and the effective mass $m^*(\omega)$ of $E//a$ at 300K and 16K. The scattering constants at 300K and 16K are almost independent of the frequency in the region higher than the dip position. The dip at *ca.* 1400cm^{-1} arises from a phonon. In the region higher than this dip the $\gamma(\omega)$-ω relation can be fitted by a straight line very well. The scattering constants at zero obtained by the extrapolation of the fitting lines are 1050cm^{-1} at 300K and 640cm^{-1} at 16K, respectively. These values agree with the results by the simple Drude model (1030cm^{-1} at 300K and 700cm^{-1} at 16K, respectively) very well. The very weak dependence of the scattering rate on the frequency indicates the Drude-like behavior of the electron along the *a*-axis, *i.e.*, free-electron behavior.

The effective mass linearly decreases with respect to the ascending frequency except the phonon positions. The effective masses at zero are $1.72m_e$ at 300K and $1.62m_e$ at 16K, respectively. These values are larger than those by the simple Drude model ($1.41m_e$ at 300K and $1.27m_e$ at 16K, respectively). Analogous linear decrease of the effective mass with respect to the ascending frequency has been observed on transition metal oxide as well[18)]. The change tendency of the effective mass at zero on lowering temperature analyzed by the generalized Drude mode is similar to that by the simple Drude-model. It is of interest to note that the shape of the phonons in the frequency dependence of the scattering constant is like those in the conductivity spectrum, while in the frequency dependence of the effective mass they are like those in the reflection spectrum.

Fig. 11 are the frequency dependence of the scattering constant and the effective mass of $E\perp a$ at 300K and 16K. Both the scattering constant and the effective mass change linearly with respect to the frequency. The scattering constant increases whereas the effective mass decreases linearly with respect to the ascending frequency except the positions of the phonon modes. The relations of $\gamma(\omega)$-ω at 300K and at 16K are almost parallel. $\gamma(0)$ is 440cm^{-1} at 300K and 30cm^{-1} at 16K, respectively. These values are very different from the results by the simple Drude model (830cm^{-1} at 300K and 320cm^{-1} at 16K, respectively). Such $\gamma(\omega)$-ω linear relation has been observed for transition metal oxide as well[16,17)]. The scattering rate is independent of the frequency for the simple Drude model. It is proportional to ω^2 for the electron-electron scattering and to ω^5 for the electron-phonon scattering. Hence, the simple Drude model may be not an exact description for the electronic behavior in the direction perpendicular to the a-axis. The linear $\gamma(\omega)$-ω relation can not be understood well yet. For (ST-TTP)$_2$AsF$_6$, the effect of the electron-electron correlation may give a effect on the direction perpendicular to a-axis, due to the small inter-stack transfer integral and the large effective mass in this direction. The effective mass at zero is $17.2m_e$ at 300K and $17.8m_e$ at 16K, respectively. These values are larger than those by the simple Drude model ($13.9m_e$ at 300K and $15.8m_e$ at 16K, respectively).

The plasma frequencies in both directions obtained by the generalized Drude model agree with the results by the simple Drude model very well at 300K, though the electron behavior in $E\perp a$ direction somewhat deviates from the simple Drude model.

3.3.3 Conductivity spectrum

The conductivity spectra of (ST-TTP)$_2$AsF$_6$ and (BDS-TTP)$_2$AsF$_6$ at room temperature were obtained from the polarized reflection spectra by Krames-Kronig transformation (Fig. 12). The CT bands appear in both directions in the low energy region. The oscillator strength of the CT band of *E//a* is apparently stronger than that of *E⊥a*. A band appears near 8,000 cm^{-1} in the NIR region of the *E⊥a* spectrum while no such dispersion can be observed in the *E//a* spectrum. The appearance of this band is similar to that in the spectrum of $(BDT\text{-}TTP)_2X$ ($X=SbF_6$, AsF_6, ClO_4, and ReO_4). As discussed in chapter 4, such band of $(BDT\text{-}TTP)_2X$ is assigned to the intra-molecular electronic transition of the monocation radical from the nest HOMO to HOMO. The peak position of this band by the Lorentz model fitting is 8210 and 7880cm^{-1} for $(ST\text{-}TTP)_2AsF_6$ and $(BDS\text{-}TTP)_2AsF_6$ at room temperature, respectively, comparing the position at 8420cm^{-1} for BDT-TTP salts. These indicate that the energy difference between the HOMO orbit and the next HOMO orbit becomes narrower after the replacement of S atoms by Se atoms. The band becomes shaper and shifts to high energy region on lowering temperature. It shifts to 8430cm^{-1} at 16K for $(ST\text{-}TTP)_2AsF_6$.

The dip appearing at *ca.* 1,400cm^{-1} in the *E//a* conductivity spectrum results from the electron-phonon interaction. The dip in the spectrum of $(BDS\text{-}TTP)_2AsF_6$ is more remarkable than that of $(ST\text{-}TTP)_2AsF_6$, thus the electron-phonon interaction in the former may be stronger than in the latter.

Fig. 13 is the *E//a* conductivity spectra of $(ST\text{-}TTP)_2AsF_6$ from 300K down to 16K. The dip becomes more remarkable at low temperature. It is fitted at various temperatures by the Fano-Drude formula (2.7) in Chapter 2. The fitting is relatively well especially at the temperatures below 250K. The fitting parameters are sensitive to both the noise of water in this region and to the fitting range. The fitting parameters in the range from 1200 to 2000cm^{-1} at room temperature are p=0.17, q=0.012, γ=125cm^{-1}, and ω_0=1417cm^{-1}. The temperature dependence of the dip seems not very strong, the fitting parameters but ω_0 do not strictly increase or decrease on lowering temperature. The phonon position ω_0 slowly shifts to lower energy region when the temperature is lowered, but the shift is only 10cm^{-1} from 300K to 16K.

Several phonons appear in the $E\perp a$ conductivity spectrum (Fig. 14). The intensity increases a little at low temperature. The positions and the intensities of these phonons are listed in Table Ⅳ for $(ST\text{-}TTP)_2AsF_6$ at 16K and for $(BDS\text{-}TTP)_2AsF_6$ at room temperature. Two CH stretching modes appears at 3077 and 3089cm^{-1} for $(ST\text{-}TTP)_2AsF_6$, comparing only one at 3070cm^{-1} for $(BDS\text{-}TTP)_2AsF_6$ at room temperature and low temperature. Only one VH stretching peak has been observed at 3089cm^{-1} for $(BDT\text{-}TTP)_2X$ ($X=AsF_6$ and SbF_6) as well. These are consistent with the symmetry of the donor molecule. The CH stretching mode shifts to lower energy region after the replacement of S atoms by Se atoms. Some phonons also show similar shift to red after the replacement of S atoms by Se atoms. The two phonons in the range between 1,000 and 1,200 cm^{-1} in the spectrum of $(BDT\text{-}TTP)_2X$ ($X=AsF_6$ and SbF_6) can not be observed in this range in the spectrum of $(ST\text{-}TTP)_2AsF_6$ and $(BDS\text{-}TTP)_2AsF_6$. Some modes in the infrared region of the spectrum of $(ST\text{-}TTP)_2AsF_6$ may also shift to lower energy region in the spectrum of $(BDS\text{-}TTP)_2AsF_6$.

The strong modes at 706 and 711cm^{-1} in the spectrum of $(ST\text{-}TTP)_2AsF_6$, which was observed in the spectrum of $(BDT\text{-}TTP)_2AsF_6$ as well, is safely assigned to the stretching modes of AsF_6 anion. Only one stretching mode of the AsF_6 anion appears in the spectrum of $(BDS\text{-}TTP)_2AsF_6$ at room temperature, and a shoulder emerges at low temperature.

3.3.4 Raman spectra of $(ST\text{-}TTP)_2AsF_6$ and $(BDS\text{-}TTP)_2AsF_6$

The vibrational modes of $(ST\text{-}TTP)_2AsF_6$ and $(BDS\text{-}TTP)_2AsF_6$ are studied by the Raman spectroscopy as well. The main attention is put on the most charge-sensitive mode. The Raman spectra of neutral ST-TTP, $(ST\text{-}TTP)_2AsF_6$ and $(BDS\text{-}TTP)_2AsF_6$ are shown in Fig. 15 from 1,300 to 1,650cm^{-1}, together with the spectra of neutral BDT-TTP and $(BDT\text{-}TTP)_2AsF_6$. The modes in this range are related to the C=C stretch of BDT-TTP. As discussed in Chapter 4, the mode at 1507cm^{-1} for neutral BDT-TTP and at 1480cm^{-1} for (BDT-

TTP)$_2$AsF$_6$ is the most charge-sensitive mode, mainly contributing by the stretch of the C=C bonds between two five-member rings. Accordingly, the modes appearing at 1503cm^{-1} for neutral ST-TTP, at 1477cm^{-1} for (ST-TTP)$_2$AsF$_6$ and at 1475cm^{-1} for (BDS-TTP)$_2$AsF$_6$ are the most charge-sensitive modes. The stretching modes of the two C=C bonds between two five-member rings of (ST-TTP)$_2$AsF$_6$ may degenerate accidentally. The most charge-sensitive mode shifts a little to lower energy with the increase of Se atoms in the donor molecule, partly due to the heavy mass of Se atom than S atom. The slight shift suggests that the replacement of S atoms by Se atoms does not give a significant effect on the electronic state of the C=C bonds between two five-member rings.

The shift of the most charge-sensitive mode from neutral ST-TTP to (ST-TTP)$_2$AsF$_6$ (26cm^{-1}) is almost the same as that from neutral BDT-TTP to (BDT-TTP)$_2$AsF$_6$ (27cm^{-1}). This is different from TMTTF/TMTSF, of which the most charge-sensitive mode almost appears at the same position for neutral TMTTF and TMTSF while appears at lower position for TMTSF salts than for TMTTF salts$^{19)}$.

3.4 Summary

The polarized reflection spectra of (ST-TTP)$_2$AsF$_6$ and (BDS-TTP)$_2$AsF$_6$ resemble those of (BDT-TTP)$_2$X (X=AsF$_6$, SbF$_6$). Strong dispersions with a significant anisotropy appear in the low energy region in two perpendicular directions. The Fermi surfaces of both compounds are open in the first Brillouin zone. The anisotropies of them resemble those of metallic BDT-TTP salts. The sequence of the intra-stack transfer integral is (BDT-TTP)$_2$AsF$_6$>(BDS-TTP)$_2$AsF$_6$>(ST-TTP)$_2$AsF$_6$. Analyzed by the generalized Drude model, the $E//a$ scattering rate is almost independent of the frequency, while the $E\perp a$ scattering rate is linearly increases with respect to the ascending frequency. The most charge-sensitive mode shifts to lower energy region with the increase of Se atoms in the donor molecule. The position shift of this mode from neutral ST-TTP molecule to $(\text{ST-TTP})_2\text{AsF}_6$ is almost the same as that from neutral BDT-TTP to $(\text{BDT-TTP})_2\text{AsF}_6$.

References:

1) D. Jérome and H. J. Schulz, *Advance in Physics,* **31** (1982) 299.

2) T. Ishiguro and K. Yamaji, *Organic Superconductors*, Springer-Verlag, (1990) Chapter 4.

3) C. S. Jacobsen, D. B. Tanner, and K. Bechgaard, *Mol. Cryst. Liq. Cryst.*, **79** (1982) 25.

4) K. Takimiay, A. Ohnishi, Y. Aso, T. Otsubo, F. Ogura, K. Kawabata, and M. Mizutani, *Bull. Chem. Soc. Jpn.*, **67** (1994) 766.

5) J. Ouyang, K. Yakushi, K. Takimiya, and T. Otsubo, *submitted*. See also Chapter 7 of this thesis.

6) C. S. Jacobsen, D. B. Tanner, and K. Bechgaard, *Phys. Rev. Lett.*, **46** (1981) 1142.

7) Y. Misaki, H. Fujiwara, T. Yamabe, T. Mori, H. Mori, and S. Tanaka, *Chem. Lett.*, (1994) 1653.

8) Y. Misaki, T. Matsui, K. Kawakami, H. Fujiwara, T. Yamabe, T. Mori, H. Mori, S. Tanaka, and M. Shiro, *Synth. Met.*, **70** (1995) 1149.

9) Y. Misaki and T. Mori, *Solid State Physics*, **33** (1998) 1014.

10) T. Mori, T. Kawamoto, Y. Misaki, K. Kawakami, H. Fujiwara, T. Yamabe, H. Mori, and S. Tanaka, *Mol. Cryst. Liq. Cryst.*, **284** (1996) 271.

11) J. Ouyang, K. Yakushi, Y. Misaki, and K. Tanaka, *J. Phys. Soc. Jpn.*, **67** (1998) 3191.

12) Y. Misaki, T. Kochi, T. Yamabe, and T. Mori, *Adv. Mater.*, **10** (1998) 588.

13) T. Mori, Y. Misaki, H. Fujiwara, and T. Yamabe, *Bull. Chem. Soc. Jpn.*, **67** (1994) 2685.

14) T. Kawamoto, T. Mori, J. Yamamura, T. Enoki, Y. Misaki, T. Yamabe, H. Mori, and S. Tanaka, *Synth. Met.*, **85** (1997) 1555.

15) T, Nakada, H. Ito, T. Ishiguro, T. Miura, Y. Misaki, T. Yamabe, and T. Mori, *Synth. Met.*, **86** (1997) 2019.

16) H. Makino, I. H. Inoue, M. J. Rezenberg, I. Hase, Y. Aiura, and S. Onari, *Phys. Rev. B,* **58**

(1998) 4384.

17) D. A. Crandles, T. Timusk, J. D. Garrett, and J. E. Greedan, *Phys. Rev. B*, **49** (1994) 16207.

18)Y. Fujishima, T. Tokura, T. Arima, and S. Uchida, *Phys. Rev. B*, **46** (1992) 11167.

19) M. Meneghetti, R. Kato, I. Zanon, C. Pecile, C. Ricotta, and M. Zanetti, *J. Chem. Phys.*, **80** (1984) 6210.

Table Ⅰ Crystal parameters of iso-structural $(ST\text{-}TTP)_2AsF_6$, $(BDS\text{-}TTP)_2AsF_6$, $(BDT\text{-}TTP)_2AsF_6$, and $(BDT\text{-}TTP)_2SbF_6$.

	$(ST\text{-}TTP)_2AsF_6$	$(BDS\text{-}TTP)_2AsF_6$	$(BDT\text{-}TTP)_2AsF_6$	$(BDT\text{-}TTP)_2SbF_6$
a/Å	6.991	7.073	6.940	6.935
b/Å	18.025	18.114	17.967	18.167
c/Å	6.479	6.5659	6.397	6.405
α	99.26	99.489	98.88	98.34
β	100.76	100.86	100.72	101.11
γ	81.31	81.38	81.25	81.50
V/Å^3	785.5	808.7	768.0	777.4

Table Ⅱ Drude parameters of (ST-TTP)$_2$AsF$_6$ and (BDS-TTP)$_2$AsF$_6$ at room temperature.

	ε_c	ω_p (10^3 cm^{-1})	γ (10^3 cm^{-1})	m^*/m_e	ω_p (calc) (10^3 cm^{-1})
(ST-TTP)$_2$AsF$_6$					
$E//a$ on (010)	2.55	8.99	1.03	1.41	8.56
$E\perp a$ on (010)	3.62	2.86	0.83	13.9	5.79
(BDS-TTP)$_2$AsF$_6$					
$E//a$ on (010)	2.84	9.22	0.91	1.30	
$E\perp a$ on (010)	3.74	2.92	0.91	13.0	

Table Ⅲ The intra- (t_{a1}, t_{a2}) and inter-stack (t_{p1}, t_{p2}, and t_{p3}) transfer integrals of (ST-TTP)$_2$AsF$_6$ and (BDS-TTP)$_2$AsF$_6$ estimated from the polarized reflection spectra at room temperature. Unit: eV

	t_{a1}	t_{a2}	t_{p1}	t_{p2}	t_{p3}
(ST-TTP)$_2$AsF$_6$[a]	-0.241	-0.241	-0.042	-0.042	0
(ST-TTP)$_2$AsF$_6$[b]	-0.212	-0.210	-0.075	-0.058	0.0099
(BDS-TTP)$_2$AsF$_6$[a]	-0.255	-0.255	-0.044	-0.044	0

a)This work.

b)Ref. 12.

Table Ⅳ Position and plasma frequency of the phonons in the $E\perp a$ conductivity spectrum of $(ST\text{-}TTP)_2AsF_6$ at 16 K and of $(BDS\text{-}TTP)_2AsF_6$ at room temperature.

$(ST\text{-}TTP)_2AsF_6$		$(BDS\text{-}TTP)_2AsF_6$		
Position (cm^{-1})	Plasma frequency (cm^{-1})	Position (cm^{-1})	Plasma frequency (cm^{-1})	Tentative assignment
706	152	706	163	AsF stretch
711	94			AsF stretch
726	83	725	111	CSe stretch
787	64			CS stretch, CC stretch
801	94			CS stretch, CC stretch
807	82			CS stretch
1255	50	1262	52	CCH stretch
1477	79	1472	76	CC stretch
3077	91	3070	126	CH Strecth
3089	88			CH Strecth

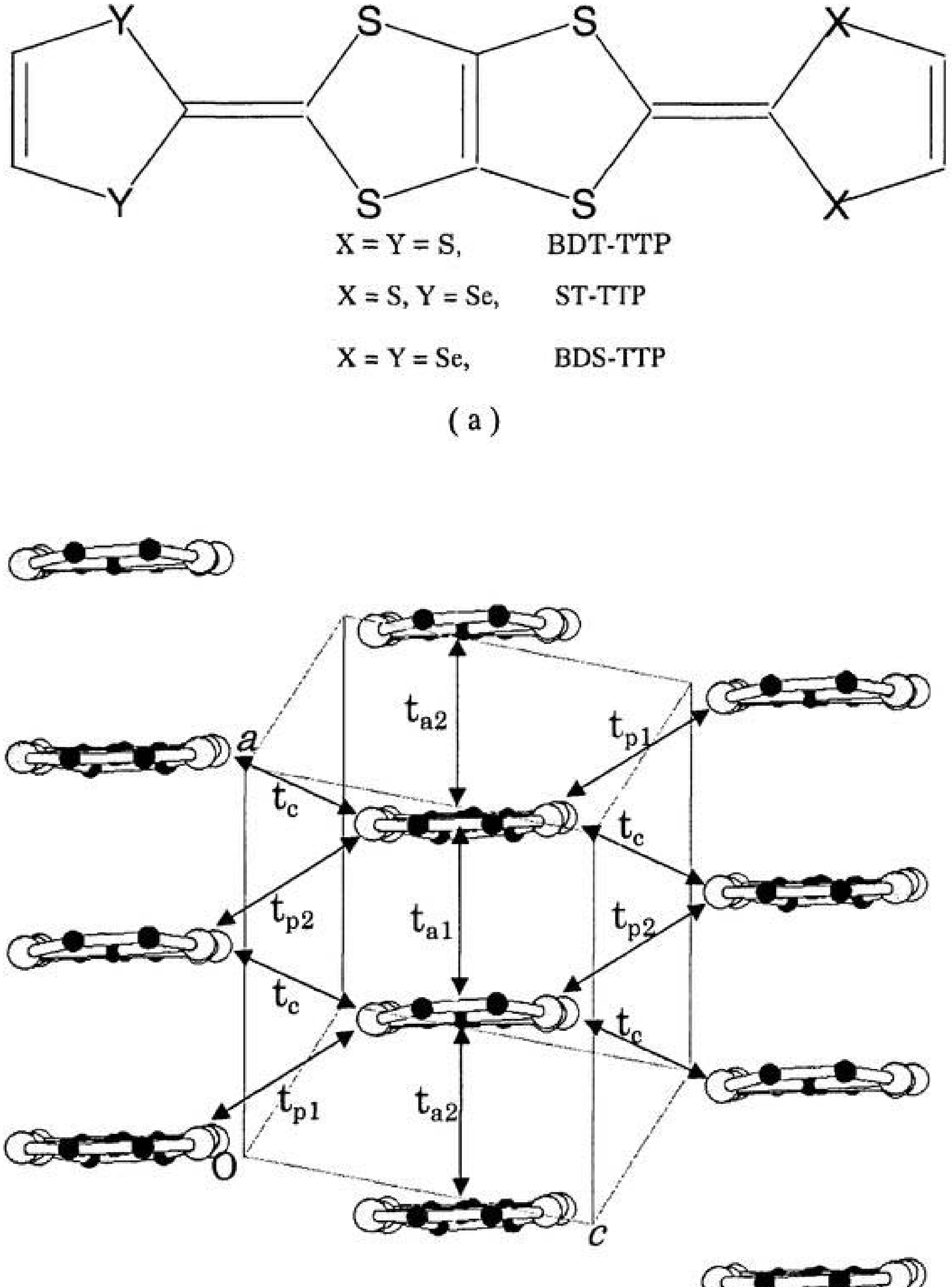

(a)

(b)

Fig. 1 (a) Chemical formula of BDT-TTP, ST-TTP and BDS-TTP. (b) Crystal structure of (ST-TTP)$_x$AsF$_6$. t_{a1}, t_{a2} are the intra-stack transfer integrals and t_{p1}, t_{p2}, t_{p3} the inter-stack transfer integrals.

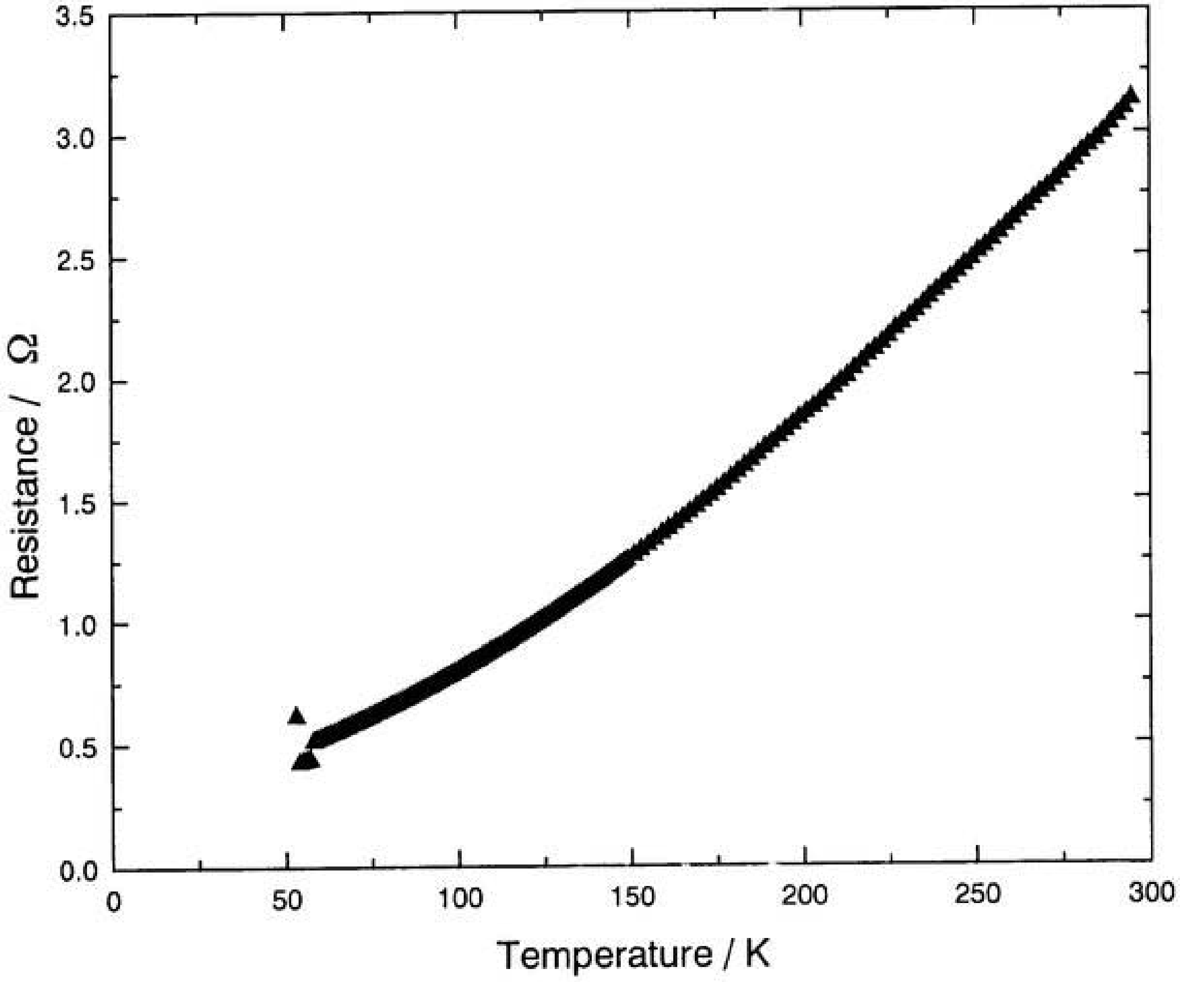

Fig. 2 Temperature dependence of the resistance of (ST-TTP)$_2$AsF$_6$ during the cooling process.

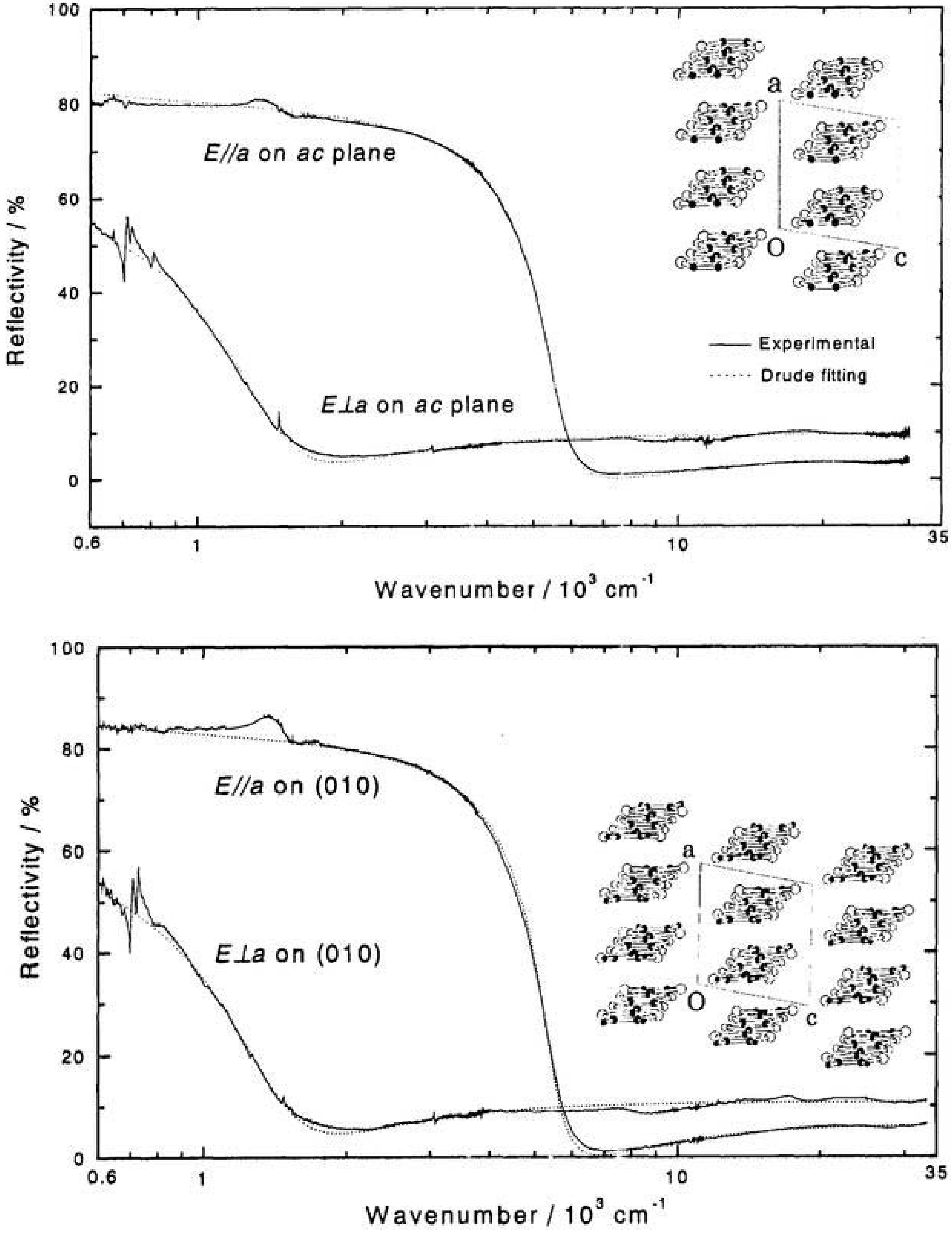

Fig. 3 Polarized reflection spectra of $(ST\text{-}TTP)_2AsF_6$ and $(BDS\text{-}TTP)_2AsF_6$ at room temperature. The solid lines are the experimental spectra and the dotted lines the Drude-model fitting. The inserts are the crystal structure projected on the (010) plane.

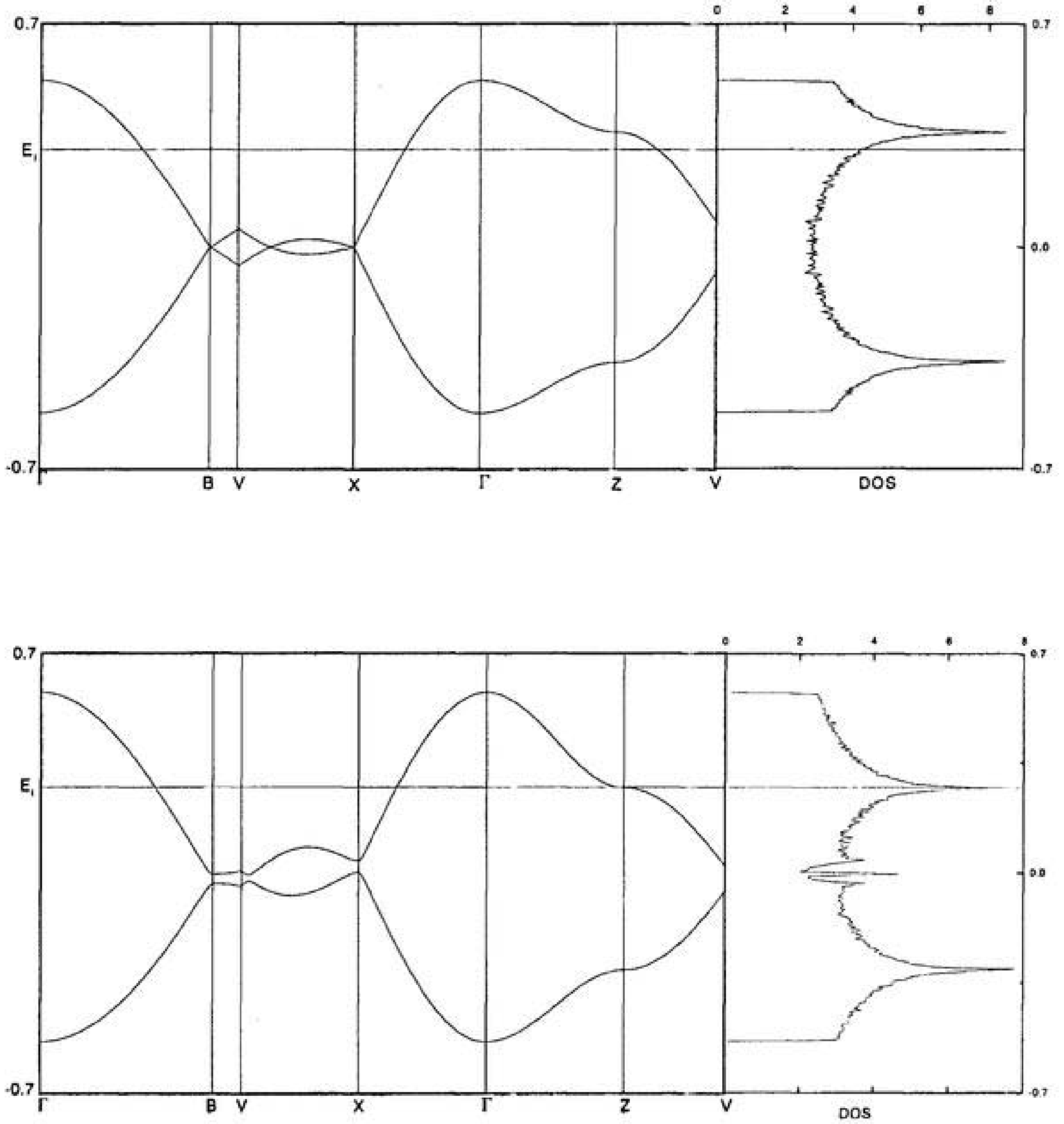

Fig. 4 Energy dispersion of $(ST\text{-}TTP)_2AsF_6$ calculated by the transfer integrals obtained experimentally (top panel) and theoretically (bottom).

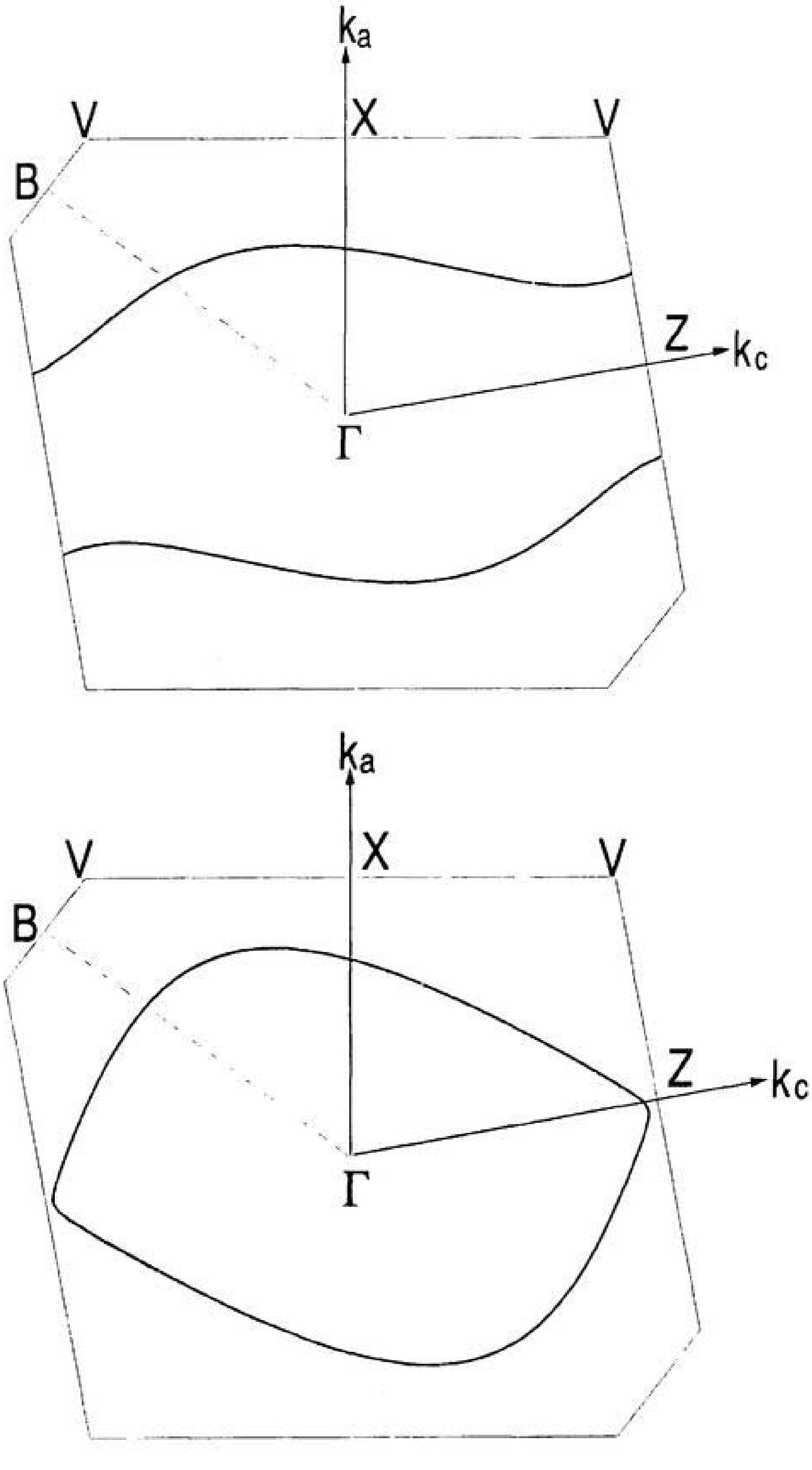

Fig 5 Fermi surface of $(ST\text{-}TTP)_2AsF_6$ calculated by use of the transfer integrals obtained experimentally (top panel) and theoretically (bottom).

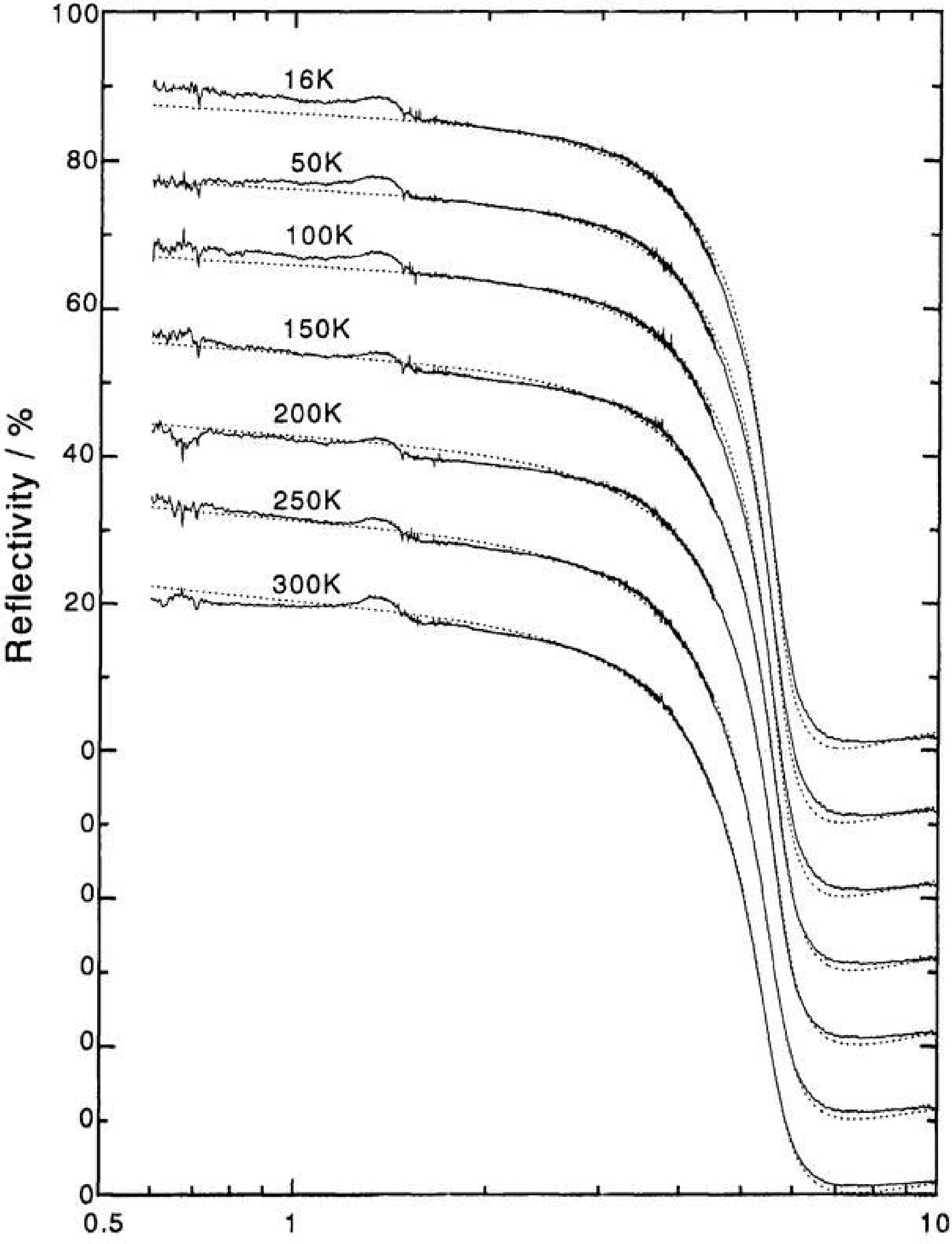

Fig. 6 *E//a* reflection spectra of $(ST\text{-}TTP)_2AsF_6$ at various temperatures. Solid lines are the experimental spectra and dotted lines the Drude-model fitting.

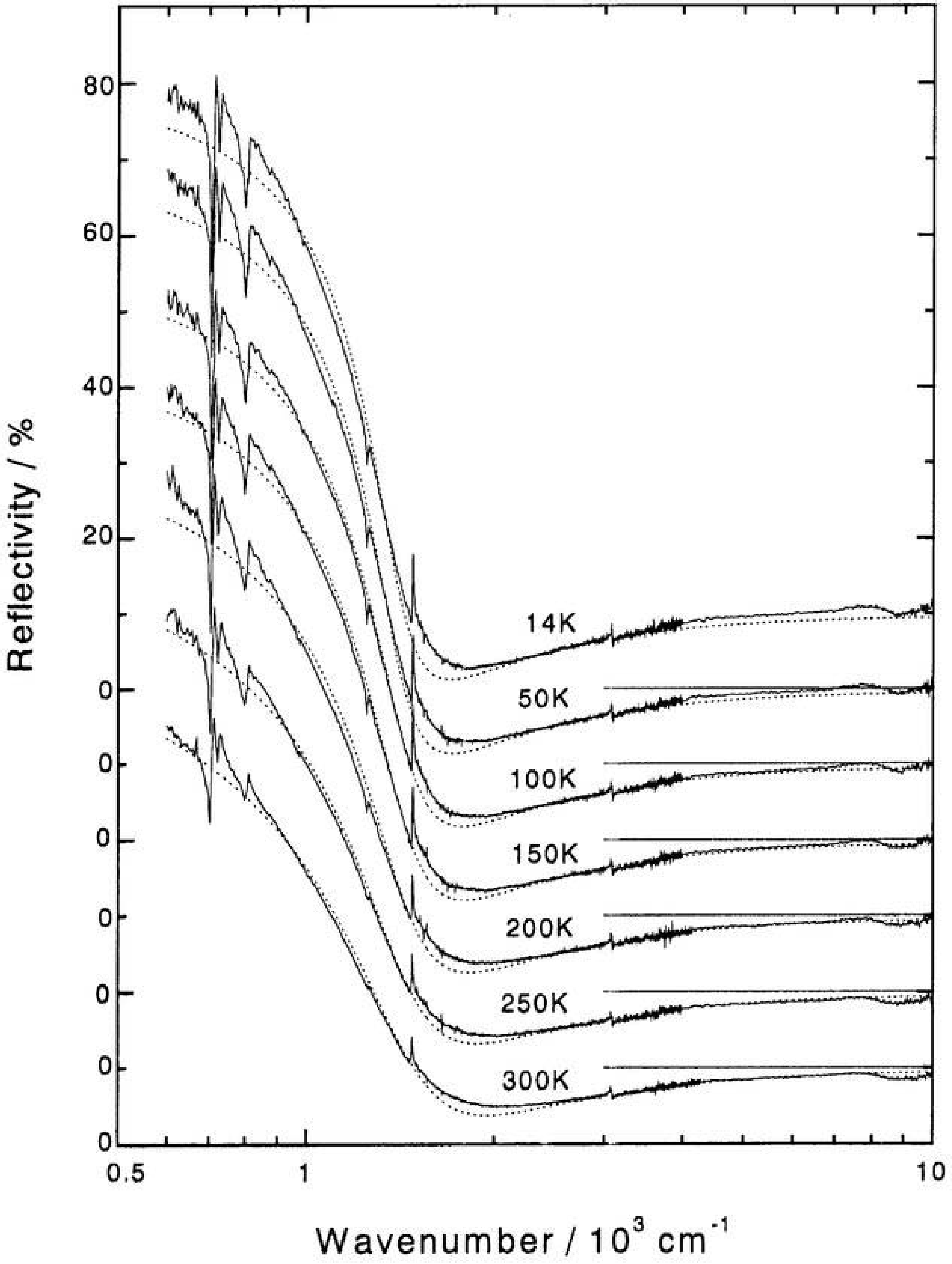

Fig. 7 $E \perp a$ reflection spectra of $(\text{ST-TTP})_2\text{AsF}_6$ at various temperatures. The solid lines are the observed spectra and the dotted lines the Drude-model fitting.

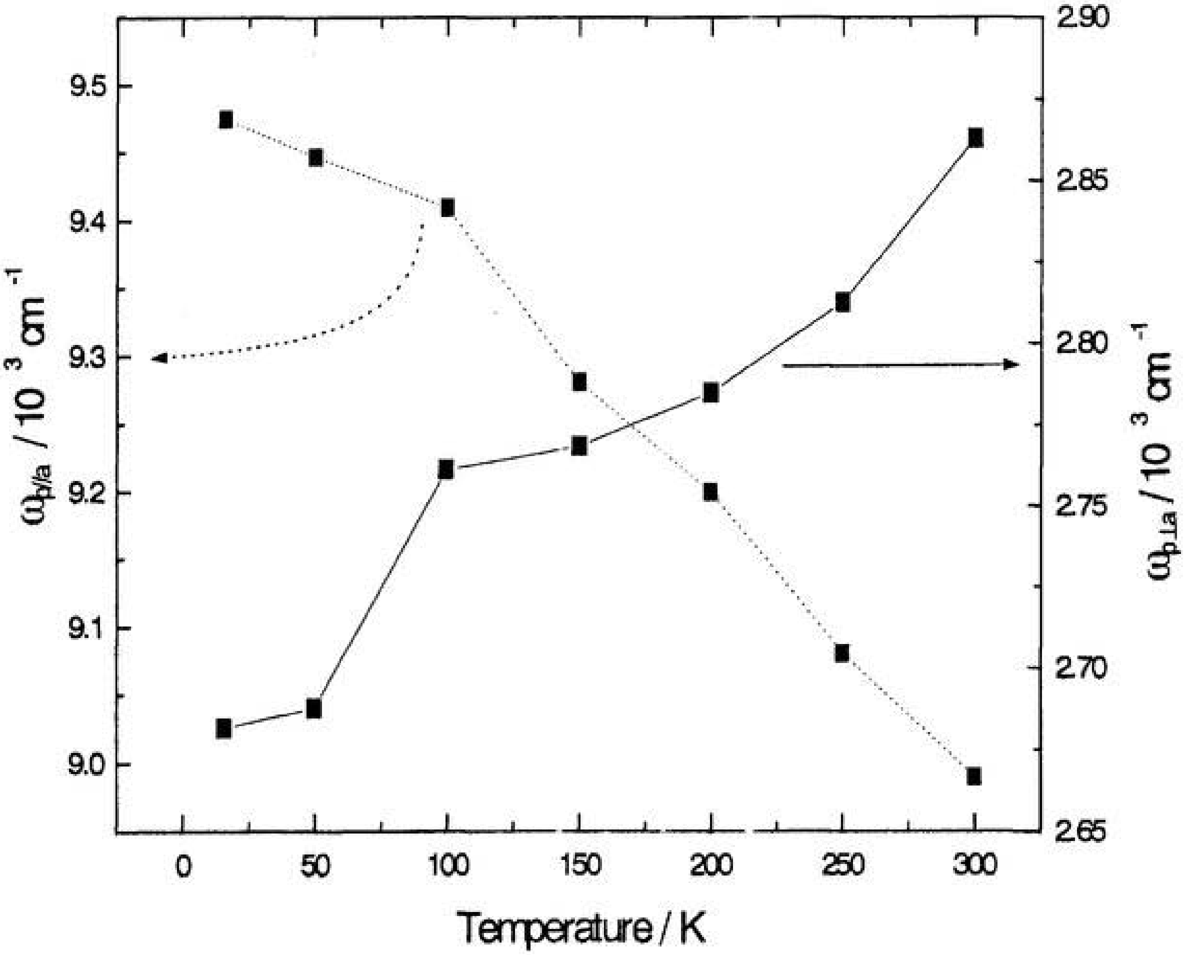

Fig. 8 Temperature dependence of the plasma frequencies of (ST-TTP)$_2$AsF$_6$.

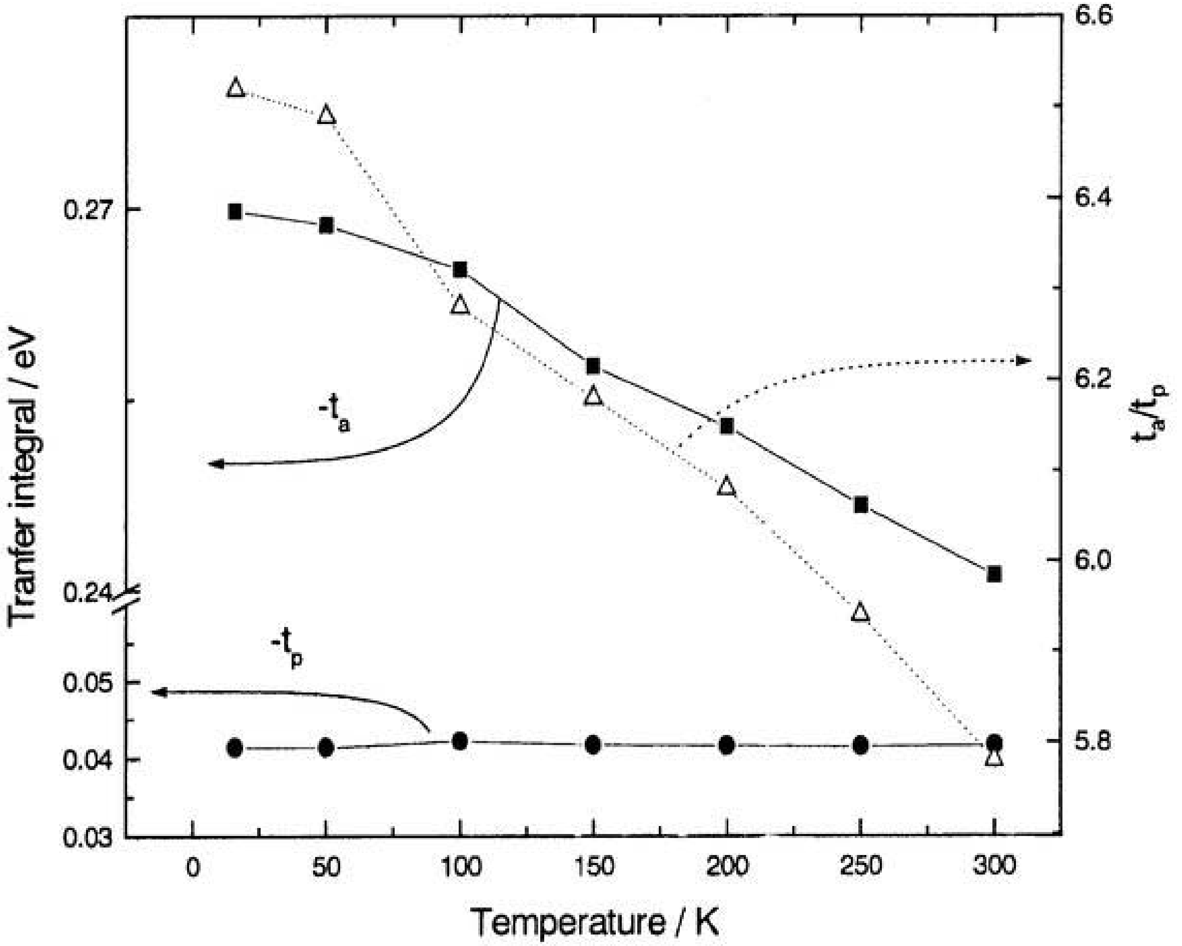

Fig. 9 Temperature dependence of the transfer integrals -t_a, -t_p, and the ratio t_a/t_p of (ST-TTP)$_2$AsF$_6$.

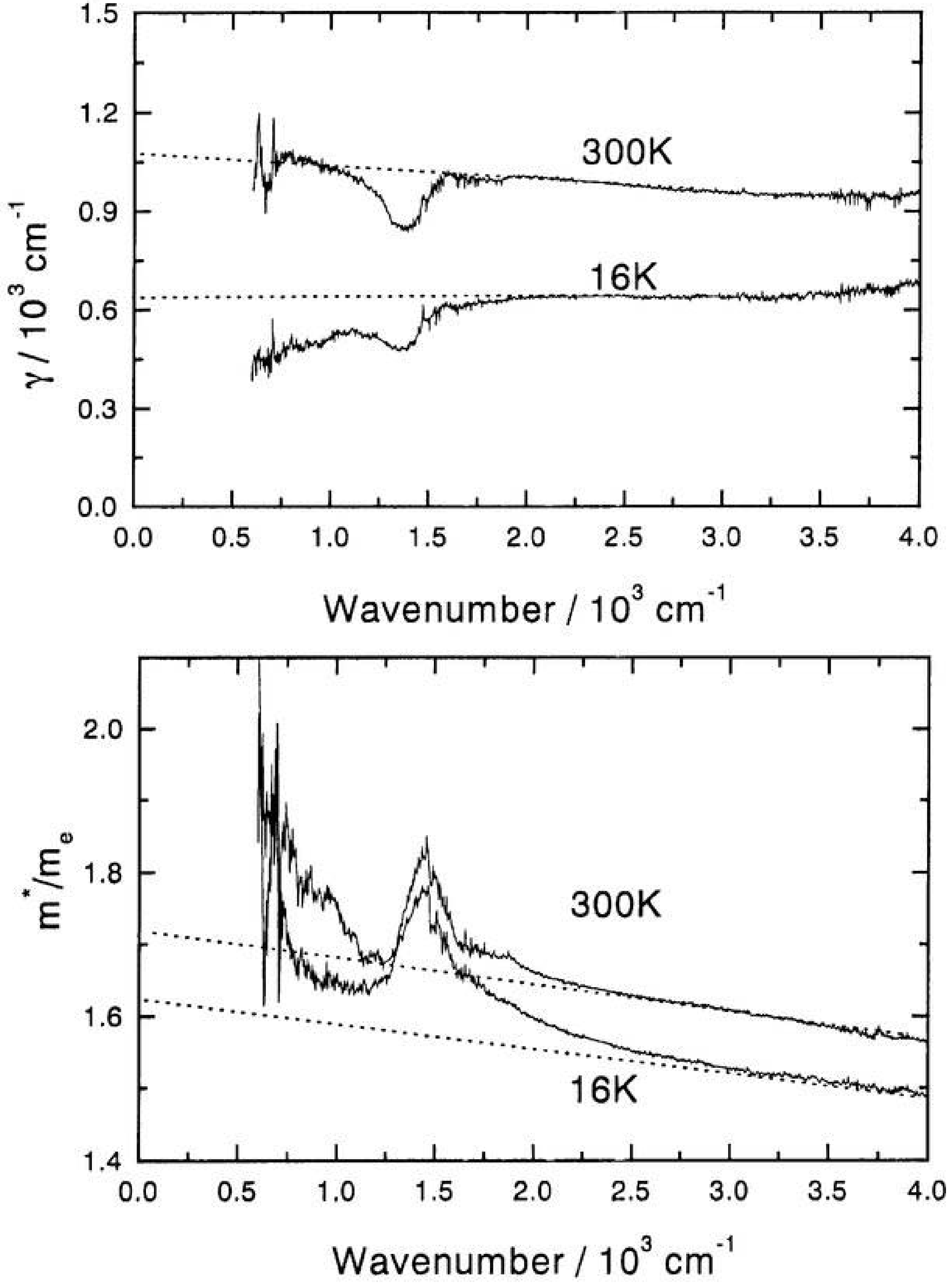

Fig. 10 *E//a* Frequency dependence of the scattering constant $\gamma(\omega)$ and the effective mass $m^*(\omega)$ of $(ST\text{-}TTP)_2AsF_6$ at 300K and 16K analyzed by the generalized Drude model.

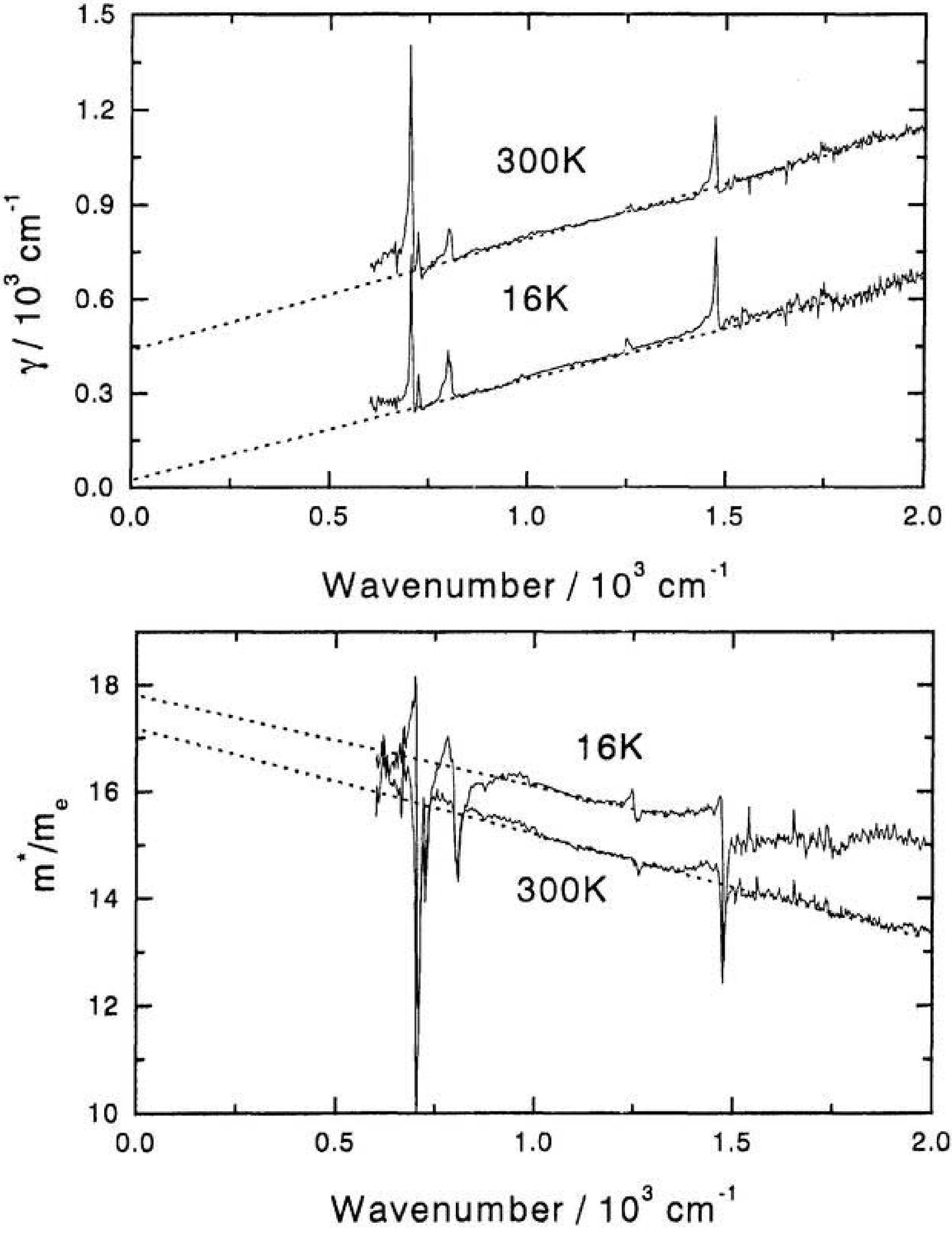

Fig. 11 $E \perp a$ Frequency dependence of the scattering constant $\gamma(\omega)$ and the effective mass $m^*(\omega)$ of (ST-TTP)$_2$AsF$_6$ analyzed by the generalized Drude-mode. The dotted lines are the fitting straight lines.

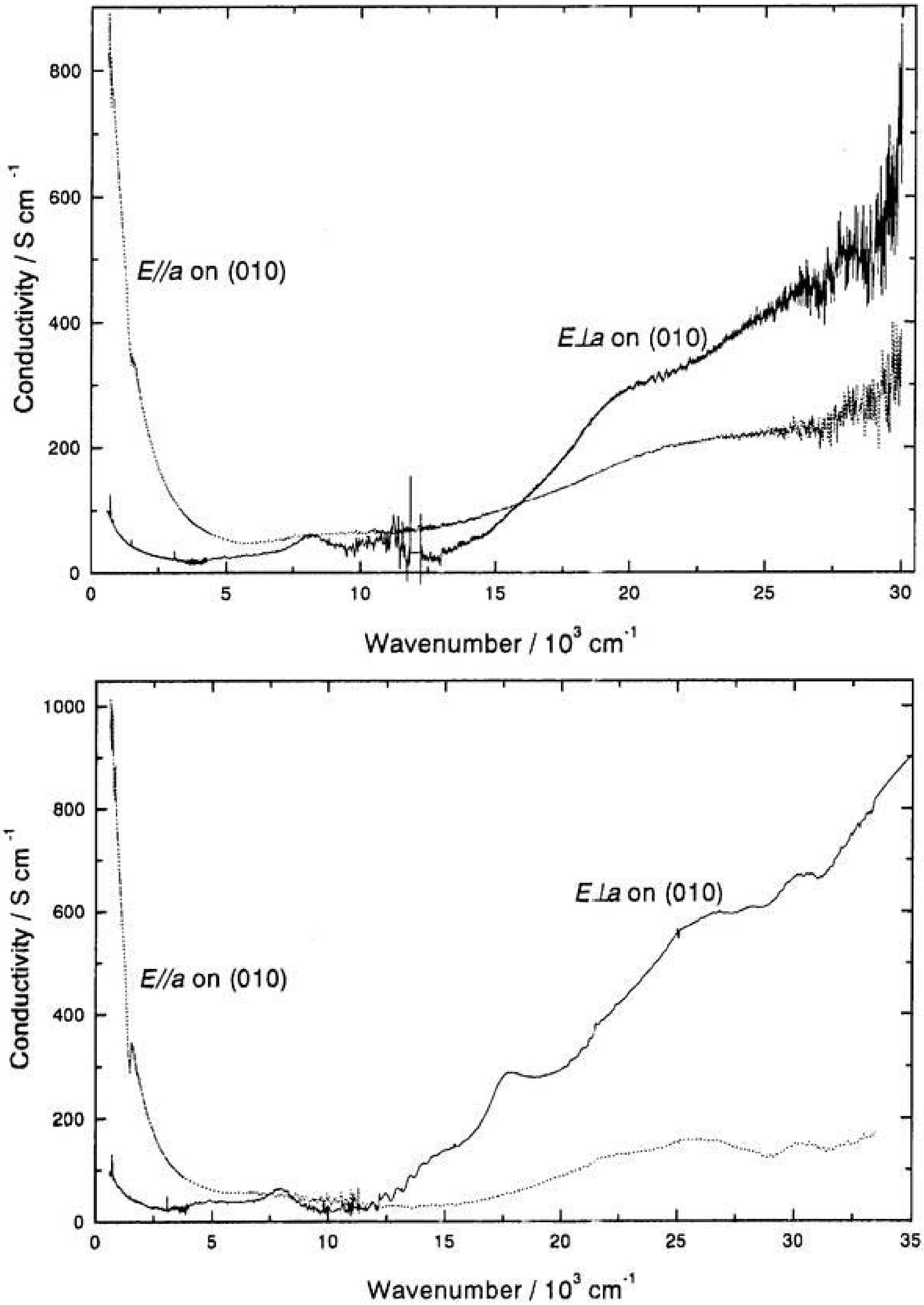

Fig. 12 Conductivity spectra of (ST-TTP)$_2$AsF$_6$ (top panel) and (BDS-TTP)$_2$AsF$_6$ at room temperature.

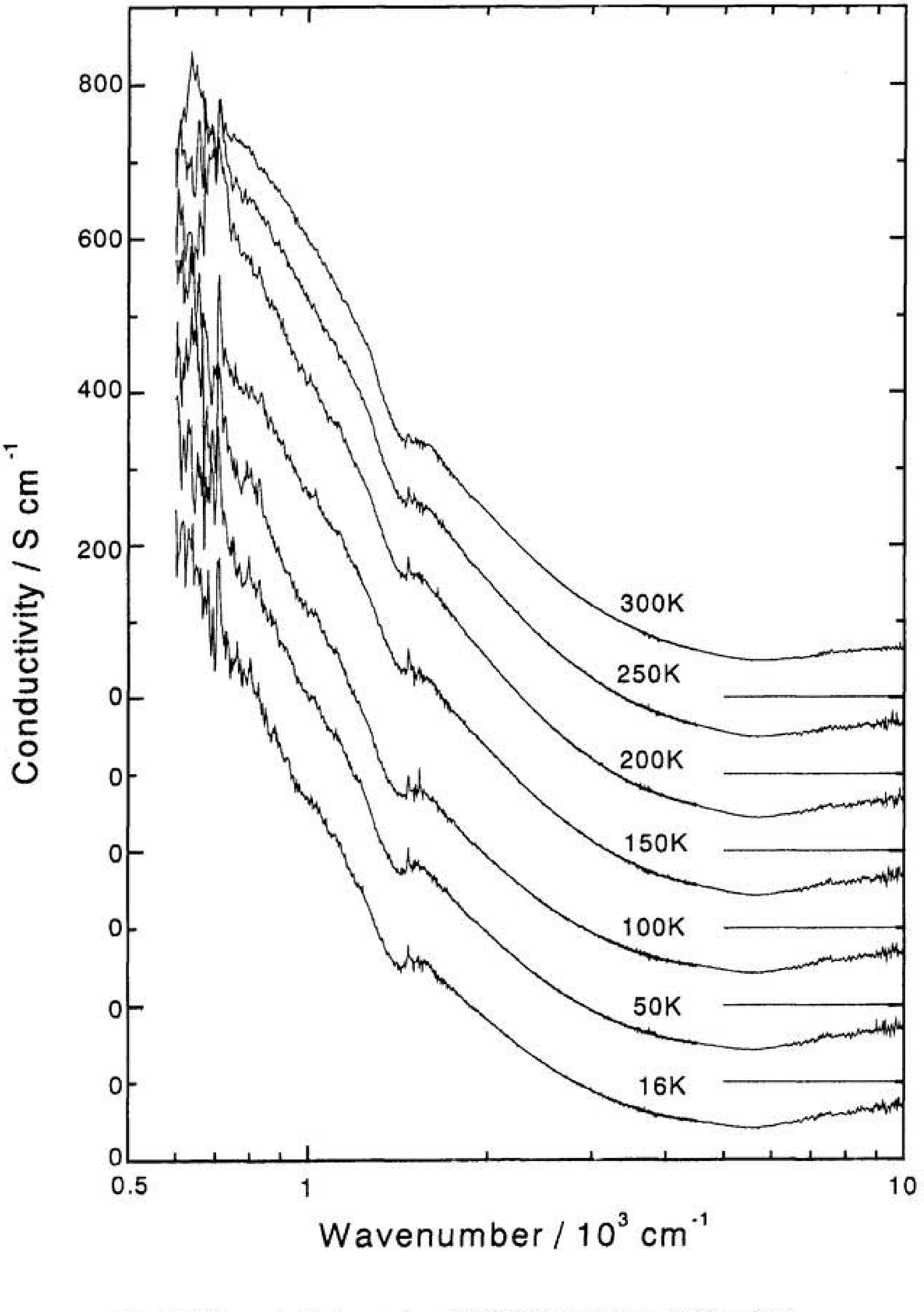

Fig. 13 *E//a* conductivity spectra of $(ST\text{-}TTP)_2AsF_6$ from 300K to 16K.

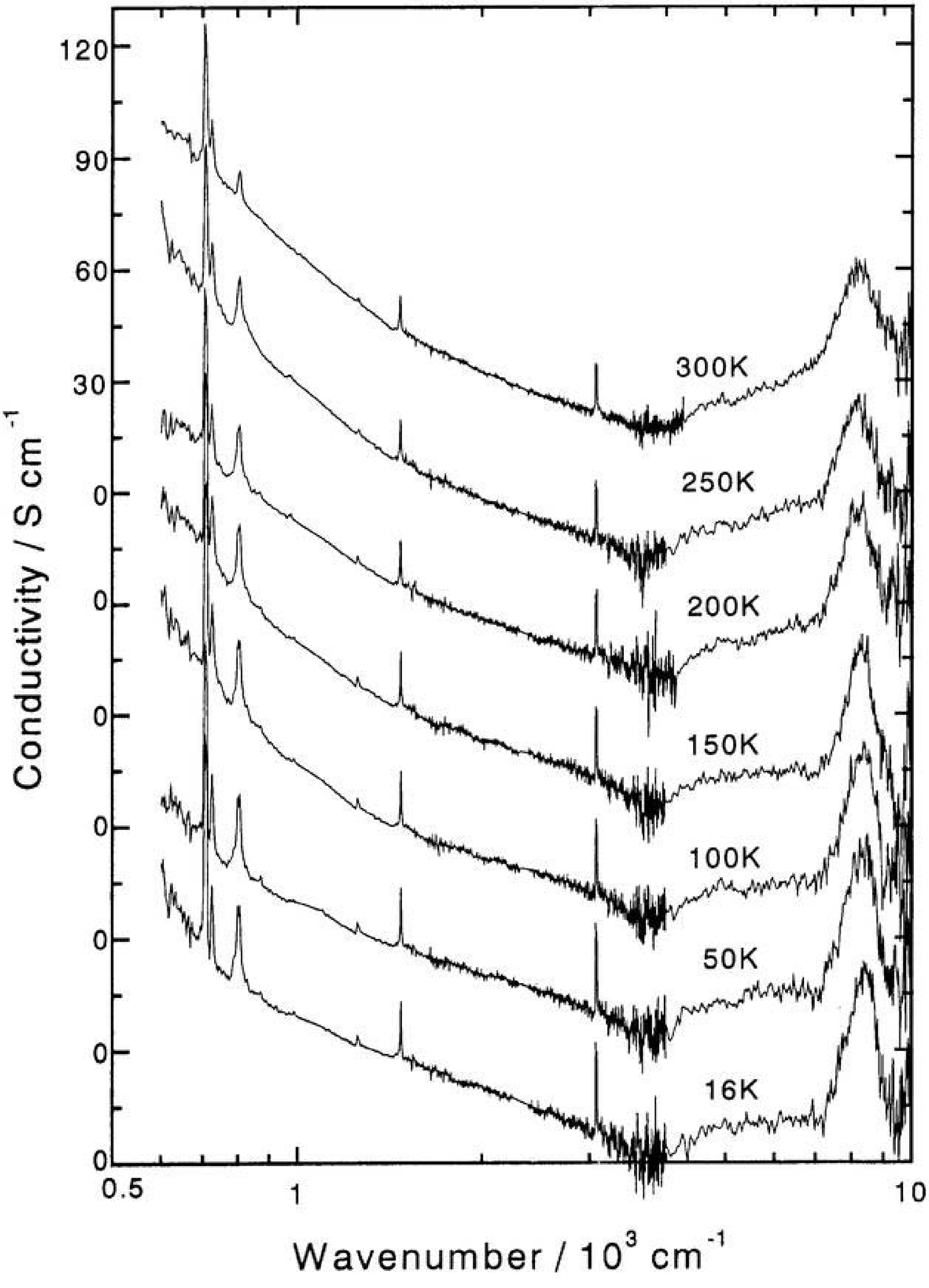

Fig. 14 $E \perp a$ conductivity spectra of (ST-TTP)$_2$AsF$_6$ from 300K to 16K.

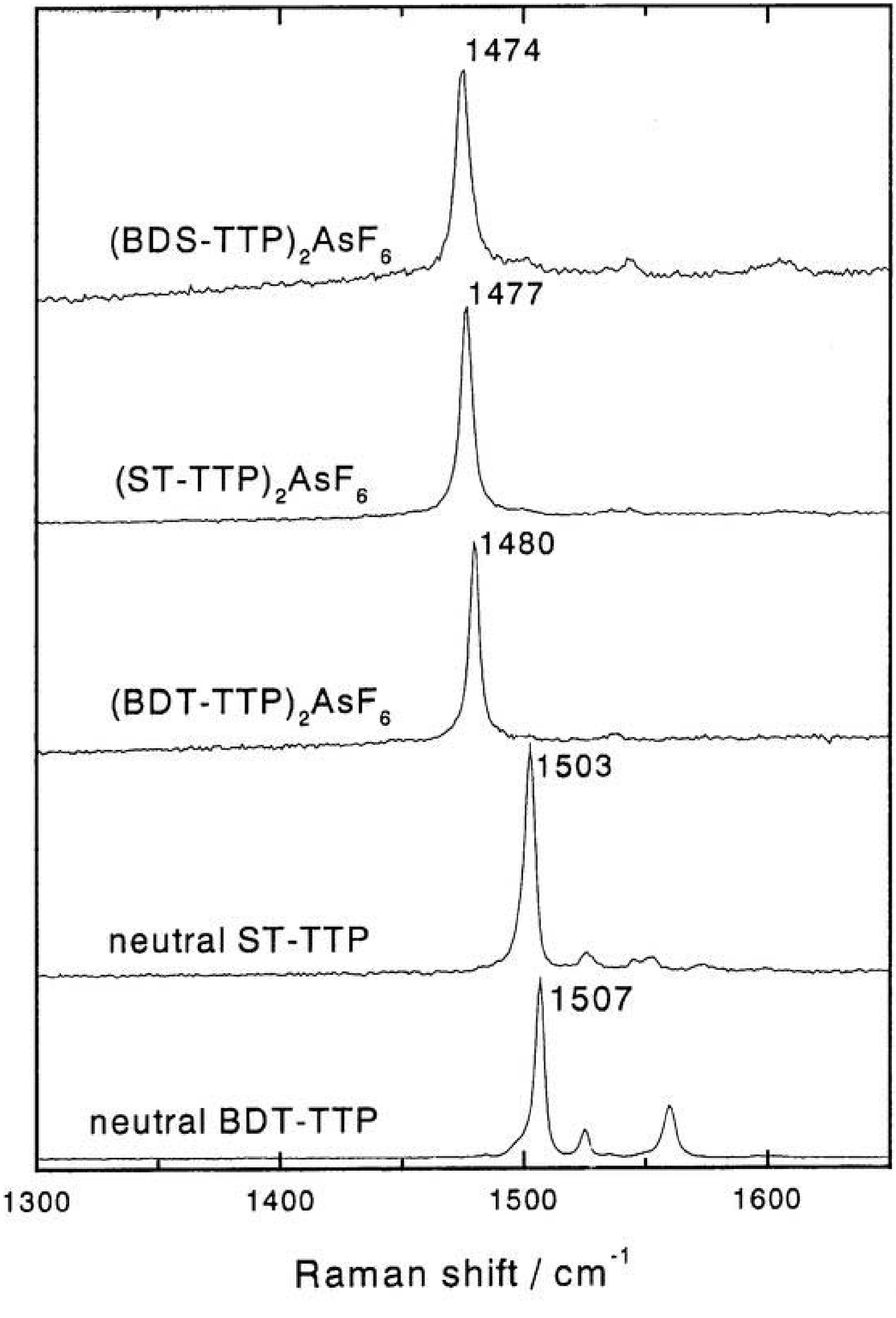

Fig. 15 Raman spectra of neutral BDT-TTP, neutral ST-TTP, (BDT-TTP)$_2$AsF$_6$, (ST-TTP)$_2$AsF$_6$, and (BDS-TTP)$_2$AsF$_6$. The numbers in the figure indicate the Raman shift of the strongest mode.

Chapter 4

Spectroscopic Study of Organic metals (BDT-TTP)$_2$Y (Y=ClO$_4$ and ReO$_4$)

J. Ouyang, K. Yakushi, Y. Misaki, and T. Tanaka

Band structure of (BDT-TTP)$_2$X (X=SbF$_6$, AsF$_6$, ClO$_4$) studied by reflection spectroscopy

Synth. Met., 103 (1999) 2207

4.1 Introduction

Many BDT-TTP salts are metallic down to liquid helium temperature, this is regarded as the result of the two-dimensional structure in the single crystals[1-3]. As discussed in Chapter 2, two-dimensional structure has been observed on the BDT-TTP salts of hexahedral anions SbF_6 and AsF_6 while the Fermi surfaces are open in the first Brillouin zone[4]. A very intriguing phenomenon in the field of organic conductor is that the crystal structure and the electronic structure strongly depend on the species of the counter anions in the crystal[5]. The space symmetries of the BDT-TTP salts of tetrahedral anions ClO_4, ReO_4 and BF_4 are *C2/c* and BDT-TTP molecules uniformly stack along the stack, in comparison with the $P\bar{1}$ space symmetry and the slightly dimerized BDT-TTP stacking structure of $(BDT\text{-}TTP)_2X$ ($X=SbF_6$, AsF_6).

The stoichiometry of $(BDT\text{-}TTP)_2Y_z$ ($Y=ClO_4$, ReO_4) is not very well determined yet. The z value is 1 and 0.86 according to the X-ray diffraction measurement and the energy dispersion spectroscopy (EDS) for $(BDT\text{-}TTP)_2(ClO_4)_z$, respectively. The discrepancy is attributable to the inaccuracy of EDS to probe S and Cl atoms. The z value is 0.72 rather than 1 for $(BDT\text{-}TTP)_2(ReO_4)_z$ consistently determined by both methods. Assuming $(BDT\text{-}TTP)_2ClO_4$ and $(BDT\text{-}TTP)_2(ReO_4)_{0.72}$, the Fermi surface calculated by the extended Hückel method is open in the first Brillouin zone for $(BDT\text{-}TTP)_2ClO_4$ while closed for $(BDT\text{-}TTP)_2(ReO_4)_{0.72}$. This significant difference of the Fermi surfaces is derived from the different z values. If these are true, very different physical properties are expected for them. However, the physical properties of them actually are very similar and like one-dimensional conductor[6]. It is very possible that the z value of the ReO_4 salt is 1 as well. The resistance of the crystal decreases when it is cooled from room temperature down to *ca.* 100 K, then some jumps occur and a hump appears in the heating run. The jumps and the hump disappear when a pressure is applied on the crystal[7]. The thermoelectric power is positive and linearly decreases on lowering temperature through the temperature. This behavior is like that of usual one-dimensional conductors but different from that of two-dimensional BEDT-TTF salts. Hence, they are regarded as metals down to liquid helium temperature like $(BDT\text{-}TTP)_2X$ ($X=SbF_6$, AsF_6). On the other hand, the intensity and the linewidth of ESR shows abnormal slightly at *ca.* 100K, a possible electronic change was proposed at this temperature by *Mori et al.*

Obviously, the study of the band structure will be very important to understand the physical properties. To date, no experiment has been conducted to study the band structure of $(BDT\text{-}TTP)_2Y_z$ ($Y=ClO_4$, ReO_4). In this Chapter, at first the charge on the donor molecule BDT-TTP of $(BDT\text{-}TTP)_2Y_z$ ($Y=ClO_4$, ReO_4) is investigated by the Raman spectroscopy. The z values are determined as 1 for both compounds. Then the band structures of them are studied by the polarized reflection spectroscopy. Two-dimensional electronic structure is observed with a significant anisotropy, the Fermi surfaces of $(BDT\text{-}TTP)_2Y_z$ ($Y=ClO_4$, ReO_4) are open in the first Brillouin zone.

4.2 Experimental

Single crystals of $(BDT\text{-}TTP)_2Y_z$ ($Y=ClO_4$, ReO_4) were grown by the electrochemical oxidation method. The crystal was black with a thin plate-like shape. The well-developed surface is (100) crystal face. The crystals with a smooth surface were chosen for the polarized reflection spectroscopy and the Raman scattering spectroscopy. The dimensions were $0.33\times0.22\times0.04mm^3$ for $(BDT\text{-}TTP)_2(ClO_4)_z$ and $0.60\times0.12\times0.04mm^3$ for $(BDT\text{-}TTP)_2(ReO_4)_z$, respectively. The polarized reflection spectrum was measured on the (100) face of the single crystal with the polarization along the crystallographic *b*- or *c*-axis. The crystal faces were determined by Enraf-Nonius CAD4 X-diffraction meter. The method to record the polarized reflection spectra is the same as that for $(BDT\text{-}TTP)_2X$ ($X=SbF_6$, AsF_6)[4). The Raman scattering was taken in back-scattering geometry by a Renishaw Ramanscope System-1000 excited by a He-Ne laser with a wavelength of 632.8nm. The laser power was decreased by a neutral filter down to 0.1mW and was focused on the 5μmϕ area of the single crystal. The incident light is polarized parallel to the *c*-axis.

The absorption spectrum of the BDT-TTP/THF solution was measured on the UV-VIS spectrophotometer HITA-CHI U-3500. The HOMO orbit of neutral BDT-TTP was calculated by HyperChem 5.1.

(BDT-TTP)Br was prepared by the chemical oxidation method. The ratio of BDT-TTP to Br was determined by EDS and also concluded according to the extremely weak ESR signal. The color is black. The crystal is needle-like with the dimension of $0.34\times0.09\times0.03\mathrm{mm}^3$. The crystal structure remains unknown. The polarized reflection spectrum was measured on the well-developed surface with the polarization parallel or perpendicular to the long edge. The methods to take the polarized reflection spectrum and the Raman scattering are the same as those on $(\mathrm{BDT\text{-}TTP})_2\mathrm{Y}_z$ ($\mathrm{Y}=\mathrm{ClO}_4$, ReO_4). The polarization of the incident light for the Raman spectroscopy is perpendicular to the long edge.

4.3 Results and Discussion

4.3.1 Raman spectra of $(BDT\text{-}TTP)_2(ClO_4)_z$ *and* $(BDT\text{-}TTP)_2(ReO_4)_z$

It has been found that the positions of some vibrational modes of the organic conductors are very sensitive to the charge on the organic donor or acceptor molecules. IR spectroscopy is not a good tool to investigate these vibration modes due to the strong dispersion of the CT band in the infrared region. For the molecules with a center of symmetry, the a_g modes sometimes appear in the IR spectrum resulted from the electron-phonon coupling. The positions are different from those of the bare phonons without electron-phonon interaction.

Raman spectroscopy is very powerful to probe the vibrational modes of organic conductors, since the positions are not affected by the electron-phonon interaction and the CT band does not appear.

Fig. 1 is the Raman spectra of neutral BDT-TTP, $(BDT\text{-}TTP)_2SbF_6$, $(BDT\text{-}TTP)_2(ClO_4)_z$ and $(BDT\text{-}TTP)_2(ReO_4)_z$ from 1200 to $1700cm^{-1}$. Three modes appear at 1507, 1526, and $1560cm^{-1}$ for neutral BDT-TTP, and the one at $1507cm^{-1}$ is very sharp and the strongest. A very sharp and strong mode appears at $1479cm^{-1}$ for both $(BDT\text{-}TTP)_2SbF_6$ and $(BDT\text{-}TTP)_2(ClO_4)_z$ and at $1478cm^{-1}$ for $(BDT\text{-}TTP)_2(ReO_4)_z$. Besides this strong mode, another relatively weak mode may appear at $1538cm^{-1}$. The Raman spectrum of $(BDT\text{-}TTP)_2AsF_6$ is the same as that of $(BDT\text{-}TTP)_2SbF_6$ in this range. Apparently, all these modes can be attributed to the C=C stretch of BDT-TTP molecule. To gain some insight into these modes, they are compared with the Raman-active modes of TTF which have been assigned very well.

In the Raman spectra of neutral TTF, the strongest mode appears at $1518cm^{-1}$ and is assigned to the a_g ν_3 mode$^{10-13)}$. It is primarily contributed by the stretch of the central C=C bond between the two five-member rings. The a_g ν_3 mode shifts to $1420cm^{-1}$ for TTF^+ monocation. The shift from neutral TTF to TTF^+ is $98cm^{-1}$. This a_g ν_3 mode is the most charge-sensitive mode of TTF, and the position linearly shifts to lower energy with respect to the increasing positive charge on $TTF^{15)}$. The linear relation is adopted to measure the charge transfer in $TTF\text{-}TCNQ^{15)}$, the result agrees with those by other approaches surprisingly well. Two factors account for the relation between the charge on the molecule and the a_g ν_3 position. One is related to the bond length. It is found that the bond length of the central C=C bond increases with respect to the further oxidation of the TTF molecule$^{14)}$. Another is the change of the HOMO electron density on the bond after the oxidation. Similar linear relation is observed on many other donor or acceptor molecules as well. For the molecules containing TTF part, such as $BEDT\text{-}TTF^{16\text{-}18)}$, $TMTTF^{19\text{-}20)}$, and $TMTSF^{19)}$, the linear relation between the position of the most charge-sensitive mode and the charge on the molecule is always observed.

BDT-TTF molecule is fused by two TTF molecules, thus it is expected that the positions of the C=C stretching modes are not very different from neutral TTF. The mode at 1507cm^{-1} of neutral BDT-TTP may correspond to the a_g ν_3 mode at 1518cm^{-1} of neutral TTF, and may be primarily contributed by the stretches of the two central C=C bonds between two-five member rings (central C=C bonds are the bonds between the two five-member rings while the fused bond is the bond fusing two TTF parts in this thesis). The stretches of the two central C=C bonds degenerate. The slight shift to red of the mode from neutral TTF to neutral BDT-TTP is presumably because the HOMO electron density on the central C=C bonds of BDT-TTP is slightly lower than that of TTF, since the number of the conjugated π-electrons in BDT-TTP is a little lower than the twice of that in TTF. The position shifts from TTF to BDT-TTP is opposite to those both from TTF to TMTTF and from TTF to BEDT-TTF. In the latter cases the position shifts to blue, because the HOMO electron density on the central C=C bond of TMTTF and BEDT-TTF is expected higher than that of TTF.

Like TTF and it salts, the bond lengths of the central C=C bonds of BDT-TTP molecule extends after the oxidation. Mori *et al.*$^{6)}$ pointed out that these central C=C bond lengths were very sensitive to the charge on BDT-TTP. These bond lengths of (BDT-TTP)$_2$ClO$_4$ are the same as (BDT-TTP)$_2$SbF$_6$, and both are longer than those of the neutral BDT-TTP. The mode at 1507cm^{-1} for neutral BDT-TTP shifts to 1479cm^{-1} for (BDT-TTP)$_2$SbF$_6$ and (BDT-TTP)$_2$AsF$_6$. By assuming a linear relation between the mode position and the charge on BDT-TTP, the position shifts to red by 56cm^{-1} from neutral BDT-TTP to BDT-TTP$^+$ monocation. This shift is only a little higher than half of the shift (-98cm^{-1}) from TTF to TTF$^+$. Concerning the loss of one HOMO electron is sustained by fused two TTF parts of BDT-TTP, this difference is very reasonable. Hence, the strongest Raman-active mode of neutral BDT-TTP and its salts is the most charge-sensitive mode.

The most charge-sensitive modes of $(BDT\text{-}TTP)_2(ClO_4)_z$ and $(BDT\text{-}TTP)_2(ReO_4)_z$ appear explicitly at the same position as those of $(BDT\text{-}TTP)_2SbF_6$ and $(BDT\text{-}TTP)_2AsF_6$. These indicate that the same charge on BDT-TTP molecule of them. Hence, the z values are 1 for both ClO_4 and ReO_4 salts. Hereafter, $(BDT\text{-}TTP)_2ClO_4$ and $(BDT\text{-}TTP)_2ReO_4$ is adopted.

4.3.2 Room temperature spectra and band structure

Fig. 2 is the crystal structure and the scheme of the transfer integrals of the $(BDT\text{-}TTP)_2ClO_4$ single crystal. The $(BDT\text{-}TTP)_2ClO_4$ crystal has a *C2/c* space symmetry with the lattice parameters being a=35.067, b=6.934, and c=12.504Å, β=102.43°. The b-axis is the unique and the stacking axis. The ClO_4 anions are at the 2-fold axis positions. The BDT-TTP molecules are located in the general positions, only one BDT-TTP molecule is independent in one unit cell. The adjacent BDT-TTP molecules in the same column are connected by the symmetry of two-fold screw axis. The BDT-TTP molecules stack uniformly in $(BDT\text{-}TTP)_2ClO_4$ single crystal, so only one intra-stack transfer integral t_b should be considered. It is different from $(BDT\text{-}TTP)_2SbF_6$, of which two intra-stack transfer integrals have to be considered due to the slightly dimerized structure. The HOMO orbit of neutral BDT-TTP calculated by Hyperchem5.1 program is a odd function with respect to the molecular plane, hence it is understandable that the intra-stack overlap of the HOMO orbits is negative between two adjacent BDT-TTP molecules for $(BDT\text{-}TTP)_2ClO_4$, in contrast to the positive overlap for $(BDT\text{-}TTP)_2X$ ($X=AsF_6$, SbF_6) which has a center of symmetry. The $(BDT\text{-}TTP)_2ReO_4$ single crystal is isostructural to $(BDT\text{-}TTP)_2ClO_4$, the lattice parameters are a=34.71, b=6.99, and c=12.50Å, β=102.44°.

The polarized reflection spectra were measured on the (100) faces of $(BDT\text{-}TTP)_2ClO_4$ and $(BDT\text{-}TTP)_2ReO_4$ single crystal with the polarization parallel b- or c-axis, as shown in

Fig. 3. The polarized reflection spectra resemble those of (BDT-TTP)$_2$SbF$_6$ and (BDT-TTP)$_2$AsF$_6$[4]. High dispersion appears at low energy region in both polarization directions with a significant anisotropy. The hump at *ca.* 1400cm^{-1} is the only phonon in the *E//b* spectrum. Several phonons appear in the *E//c* spectrum. The reflection spectra in both directions can be fitted by the simple Drude model very well except the phonons. Drude-Lorentz model are used to fit the *E//c* spectrum as well by considering the relative strong phonons in the IR range, the parameters of Drude part is very close to those by the simple Drude model. The fitting Drude parameters are listed in Table I. Like (BDT-TTP)$_2$X (X=AsF$_6$, SbF$_6$), the plasma edge of the *E//c* spectrum is not over-damped. The plasma frequency of (BDT-TTP)$_2$ClO$_4$ along the stacking axis is a little larger while that of (BDT-TTP)$_2$ReO$_4$ is smaller than that of (BDT-TTP)$_2$SbF$_6$ and (BDT-TTP)$_2$AsF$_6$.

The effective mass ratios $m^*_{//b}/m^*_{//c}$ are 0.10 for both (BDT-TTP)$_2$ClO$_4$ and (BDT-TTP)$_2$ReO$_4$, suggesting a same anisotropy in them. These effective mass anisotropies of (BDT-TTP)$_2$Y (Y=ClO$_4$, ReO$_4$) are the same as those of (ST-TTP)$_2$AsF$_6$ and (BDS-TTP)$_2$AsF$_6$, and are between that of BDT-TTP)$_2$SbF$_6$ ($m^*_{//}/m^*_{\perp}$=0.11) and of (BDT-TTP)$_2$AsF$_6$ ($m^*_{//}/m^*_{\perp}$=0.08).

The plasma frequencies along both the *b*- and the *c*-axis of (BDT-TTP)$_2$ClO$_4$ are calculated by the equation (2.1) in Chapter 2 and the relation between the electronic energy and the transfer integrals expressed by equation (4.1), by using the transfer integrals calculated by Mori *et al.*[6], t_b=0.254, t_{p1}=-0.094, t_{p2}=0.002, and t_{p3}=-0.081eV. The calculated $\omega_{p//b}$ agrees with the experimental result relatively well, while the calculated $\omega_{p//c}$ is almost twice as the experimental value. The agreement between the calculation and the experiment is similar to that of (BDT-TTP)$_2$X (X=AsF$_6$, SbF$_6$). This indicates that the inter-stack transfer integrals of (BDT-TTP)$_2$Y (Y=ClO$_4$, ReO$_4$) may be over-estimated by the extended Hückel calculation by Mori *et al*, like the case of (BDT-TTP)$_2$X (X=AsF$_6$, SbF$_6$).

Four BDT-TTP molecules in one unit cell of $(BDT\text{-}TTP)_2Y$ ($Y=ClO_4$, ReO_4) result in four energy bands. The electron energies of the bands, which can not be expressed by a simple equation as for $(BDT\text{-}TTP)_2X$ ($X=SbF_6$, AsF_6), are the eigenvalues of the following eigen-equation according to the tight-binding approximation:

$$\begin{bmatrix} -E & t_b + t_b e^{ikb} & t_{p1} + t_{p3} e^{-ikc} & t_{p2} + t_{p2} e^{ik(b-c)} \\ t_b + t_b e^{-ikb} & -E & t_{p2} + t_{p2} e^{-ikc} & t_{p3} + t_{p1} e^{-ikc} \\ t_{p1} + t_{p3} e^{ikc} & t_{p2} + t_{p2} e^{ikc} & -E & t_b + t_b e^{ikb} \\ t_{p2} + t_{p2} e^{-ik(b-c)} & t_{p3} + t_{p1} e^{ikc} & t_b + t_b e^{-ikb} & -E \end{bmatrix} = 0 \qquad (4.1)$$

Considering the transfer integrals of $(BDT\text{-}TTP)_2ClO_4$ calculated by Mori *et al.* $t_b=0.254$, $t_{p1}=-0.094$, $t_{p2}=0.002$, and $t_{p3}=-0.081eV$, it is reasonable to approximate $t_{p1}=t_{p3}=t_p$, $t_{p2}=0$. Same approximation is adopted for $(BDT\text{-}TTP)_2ReO_4$ as well. The transfer integrals t_b and t_p are estimated from the plasma frequencies $\omega_{p//b}$ and $\omega_{p//c}$ by equation (2.1) and (4.1), as listed in Table Ⅱ. The estimated t_b agrees with the calculated very well while the estimated t_p are almost half of t_{p1} or t_{p2}. The agreement between the experimental estimation and the theoretical calculation is analogous to that of $(BDT\text{-}TTP)_2X$ ($X=SbF_6$, AsF_6). The absolute value of the intra-stack transfer integral of $(BDT\text{-}TTP)_2ClO_4$ is very close to $(BDT\text{-}TTP)_2X$ ($X=SbF_6$, AsF_6). This is because the inter-molecular distances along the stack are comparable in the single crystals of them (3.467, 3.4675, and 3.47Å for ClO_4, SbF_6 and AsF_6 salts, respectively). The intra-stack transfer integral of $(BDT\text{-}TTP)_2ReO_4$ is smaller than $(BDT\text{-}TTP)_2X$ ($X=ClO_4$, SbF_6, and AsF_6), being attributed to the larger inter-molecular distance 3.495Å along the stack in $(BDT\text{-}TTP)_2ReO_4$ single crystal.

The energy band structure of $(BDT\text{-}TTP)_2ClO_4$ is calculated by using the transfer integrals obtained from the experiment and from the theoretical calculation (Fig.4). The band structure and the density of state (DOS) by the experiment is symmetrical with respect to $E=0$, owning to the approximation: $t_{p1}=t_{p3}$, and $t_{p2}=0$. The energy at point Γ of the third band by the both methods is higher than the Fermi energy, but the experimental one is more remarkable.

The similar situation is observed on the DOS. The energy bandwidths are 1.24 and 1.17eV for $(BDT\text{-}TTP)_2ClO_4$ and $(BDT\text{-}TTP)_2ReO_4$, respectively. These bandwidths agree with the results by the thermoelectric power measurement very well[21)].

Consequently, the Fermi surface of $(BDT\text{-}TTP)_2ClO_4$ is open in the first Brillouin zone by both the experimental and theoretical methods (Fig. 5). It is more one-dimensional by the optical experiments. The Fermi surface of $(BDT\text{-}TTP)_2ReO_4$ is open in the first Brillouin zone as well, since the ratio t_p/t_b = 0.19 is much lower than the critical value 0.35 proposed by Jacobenson[22)]. Such one-dimensional structure of $(BDT\text{-}TTP)_2ReO_4$ can interpret the results of the thermoelectric power and the ESR results well.

Like $(BDT\text{-}TTP)_2X$ ($X=AsF_6$, SbF_6), $(BDT\text{-}TTP)_2Y$ ($Y=ClO_4$, ReO_4) have a dimensionality between $(BEDT\text{-}TTF)_2I_3$ and $(TMTSF)_2PF_6$. $(BEDT\text{-}TTF)_2I_3$ is a two-dimensional conductor and Peierls-type phase transition does not appears down to extremely low temperature, while metal-insulator phase transition occurs at 15K for $(TMTSF)_2PF_6$. The Peierls transition is lowered when the dimensionality increases. Jerome and Schulz[5a)] proposed a rough gauge to estimate the Peierls transition temperature by investigating the $t_{p\perp}/t_{p//}$ ratio. When this ratio is larger than 1/5, the Peierls transition is suppressed through the temperature. Evidently, the $t_{p\perp}/t_{p//}$ value of BDT-TTP salts is around this value.

4.3.3 Temperature dependence of the reflection spectra of $(BDT\text{-}TTP)_2ClO_4$

The polarized reflection spectra of $(BDT\text{-}TTP)_2ClO_4$ are measured from room temperature down to 16K. Fig. 6 is the *E//b* reflection spectra at various temperatures. The reflectivity of the CT band increases on lowering temperature. The hump appears similarly at every temperature. The spectrum at any temperature can be fitted by the Drude model very well except the region below 1,400cm^{-1}, it is consistent with the metallic conductivity through the temperature. Fig. 7 is the *E//c* reflection spectra at various temperatures. The reflectivity of the CT increases at low temperature. The reflectivity at 600cm^{-1}, which is 57% at 300K, reaches to almost 80% at 16K. The intensities of some vibration modes increase at low temperature. The reflection spectrum at any temperature can be fitted by the Drude-Lorentz model very well. The *E//b* and the *E//c* plasma frequencies are plotted against the temperature (Fig. 8). $\omega_{p//b}$ increases at first on lowering temperature and then becomes less sensitive to the temperature below 150K. $\omega_{p//c}$ at first decreases on lowering temperature and then becomes almost insensitive to the temperature below 200K.

The transfer integrals t_b and t_p were estimated from the plasma frequencies at every temperature by adopting same crystal parameters at room temperature. The temperature dependence of t_b, $-t_p$, and the ratio $-t_b/t_p$ is shown in Fig. 9. The intra-stack transfer integral t_b increases on lowering temperature, while the inter-stack transfer integral t_p is almost insensitive to the temperature. The ratio $-t_b/t_p$ at first increases on lowering temperature from 300K to 100K, then becomes almost temperature-independent down to 16K. (BDT-TTP)$_2$ClO$_4$ becomes more one-dimensional from 300K down to 100K, analogous to that of (BDT-TTP)$_2$SbF$_6$. It is believed that the lattice lengths shorten at low temperature without significant change of the crystal structure. Thus the change of the transfer integrals of (BDT-TTP)$_2$ClO$_4$ indicates the compression of the crystal is easier along the stacking direction than the direction perpendicular to the stacking direction.

4.3.4 Conductivity spectra

Fig. 10 is the conductivity spectra of (BDT-TTP)$_2$Y (Y=ClO$_4$, ReO$_4$) at room temperature by the Krames-Kronig transformation of the polarized reflection spectra. Obviously, the CT bands appear in the low frequency region in both directions.

Some electronic transition bands are observed in the NIR and the visible region. A weak band appears near 8,000 cm^{-1} in the NIR region of the *E//c* spectrum, but such dispersion can not be found in the *E//b* spectrum. To gain some insight into this band, the conductivity spectra of $(BDT\text{-}TTP)_2ClO_4$ are compared with those of (BDT-TTP)Br and the absorption spectrum of neutral BDT-TTP (Fig. 11). The long edge of neutral (BDT-TTP)Br is inferred to be the stacking direction due to the appearance of the CT band. The strong appearance of some vibrational modes in the spectrum perpendicular to the long edge make us believe that this direction may parallel to the long BDT-TTP molecular axis, which is different from the *c*-axis of $(BDT\text{-}TTP)_2ClO_4$. The symmetrical band at 6,500cm^{-1} which can not be regarded as a CT band may correspond to the band at *ca.* 8,000cm^{-1} of $(BDT\text{-}TTP)_2ClO_4$. Hence, the band near 8,000cm^{-1} in the *E//c* spectrum of $(BDT\text{-}TTP)_2Y$ ($Y=ClO_4$, ReO_4) is the intra-molecule electronic transition of BDT-TTP$^+$ radical, which can not be observed in the absorption spectrum of neutral BDT-TTP. This assignment is supported by the study on for BEDT-TTF[23,24] and BPDT-TTF[25] salts (BPDT-TTF denotes bis(propylenedithio)-tetrathiafulvalene), of which similar weak band is also observed in the NIR region and is assigned to the intra-molecule transition of the cation radical. Other bands in the visible region of $(BDT\text{-}TTP)_2ClO_4$ and (BDT-TTP)Br can be observed accordingly in the absorption spectrum of neutral BDT-TTP, they are assign to the intra-BDT-TTP electronic transition.

The intra-BDT-TTP$^+$ transition band becomes stronger and sharper at low temperature (Fig. 13). The center position of this band obtained by the Lorentz-mode fitting is 8,420cm^{-1} at 300K and shifts to 8,640cm^{-1} at 16K. Such shift is similar to that of BEDT-TTF salts. The integrated intensity of this band at 16K is almost twice as that at 300K.

The only one phonon mode at *ca.* 1400cm^{-1} in the *E//b* conductivity spectrum of $(BDT\text{-}TTP)_2Y$ ($Y=ClO_4$, ReO_4) is analogous to that of $(BDT\text{-}TTP)_2SbF_6$. The dip in this direction is a vibronic mode resulted from the electron-phonon coupling. The appearance of the a_g mode along the stacking direction has been interpreted as the result of the unequivalence between two adjacent molecules caused by the dimer structure[26]. This interpretation seems well for

$(BDT\text{-}TTP)_2SbF_6$ but fails for $(BDT\text{-}TTP)_2ClO_4$, since the BDT-TTP molecules uniformly stack along the stacking direction in the $(BDT\text{-}TTP)_2ClO_4$ crystal.

No significant change can be observed from 600 to 10,000cm^{-1} in the *E//b* conductivity spectra of $(BDT\text{-}TTP)_2ClO_4$ when the temperature is lowered from 300K down to 16K (Fig. 12). Some vibrational modes in the *E//c* conductivity spectra become a little stronger at low temperature (Fig. 13). The positions and the intensities of the phonon modes at 16K are listed in Table Ⅲ.

The CH stretching mode is a broad peak for $(BDT\text{-}TTP)_2ClO_4$ at room temperature. It splits into two peaks below 200K and into four peaks below 75K, in comparison with the single peak at 3084cm^{-1} for $(BDT\text{-}TTP)_2SbF_6$ through the temperature. The four CH stretching modes appear at 3092, 3078, 3064, and 3049cm^{-1} at 16K. Therefore, the four CH stretching modes of $(BDT\text{-}TTP)_2ClO_4$ are unequivalent at least at low temperature while they degenerate for $(BDT\text{-}TTP)_2SbF_6$. The modes at 3092 and 3078cm^{-1} appear at higher positions than neutral BDT-TTP, suggesting that the conduction electrons of BDT-TTP molecule may be delocalized over the hydrogen atom.

The vibartional modes of ClO_4 show some change at low temperature. At room temperature, three bands appear at 1122, 1107, and 1072cm^{-1}, which can be assigned to the f_2 ν_3 mode of ClO_4. At 125K, a new peak appears so that there are four bands at 1127, 116, 1096, and 1071cm^{-1} for the f_2 ν_3 mode of ClO_4. Such change of the ClO_4 vibrational modes has also been observed on $(TMTTF)_2ClO_4$ 19). It is not clear whether the change of the ClO_4 and the CH vibrational modes is related to the possible electronic structure change at *ca.* 100K observed by the ESR measurement 6).

4.4 Summary

In the Raman spectra of the BDT-TTP salts of ClO_4 and ReO_4, the most charge-sensitive modes appear at the same position as those of $(BDT\text{-}TTP)_2X$ ($X=AsF_6$, SbF_6). Therefor, the stoichiometries of the ClO_4 and ReO_4 salts are determined as $(BDT\text{-}TTP)_2ClO_4$ and $(BDT\text{-}TTP)_2ReO_4$. The polarized reflection spectra of $(BDT\text{-}TTP)_2ClO_4$ and $(BDT\text{-}TTP)_2ReO_4$ resemble those of $(BDT\text{-}TTP)_2X$ ($X=AsF_6$, SbF_6). The anisotropies of the effective masses of both compounds are between that of $(BDT\text{-}TTP)_2SbF_6$ and $(BDT\text{-}TTP)_2AsF_6$. The intra-stack transfer of $(BDT\text{-}TTP)_2ClO_4$ is comparable with that of $(BDT\text{-}TTP)_2X$ ($X=AsF_6$, SbF_6) while higher than $(BDT\text{-}TTP)_2ReO_4$, which is consistent with the inter-BDT-TTP distances along the stack. The Fermi surfaces of both compounds are open in the first Brillouin zone. The band near 8,000 cm^{-1} in the *E//c* spectrum is assigned to the intra-$BDT\text{-}TTP^+$ transition. It shifts to higher energy region and becomes sharper on lowering temperature.

References:

1) Y. Misaki and T. Mori, *Solid State Physics,* **33** (1998) 1014.

2) Y. Misaki, H. Fujiwara, T. Yamabe, T. Mori, H. Mori, and S. Tanaka, *Chem. Lett.*, (1994) 1653.

3) T. Nakada, T. Ishiguro, T. Miura, T. Misaki, T. Yamabe, and T. Mori, *J. Phys. Soc. Jpn.*, 67 (1998) 355.

4) J. Ouyang, K. Yakushi, Y. Misaki, and K. Tanaka, *J. Phys. Soc. Jpn.*, **67** (1998) 3191.

5) There are some very good reviews related to this phenomenon, such as: (a) D. Jérome and H. J. Schulz, *Advances in Physics*, **31** (1982) 299; (b) T. Ishiguro and K. Yamaji, *Organic superconductors*, Spinger-Verlag, Berlin, (1990); (c) J. M. Williams, J. R. Ferraro, R. J. Thorn, K. d. Carlson, U. Geiser, H. H. Wang, A. M. Kini, and M.-H. Whangbo, *Organic superconductors: synthesis, structure, properties, and theory*, Prentice hall, Inc., London, (1990).

6) T. Mori, Y. Misaki, H. Fujiwara, and T. Yamabe, *Bull. Chem. Soc. Jpn.*, **67** (1994) 2685.

7) T. Kawamoto, T. Mori, J. Yamaura, T. Enoke, Y. Misaki, T. Yamabe, H. Mori, and S. Tanaka, *Synth. Met.*, **85** (1997) 1555.

8) T. Mori and H. Inokuchi, *J. Phys. Soc. Jpn.*, **57** (1984) 3674.

9) A. J. Berlinsky, Y. Hoyano, and L. Weiler, *Chem. Phys. Lett.*, **45** (1977) 419.

10) R. Bozio, A. Girlando, and C. Pecile, *Chem. Phys. Lett.*, **52** (1977) 503.

11) N. O. Lipari, M. J. Rice, C. B. Duke, R. Bozio, A. Girlando, and C. Pecile, *Int. J. Quan. Chem.: Quan. Chem. Symp.*, **11** (1977) 583.

12) R. Bozio, I. Zanon, A. Girlando, and C. Pecile, *J. Chem. Phys.*, **71** (1979) 2282.

13) R. Bozio and C. Pecile, *J. Phys. C: Solid St. Phys.,* **13** (1980) 6205.

14) R. Williams, C. L. Ma, S. Samson, S. K. Khanna, and R. B. Somoano, *J. Chem. Phys.*, **72**

(1980) 3781.

15) R. P. van Duyne, T. W. Cape, M. R. Suchanski, and A. R. Siedle, *J. Phys. Chem.*, **90** (1986) 739.

16) M. E. Kozlov, K. I. Pokhodnia, and A. A. Yurchenko, *Spectrochim. Acta*, **43A** (1983) 323.

17) M. E. Kozlov, K. I. Pokhodnia, and A. A. Yurchenko, *Spectrochim. Acta*, **45A** (1989) 437.

18) K. D. Truong, D. Achkir, S. Jandl, and M. Poirier, *Phys. Rev. B*, **51** (1995) 16168.

19) R. Bozio, M. Meneghetti, and C. Pecile, *J. Chem. Phys.*, **76** (1982) 5785.

20) M. Meneghetti, R. Bozio, I. Zanon, C. Pecile, C. Ricotta, and M. Zanetti, *J. Chem. Phys.*, **80** (1984) 6210.

21) As in reference 6) by Mori et al, the bandwidths $4t_b$ estimated from the temperature dependence of the thermoelectric power are 1.3 and 2.2 eV for $(BDT\text{-}TTP)_2ClO_4$ and $(BDT\text{-}TTP)_2(ReO_4)_{0.72}$, respectively. It is 1.06 eV when $(BDT\text{-}TTP)_2ReO_4$ is regarded.

22) C. S. Jacobsen, in *Low-dimensional conductors and superconductors*, ed. by D. Jérome and L. G. Caron, Plenum Press, New York, (1987) 253.

23) M. Tamura, H. Tajima, K. Yakushi, H. Kuroda, A. Kobayashi, R. Kato, and H. Kobayashi, *J. Phys. Soc Jpn.*, **60** (1991) 3861.

24) M. Tamura, K. Yakushi, H. Kuroda, A. Kobayashi, R. Kato, and H. Kobayashi, *J. Phys. Soc. Jpn.*, **57** (1988) 3239.

25) K. Yakushi, H. Tajima, T. Ida, M. Tamura, H. Hayashi, H. Kuroda, A. Kobayashi, H. Kobayashi, and R. Kato, *Synth. Met.*, **24** (1988) 301.

26) M. J. Rice, *Solid State Commun.*, **31** (1979) 93.

Table I Drude-model parameters of $(BDT\text{-}TTP)_2ClO_4$ and $(BDT\text{-}TTP)_2ReO_4$ at room temperature. The parameters of *E//c* is the Drude part by fitting the *E//c* reflection spectrum Drude-Lorentz model by Drude-Lorentz model.

	ε_c	γ (10^3 cm^{-1})	ω_p (10^3 cm^{-1})	m^*/m_e	ω_p(calc) (10^3 cm^{-1})
$(BDT\text{-}TTP)_2ClO_4$					
E//b on (100)	2.86	0.85	9.42	1.36	9.12
E//c on (100)	3.60	0.89	2.99	13.5	5.56
$(BDT\text{-}TTP)_2ReO_4$					
E//b on (100)	2.86	8.92	9.21	1.42	
E//c on (100)	3.64	0.86	2.97	13.7	

Table Ⅱ The intra-(t_b) and inter-stack (t_{p1}, t_{p2}, t_{p3}) transfer integrals of (BDT-TTP)$_2$ClO$_4$ and (BDT-TTP)$_2$ ReO$_4$.

	t_b	t_{p1}	t_{p3}	t_{p2}
(BDT-TTP)$_2$ ClO$_4$[a]	0.261	-0.048	-0.048	0
(BDT-TTP)$_2$ ClO$_4$[b]	0.254	-0.094	-0.081	0.002
(BDT-TTP)$_2$ ReO$_4$[a]	0.245	-0.047	-0.047	0

[a] This work. Estimated from the optical experiments

[b] Ref. 6. Calculated by the extended Hückel method.

Table Ⅲ Positions and plasma frequencies of the phonon modes in the *E*//*c* conductivity spectrum of $(BDT\text{-}TTP)_2ClO_4$ at 16K. The plasma frequency is defined by $\omega_p^2 = \frac{2}{\pi\varepsilon_0}\int\sigma(\omega)d\omega$.

Position (cm^{-1})	Plasma frequency (cm^{-1})	Tentative assignment
809	83	CS stretch
852	40	CS stretch, CC stretch
883	62	CS stretch, CC stretch
1022	29	
1071	48	ClO stretch
1096	70	ClO stretch
1116	132	ClO stretch
1127	57	ClO stretch
1245	31	CCH bend
1254	26	CCH bend
1262	25	CCH bend
1474	56	C=C stretch
1481	81	C=C stretch
1569	58	C=C stretch
3049	57	CH stretch
3064	88	CH stretch
3078	95	CH stretch
3092	44	CH stretch

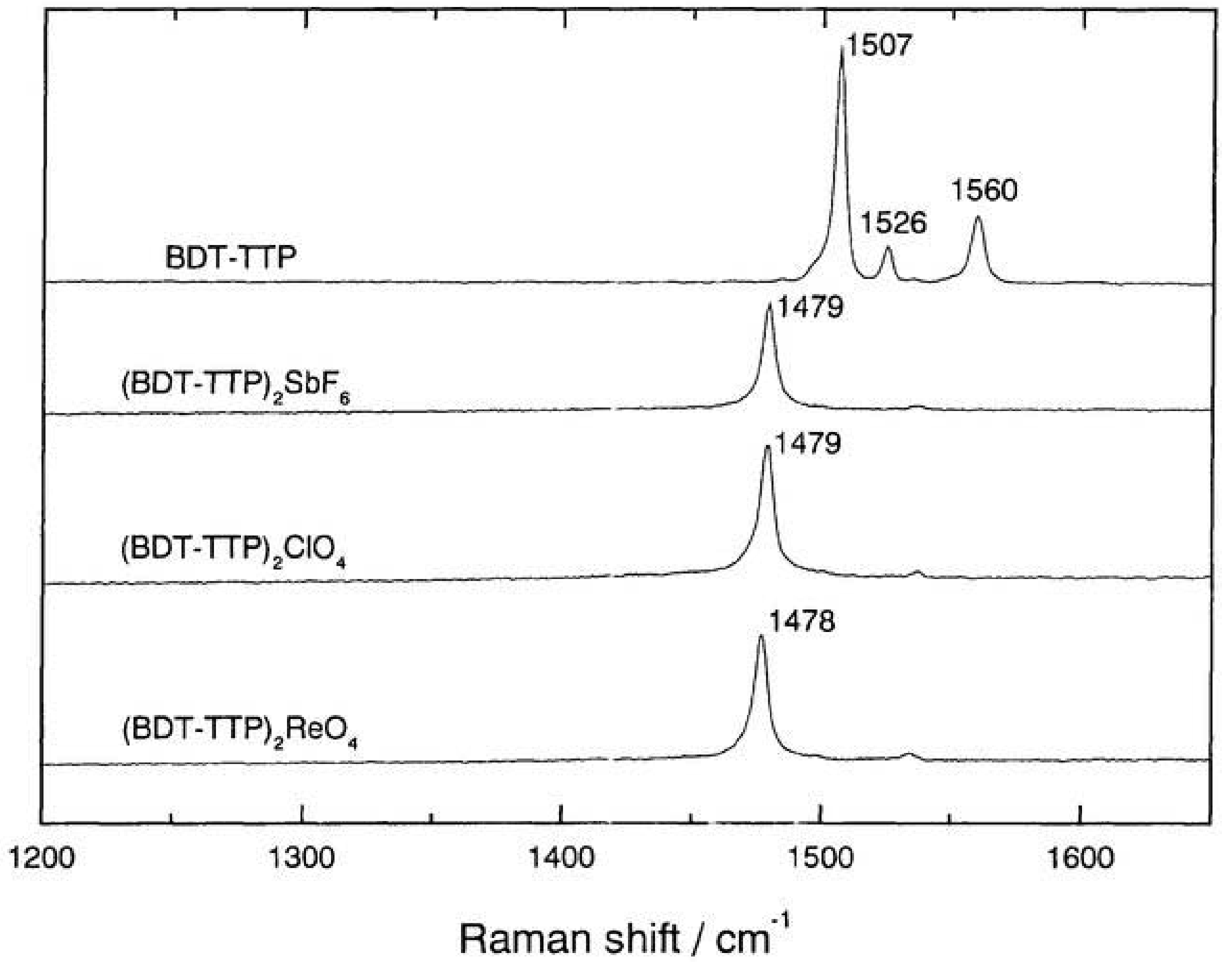

Fig. 1 Raman spectra of neutral BDT-TTP, (BDT-TTP)$_2$SbF$_6$, (BDT-TTP)$_2$ClO$_4$, and (BDT-TTP)$_2$ReO$_4$. The numbers indicate the positions of the modes.

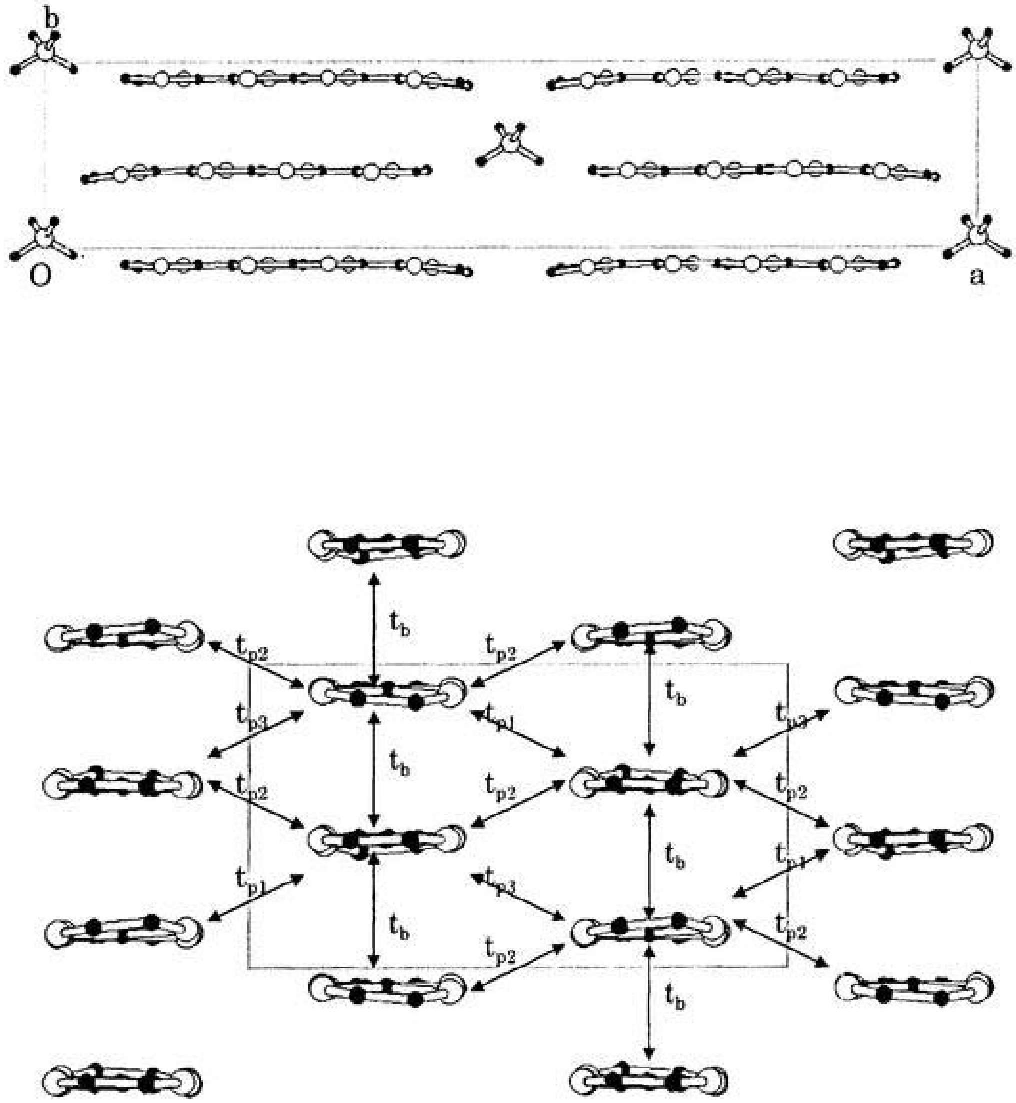

Fig. 2 Crystal structure of (BDT-TTP)$_2$ClO$_4$ viewed along the *c*-axis (top panel), and the conducting sheet viewed along the long molecular axis (bottom). t_b is the intra-stack transfer integral and t_{p1}, t_{p2}, t_{p3} are the inter-stack transfer integrals.

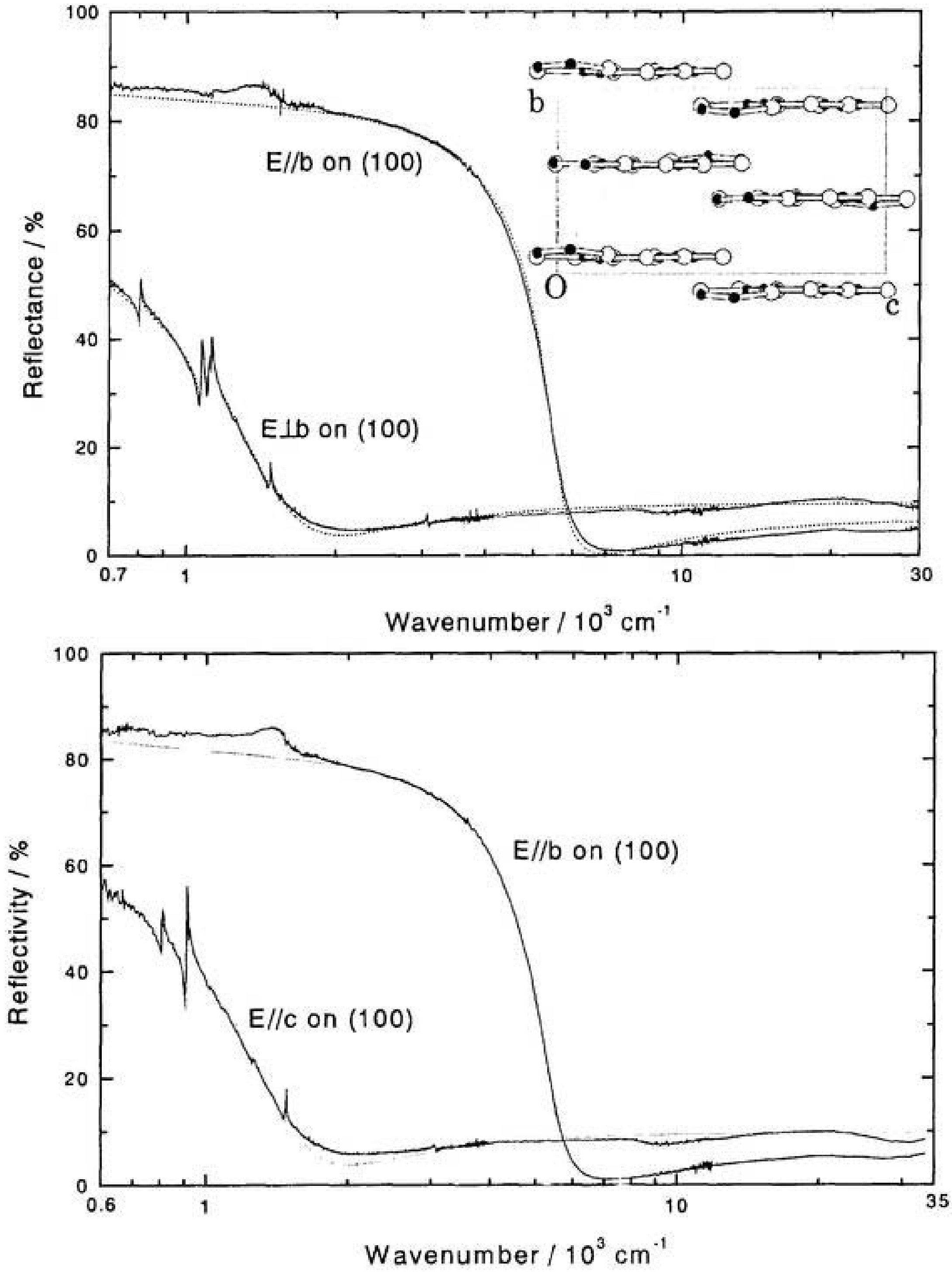

Fig. 3 Polarized reflection spectra of $(BDT\text{-}TTP)_2ClO_4$ (top panel) and $(BDT\text{-}TTP)_2ReO_4$ (bottom) at room temperature. The solid lines are the observed reflectivities and the dotted lines are the Drude-model fittings. The insert in the top panel shows the arrangement of BDT-TTP molecules projected onto (100) plane.

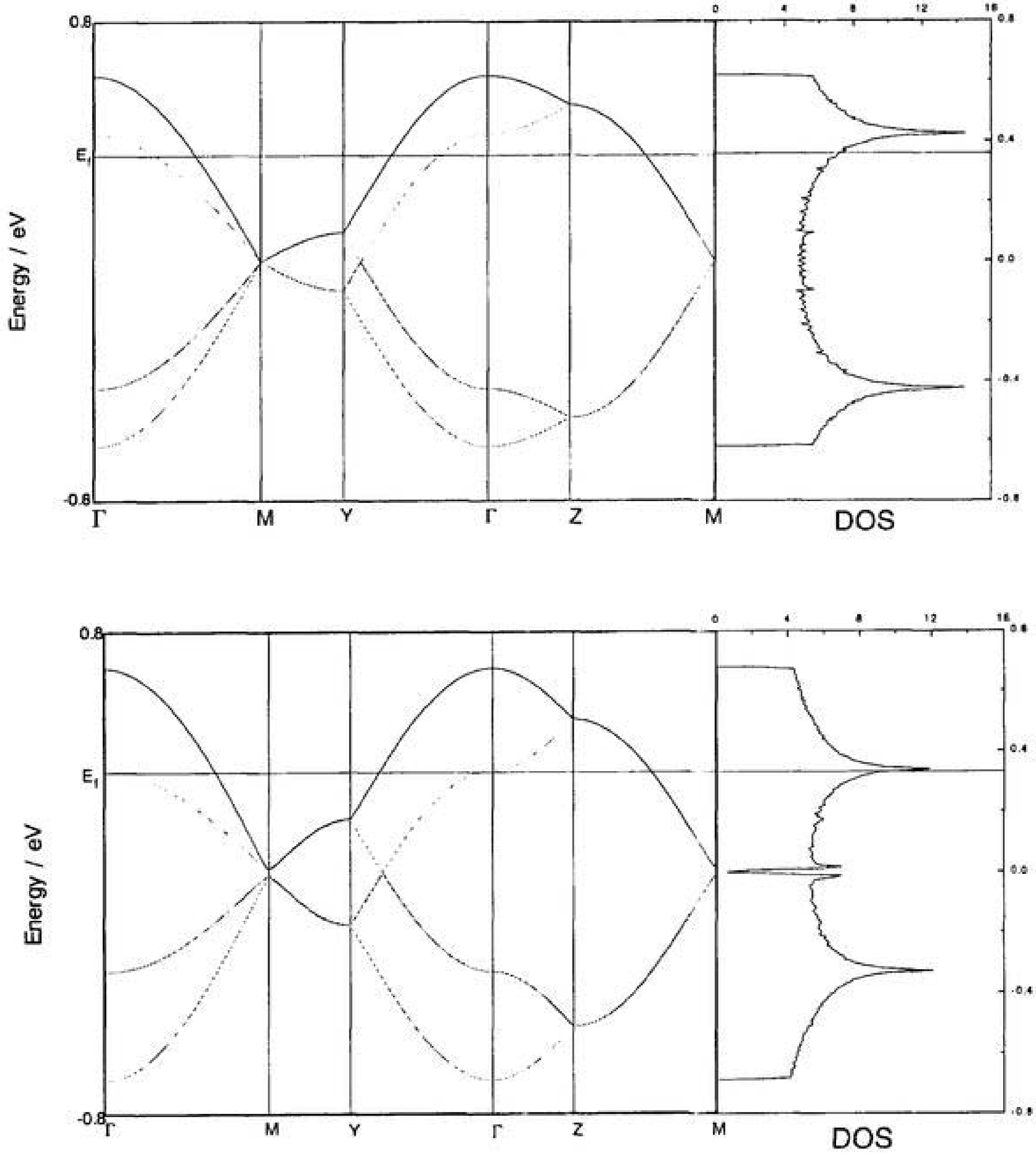

Fig. 4 Energy band of $(BDT\text{-}TTP)_2ClO_4$. calculated by using the transfer integrals obtained by the optical experiments (top panel) and by the extended Hückel calculation (bottom).

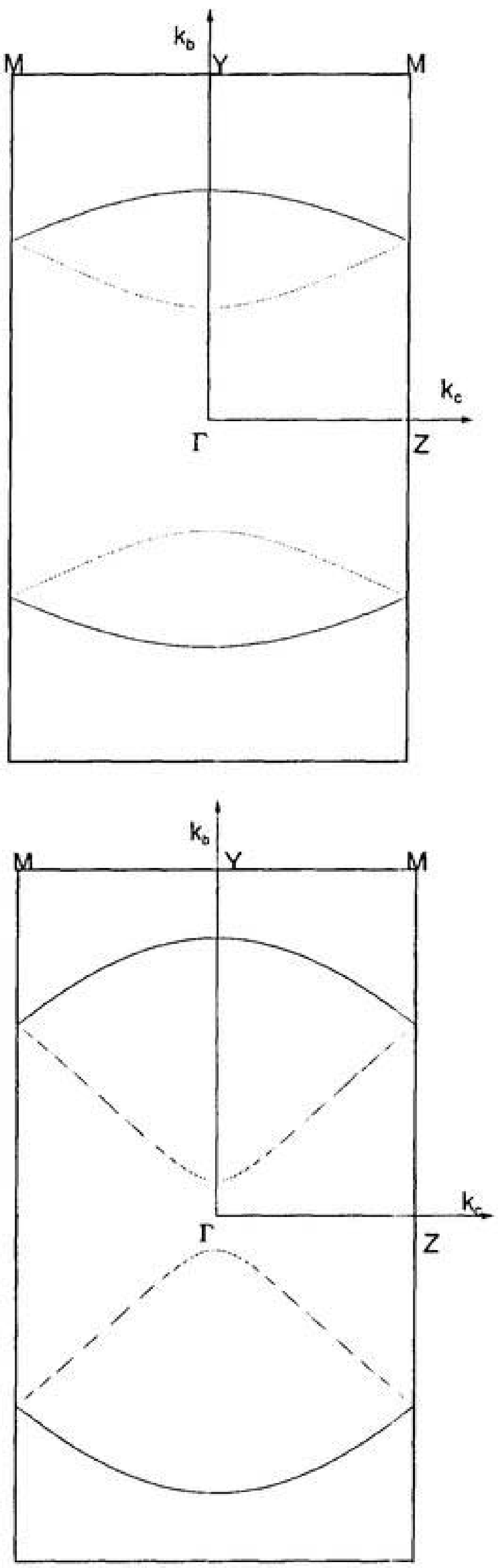

Fig. 5 Fermi surface of (BDT-TTP)$_2$ClO$_4$ experimentally (top one) and theoretically (bottom). The dotted lines correspond to the third band and the solid lines to the highest band in Fig. 4.

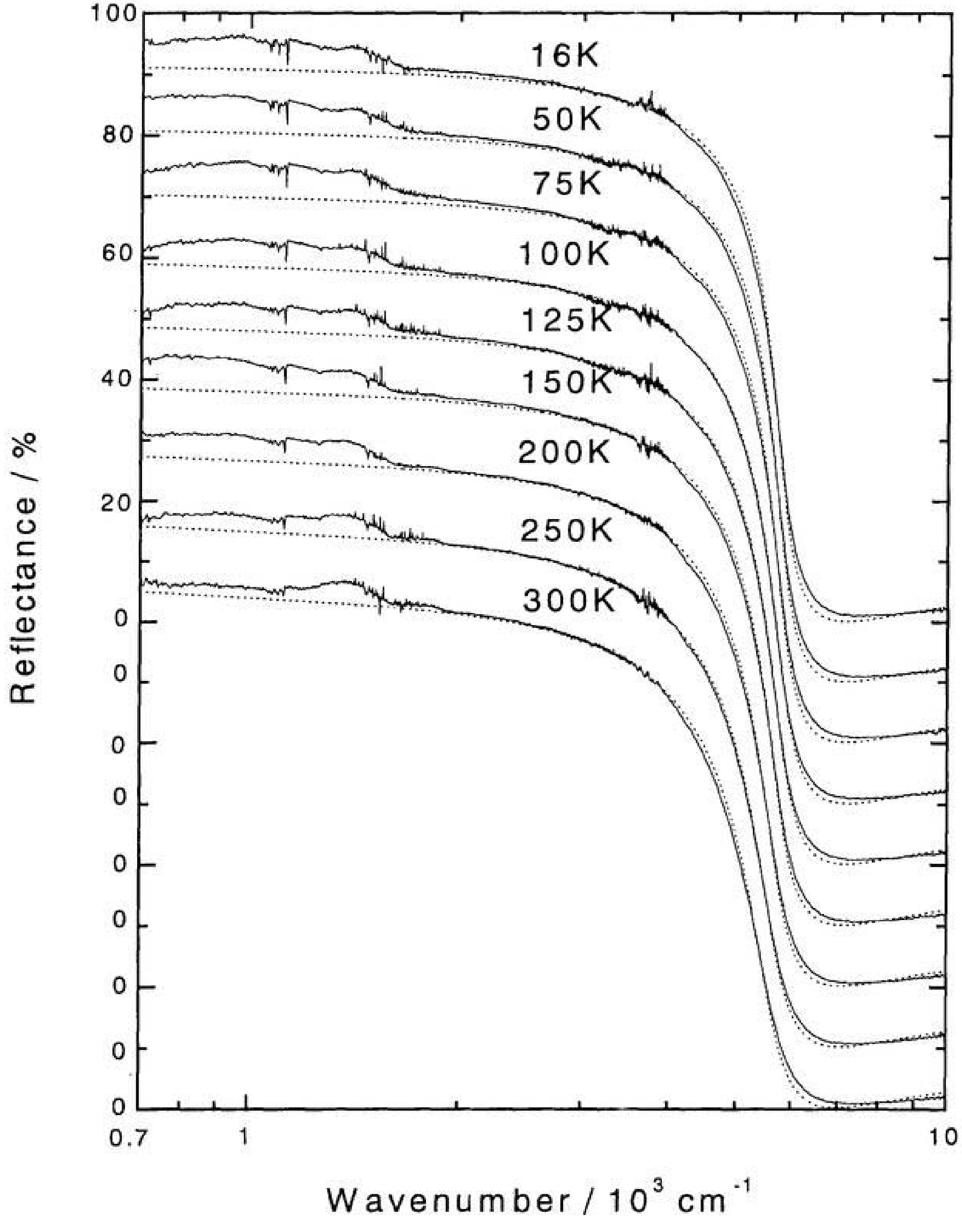

Fig. 6 *E//b* reflection spectra of $(BDT\text{-}TTP)_2ClO_4$ at various temperatures. The solid lines are the observed, and the dotted lines are the Drude-model fitting.

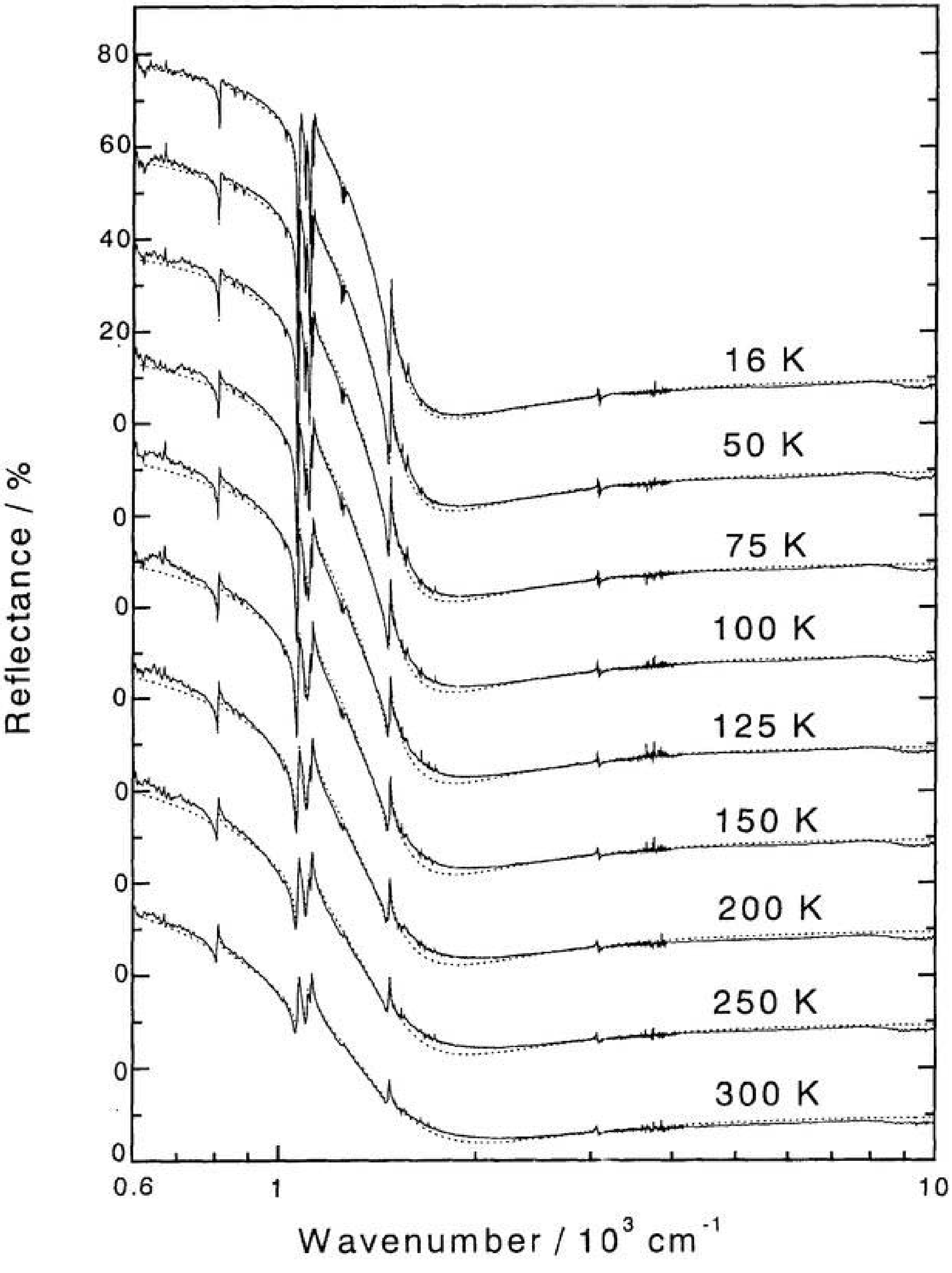

Fig. 7 *E//c* reflection spectra of (BDT-TTP)$_2$ClO$_4$ at various temperatures. The solid lines are the observed, and the dotted lines are the Drude-model fitting.

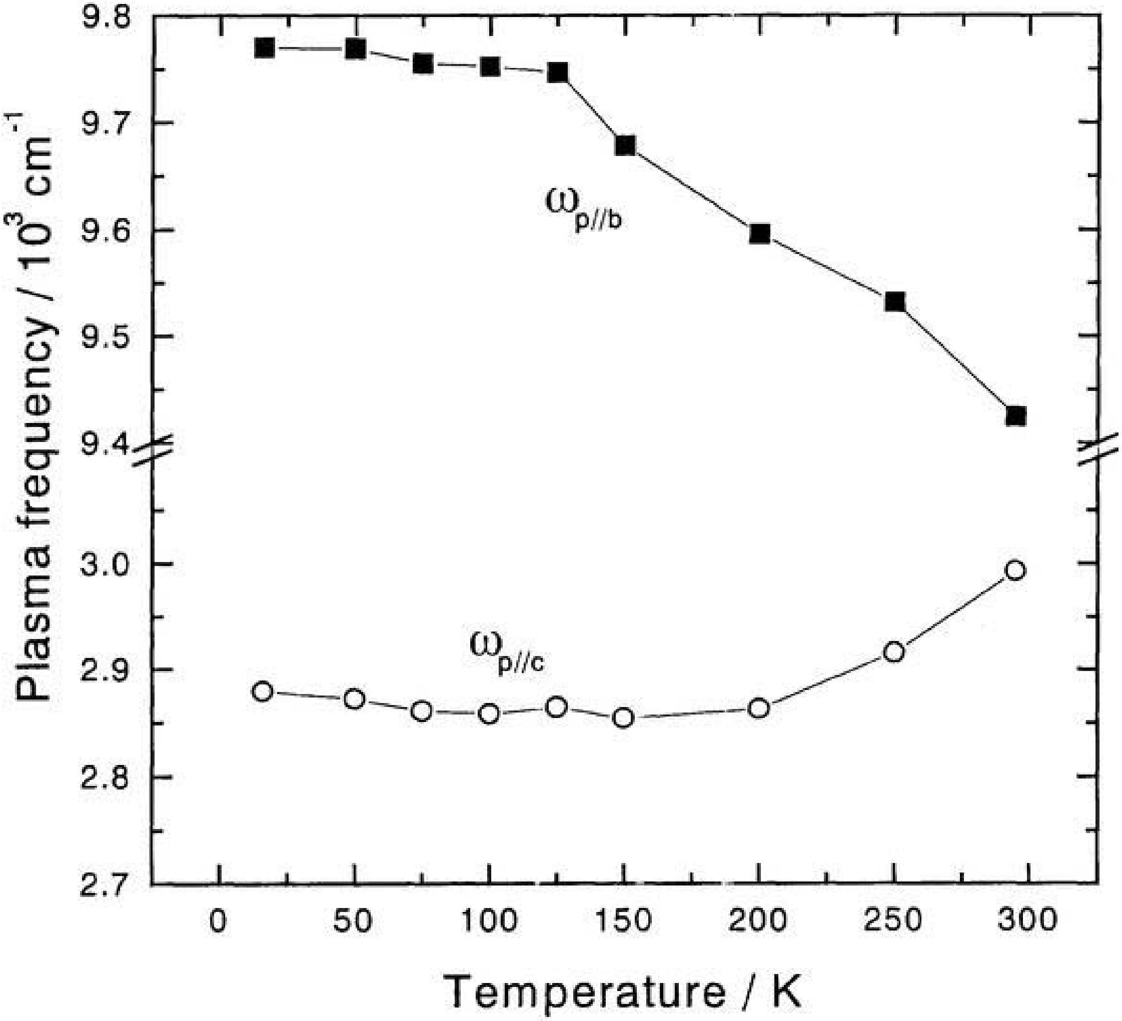

Fig 8 Temperature dependence of the plasma frequencies of $(BDT\text{-}TTP)_2ClO_4$. The solid squares correspond to $\omega_{p//b}$ and the open circles to $\omega_{p//c}$.

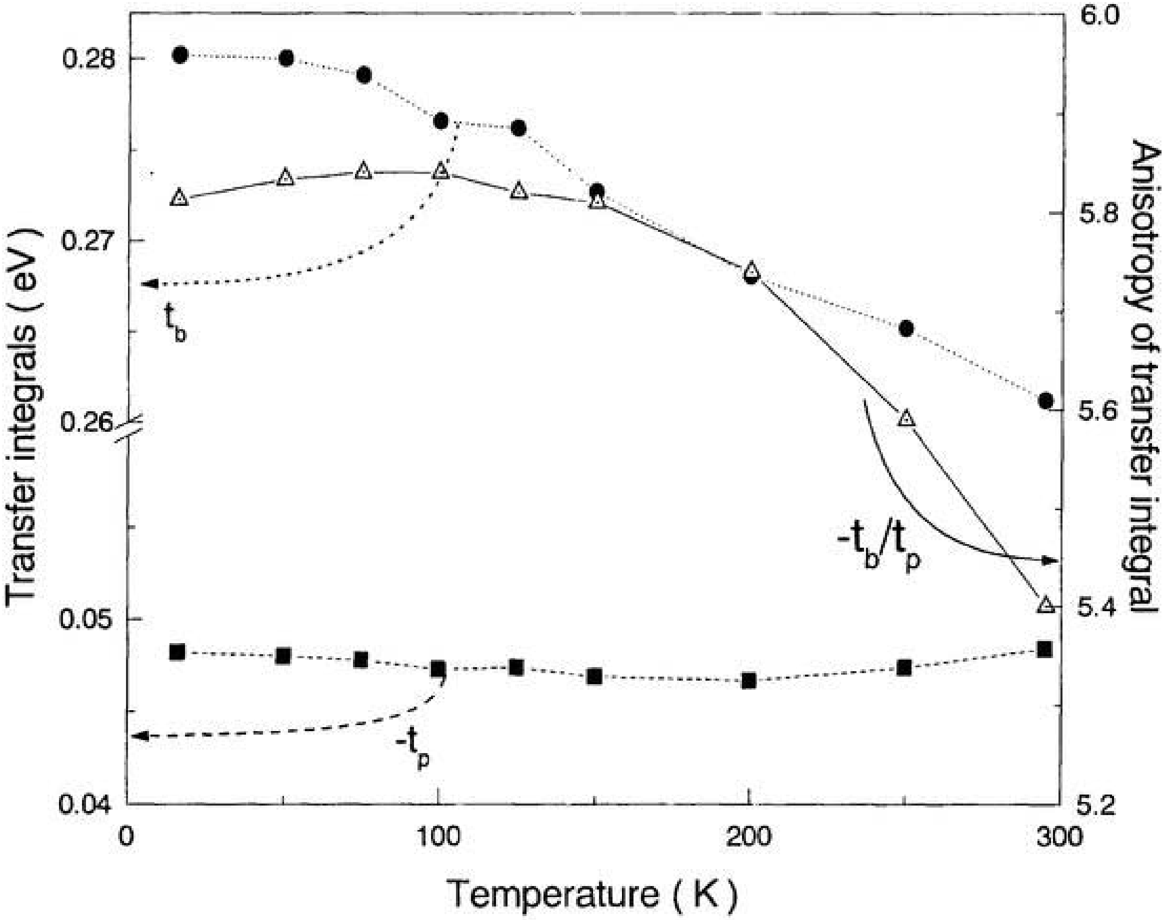

Fig. 9 Temperature dependence of transfer integral t_b (circle) , $-t_p$ (square) and the ratio $-t_b/t_p$ (triangle) of $(BDT\text{-}TTP)_2ClO_4$.

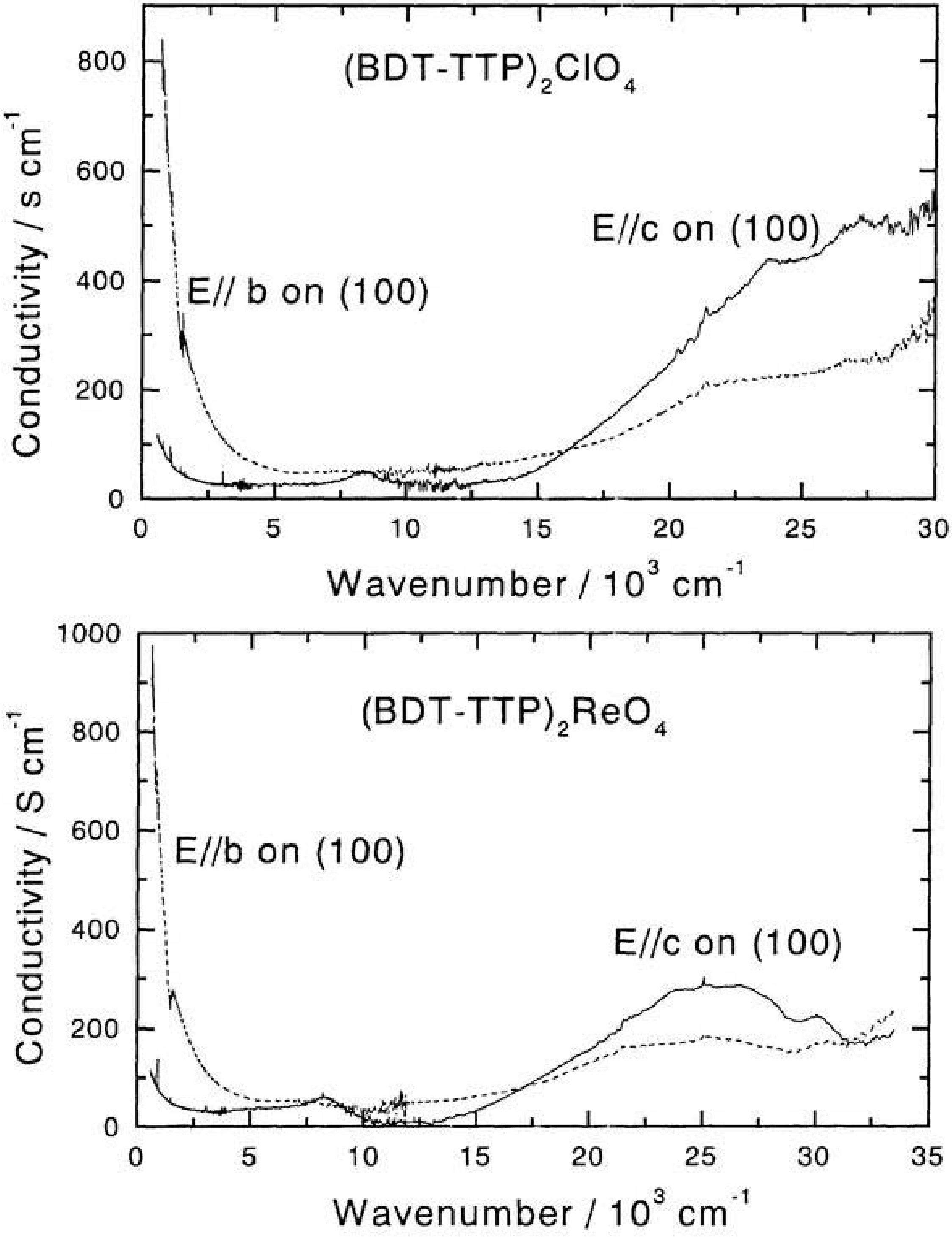

Fig 10 Conductivity spectra of (BDT-TTP)$_2$ClO$_4$ (top panel) and (BDT-TTP)$_2$ReO$_4$ (bottom). Dashed lines are the spectra along *b*-axis and solid lines the spectra along *c*-axis.

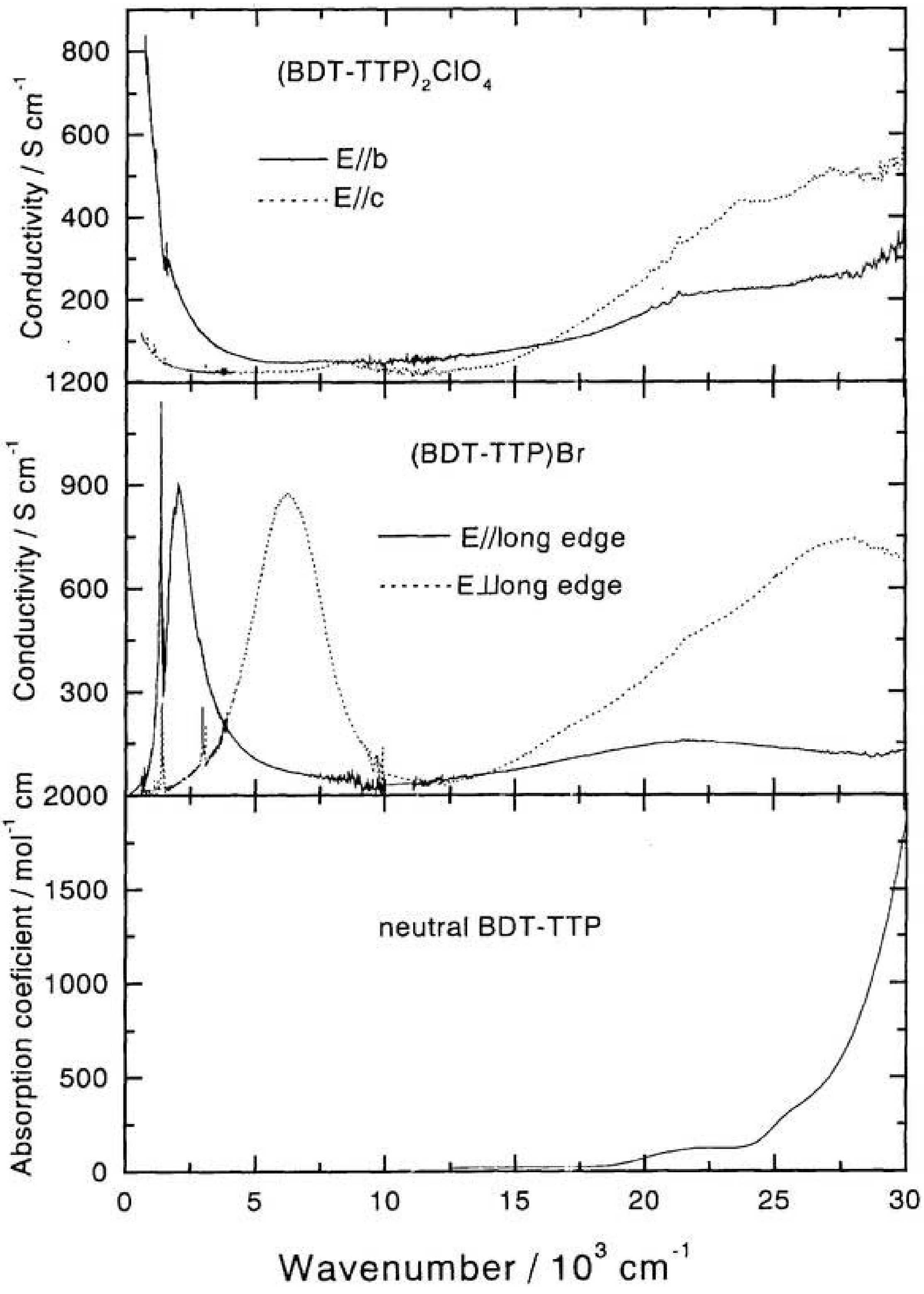

Fig. 11 Conductivity spectra of (BDT-TTP)$_2$ClO$_4$ (top panel) and (BDT-TTP)Br (middle) at room temperature and absorption spectrum of neutral BDT-TTP/THF solution (bottom).

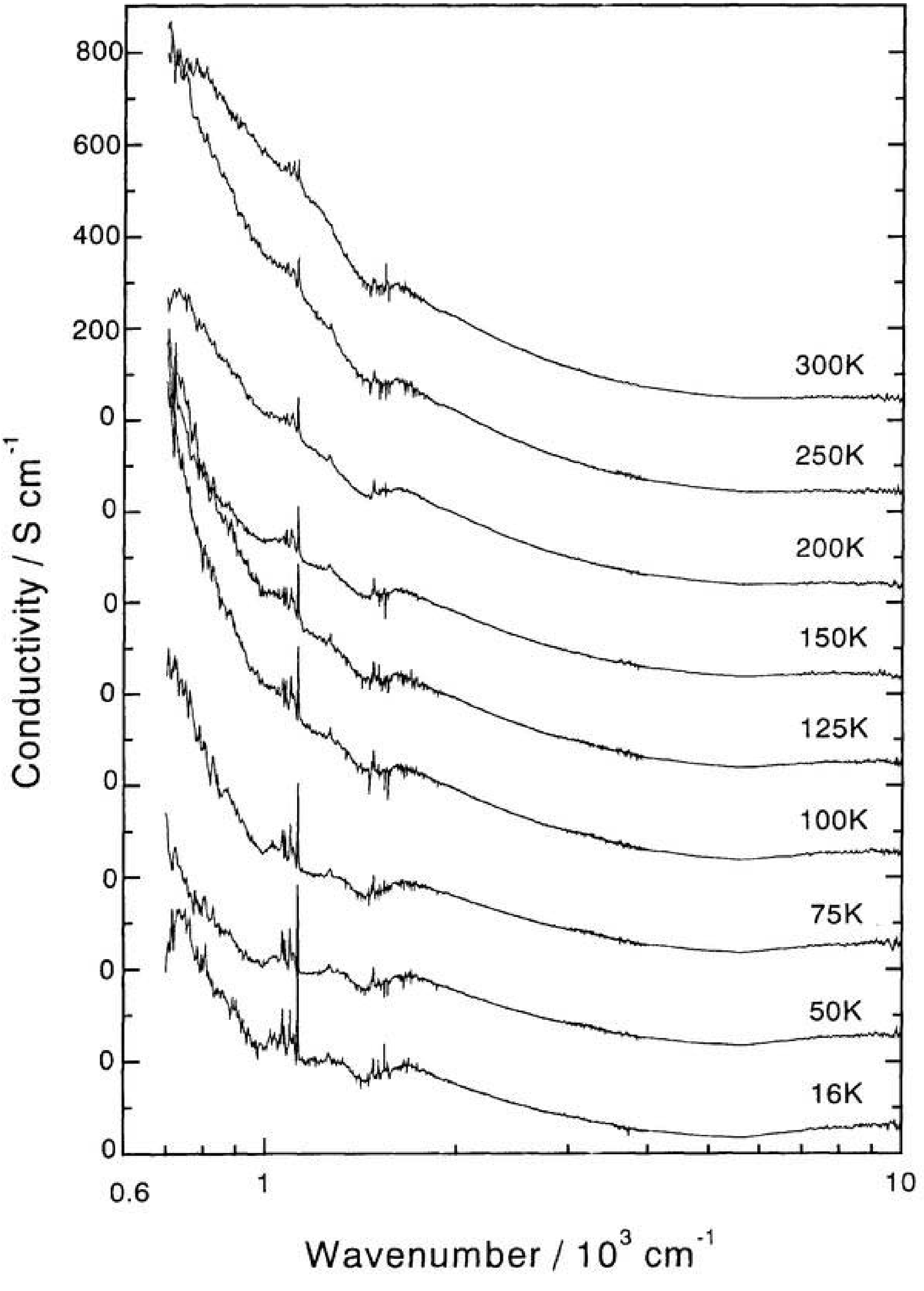

Fig. 12 *E//b* conductivity spectra of $(BDT\text{-}TTP)_2ClO_4$ at various temperatures.

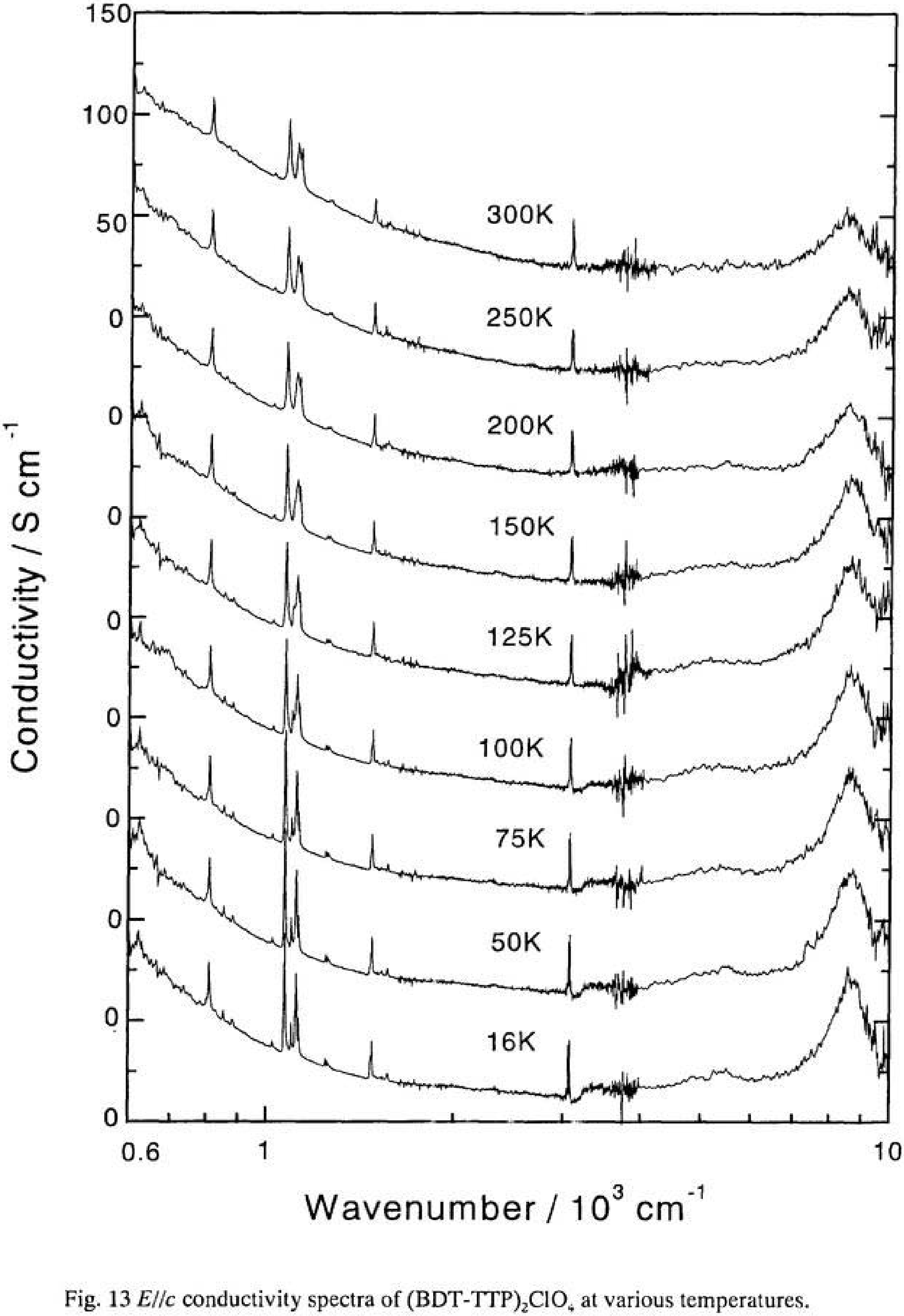

Fig. 13 *E//c* conductivity spectra of (BDT-TTP)$_2$ClO$_4$ at various temperatures.

Chapter 5

Phase Transition of θ-(BDT-TTP)$_2$Cu(NCS)$_2$

5.1 Introduction

BDT-TTP is a very good donor to form stable organic charge-transfer salts. Many BDT-TTP salts have been prepared with inorganic anions[1-4]. Many 2:1 BDT-TTP salts, such as $(BDT\text{-}TTP)_2X$ ($X=SbF_6$, AsF_6, ClO_4, and ReO_4) exhibit metallic behavior down to liquid helium temperature. This metallic stability at low temperature is regarded as the result of the two-dimensional electronic structure in the single crystal. Two-dimensional structure with a significant anisotropy in these salts has been observed while the Fermi surfaces are open in the first Brillouin zone[5]. Though the dimensionality of many 2:1 BDT-TTP salts are between TMTSF and BEDT-TTF salts which exhibit superconductive behavior at low temperature, no superconductivity has been observed on the BDT-TTP salts yet. In the field of organic conductor, $Cu(NCS)_2$ anion is a very interesting anions. Many organic salts of $Cu(NCS)_2$ shows superconductivity at low temperature[6-8], such as the κ-$(BEDT\text{-}TTF)_2Cu(NCS)_2$ exhibiting T_c higher than 10K. In the family of the 2:1 BDT-TTP salts, θ-$(BDT\text{-}TTP)_2Cu(NCS)_2$ shows peculiar crystal structure and physical properties. The BDT-TTP stacking for is θ-type in the θ-$(BDT\text{-}TTP)_2Cu(NCS)_2$ crystal, compared with β-type form in the crystal of $(BDT\text{-}TTP)_2X$ ($X=SbF_6$, AsF_6, ClO_4 and ReO_4). Calculated by the Hückel method by Misaki[9], the inter-stack transfer integral of θ-$(BDT\text{-}TTP)_2Cu(NCS)_2$ is even larger than the intra-stack transfer integral and the Fermi surface is close in the first Brillouin zone. On the other hand, θ-$(BDT\text{-}TTP)_2Cu(NCS)_2$ is a semiconductor at room temperature. The crystal structure and conductive behavior suggest a peculiar electronic structure in θ-$(BDT\text{-}TTP)_2Cu(NCS)_2$.

A comparative study of the electronic structure of θ-$(BDT\text{-}TTP)_2Cu(NCS)_2$ with other metallic BDT-TTP salts will benefit the understanding of the conduction mechanism of organic conductors. To date, no experiment has been conducted to study the electronic structure of θ-$(BDT\text{-}TTP)_2Cu(NCS)_2$. We study the electronic structure of θ-(BDT-

TTP)$_2$Cu(NCS)$_2$ by the resistance measurement, the polarized reflection spectroscopy, Raman spectroscopy and ESR spectroscopy. A phase transition was observed at *ca.* 250K by the resistance measurement. This phase transition is confirmed by other experiments.

5.2 Experimental

The (BDT-TTP)$_2$Cu(NCS)$_2$ single crystals were grown by the electrochemical oxidation methods. θ-(BDT-TTP)$_2$Cu(NCS)$_2$ single crystal is needle-like with a rectangle shape. The color of the single crystal is black. The well-developed surface is the (100) crystal face, it is very shiny and smooth. The crystal surface was determined by the X-ray diffraction method using Enraf-nonius CAD4 diffractometer.

The resistances were measured along the *b*-axis of the single crystal by the use of PPMS. The method is the same as the resistance measurement of DMTSA and DMTTA salts[10)].

A single crystal with the dimension being $1.00\times0.22\times0.01\text{mm}^3$ was used for the measurement of the polarized reflection spectrum and the Raman spectrum. The reflection spectrum was taken on the (100) plane with the polarization along the *b*- or the *c*-axis. The Raman spectrum was measured with the polarization of the incident light along the *c*-axis. The approaches to record the polarized reflection spectrum and the Raman spectrum are the same as those for the metallic BDT-TTP salts[5)].

ESR of θ-(BDT-TTP)$_2$Cu(NCS)$_2$ was taken by Brucker ESP-300E, equipped with a cryostat of Oxford Instrument ESR 900 combined with the temperature controller IRC4. Both the polycrystal and the single crystals were used for ESR measurement. 0.26mg θ-(BDT-TTP)$_2$Cu(NCS)$_2$ polycrystal were measured from 10K to 300K, and the susceptibility of θ-(BDT-TTP)$_2$Cu(NCS)$_2$ at room temperature was determined by comparing the integrated ESR intensity with that of 0.21mg DHHP under the same conditions. The sample was weighed by Mettler Toledo AT261 balance within the accuracy of 0.01 mg. Five single crystals were aligned and mounted on a quartz rod by a small amount of silicon vacuum grease with the *bc* face attaching to the surface of the quartz. The orientational study was accomplished by using a geniometer which enable one to rotate the sample 360° around a single axis. Two kinds of sample alignments were adopted with different crystallographic axis as the rotating axis, one is the by rotating the *b*-axis and another by rotating the *c*-axis. The ESRs of *H//b*, *H//c* and *H//a'* (*b*- and *c*- are the crystallographic axes of the single crystal, *a'* is the direction perpendicular to the *bc* face) were measured from 3K to 300K.

The charge distribution in neutral BDT-TTP molecule, BDT-TTP$^+$ monocation and NCS$^-$ anion and the vibrational modes of NCS$^-$ anion were calculated by the semi-empirical PM$_3$ method provided by HyperChem 5.1 program.

Another modified (BDT-TTP)$_2$Cu(NCS)$_2$ single crystal was found, of which the crystal structure remains unknown, θ'-(BDT-TTP)$_2$Cu(NCS)$_2$ is used to represent it. The single crystal has a thin hexagonal plate-like shape. The dimension is 0.50×038×0.01mm^3. The surface is often attached by some small single crystals. The crystal with smooth and clean surface was chosen for the polarized reflection spectroscopy and Raman spectroscopy. The resistance, the polarized reflection spectrum and the Raman spectrum were measured by the same methods as for θ-(BDT-TTP)$_2$Cu(NCS)$_2$.

5.3 Results and discussion

5.3.1 Transport property

The θ-(BDT-TTP)$_2$Cu(NCS)$_2$ single crystal has a *Cc* space symmetry with the lattice parameters being a=37.716, b=4.007, c=10.957Å, and β=102.4°. The *b*-axis is the unique and the stacking axis. The Cu(NCS)$_2$ anions are disordered in the crystal. The BDT-TTP molecules stack uniformly along the *b*-axis with a tilted angle between the stacking direction and the normal of the BDT-TTP molecular plane (Fig. 1). The BDT-TTP molecules in the neighboring columns are connected by the symmetry of the glide plane. The inter-BDT-TTP distance is 4.007Å along the stacking direction, much longer than the metallic BDT-TTP salts, indicating a small intra-stack transfer integral in the θ-(BDT-TTP)$_2$Cu(NCS)$_2$ single crystal. The dihedral angle θ between two BDT-TTP molecular planes in the neighboring columns is 134°.

Three θ-(BDT-TTP)$_2$Cu(NCS)$_2$ single crystals were used for the resistance measurement along the *b*-axis. The conductivity at room temperature is around 30 Scm^{-1}. The samples were cooled from 350K to 5K and heated to 350K (Fig. 2). The three single crystals exhibit same behavior. The resistance increases on lowering temperature, it becomes too high to be measurable below 100K. The behavior during the heating run repeats that during the cooling run very well. No hysteria appears, while hysteria is a very normal phenomenon for many metallic BDT-TTP salts[2)]. Evidently, θ-(BDT-TTP)$_2$Cu(NCS)$_2$ is a semiconductor through the temperature. The electric resistance drastically increases below 290K. The most rapid change takes place about 250K, suggesting a phase transition at *ca.* 250K. The *logR-1/T* relation can be fitted very well by a straight line before and the after the phase transition. The activation energy E_a is 30-44meV in the temperature region of 325-350K and increases to 100meV in the temperature region of 100-200 K. The latter E_a value is the same as that of β'-(BEDT-TTF)$_2$ICl$_2$[11)].

The semiconductive behavior is derived from the localization of the electrons in the crystal. This electron localization is believed not to be caused by a strong disorder despite the Cu(NCS)$_2$ anions are disordered in the crystal. If the disorder is the origin of the electron localization, the conductivity behavior and E_a should exhibit a strong sample-dependence.

At first, the behavior of θ-(BDT-TTP)$_2$Cu(NCS)$_2$ is understood according to the crystal structure. Mori *et al*[12, 13)], have found that the conductive properties of θ-type BEDT-TTP salts can be anticipated according to the dihedral angle θ, since the U/W value increases with the increase of the angle θ. They pointed out that the salt changes from a metal to an insulator when θ is larger than 125°. An example is θ-(BEDT-TTF)$_2$Cu$_2$(CN)[N(CN)$_2$]$_2$[14] of which the dihedral angle θ is 132°. Hence, it is a semiconductor with the E_a value of 85-95meV at room temperature. The dihedral angle is very close to that of θ-(BDT-TTP)$_2$Cu(NCS)$_2$, thus θ-(BDT-TTP)$_2$Cu(NCS)$_2$ is anticipated to be a semiconductor in terms of the criterion of θ-BEDT-TTF salts. Moreover, θ-(BEDT-TTF)$_2$Cu$_2$(CN)[N(CN)$_2$]$_2$ also exhibit a semiconductor-semiconductor phase transition at 220K.

To further understand the conductive behavior of θ-(BDT-TTP)$_2$Cu(NCS)$_2$, the energy band structure is considered. The scheme of the transfer integrals is shown in Fig.1. These transfer integrals calculated by Misaki[9] are t_b=-0.041, t_{p1}=-0.086, and t_{p2}=-0.091eV. The intra-stack transfer integral t_b is almost one-sixth as that of metallic (BDT-TTP)$_2$X (X=AsF$_6$, SbF$_6$, ClO$_4$, and ReO$_4$), due to the longer inter-molecular distances in θ-(BDT-TTP)$_2$Cu(NCS)$_2$. The two inter-stack transfer integrals t_{p1} or t_{p2} from the one BDT-TTP molecule to the neighboring two BDT-TTP molecules in the neighboring column are almost the same, and they are comparable with the larger inter-stack transfer integral of the metallic BDT-TTP salts of which another inter-stack transfer integral is negligible. Hence, the sum of the inter-stack transfer integral of θ-(BDT-TTP)$_2$Cu(NCS)$_2$ is almost twice as that of metallic (BDT-TTP)$_2$X (X=AsF$_6$, SbF$_6$, ClO$_4$, and ReO$_4$).

Two energy bands are formed by the HOMOs of two BDT-TTP molecules in one unit cell. In terms of the tight-binding approximation, the energy dispersions are expressed by:

$$E(k_b, k_c) = 2t_b \cos(k_b b) \pm |H_{12}| \tag{5.1}$$

$$\text{with } H_{12}^2 = 2(1 + \cos(k_c c))(t_{p1}^2 + t_{p2}^2 + 2t_{p1}t_{p2}\cos(k_b b))$$

where, k_b and k_c are the vectors along b^* and c^* in the reciprocal space, respectively.

According to this equation and the calculated transfer integrals, the Fermi surface is close in the first Brillouin zone. The largest energy split is observed at the point $\Gamma(0, 0)$, of which the energy is:

$$E_\Gamma = 2t_b \pm 2\left|t_{p1} + t_{p2}\right|, \tag{5.2}$$

the + and - signs denote the upper and the lower bands, respectively. Thereby, the energy bandwidth of θ-(BDT-TTP)$_2$Cu(NCS)$_2$ is determined by the inter-stack transfer integrals and is 0.71eV by using the transfer integrals calculated by the extended Hückel method by Misiki. As studied on (BDT-TTP)$_2$X (X=AsF$_6$, SbF$_6$, ClO$_4$, and ReO$_4$) by the optical experiments before, the inter-stack transfer integrals are always over-estimated by the extended Hückel calculation. The calculated values are always about twice as the values estimated from the experiments. Likewise, it is very possible that the inter-stack transfer integrals of θ-(BDT-TTP)$_2$Cu(NCS)$_2$ is over-estimated by the extended Hückel calculation as well. If $t_{p1}/2$ and $t_{p2}/2$ are adopted, the bandwidth of θ-(BDT-TTP)$_2$Cu(NCS)$_2$ is 0.35eV. Apparently, this bandwidth is very narrow, in comparison with the bandwidth larger than 1eV of the metallic BDT-TTP salts.

The calculated two-dimensional structure of θ-(BDT-TTP)$_2$Cu(NCS)$_2$ can not interpret the semiconductor behavior. This suggests that the electron-electron correlation may play an important role for the conduction mechanism. So the U value should be compared with the bandwidth. A small Coulomb repulsion U is expected in BDT-TTP salts[15)], according to the small ΔE between the first (E_1) and the second oxidation potential (E_2), due to the large number of the conjugated electrons in one molecule. Small U of 0.49 eV at room temperature has been observed in the 1:1 metallic salt (TTM-TTP)I$_3$[16,17)]. This U value is very smaller, compared with the typical U value of about 1eV for organic conductor. Since TTM-TTP is a very simple derivative of BDT-TTP and the ΔE values of them are very close[15,18)], the U value of BDT-TTP is expected to be very close to that of TTM-TTP. Evidently, this U value is larger than the bandwidth 0.35eV of θ-$(BDT\text{-}TTP)_2Cu(NCS)_2$, thus a gap exists between the upper and lower Hubbard bands. Hence, θ-$(BDT\text{-}TTP)_2Cu(NCS)_2$ is probably a Mott insulator.

5.3.2 Polarized reflection spectrum at room temperature

The polarized reflection spectra were measured at room temperature from 600 to 30,000cm^{-1} on the (100) surface of the θ-$(BDT\text{-}TTP)_2Cu(NCS)_2$ single crystal with the polarization along the *b*- and the *c*-axis (Fig. 3). Obviously, the broad band in the infrared region is the charge transfer band, which appears in both directions indicating a two-dimensional structure in the crystal. The reflectivity in infrared region is not so high below 40%. The minimum point of the CT band is below 5,000 cm^{-1} along *c*-axis and below 4,000 cm^{-1} along *b*-axis. These polarized reflection spectra confirm the semiconductive properties of the single crystal at room temperature. Hence, θ-$(BDT\text{-}TTP)_2Cu(NCS)_2$ is a two-dimensional semiconductor.

Up until now, it is very difficult to estimate the transfer integrals of a two-dimensional Mott insulator from the polarized reflection spectra. It is worth comparing the polarized reflection spectrum of Mott insulator θ-$(BDT\text{-}TTP)_2Cu(NCS)_2$ with the metallic BDT-TTP salts, to gain some insight into the effect of U/W on the reflection spectrum. Fig. 4 are the polarized reflection spectra of θ-$(BDT\text{-}TTP)_2Cu(NCS)_2$ and metallic $(BDT\text{-}TTP)_2ClO_4$. Calculated by the extended Hückel method, the intrastack transfer integral of the former is almost 1/6 of the latter, whereas the interstack transfer integral of the former is almost twice of the latter. Along the stacking direction, the CT band of θ-$(BDT\text{-}TTP)_2Cu(NCS)_2$ is much weaker than that of $(BDT\text{-}TTP)_2ClO_4$. The reflectivity of the former is only about 20%, in contrast to almost 90% of the latter. The minimum position of the former is lower than 4,000 cm^{-1} while the latter shows the minimum position higher than 7,000cm^{-1}. In the spectra perpendicular to the stacking direction, the CT band of $(BDT\text{-}TTP)_2ClO_4$ is much steeper than θ-$(BDT\text{-}TTP)_2Cu(NCS)_2$. The reflectivity at 600cm^{-1} is higher than 50% for $(BDT\text{-}TTP)_2ClO_4$ while is lower than 40% for θ-$(BDT\text{-}TTP)_2Cu(NCS)_2$, despite the minimum position of the CT band of the former (a little higher than 2,000 cm^{-1}) is much lower than the latter (higher than 5,000 cm^{-1}).

The conductivity spectra of θ-$(BDT\text{-}TTP)_2Cu(NCS)_2$ at room temperature were calculated from the polarized reflection spectra (Fig. 5). The oscillator strength of the CT band along *c*-axis is much stronger that along *b*-axis. The plasma frequencies in both directions are calculated by integrating the conductivity of the CT band[19]:

$$\omega_p^2 = \frac{2}{\varepsilon_0 \pi} \int_0^{5000} \sigma(\omega) d\omega . \tag{5.3}$$

The plasma frequencies are 2.7×10^3 and 5.1×10^3 cm^{-1} for *E//b* and *E//c*, respectively. The ratio of the oscillator strengths $\omega_{p//b}{}^2/\omega_{p//c}{}^2=0.28$, this is consistent with the fact $t_b<t_{p1}+t_{p3}$.

The plasma frequency defined by (5.3) has a different physical meaning from the one-electron plasma frequency of the Drude mode. The one-electron plasma frequencies in both directions can be calculated from the transfer integrals according to the equation (5.1) and (2.1), it should be different from the value by (5.3) since the CT band of θ-$(BDT\text{-}TTP)_2Cu(NCS)_2$ arises from the electronic transition across the band gap rather than the intra-band transition. They are 2.2×10^3cm^{-1} and 6.9×10^3cm^{-1} for *E//b* and *E//c*, respectively, by using the transfer integrals t_b=-0.041, t_{p1}=-0.086/2, and t_{p2}=-0.091/2eV. It is somewhat surprising that the two set of plasma frequencies are not very different.

Several phonon modes appear in both directions. The dips arising from the electron-phonon coupling appear at *ca.* 1,400 cm^{-1} in both directions. This is different from metallic $(BDT\text{-}TTP)_2X$ (X=SbF_6, AsF_6, ClO_4, and ReO_4), of which only one dip appears in the spectrum along the stacking direction. The positions of the dips in both directions are the same as that of $(BDT\text{-}TTP)_2X$ (X=SbF_6, AsF_6, ClO_4, and ReO_4). Two weak bands appear at

3,046 and 3,055cm^{-1} in the *E//c* spectrum, being assigned to the CH stretching modes. The intensities are very week, partly due to the tilted angle between the molecular plane and the stacking direction. The band at 800cm^{-1} appearing in both directions is assigned to the CS stretching mode of BDT-TTP, since such mode has been observed in the spectrum of metallic BDT-TTP salts with the polarization perpendicular to the stacking direction.

Some phonon modes of the anion can be observed as well. The CN stretching modes appear at 2,116 cm^{-1} with a very weak shoulder at 2,121 cm^{-1} in the *E//c* spectrum and at 2,122 cm^{-1} in the *E//b* spectrum. The two bands suggest two distinctive CN environments. The positions of the CN modes are higher than those of κ-(BEDT-TTF)$_2$Cu(NCS)$_2$[20] at 2,113 and 2,074cm^{-1}. Some insight can be gained into the orientation of the anion according to the anisotropy of the phonon modes. The CN bond at 2,116cm^{-1} is perpendicular to the *b*-axis, while the CN bond at 2,122cm^{-1} is nearly perpendicular to the *c*-axis. A very sharp band appears at 648cm^{-1} with a shoulder at 659cm^{-1} in the *E//b* spectrum. Such bands can not be observed in the spectrum of the metallic BDT-TTP salts. They are assigned to the CS stretching modes of the Cu(NCS)$_2$ anion. These band positions are comparable with the position of the CS stretching mode of NCS$^-$ anions calculated by PM$_3$ method provided by HyperChem 5.1 program.

Some electronic bands appear in the NIR and visible region. They correspond to the intra-molecular electronic transition. In the spectrum of (BDT-TTP)$_2$X (X=SbF$_6$, AsF$_6$, ClO$_4$, and ReO$_4$), the intra-BDT-TTP$^+$ transition is observed near 8,000cm^{-1} in the NIR region. Such band can not be observed in the same region of the θ-(BDT-TTP)$_2$Cu(NCS)$_2$ spectra.

5.3.3 Temperature dependent reflection spectra

The *E//b* polarized reflection spectrum was measured from 300K down to 16K (Fig. 6). The reflectivity at low wavelength region decreases on lowering temperatures, which is so low at 16K so that the inference effect at the crystal surface appears. A broad peak which can not be observed at 300K appears near 3,000cm^{-1} at 16K. The change of the phonon modes is very interesting. The dip at *ca.* 1,400cm^{-1} becomes less remarkable at low temperature and a new peak appears at this region. The sharp peak at 648cm^{-1} explicitly splits into two peaks at 16K. This split can be observed even at 260K before the appearance of the interference. The *E//c* reflection spectrum shows similar temperature dependence. The reflectivity at low wavenumber region decreases on lowering temperature and the inference effect appears at 16K (Fig. 7). The broad peak at *ca.* 3,000cm^{-1} is conspicuous at 16K. The phonon at *ca.* 1,400cm^{-1} changes significantly, the remarkable dip at room temperature becomes less remarkable when the temperature is lowered. At last it turns into a remarkable peak at 16K.

The *E//b* conductivity spectra show a systematic change on lowering temperature (Fig. 8). The conductivity at the low wavenumber region decreases and the CT band shifts to the higher energy region on lowering temperature. The position of the maximum conductivity of the CT band is not very clear at room temperature, which may be in the dip region or lower region. It shifts to *ca.* 2,100cm^{-1} at 220K and to *ca.* 2,500cm^{-1} at 16K. The broad band near 3,000cm^{-1} can be observed very explicitly at 16K, which slightly appear at 270K and can not be observed at 300K. This band may be a new electronic transition band at low temperature. A possible reason about this band is that the charge of BDT-TTP changes at low temperature, as pointed out by Tajima[21)].

The shift of the spectroscopic weight of the CT band in the *E//c* spectra on lowering temperature is more remarkable than that in the *E//b* spectra (Fig. 9). At 16K, the onset energy of the CT band is comparable with the energy gap obtained by the resistance measurement. The broad band near 3,000cm^{-1} at 16K is more remarkable in the *E//c* spectrum than in the *E//b* spectrum.

Fig. 10 is the temperature dependences of the oscillator strength ω_p^2 in both directions and the ratio $\omega_{p//b}^2/\omega_{p//c}^2$. $\omega_{p//b}^2$ and $\omega_{p//c}^2$ decrease on lowering temperature from 300K to 240K, then become almost insensitive to the temperature down to 220K. It is known that the oscillation strength of the CT band depends on the transfer integral, thus the intra- and inter-stack transfer integrals decrease through the phase transition. These leads to the increase of the *U*/*W* value after the phase transition. Hence, the energy gap increases after the phase transition, consistent with the results by the resistance measurement.

The ratio $\omega_{p//b}^2/\omega_{p//c}^2$ decreases on lowering temperature from 300K to 250K and then becomes insensitive to the temperature down to 220K. This suggests that the crystal becomes more one-dimensional after the phase transition. It is worth noting that the metallic BDT-TTP salts becomes more one-dimensional as well at low temperature, despite no phase transition.

Besides the CT band, some phonons also significantly change on the lowering temperature. The very broad dip at *ca.* 1,400cm^{-1} in the *E*//*b* spectrum (Fig. 8), which is an a_g mode and primarily contributed by the C=C stretch of the BDT-TTP molecules, becomes less remarkable on lowering temperature. It almost can not be observed at 220K. Simultaneously, a new very narrow dip can be observed at 1,402cm^{-1} at 270K and becomes stronger on lowering temperature. The peak at 802cm^{-1} at 300K, which has been assigned to the CS stretching mode of the BDT-TTP molecule, shows split at low temperature. The split can be observed at 270K and becomes remarkable at lower temperature. This peak turns into two peaks at 798 and 806cm^{-1} at 16K. The integrated area of this band decreases on lowering temperature from 300 to 240K, then increases a little down to 220K (Fig. 11).

The phonons of the anion in the *E*//*b* spectrum exhibit very interesting change at low temperature as well. The peak at 648cm^{-1} at 300K, which has been assigned to the CS stretch mode of the anion, splits at low temperature. The split can be observed at 250K and two peaks are observed at 642 and 648cm^{-1} at 16K. The CN stretching mode at 2,122cm^{-1} gradually shifts to higher energy region on lowering temperature, and the integrated area at first decreases on lowering temperature from 300K to 150K then increases down to 16K (Fig. 12). The position and the integrated area of the CN mode do not show any drastic change through the phase transition.

The dip at *ca.* 1,400cm^{-1} in the *E//c* spectrum changes significantly as well (Fig. 9). On lowering temperature, the dip becomes less remarkable and turns into a peak at low temperature. This dip-to-peak change is due to the shift of the CT band. The change of this phonon mode in this direction is different from that along *b*-axis. The phonon mode at 800cm^{-1} does not split at low temperature, while its intensity decreases on lowering temperature from 300K to 250K and then becomes almost temperature-independent down to 220K (Fig. 11). Three modes appearing at 2,912, 2,976 and 3,062cm^{-1} are assigned to the CH stretching modes of the BDT-TTP molecule. The bands at 2,912 and 2,976cm^{-1} are much lower than that of the metallic BDT-TTP salts.

The phonon modes of the anion in the *E//c* spectrum also change on lowering temperature. Apparently, the CN stretch mode becomes very sharp at low temperature. The position of the band at 2,116cm^{-1} is invariant in the temperature range from 300 to 230K, then shifts to higher wavenumber region on lowering temperature (Fig.12). These suggest the environment of this CN bond maybe change significantly after the phase transition. The integrated area does not have a strong dependence on the temperature, especially in the temperature range from 300 to 220K.

5.3.4 Raman spectroscopy

Fig. 13 is the Raman spectra of θ-(BDT-TTP)$_2$Cu(NCS)$_2$ from 1,200 to 1,650cm^{-1} at room temperature under various conditions of power and exposure time. As mentioned in the previous chapters, the vibrational modes in this range arise from the C=C stretch of the BDT-TTP molecule. Only one broad peak appears at 1,486 cm^{-1} when the power of the laser light is low and the exposure time is short. A new mode appears at 1,418cm^{-1}, when a strong power and/or long exposure time are adopted. This is an irreversible change, indicating a chemical reaction may take place under the exposure to the laser light. Such instability of the crystal was observed on other BDT-TTP salts as well.

The above Raman spectra were recorded by using He-Ne laser source. Ar laser source with the wavelength at 515nm has been adopted for the measurement of the Raman spectrum of θ-(BDT-TTP)$_2$Cu(NCS)$_2$ as well. Under the same conditions, the signal to noise is much worse by using Ar laser source than by using He-Ne laser source, while almost the same active modes appear. The crystal is subject to be damaged when the Ar laser source is used. Hence, the He-Ne laser source was employed for the measurement of the Raman spectrum.

Every spectrum of θ-(BDT-TTP)$_2$Cu(NCS)$_2$ was measured at least three times, to obtain the correct data. Table Ⅰ lists the positions of the Raman-active modes of θ-(BDT-TTP)$_2$Cu(NCS)$_2$ at room temperature, together with the metallic salts (BDT-TTP)$_2$AsF$_6$ and (BDT-TTP)$_2$SbF$_6$ and neutral BDT-TTP. A complete assignment of these modes is not possible yet. The Raman-active modes of TTF and TTF$^+$ which have been assigned very well[26,27)] are listed as well to gain some insight into some modes of BDT-TTP, owning to the structural similarity between the BDT-TTP and TTF molecules. As discussed in Chapter 4, the sharp mode at 1,507cm^{-1} of neutral BDT-TTP is the most charge-sensitive a_g mode. The corresponding mode in the Raman spectrum of θ-(BDT-TTP)$_2$Cu(NCS)$_2$ appears at 1,486cm^{-1}. This mode is very broad, in contrast to the sharp mode for (BDT-TTP)$_2$X (X=AsF$_6$, SbF$_6$, ClO$_4$, and ReO$_4$), suggesting the charge distribution is not homogeneous in the θ-(BDT-TTP)$_2$Cu(NCS)$_2$ single crystal even at room temperature.

The Raman spectrum of θ-(BDT-TTP)$_2$Cu(NCS)$_2$ was measured from 300K down to 5K. Almost all modes becomes very strong at low temperature, especially at 5K the intensities of many modes become more than ten time higher than at room temperature. The enhancement of the intensity is presumably attributable to the oscillation between the electronic transition band and the laser light. However, the *E*//*c* polarized reflection spectrum in the visible range from 11,500 to 33,000cm^{-1} almost does not change from room temperature down to 16K.

Let us at first pay attention to the temperature dependence of the Raman spectrum in the range from 1,200 to 1,600cm^{-1} (Fig. 14(a)). At 300K, only one broad band appears at 1,486cm^{-1}, which is the most charge-sensitive mode. This band significantly changes on lowering temperature. It spits into several bands at 5K. This suggests that a charge disproportionation may take place through the phase transition.

The Raman-active modes in other range also change significantly on lowering temperature. The bands in the range from 150 to 600cm^{-1} is related to the CCC bend, SCC bend, CSC bend and CS stretch (Fig. 14(b)). The band at 166cm^{-1} at 300K, which is explicitly lower than the band at 180cm^{-1} of neutral BDT-TTP, is also sensitive to the charge on BDT-TTP. At 5K, three news bands appear at 173,184, and 188cm^{-1} around this region. The band at 306cm^{-1} at 300K, to which the corresponding band appears at 319cm^{-1} for neutral BDT-TTP, may originate from the CS stretching and CCS bending modes. This band splits into two bands at 303 and 311cm^{-1} at 5K. The band at 415cm^{-1}, which is higher than that the band at 396cm^{-1} for neutral BDT-TTP, splits into two bands at 412 and 424cm^{-1} at 5K. The band at 501cm^{-1}, which is higher than that at 486cm^{-1} of neutral BDT-TTP, may derive from the CS stretching mode and may correspond to the a_g ν_6 mode of TTF. It splits into three bands at 497, 502 and 506cm^{-1} at 5K.

The bands in the range from 700 to 1,200cm^{-1} are very weak at room temperature (Fig. 14 (c)), which are related to the CS stretch of the BDT-TTP molecule. The most remarkable change in this range on lowering temperature is that the broad band from 966 to 1007cm^{-1} at 300K becomes sharper and gradually shifts to higher energy region. It turns into a very sharper band at 1,006cm^{-1} at 5K.

The CN stretching modes of the anion shifts to higher energy region on lowering temperature (Fig. 14 (d)). They appear at 2,116 and 2,126cm^{-1} at 300K and shift to 2,124 and 2,135cm^{-1} at 5K. A weak band is also observed between these two bands at low temperature. The CH stretching mode can not be observed at room temperature, but it strongly appears at 3,018cm^{-1} at 5K. Besides the bands which can be observed even at 300K, many new bands appear at low temperature as well. Some new bands are very difficult to be understood.

The change of the Raman-active modes except the most charge-sensitive mode further demonstrates that the charge disproportionation takes place through the phase transition. In addition, the split of some IR-active modes observed by the polarized reflection spectroscopy also suggests such change through the phase transition.

5.3.5 Madelung energy

When the charge disproportionation takes place, the lattice energy should change accordingly. The Madelung energy of the θ-(BDT-TTP)$_2$Cu(NCS)$_2$ single crystal is calculated by the Ewald method[28)]. The charge distribution in neutral BDT-TTP molecule and in BDT-TTP monocation radical were calculated by the semi-empirical PM$_3$ method, as listed in Table Ⅱ. As demonstrated by many people[29,30)], the lattice energy of the crystal is almost independent of the calculation methods to the charge distribution of the molecule. The charge C_i on the atom i of BDT-TTP with fracture charge x was regarded as $C_i=x(C_{i+}-C_{i0})+C_{i0}$, where C_{i+} and C_{i0} denote the charge on the atom i of neutral and monocation BDT-TTP molecules, respectively. When the anion is considered, the unit cell must be double along the *b*-axis. The charge on the Cu atom of the Cu(NCS)$_2$ anion is regarded as *+1*, and the charges on N, C, and S atoms are regarded as the charges on these atoms of N=C=S$^-$ anion calculated by PM$_3$ method. The problem to calculate the lattice energy is the stacking form of the anions in the single crystal since they are disordered. The stacking form shown in the insert of Fig. 15 is adopted for the calculation of the Madelung energy, after referring to the stacking form of the anions in the κ-(BEDT-TTF)$_2$Cu(NCS)$_2$ crystal structure[7]. The polarization of the molecule is not considered during the calculation and the crystal parameters at room temperature are always adopted.

The Madelung energy E_M is −1.37eV for a homogeneous charge distribution, namely one hole is shared equivalently by two BDT-TTP molecules. Analogous calculation is conducted for (BDT-TTP)$_2$SbF$_6$ of which the anions are not disordered, the Madelung energy E_M is −1.02eV. These calculated Madelung energies are reasonable for organic crystals. The absolute E_M value of θ-(BDT-TTP)$_2$Cu(NCS)$_2$ increases when the charge disproportionation occurs (Fig. 15), suggesting the single crystal becomes more stable after the charge disproportionation. The E_M value depends not only on the charge disproportion but also on the charge configuration. The Madelung energy E_M is calculated with different charge configuration when one hole is localized on one BDT-TTP molecule (Table Ⅲ). The most favorable configuration is that the two holes in one unit cell are localized on molecule 1 and 4. This configuration agrees with the results by Seo and Fukuyama[31] considering the electronic configuration of θ-type BEDT-TTF salts in terms of the spin interaction and by Tajima[21] considering the charge configuration in terms of the conductivity spectrum.

The bandwidth will decrease if the hole becomes localized on one molecule. The gain of the lattice energy from the complete delocalized state to the complete localized state (Two holes localizes on molecule 1 and 4 in one unit cell) is 0.76eV for θ-(BDT-TTP)$_2$Cu(NCS)$_2$. This energy gain is larger than the bandwidth. A comparative calculation is carried out for (BDT-TTP)$_2$SbF$_6$, the energy gain of the lattice energy is 0.72eV, which is comparable with θ-(BDT-TTP)$_2$Cu(NCS)$_2$. The energy gain of (BDT-TTP)$_2$SbF$_6$ is much smaller than the bandwidth. From the viewpoint of the energy, the charge disproportionation can take place for θ-(BDT-TTP)$_2$Cu(NCS)$_2$ while not for (BDT-TTP)$_2$SbF$_6$.

5.3.6 ESR of the polycrystal and the single crystal

The susceptibility of θ-(BDT-TTP)$_2$Cu(NCS)$_2$ is 4×10^{-4}emu mol^{-1} at room temperature. This susceptibility is comparable with (TTM-TTP)I$_3$ 17) while almost half of that of (BDT-TTP)$_2$BF$_4$ 32). Compared with BEDT-TTF salts, the susceptibility of θ-(BDT-TTP)$_2$Cu(NCS)$_2$ is comparable with the metallic κ-(BEDT-TTF)$_2$Cu(NCS)$_2$ 33), β-(BEDT-TTF)$_2$I$_3$, and θ-(BEDT-TTF)$_2$CsZn(SCN)$_4$ 12), while is almost half as some Mott insulator 14,35,36), such as θ-(BEDT-TTF)$_2$Cu$_2$(CN)[N(CN)$_2$]$_2$ and α-(BEDT-TTF)$_2$AuBr$_2$. The susceptibility increases on lowering temperature from 300K down to 10K (Fig. 16). The reciprocal susceptibility $1/\chi$ is plotted against the temperature. Below 240K, the temperature dependence of the susceptibility can be fitted by the Curie-Weiss model very well with the Curie constant C=0.143, θ=19K, and the magnetic moment of $0.62\mu_B$. It is not clear now why the magnetic moment is so small.

The g-factor and the linewidth are strongly dependent of the angle between the magnetic field and the orientation of the single crystal at room temperature (Fig. 17). The angular dependence of the g-factor does not change too much while the linewidth becomes almost independent of the angle at 3K.

The g-factor is 2.011-2.012, 2.004 and 2.002 along the *a'*, *c*-, and *b*-axis at room temperature, respectively. These values are comparable with those of (BDT-TTP)$_2$ClO$_4$ 37) and (TTM-TTP)I$_3$ 17). The crystallographic axes are different from the axes of the BDT-TTP molecule, but the *a'*, *c*- and *b*- axis are somewhat along the long axis, short axis and the axis perpendicular to the BDT-TTP molecular plane. The BDT-TTP molecules may have a similar relation between the g-factors and the molecular axes to that of BEDT-TTF molecule 38), namely largest g-factor along the long molecule axis, middle g-factor along the short molecule axis and smallest g-factor along the direction perpendicular to the molecular plane.

The linewidths are 90-105, 64 and 61 G for the *H* // *a'*, *c*- and *b*-axis at room temperature, respectively. The linewidths are much larger than those of β-type BDT-TTP salts[37]. On the other hand, they are also larger than κ-$(BEDT\text{-}TTF)_2Cu(NCS)_2$[39] and θ-$(BEDT\text{-}TTF)_2Cu_2(CN)[N(CN)_2]_2$[14]. The difference of the *g*-factor between θ- and β-type BDT-TTP salts resembles the relation between the θ- and β-type BEDT-TTF salts. The linewidths of θ-$(BDT\text{-}TTP)_2Cu(NCS)_2$ decrease to about 10G in the three directions at 3K.

The ESRs of the single crystal were measured from 300K down to 3K. The *H//a' g*-value increases rapidly on lowering temperature from 300 to 250K, then becomes almost independent to the temperature, at last slowly decrease from 50K down to 3K (Fig. 18). The *H//c g*-value increases a little on lowering temperature from 300 to 250K, then becomes temperature-independent. The *H//b* g-value is insensitive to the temperature. The temperature dependence of the *g*-value from 300 to 250K also suggests the significant change of the electronic structure through the phase transition.

The behaviors of the linewidthes in the three directions are similar. The linewidths drastically decrease on lowering temperature from 300 to 200K, then become almost independent of the temperature (Fig. 19). The drastic drop of the linewidths during the phase transition is because the localization of the electrons eliminates the scattering rate of the charge carrier. Below 200K, the linewidths in three directions are very close.

The temperature dependence of the integrated ESR intensity in three directions resembles the behavior of the polycrystal from 300 to 10K (Fig. 20). The intensity increases on lowering temperature from 300 to 10K and the relation between $1/\chi$ and the temperature in the temperature region of 10-250K can be fitted by straight line very well. The temperature dependence of the linewidth and the intensity confirms the phase transition at *ca.* 250K

The ESR intensity at 3K is lower than in 10K, especially the *H//c* intensity drops very much from 10K to 3K. Another phase transition thus may take place between 10K and 3K. This phase transition was not probed by the resistance measurement due to the very high resistance in this temperature region. Hence, θ-(BDT-TTP)$_2$Cu(NCS)$_2$ may be an antiferromagnetor with a very low exchange energy. This may account for the not very large magnetic moment derived from the Curie-Weiss model between 10 and 240K.

5.3.7 Physical properties of another modified (BDT-TTP)$_2$Cu(NCS)$_2$

Another modified (BDT-TTP)$_2$Cu(NCS)$_2$ single crystal has been found, of which the crystal structure remains unknown. In this chapter θ'-(BDT-TTP)$_2$Cu(NCS)$_2$ is used to represent it. It can be distinguished from the θ-(BDT-TTP)$_2$Cu(NCS)$_2$ single crystal from the shape and the polarized reflection spectrum. It exhibits very different electrical and optical properties from θ-(BDT-TTP)$_2$Cu(NCS)$_2$.

5.3.7.1 Electrical properties

Three single crystals were used for the resistance measurement from 300 K to 5K and then from 5K to 300K (Fig. 21). The behavior shows some dependence on the sample. No hysteria appears for the sample 3 and the heating run can repeat the cooling run very well. For other two samples, a weak hysteria appear between 200K and 250K in the cooling and heating run, and the heating behavior below 200K can repeat the cooling very well. The resistances exhibit very weak temperature dependence in the temperature range from 300K to 100K. The temperature dependence is so weak that it is difficult to judge whether the crystal is a metal or an insulator in this temperature region only according to the resistance measurement. The impurities and the defects may play a role for the conduction mechanism. Such electrical behavior is like a narrow gap semiconductor or a narrow band semi-metal. Combined with results of the optical spectroscopic results, the θ'-(BDT-TTP)$_2$Cu(NCS)$_2$ single crystal is regarded as a semiconductor through the temperature for the time being.

Below 50K, the resistance drastically increases on lowering temperature. It seems that a phase transition takes place below 50K. The relation of *lnR-1/T* from 30K to 5K can be fitted by a straight line very well. The activation energy obtained by this fitted is *ca.* 1.5meV. This gap is much smaller than many organic semiconductors.

5.3.7.2 Polarized reflection spectroscopy at room temperature

The polarization reflection spectra were measured on the surface of the θ'-(BDT-TTP)$_2$Cu(NCS)$_2$ single crystal at room temperature, with the polarization along and perpendicular to the long edge of the single crystal (Fig. 22). Since the crystal is very thin, very strong noise coming from the interference effect appears in the NIR region higher than 7,000cm^{-1}, thus only the refletivities from 600 to 7,000cm^{-1} are presented. Some insight into the stacking form of the BDT-TTP molecules and the Cu(NCS)$_2$ anions can be gained from the polarized reflection spectra in both directions. The CH stretching mode appears at 3,062 cm^{-1} in the spectrum of $E \perp$ long edge, while it can not be observed in the spectrum of E // long edge. These suggest that the direction perpendicular to the long edges may be almost parallel the BDT-TTP molecular plane, and the direction along the long edge may be the stacking direction. The band at 802cm^{-1} appears in both directions, like that of θ-(BDT-TTP)$_2$Cu(NCS)$_2$. As assigned for θ-(BDT-TTP)$_2$Cu(NCS)$_2$, this band is the CS stretching mode of the BDT-TTP molecule in the crystal. Thereby, a tilted angle is expected between the stacking direction and the normal to the BDT-TTP molecular plane in θ'-(BDT-TTP)$_2$Cu(NCS)$_2$ single crystal, analogous to θ-(BDT-TTP)$_2$Cu(NCS)$_2$. Two bands at 2,082 and 2,096cm^{-1} are assigned to the CN stretching modes of the anion. These positions are lower than those of both θ-(BDT-TTP)$_2$Cu(NCS)$_2$ and κ-(BEDT-TTF)$_2$Cu(NCS)$_2$[20]. These CN stretching modes only appears in the spectrum of E // long edge, they can not be observed in the spectrum of $E \perp$ long edge. A broad peak at about 650cm^{-1}, which can be assigned to the CS stretch of the anion like that of θ-(BDT-TTP)$_2$Cu(NCS)$_2$, only appears in the spectrum of

E // long edge. This anisotropy of the phonon modes of the anion suggests that the molecular plane of the $Cu(NCS)_2$ anion is perpendicular to the direction perpendicular to the long edge. Hence, the stacking form of the $Cu(NCS)_2$ anions is different in θ'-$(BDT\text{-}TTP)_2Cu(NCS)_2$ from in θ-$(BDT\text{-}TTP)_2Cu(NCS)_2$.

The CT band appears at low wavenumber region in both directions. The reflectivities at 600cm^{-1} is 30% and 44% in the spectrum of *E* // and *E* ⊥ long edge, respectively. They are a little higher than those of θ-$(BDT\text{-}TTP)_2Cu(NCS)_2$. The low reflectivity suggests the single crystal may be a semiconductor at room temperature. The minimum point of the CT band locates at *ca.* 4,500cm^{-1} for *E* ⊥ long edge and *ca.* 3,500cm^{-1} for *E* // long edge, respectively.

The strength of the CT band is stronger along the long edge than perpendicular to the long edge (Fig. 23). The plasma frequencies ω_p defined by equation 5.3, are 3.3×10^3 and 5.3×10^3cm^{-1} for the parallel and perpendicular directions, respectively, by integrating the conductivity of the CT band from 0 to 6,000cm^{-1}. These plasma frequencies are higher than those of θ-$(BDT\text{-}TTP)_2Cu(NCS)_2$. Since $\omega_{p\perp}$ is larger than $\omega_{p//}$, the inter-stack transfer integral may be larger than the intra-stack transfer integral. The ratio of the oscillator strength $\omega^2_{p\perp}/\omega^2_{p//}$ is 2.5, lower than that of θ-$(BDT\text{-}TTP)_2Cu(NCS)_2$. Thus θ'-$(BDT\text{-}TTP)_2Cu(NCS)_2$ may be more isotropic than θ-$(BDT\text{-}TTP)_2Cu(NCS)_2$.

The phonon modes in the conductivity spectra are relative simple. The dips appearing in both directions are very remarkable. Both dips arise from the electron-phonon interaction, contributed by the C=C stretch of the BDT-TTP molecules. They are very broad and the positions are comparable with that of θ-$(BDT\text{-}TTP)_2Cu(NCS)_2$.

5.3.7.3 Polarized reflection spectroscopy at room temperature

The polarized reflection spectra were measured from 300K down to 16K. The spectrum does not change significantly at low temperature. The reflectivity of *E* // long edge systematically increases on lowering temperature (Fig. 24). The reflectivity at 600 cm^{-1} is 30% at 300K and increases to 35% at 16K. The CT band becomes steeper at low temperature. The reflectivity of the CT band of $E \perp$ long edge also increases on lowering temperature (Fig. 25). The reflectivity at 600cm^{-1} is 45% at 300K and increases to 55% at 16K. In this direction, the reflectivity between 1,000 and 1,400cm^{-1} increases more than the reflectivity below 1,000 cm^{-1}.

The spectroscopic weight of the CT band of E // long edge shifts to lower wavenumber region with the lowering temperature from 300K down to 50K (Fig. 26). The peak position of the CT band explicitly appears at 300K, it shifts to red on lowering temperature and can not be observed in the spectrum at 50K. But the spectroscopic weight may shift a little to higher energy region from 50K to 16K. This change may be related to the phase transition below 50K. The spectroscopic weight of the CT band of $E \perp$ long edge shifts to lower energy region on lowering temperature as well from 300K down to 16K (Fig. 27). The peak position of the CT band many be at 1,200cm^{-1} at 300K and shifts to 1,050cm^{-1} at 16K. The phonons do not show any significant change from 300K down to 16K on lowering temperature.

5.3.7.4.Raman spectroscopy

The Raman spectrum of θ'-(BDT-TTP)$_2$Cu(NCS)$_2$ was measured with the polarization of the incident light perpendicular to the long edge. The Raman spectrum from 150 to 1,800cm^{-1} is very similar to that of θ-(BDT-TTP)$_2$Cu(NCS)$_2$ at room temperature. The charge-sensitive band appears at 1,484cm^{-1} at room temperature, a little lower than that of θ-(BDT-TTP)$_2$Cu(NCS)$_2$. This band is also broad, indicating the charge distribution is not homogeneous in the crystal as well. This mode almost does not change on lowering temperature from 300K to 130K (Fig. 28 (a)). It becomes broader on lowering temperature below 130K. The split of the band can be observed below 70K. At 5K, it splits into three bands at 1468, 1481 and 1498cm^{-1}. These suggest that a charge disproportionation takes place below 70K. The Raman spectrum from 150 to 700cm^{-1} almost does not change too much except the enhancement of the some modes (Fig. 28 (b)). A possible split is the band at 167cm^{-1} at 300 K which becomes two bands at 157 and 164cm^{-1}. The band at 978cm^{-1} at room temperature becomes broader on lowering temperature down to 150K (Fig. 28 (c)), it is very clear this mode shifts to higher energy region below 150K. At 5K it appears at 1,002cm^{-1} and becomes very sharp. The intensity of all modes does not increase too much at 5K, different from that of θ-(BDT-TTP)$_2$Cu(NCS)$_2$.

The CN stretching modes of the anions, which can be observed only when the polarization of the incident light parallel the long edge of the crystal, appear at 2,075 and 2,095cm^{-1} at room temperature The positions are lower than that in θ-(BDT-TTP)$_2$Cu(NCS)$_2$. These also suggest the environment of the CN bonds is different in θ'-(BDT-TTP)$_2$Cu(NCS)$_2$ from in θ-(BDT-TTP)$_2$Cu(NCS)$_2$. Combined the results by the polarized reflection spectroscopy and the Raman spectroscopy, it is certain that the stacking structure of the Cu(NCS)$_2$ anions is very different in both crystals.

5.4 Summary

θ-(BDT-TTP)$_2$Cu(NCS)$_2$ is probably a Mott insulator, although it is expected to be a two-dimensional metal from the calculation of the band structure. The phase transition is observed at *ca.* 250K in the electrical resistance measurement. The activation energy changes from 30-40meV before the phase transition to 100meV. The polarized reflection spectra suggest two dimensional electronic structure and larger inter-stack transfer integral than the intra-stack transfer integral. The spectroscopic weight of the CT band shifts to higher energy region below the phase transition temperature. The onset energy of the *E//c* CT band at 16K is comparable with the energy gap estimated from the resistance measurement. The charge sensitive mode in the Raman spectrum splits into several modes at low temperature, suggesting the charge disproportionation through the phase transition. The spin susceptibility increases on lowering temperature down to 10K, conforming the Curie-Weiss law with the magnetic moment of $0.62\mu_B$. The variations of the g-value and the linewidth of ESR signal with the temperature confirm the phase transition. Another modified $(BDT\text{-}TTP)_2Cu(NCS)_2$ crystal has been found, which exhibits very different physical properties from θ-$(BDT\text{-}TTP)_2Cu(NCS)_2$. A phase transition, caused by the charge disproportionation, takes place below 50K.

References:

1) Y. Misaki and T. Mori, *Solid State Physics*, **33** (1998) 1014.

2) Y. Misaki, H. Fujiwara, T. Yamabe, T. Mori, H. Mori, and S. Tanaka, *Chem . Lett.*, (1994) 1653.

3) T. Mori, T. Kawamoto, Y. Misaki, K. Kawamoto, H. Fujiwara, T. Yamabe, H. Mori, and S. Tanaka, *Mol. Cryst. Liq. Cryst.*, **284** (1996) 271.

4) T. Mori, Y. Misaki, H. Fujiwara, and T. Yamabe, *Bull. Chem. Soc. Jpn.*, **67** (1994) 2685.

5) J. Ouyang, K. Yakushi, Y. Misaki, and K. Tanaka, *J. Phys. Soc. Jpn.*, **67** (1998) 3191. See also Chapter 2, 3, and 4 of this thesis.

6) S. Gärtner, E. Gogu, I. Heinen, H. J. Keller, T. Klutz, D. Schweitzer, *Solid State Commun.*, **65** (1988) 1531.

7) H. Urayama, H. Yamochi, G. Saito, K. Nozawa, T. Sugano, M. Kinoshita, S. Sato, K. Oshima, A. Kawamoto, and J. Tanaka, *Chem. Lett.*, (1988) 55.

8) M. A. Beno, H. H. Wang, A. W. Kini, K. D. Carlson, U. Geiser, U. K. Kwok, J. E. Thompson, J. M. Williams, J. Ren, and M.-H. Whangbo, *Inorg. Chem.*, **29** (1990) 1599.

9) Y. Misaki, private communication.

10) J. Ouyang, J. Dong, K. Yakushi, K. Takimiya, and T. Otsubo, *J. Phys. Soc. Jpn.*, in press . See also Chapter 6 of this thesis.

11) T. J. Emge, H. H. Wang, M. K. Bowman, C. M. Pipan, K. D. Carlson, M. A. Beno, L. N. Hall, B. A. Anderson, J. M. Williams, and M.-H. Whangbo, *J. Am. Chem. Soc.*, **109** (1987) 2016.

12) H. Mori, S. Tanaka, and T, Mori, *Phys. Rev. B*, **57** (1998) 12023.

13) T. Mori, H. Mori, and S. Tanaka, *Bull. Chem. Soc. Jpn.*, **72** (1999) 179.

14) T. Komatsu, H. Sato, T. Nakamura, N.Matsukawa, H. Yamochi, G. Saito, M. Kusunoki, K.

Sakaguchi, and S. Kagoshima, *Bull. Chem. Soc. Jpn.*, **68** (1995) 2233.

15) Y. Misaki, T. Matsui, K. Kawakami, H. Nishikawa, T. Yamabe, and M. Shiro, *Chem. Lett.*, (1993) 1337.

16) H. Tajima, M. Arifuku, T. Ohta, T. Mori, Y. Misaki, T. Yamabe, H. Mori, and S. Tanaka, *Synth. Met.*, **71** (1995) 1951.

17) T. Mori, T. Kawamoto, J. Yamaura, T. Enoki, Y. Misaki, T. Yamabe, H. Mori, and S. Tanaka, *Phys. Rev. Lett.*, **79** (1997) 1702.

18) Y. Misaki, H. Nishikawa, K. Kawakami, S. Koyanagi, T. Yamabe, and M. Shiro, *Chem. Lett.*, (1992) 2321.

19) J. Dong, K. Yakushi, K. Takamiya, and T. Otsubo, *J. Phys. Soc. Jpn.*, **67** (1998) 971.

20) K. Kornelsen, J. E. Eldridge, H. H. Wang, and J. M. Williams, *Phys. Rev. B*, **44** (1991) 5235.

21) H. Tajima, *Annual Meeting of the Physical Society of Japan in Spring*, Hiroshima, (1999).

22) Y. Okimoto, T. Katsufuji, Y. Okada, T. Arima, and Y. Tokura, *Phys. Rev. B*, **51** (1995) 9581.

23) T. Katsufuji, Y. Okimoto, and Y. Tokura, *Phys. Rev. Lett.*, **75** (1995) 3497.

24) M. Kasuya, Y. Tokura, T. Arima, H. Eisaki, and S. Uchida, *Phys. Rev. B*, **47** (1993) 6197.

25) A. J. Berlinsky, Y. Hoyano, and L. Weiler, *Chem. Phys. Lett.*, **45** (1977) 419.

26) R. Beno, I. Zanon, A. Girlando, and C. Pecile, *J. Chem. Phys.*, **71** (1979) 2282.

27) R. Beno, A. Girlando, and C. Pecile, *Chem. Phys. Lett.*, **52** (1977) 503.

28) R. M. Metzger, *J. Chem. Phys.*, **57** (1972) 1870.

29) R. M. Metzger, *J. Chem. Phys.*, **57** (1972) 1876.

30) T. Ida, K. Yakushi, and H. Kuroda, *J. Chem. Phys.*, **91** (19899 3450.

31) H. Seo and H. Fukuyama, *J. Phys. Soc. Jpn.*, **67** (1998) 1848.

32) T. Kawamoto, T. Mori, J. Yamaura, T. Enoki, Y. Misaki, T. Yamabe, H. Mori, and S. Tanaka, *Synth. Met.*, 85 (1997) 1555.

33) K. Nozawa, T. Sugano, H. Urayama, H. Yamochi, G. Saito, and M. Kinoshita, *Chem. Lett.*, (1988) 617.

34) B. Rothaemel, L. Forró, J. R. Cooper, J. S. Schilling, M. Weger, P. Bele, H. Brunner, D. Schweitzer, and H. J. Keller, *Phys. Rev. B*, **34** (1986) 704.

35) S. D. Obertelli, R. H. Friend, D. R. Talham, M. Kurmoo, and P. Day, *J. Phys.: Condens. Matter*, **1** (1989) 5671.

36) N. Yoneyama, A. Miyazaki, T. Enoki, and G. Saito, *Bull. Chem. Soc. Jpn.*, **72** (1999) 639.

37) T. Mori, Y. Misaki, H. Fujiwara, and T. Yamabe, *Bull. Chem. Soc. Jpn.*, **67** (1994) 2685.

38) T. Sugano, G. Saito, and M. Kinoshita, *Phys. Rev. B*, **35** (1987) 6554.

39) K. Kornelsen, J. E. Eldridge, H. H. Wang, and J. M. Williams, *Solid State Commun.*, **74** (1990) 501.

Table I Raman-active modes of θ-$(BDT\text{-}TTP)_2Cu(NCS)_2$, $(BDT\text{-}TTP)_2SbF_6$, $(BDT\text{-}TTP)_2AsF_6$, and neutral BDT-TTP. The data of TTF crystal and TTF^+ solution are listed as well. The assignment is about the modes of TTF and TTF^+. The correspondence between TTF and BDT-TTP is very tentative.

θ-$(BDT\text{-}TTP)_2Cu(NCS)_2$	$(BDT\text{-}TTP)_2SbF_6$	$(BDT\text{-}TTP)_2AsF_6$	BDT-TTP	TTF[a)]	TTF^+[b)]	assignment[c)]
166	167	168	180			
241				244	265	a_g, ν_7 (H_1,H_2)
306	307	307	319	316		(K_3,H_4)
		397				
415	414	414	396			
	420	420	410	414	460	
469	476	476	458			
489	498	491				
		499				
501	504	503	486	472	501	a_g, ν_6 (K_3)
			513	495		
				612		
		680		659	661	
				742	754	a_g, ν_5 (K_4)
779		787		781	836	K_3
				804		K_4,H_3
				846		
980	985	985		859		
	987	989		983		
998	991					
1051	1060	1060	1041	1002	1066	K_3,H_4
1090	1091	1098	1089	1091	1072	a_g, ν_4 (H_5)
	1105	1106				
1486	1479	1480	1507	1518	1420	a_g, ν_3 (K_1)
			1525			
1538	1537	1538	1560	1555	1505	a_g, ν_2 (K_2)

K1, central C=C stretch; K2, ring C=C stretch; K3, K4, CS stretch; H1, CCC bend; H2, CSC bend; H3, ring SCC bend; H4 external CCS.

[a)] Raman-active modes of TTF solid. Ref. 24.

[b)] Raman-active modes of TTF^+ solution. Ref. 25.

[c)] Ref. 25 and 26.

Table Ⅱ Point-charge distribution in neutral and monocation molecules of BDT-TTP calculated by the semi-empirical PM$_3$ method. The charge distribution of the Cu(NCS)$_2$ anion is listed as well.

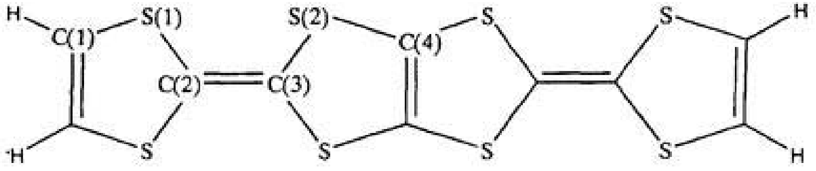

Atomic label	Neutral BDT-TTP	BDT-TTP monocation
C(1)	-0.258	-0.240
C(2)	-0.273	-0.318
C(3)	-0.405	-0.417
C(4)	-0.269	-0.397
S(1)	0.280	0.387
S(2)	0.295	0.491
H	0.156	0.178

Charge distribution on the Cu(NCS)$_2$ anion: Cu: +*1*, N: *-0.357*, C: *-0.137*, S: *-0.509*.

Table Ⅲ The Madelung energy E_M of θ-(BDT-TTP)$_2$Cu(NCS)$_2$ when the *+1* charge localized on one BDT-TTP molecule and another BDT-TTP is in neutral state. The numbers 0 and 1 in the table denote the charge on the molecules.

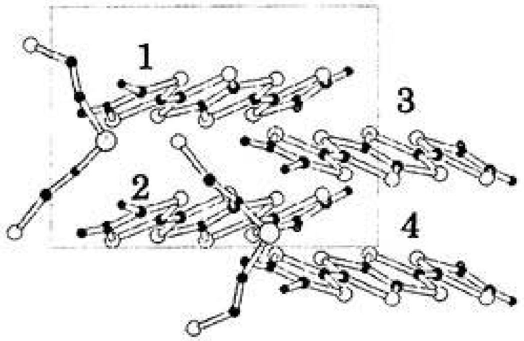

Charge on BDT-TTP molecule				E_M / eV
Molecule 1	Molecule 2	Molecule 3	Molecule 4	
1	0	0	1	-2.13
0	1	0	1	-2.09
1	0	1	0	-2.09
0	1	1	0	-2.05
1	1	0	0	-2.02
0	0	1	1	-2.02

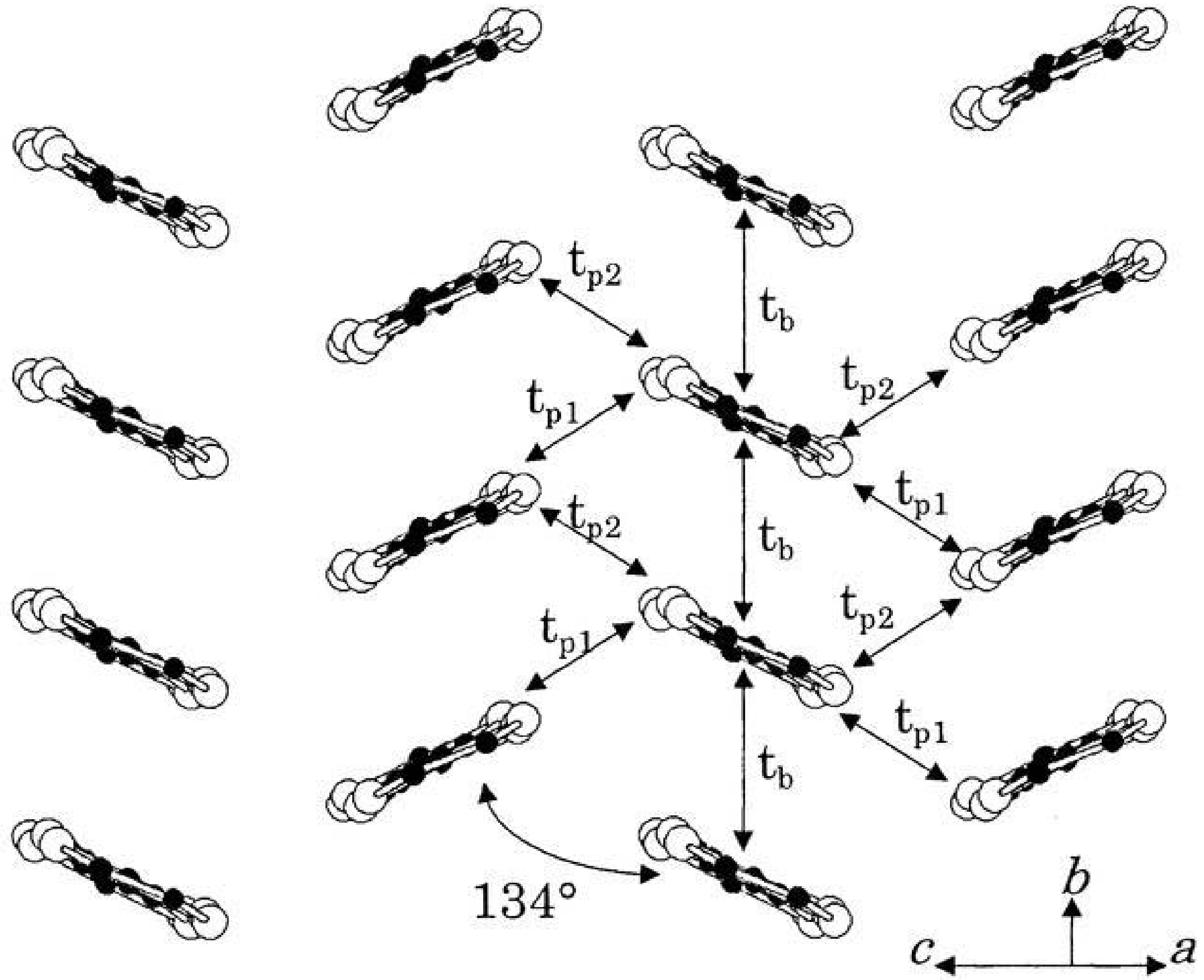

Fig. 1 Crystal structure of θ-(BDT-TTP)$_2$Cu(NCS)$_2$ viewed along the long molecular axis. t_b is the intra-stack transfer integral, t_{p1} and t_{p2} are the inter-stack transfer integrals.

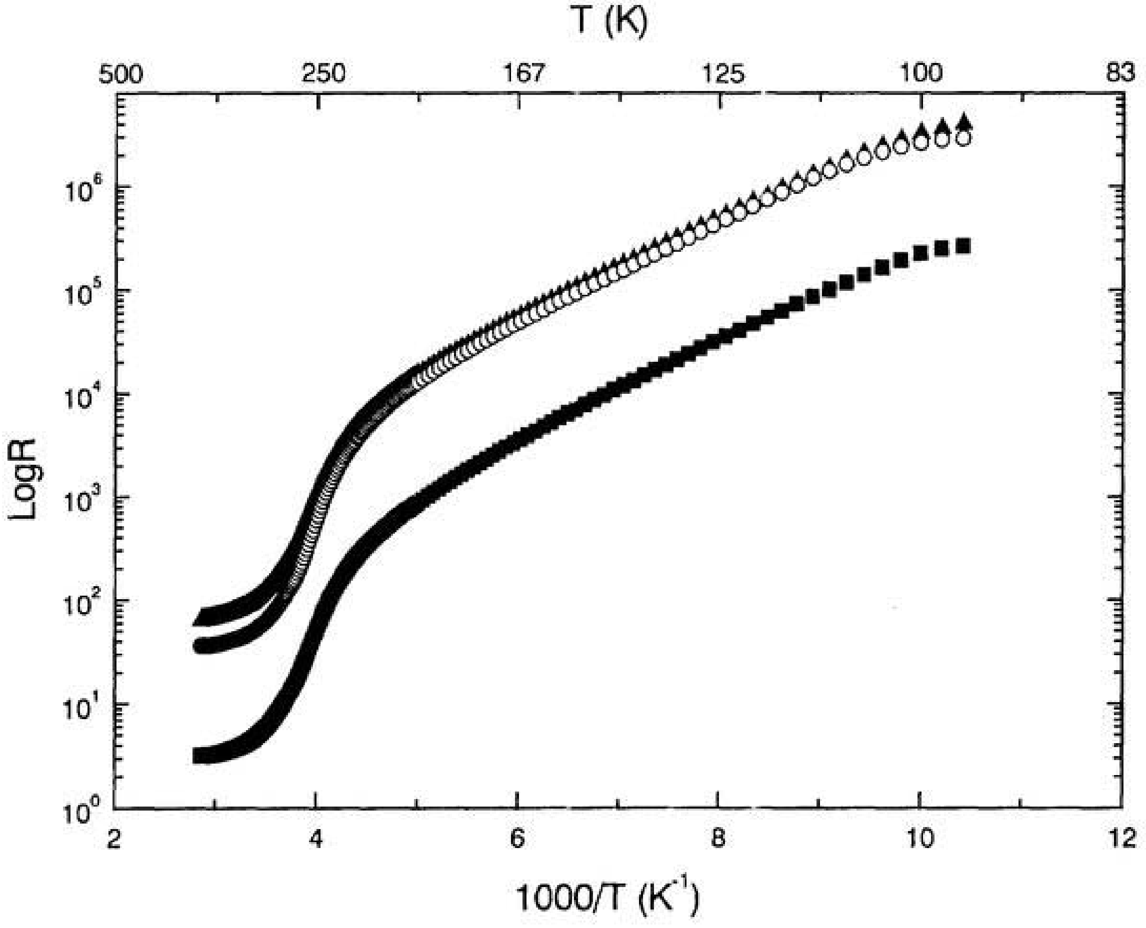

Fig. 2 Temperature dependence of the resistance of θ-$(BDT\text{-}TTP)_2Cu(NCS)_2$ single crystal. Note the resistance is in logarithmic scale and the temperature of the bottom axis is in reciprocal K.

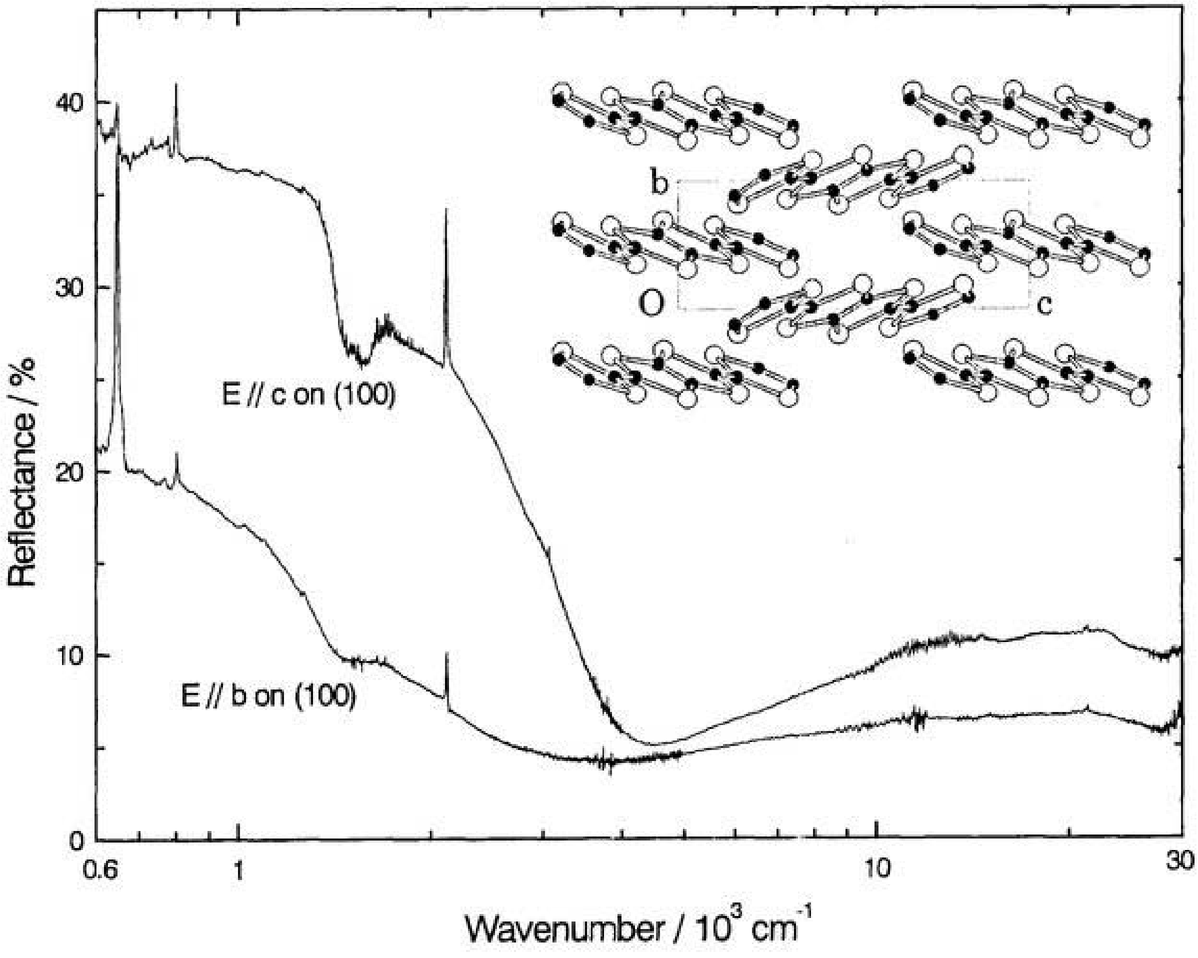

Fig. 3 Polarized reflection spectra of θ-(BDT-TTP)$_2$Cu(NCS)$_2$ at room temperature. The insert is the project of the crystal on the (100) plane.

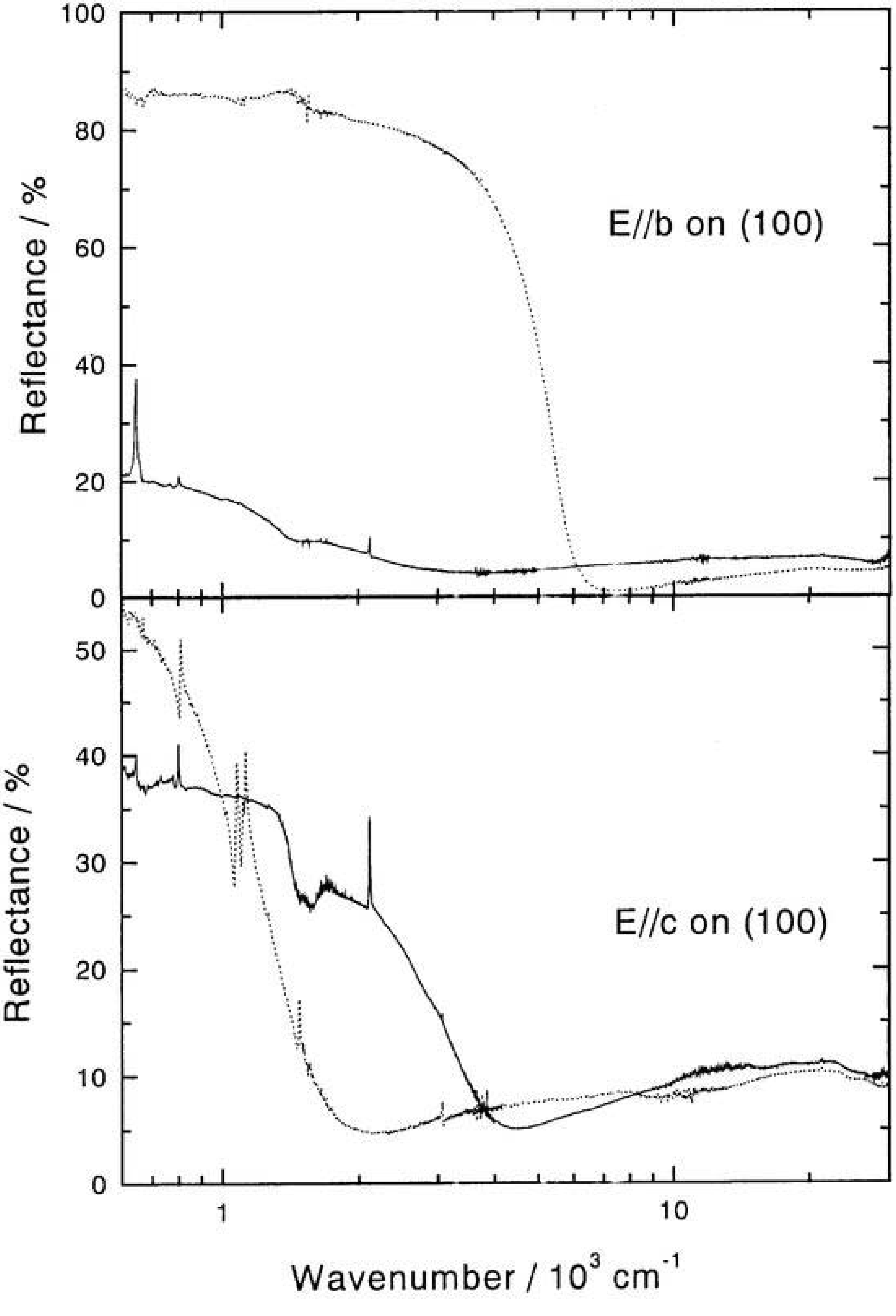

Fig. 4 Comparison of the polarized reflection spectra of the θ-(BDT-TTP)$_2$Cu(NCS)$_2$ and (BDT-TTP)$_2$ClO$_4$ single crystals at room temperature. The polarization spectra are measured on the (100) surface of both crystals.

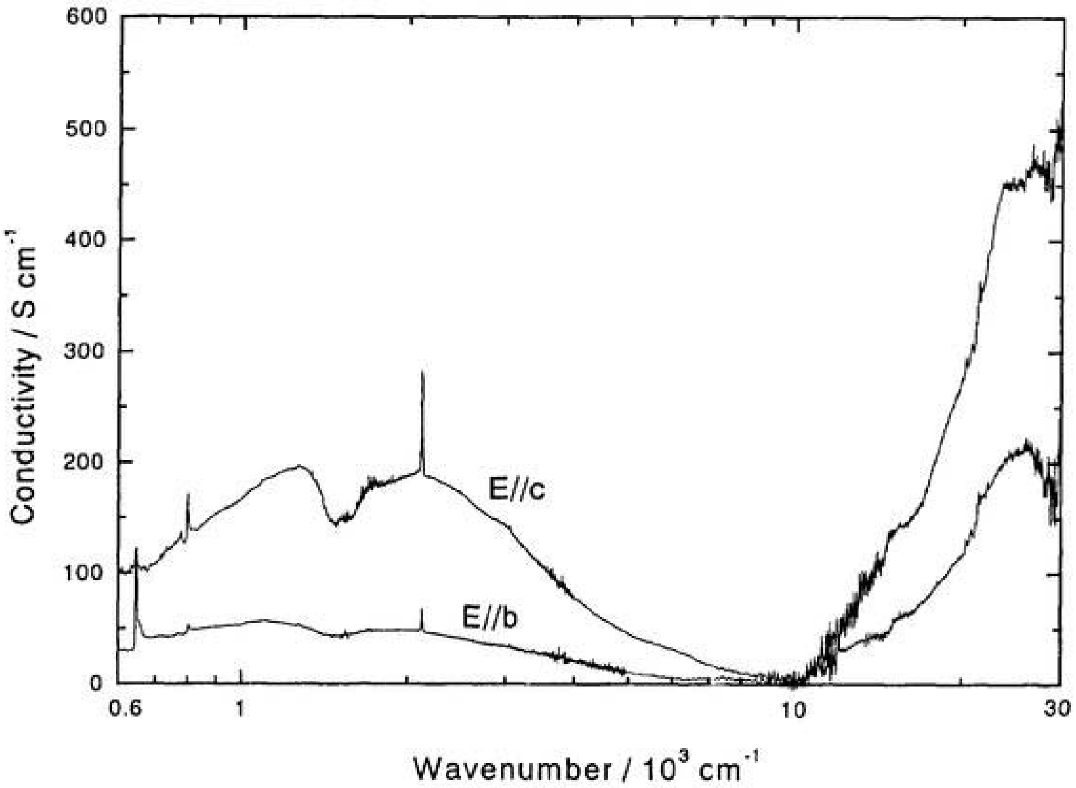

Fig. 5 Conductivity spectra of θ-(BDT-TTP)$_2$Cu(NCS)$_2$ obtained by Krames-Kronig transformation of the polarized reflection spectra.

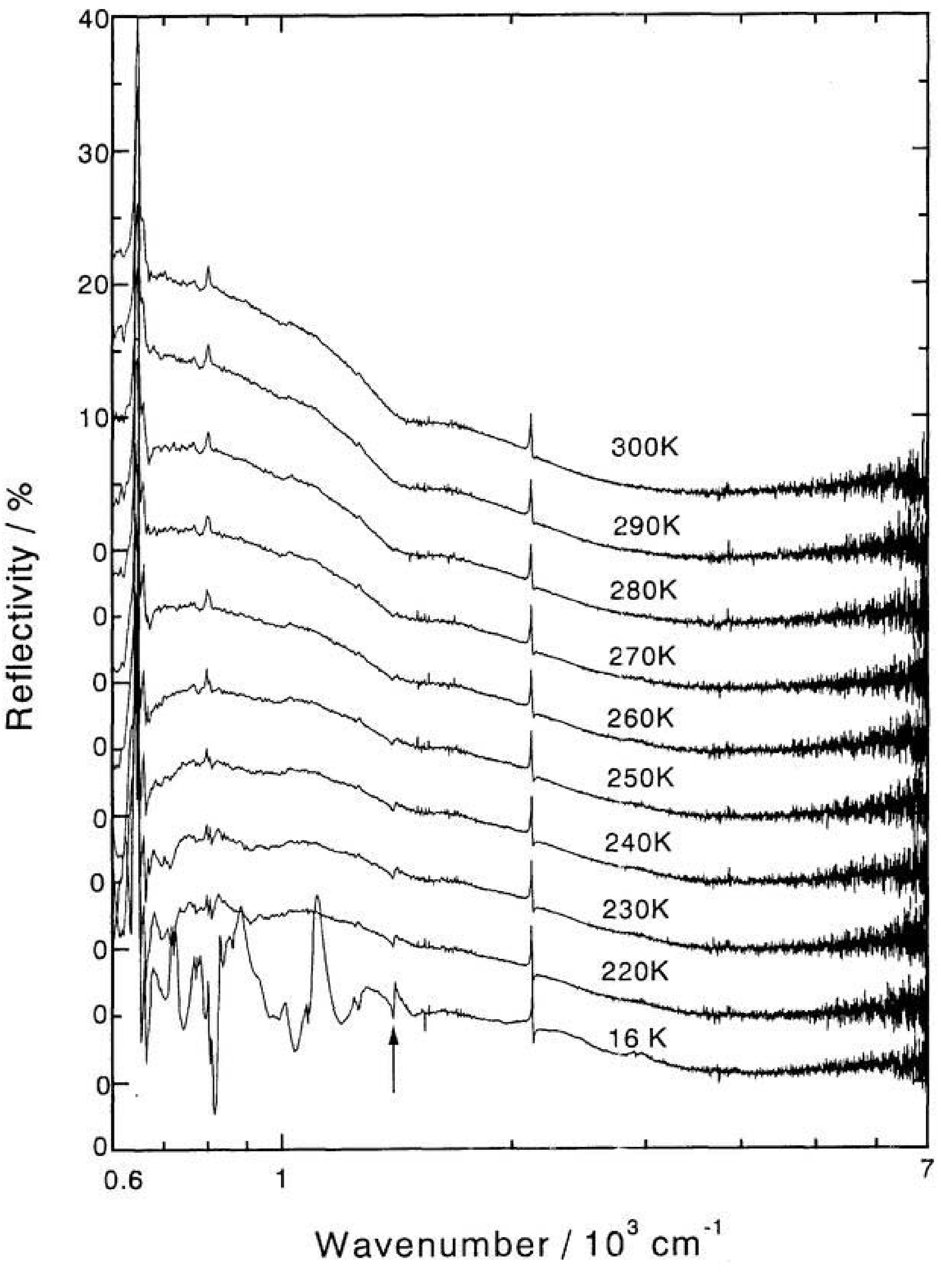

Fig. 6 *E//b* reflection spectra of θ-(BDT-TTP)$_2$Cu(NCS)$_2$ at various temperatures. The arrow indicates the new appearance of the new peak at low temperatures.

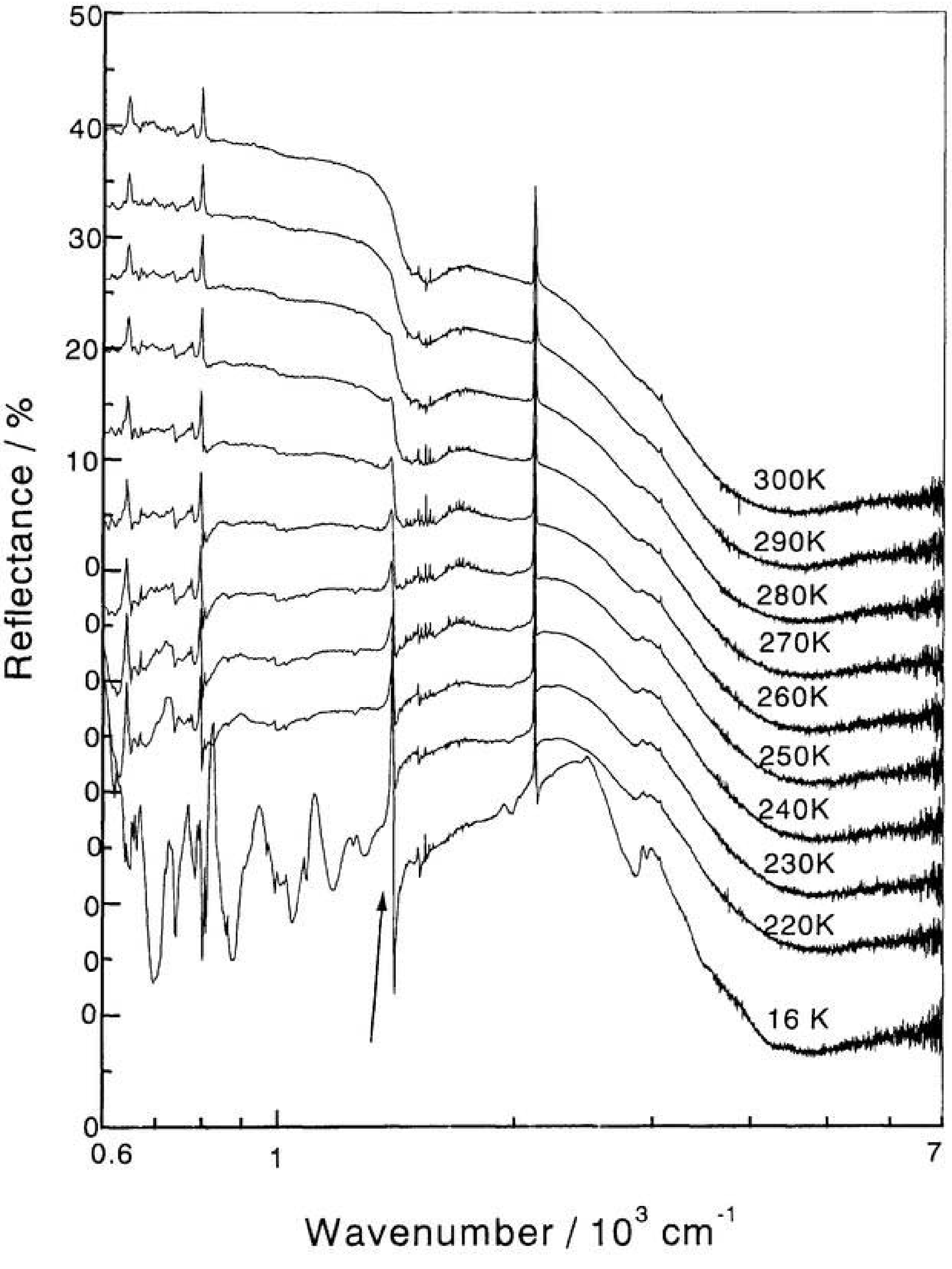

Fig. 7 $E//c$ reflection spectra of θ-(BDT-TTP)$_2$Cu(NCS)$_2$ at various temperatures. The arrow indicates the appearance of the new peak at low temperatures.

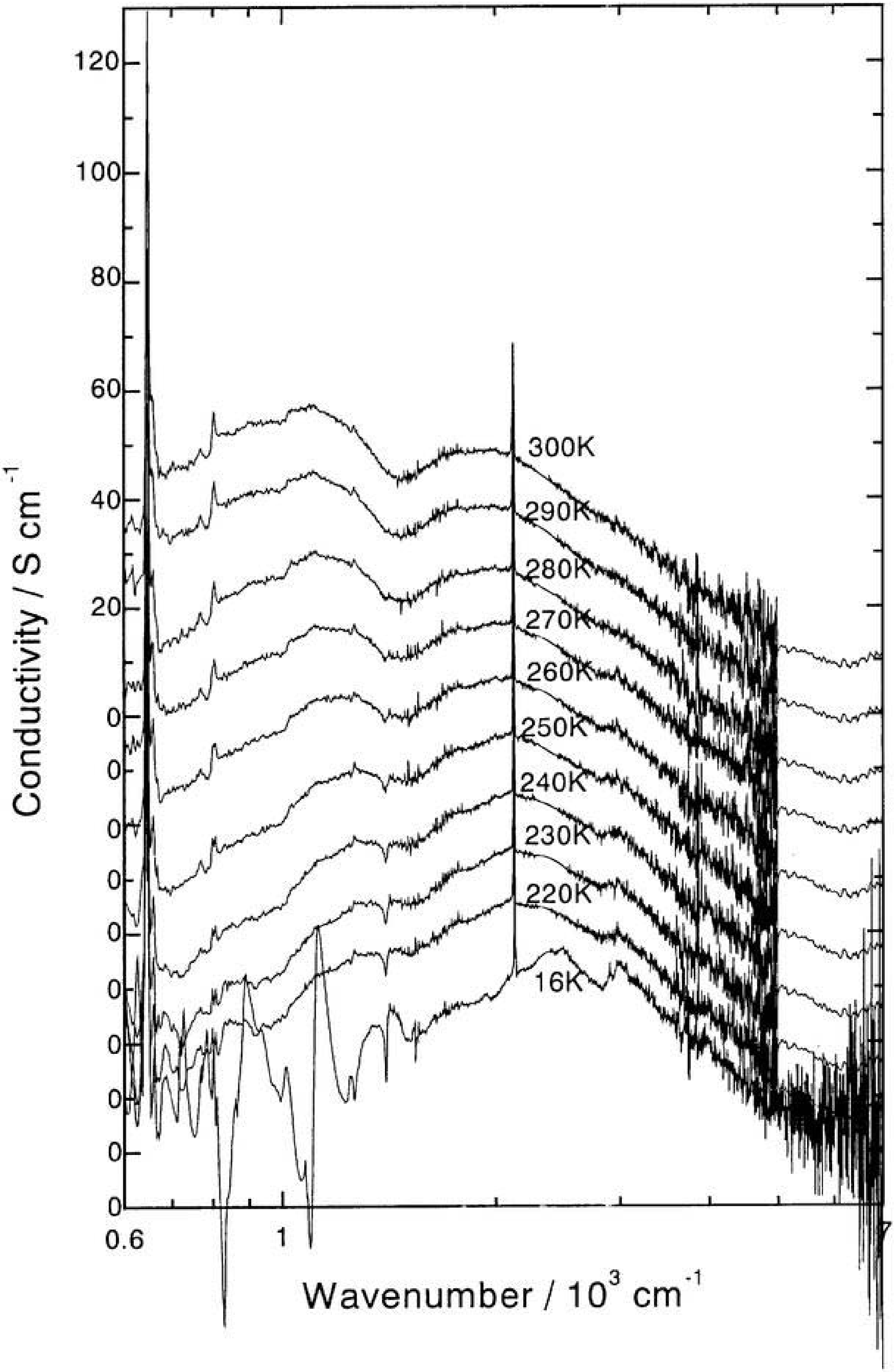

Fig. 8 *E*//*b* conductivity spectra of θ-(BDT-TTP)$_2$Cu(NCS)$_2$ at various temperatures.

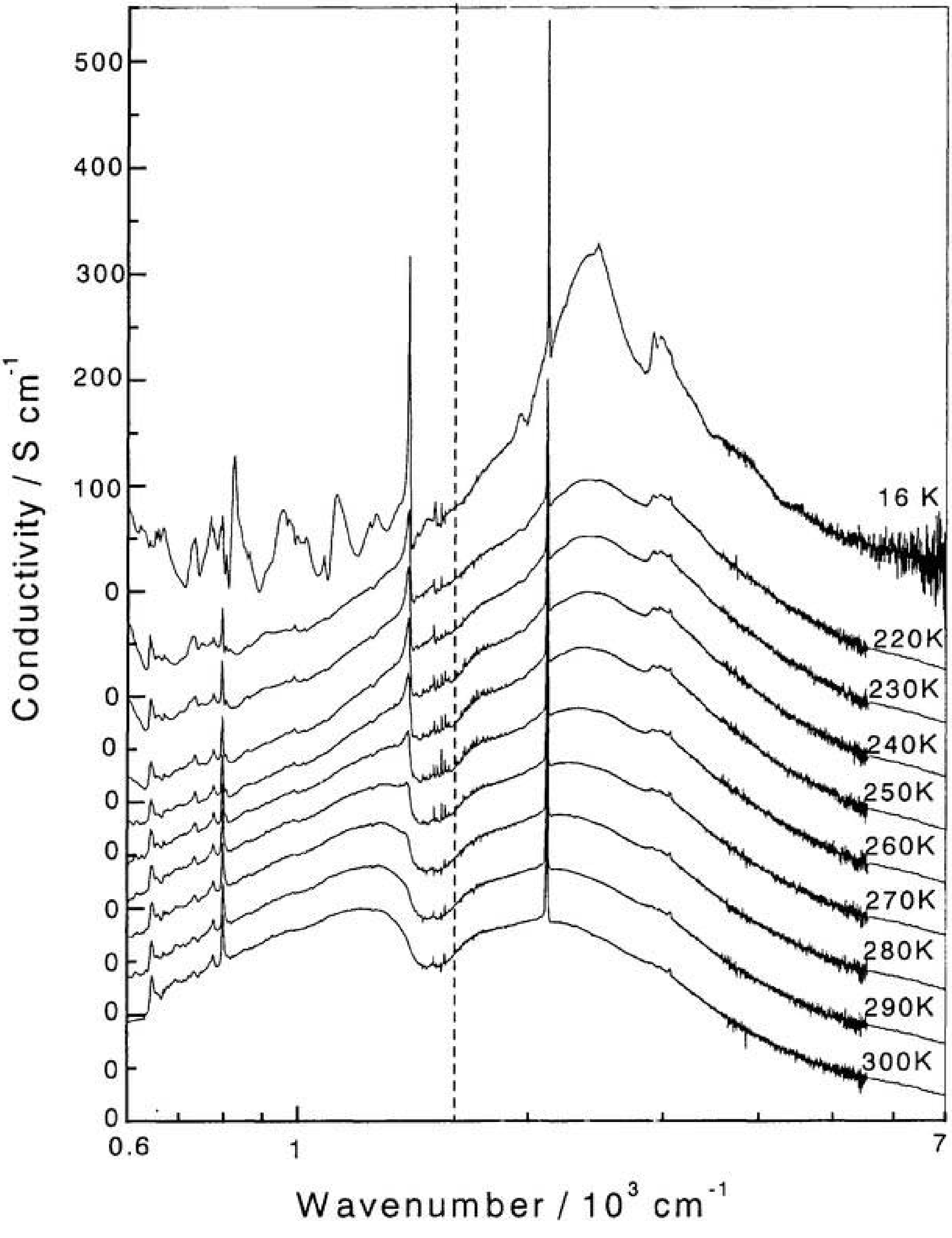

Fig. 9 *E//c* conductivity spectra of θ-(BDT-TTP)$_2$Cu(NCS)$_2$ at various temperatures. The vertical dashed line indicates the position of the energy gap between 100 and 200K obtained by the resistance measurement.

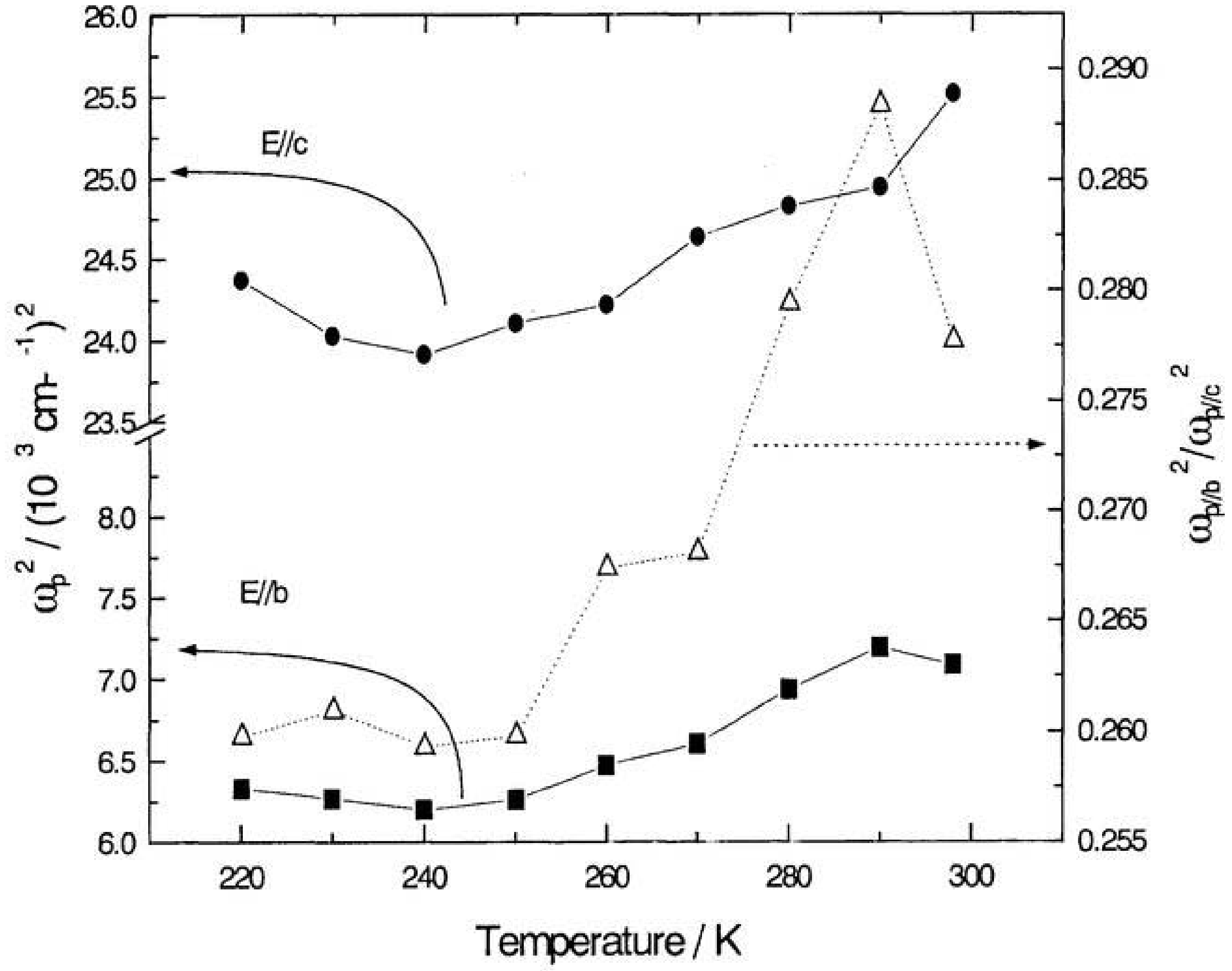

Fig. 10 Temperature dependence of the oscillator strengthes of the CT band and the ratio $\omega^2_{p//b}/\omega^2_{p//c}$ of θ-(BDT-TTP)$_2$Cu(NCS)$_2$.

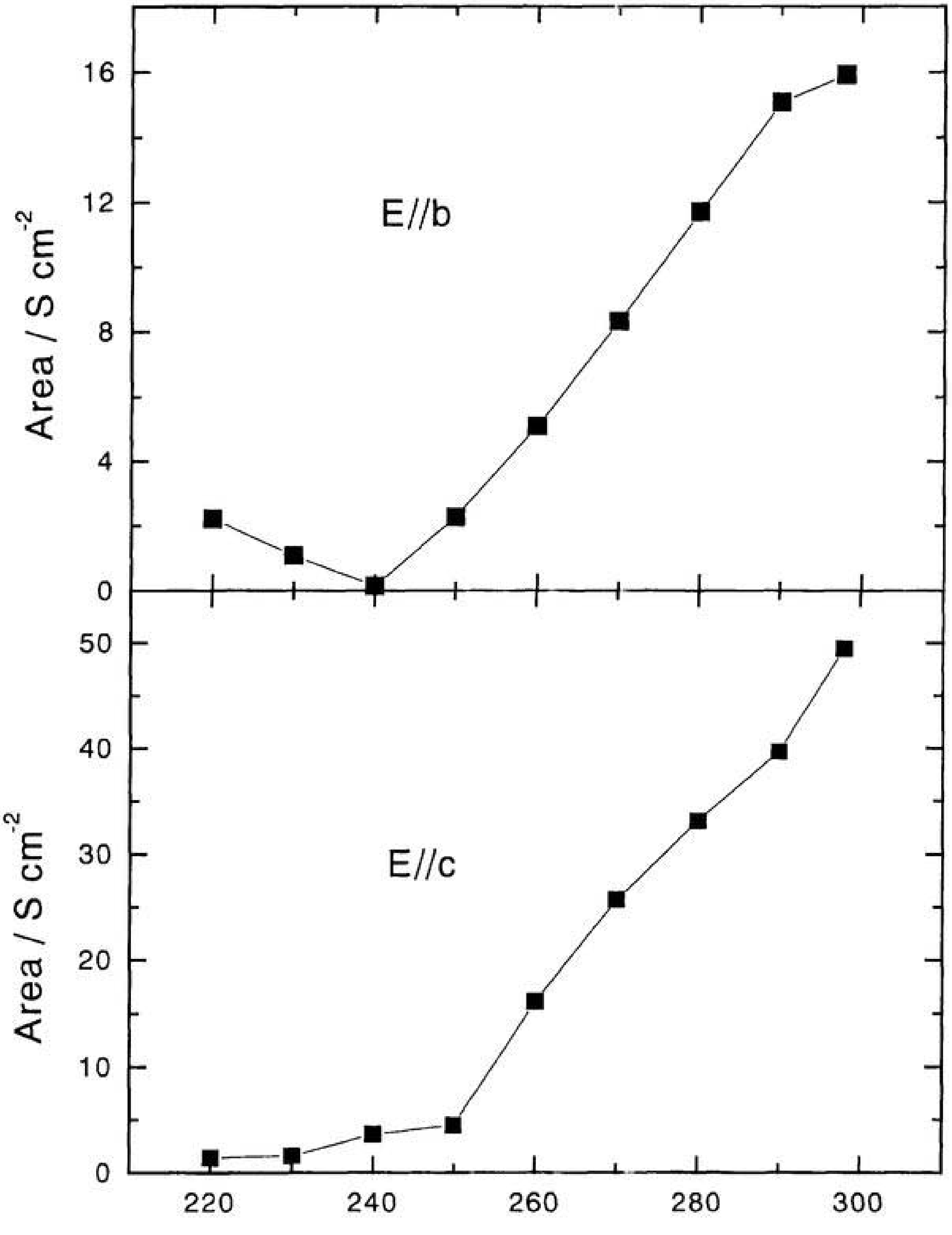

Fig. 11 Temperature dependence of the integrated area of the phonon mode at 800cm^{-1} in the conductivity spectra of *E//b* (top panel) and *E//c* (bottom).

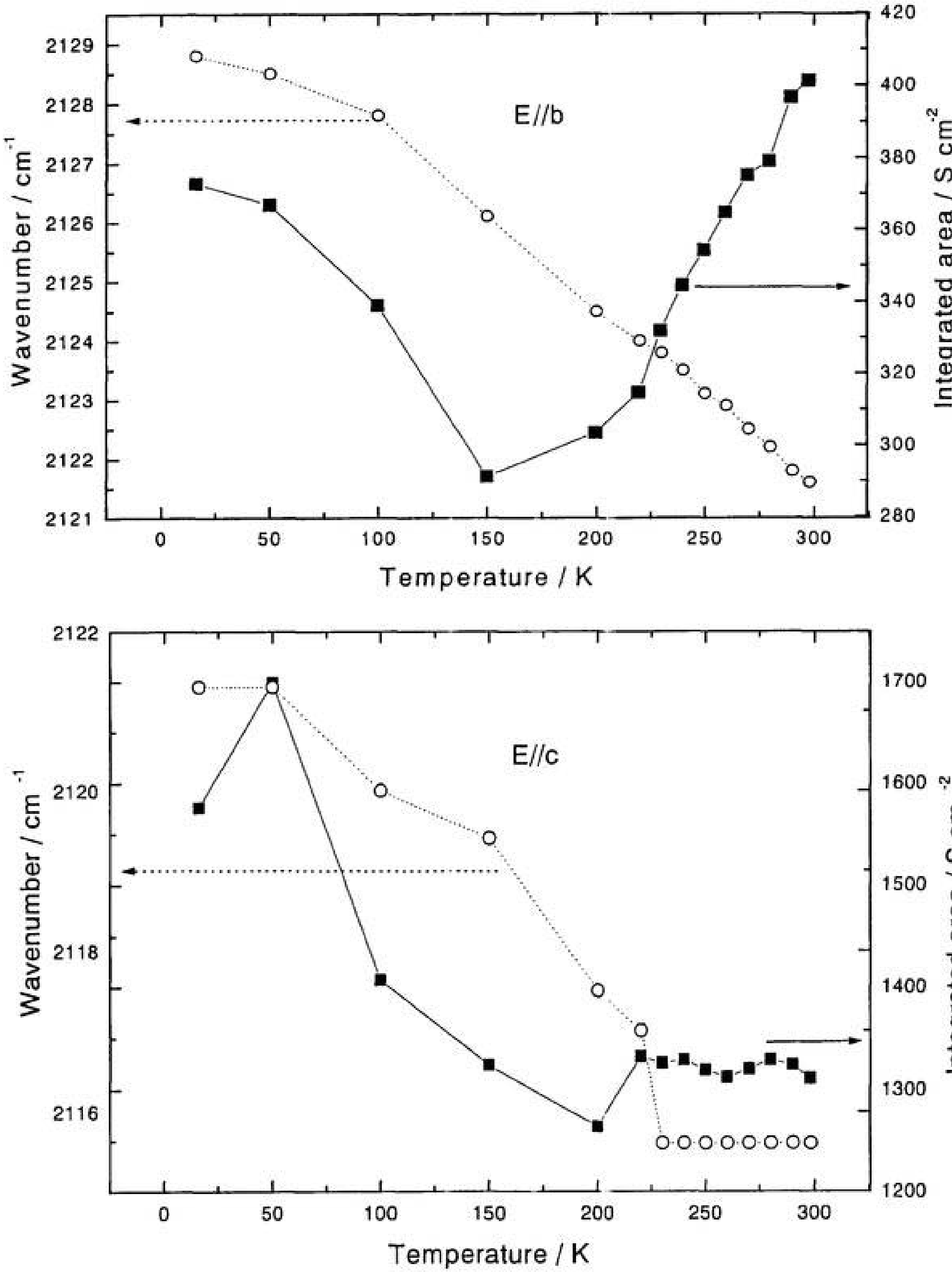

Fig. 12 Temperature dependence of the position and the integrated area of CN stretching mode in *E*// *b* (top panel) and *E*//*c* (bottom) conductivity spectra of θ-(BDT-TTP)$_2$Cu(NCS)$_2$.

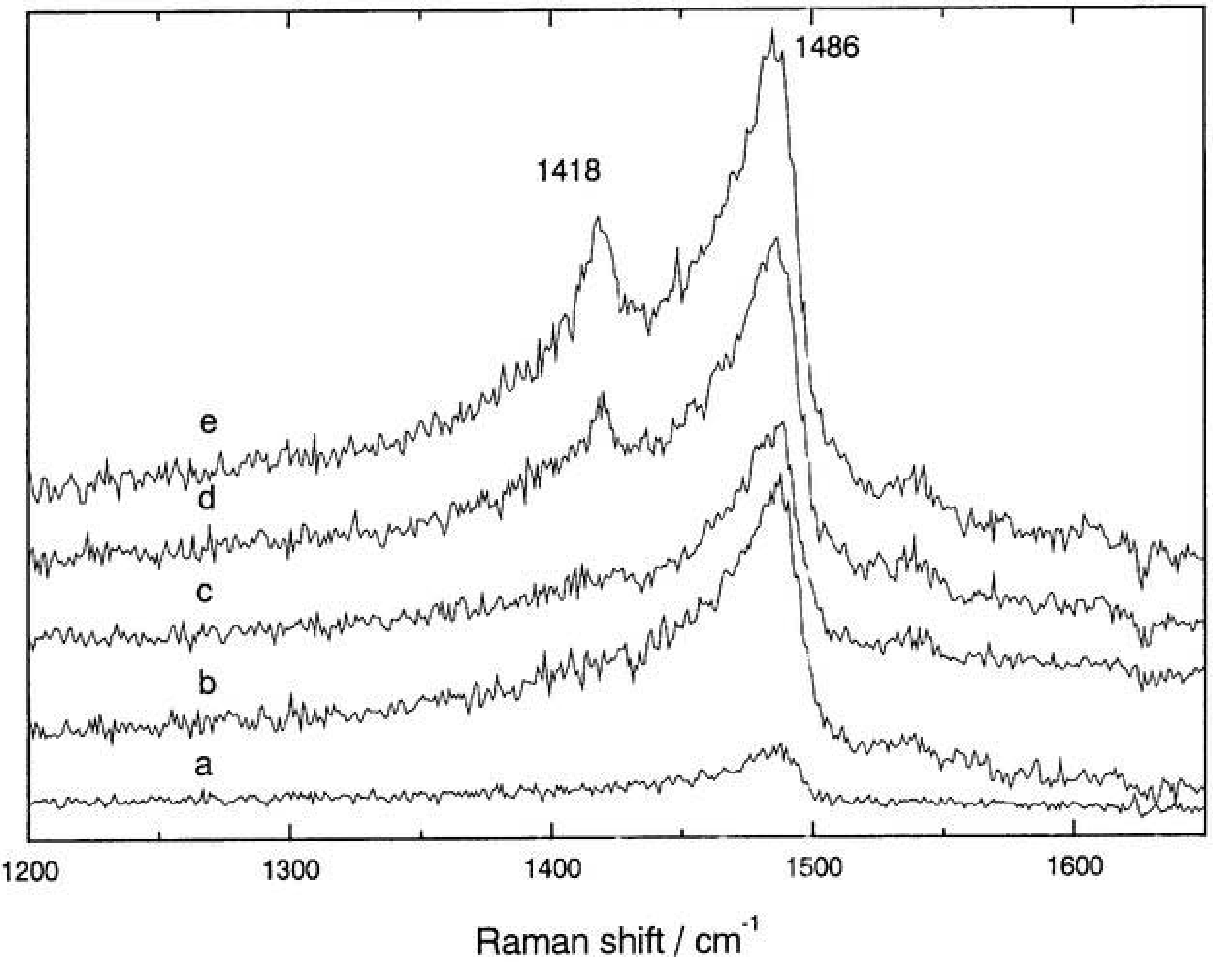

Fig. 13 Raman spectra of θ-(BDT-TTP)$_2$Cu(NCS)$_2$ by using different power and exposure time. (a) 1%, 30sec; (b) 1%, 150sec; (c) 3%, 60sec; (d) 3%, 90sec; (e) 3%, 150sec. The percent is the value of the filter to attenuate the power of 50mW .

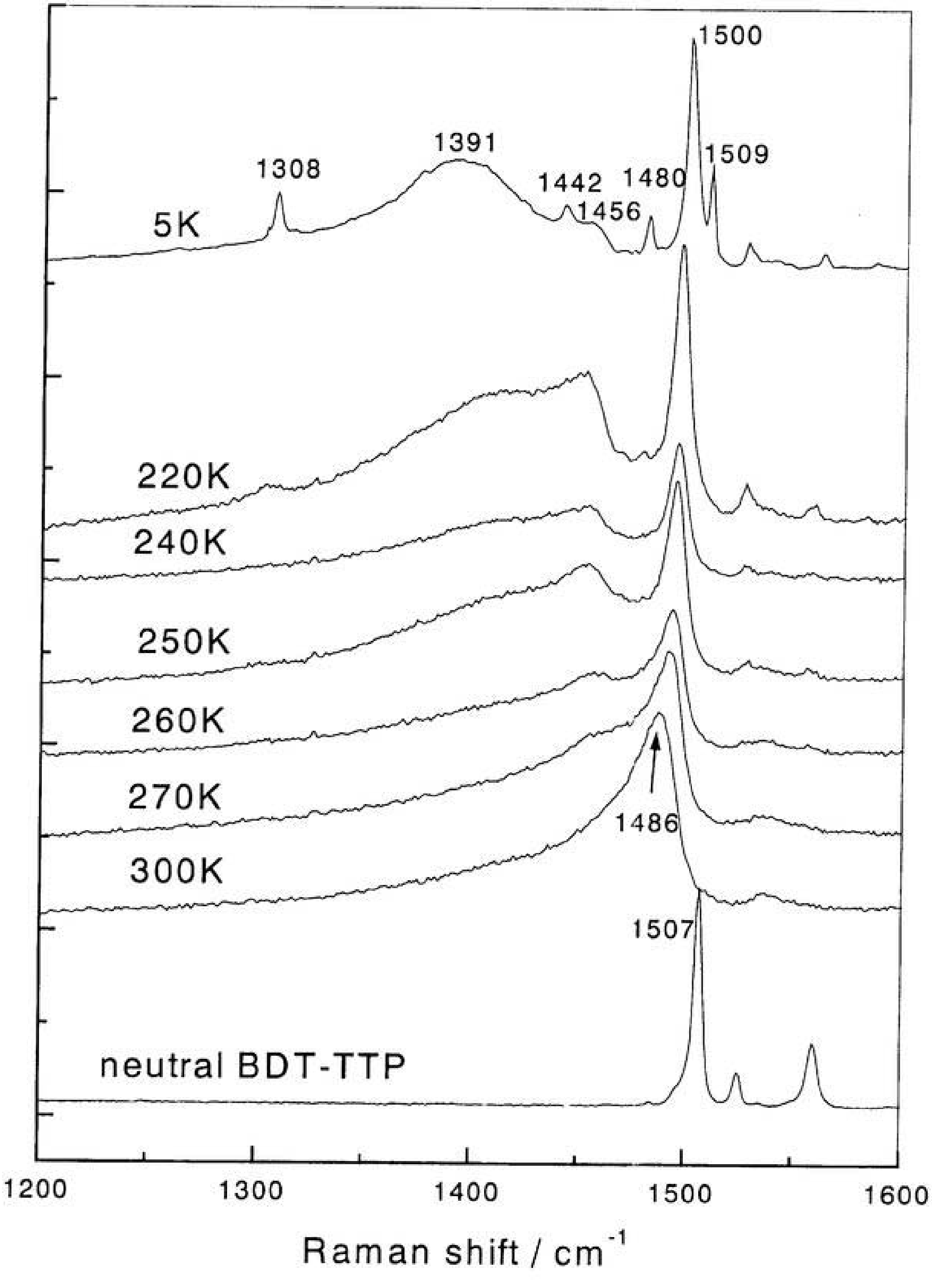

Fig. 14 (a) Raman spectra of θ-(BDT-TTP)$_2$Cu(NCS)$_2$ at various temperatures. Raman spectrum of neutral BDT-TTP at room temperature is also presented.

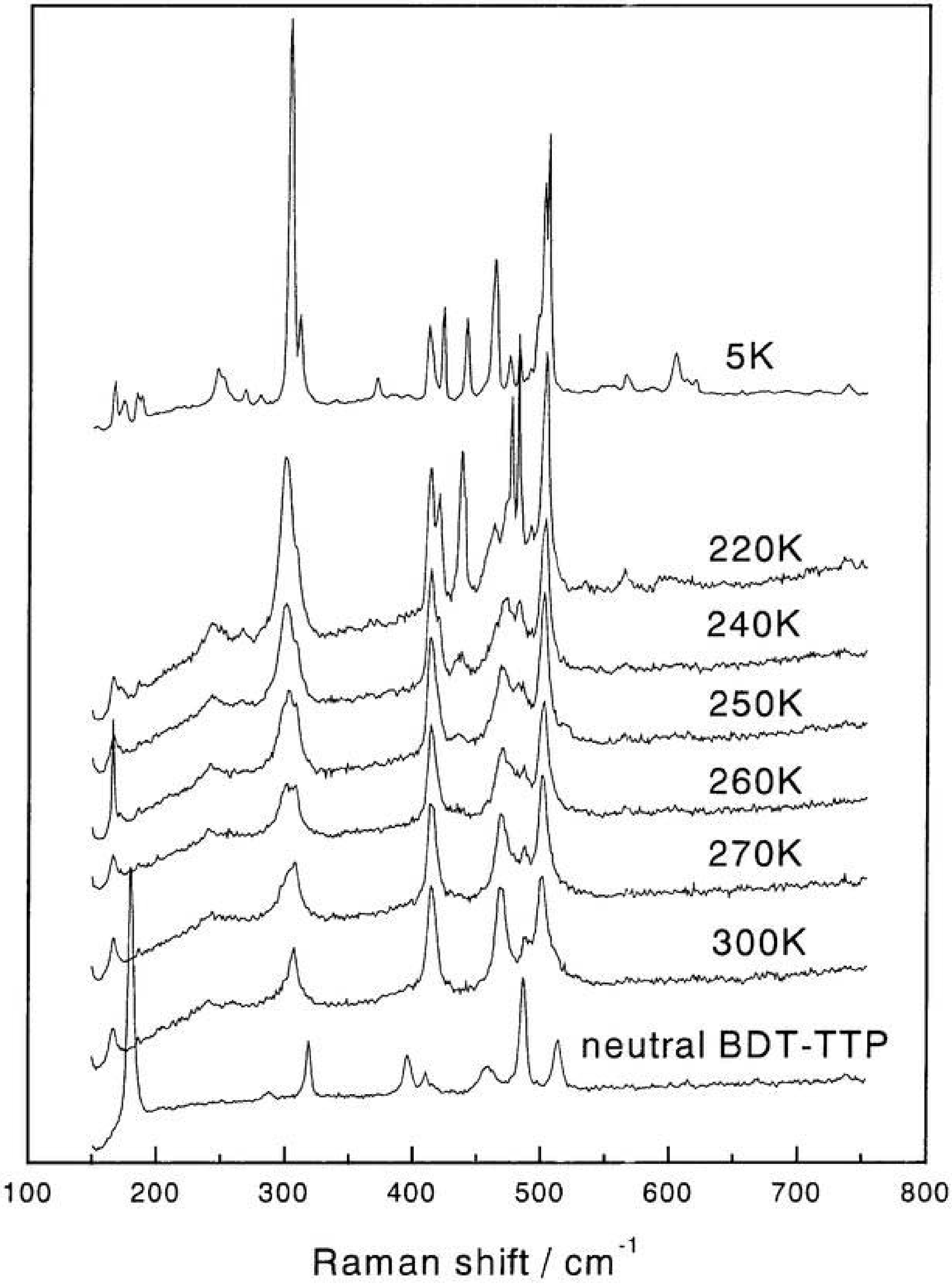

Fig. 14 (b) Raman spectra of θ-(BDT-TTP)$_2$Cu(NCS)$_2$ at various temperatures. Raman spectrum of neutral BDT-TTP at room temperature is also presented.

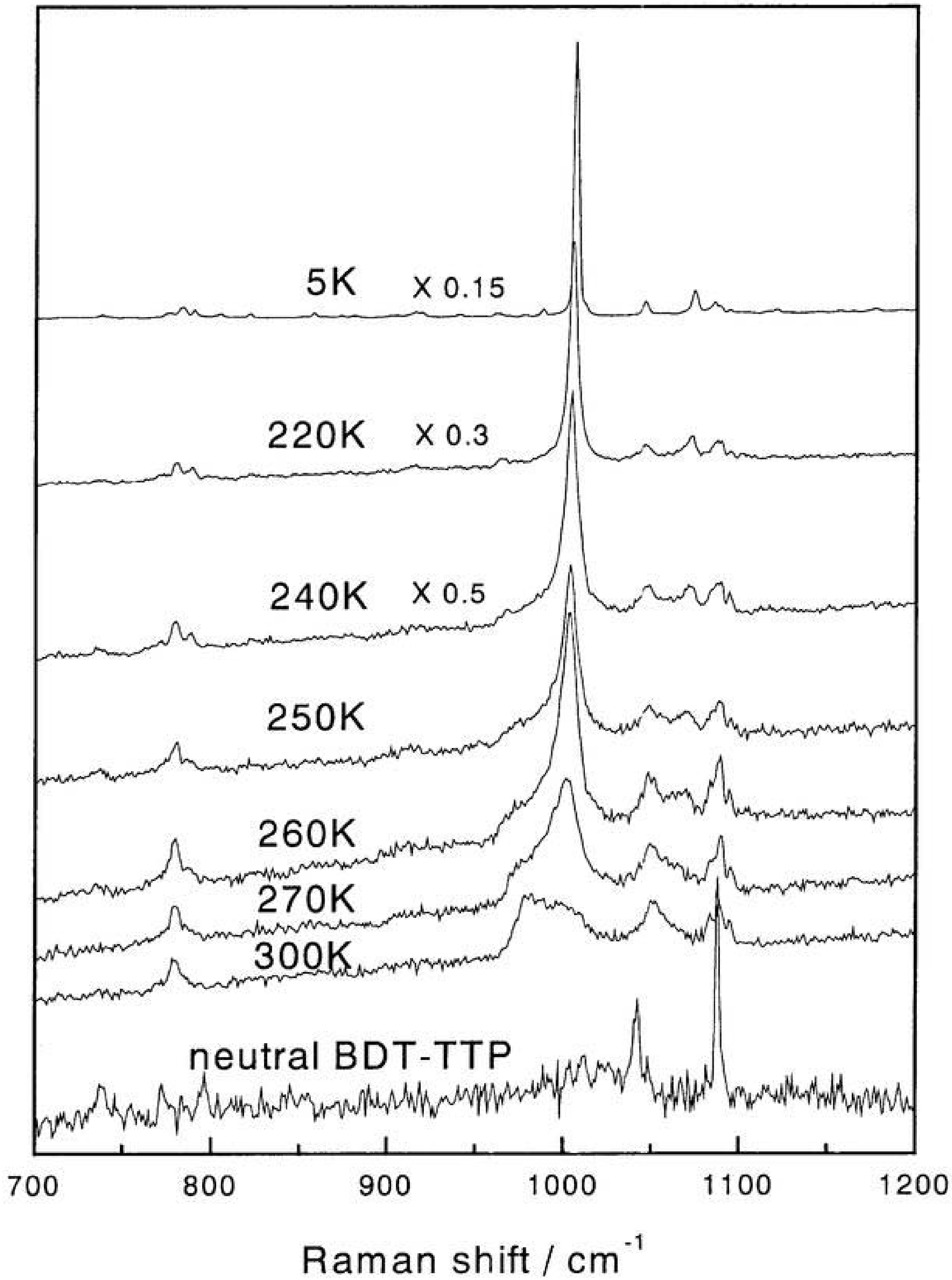

Fig. 14 (c) Raman spectra of θ-(BDT-TTP)$_2$Cu(NCS)$_2$ at various temperatures. Raman spectrum of neutral BDT-TTP at room temperature is also presented.

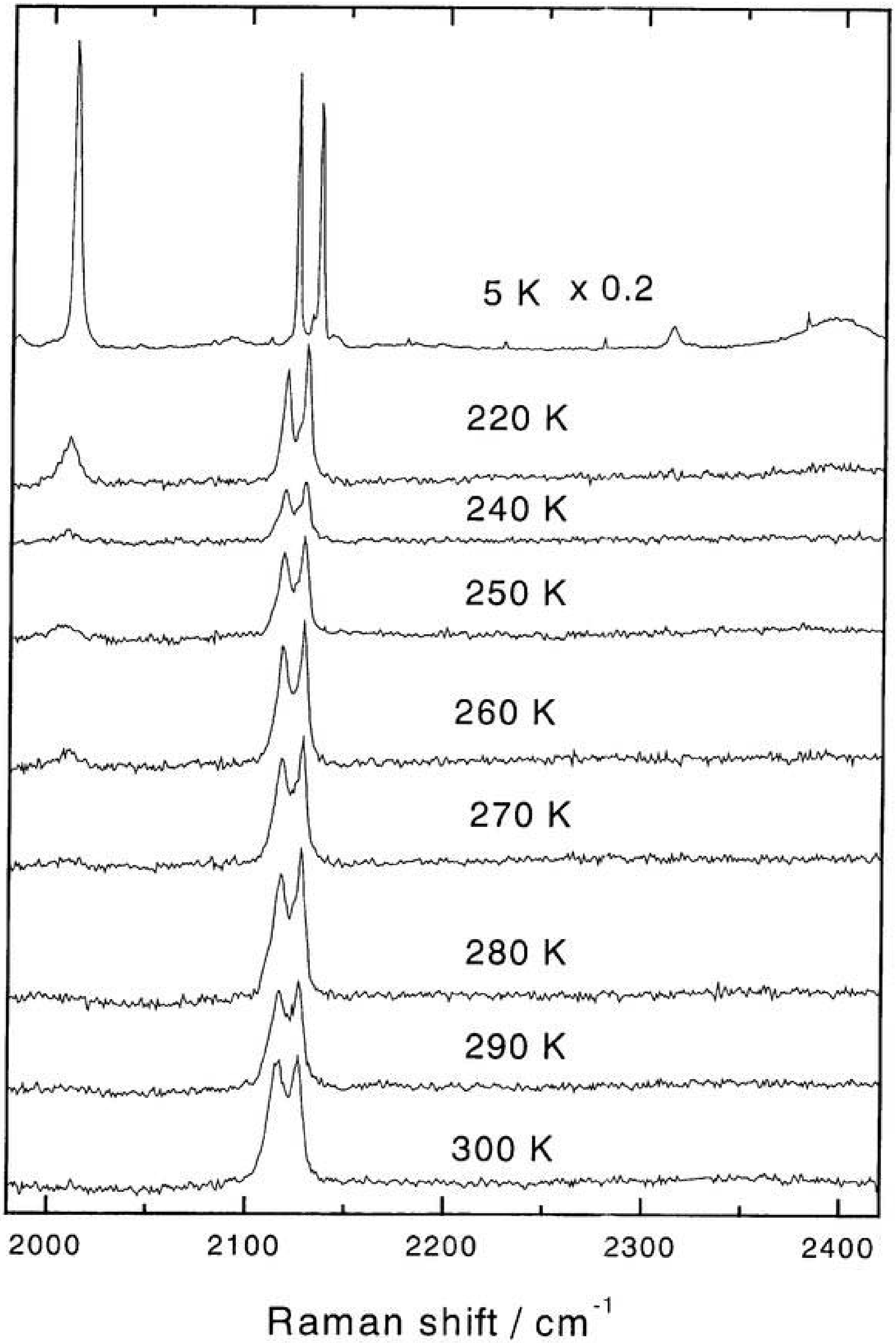

Fig. 14 (d) Raman spectra of θ-(BDT-TTP)$_2$Cu(NCS)$_2$ at various temperatures.

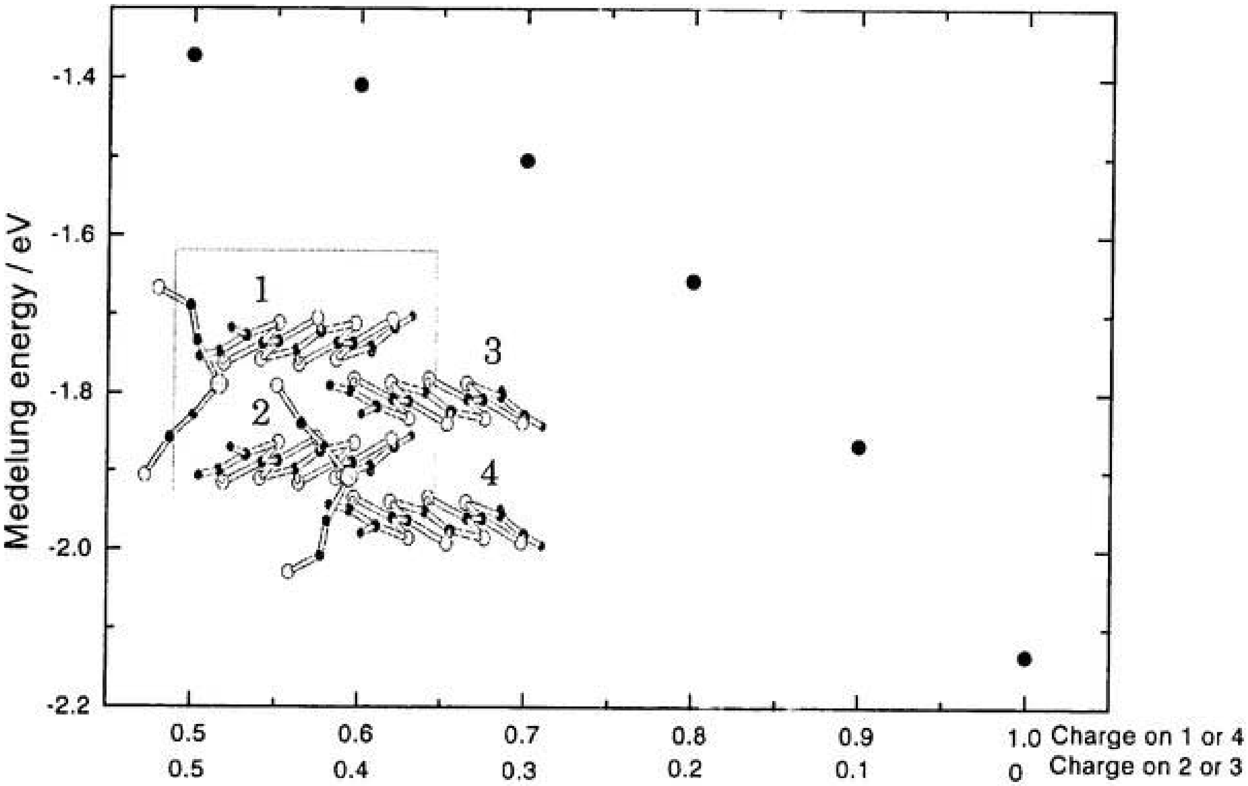

Fig. 15 Madelung energy of θ-(BDT-TTP)$_2$Cu(NCS)$_2$ with different charge disproportion.

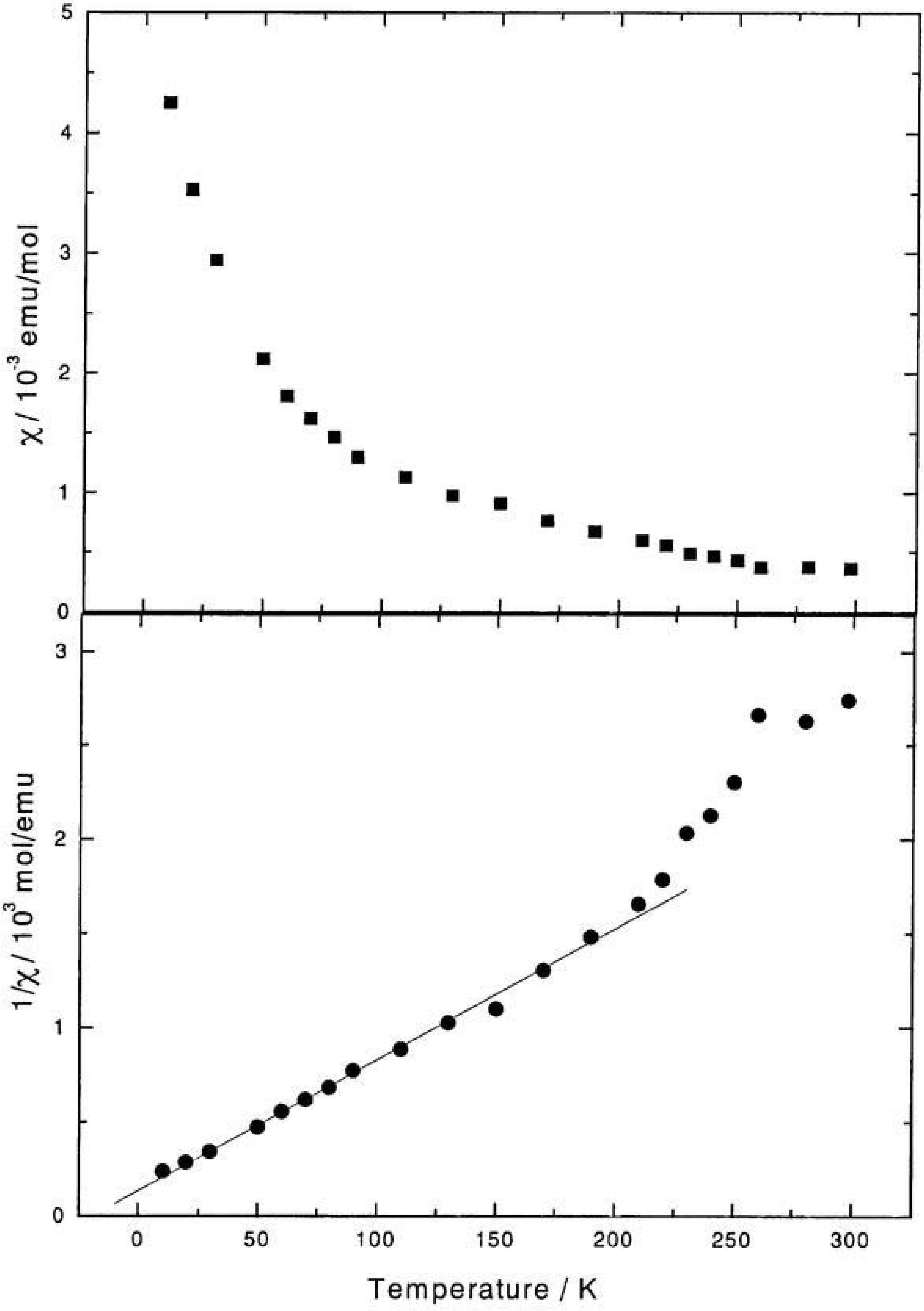

Fig. 16 Temperature dependence of the susceptibility of θ-(BDT-TTP)$_2$Cu(NCS)$_2$ obtained by ESR experiments. The Solid line is the Curie-Weiss model fitting.

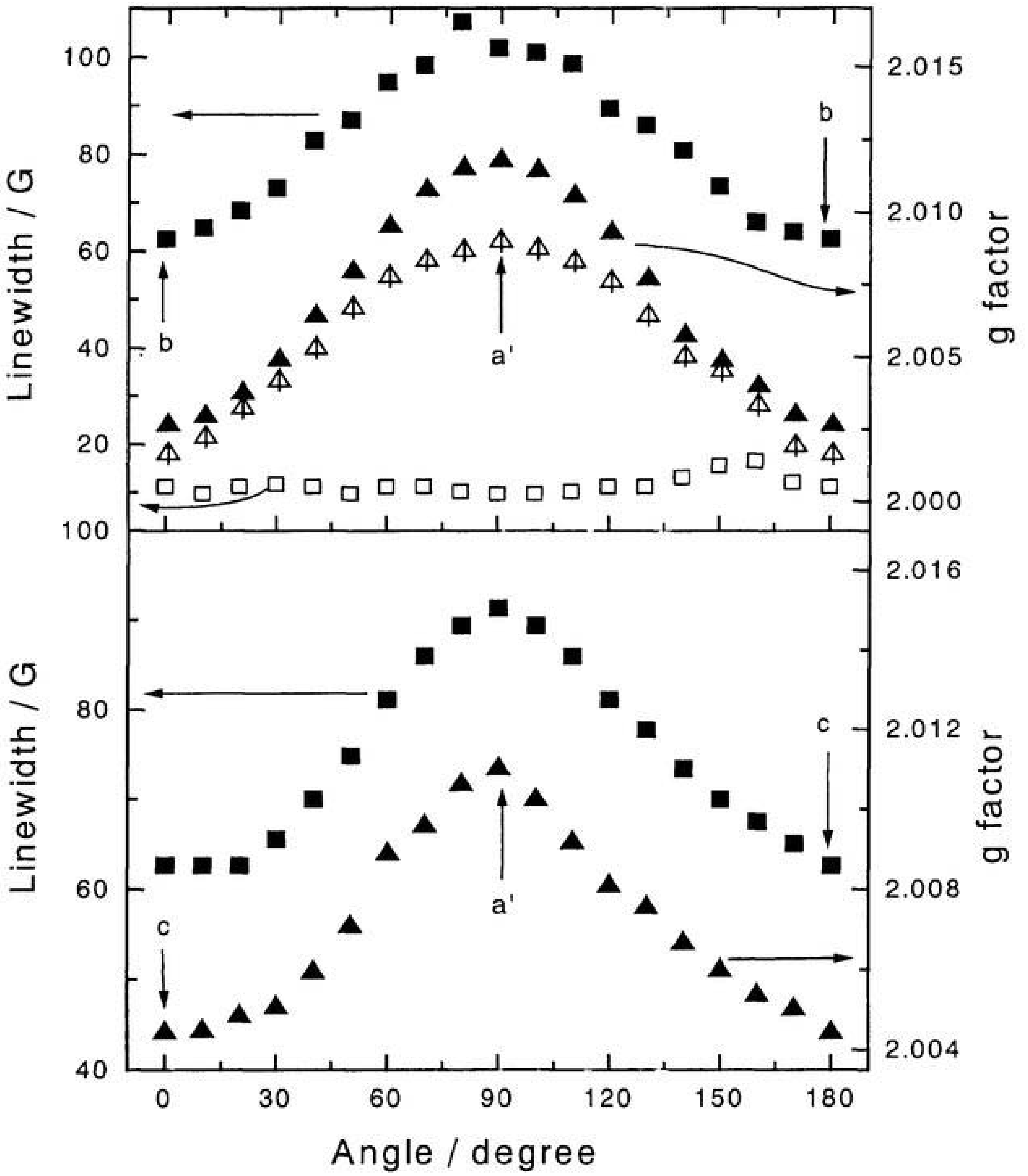

Fig. 17 Angular dependence of the linewidth and the *g*-factor of θ-(BDT-TTP)$_2$Cu(NCS)$_2$. The upper panel is the results by rotating the *c*-axis of the single crystal in the magnetic field at room temperature (solid style) and at 3K (open style), and the bottom is the results by rotating *b*-axis. The squares correspond to the linewidth and the triangles the *g*-factor. *a'* is the direction perpendicular to the *bc* plane.

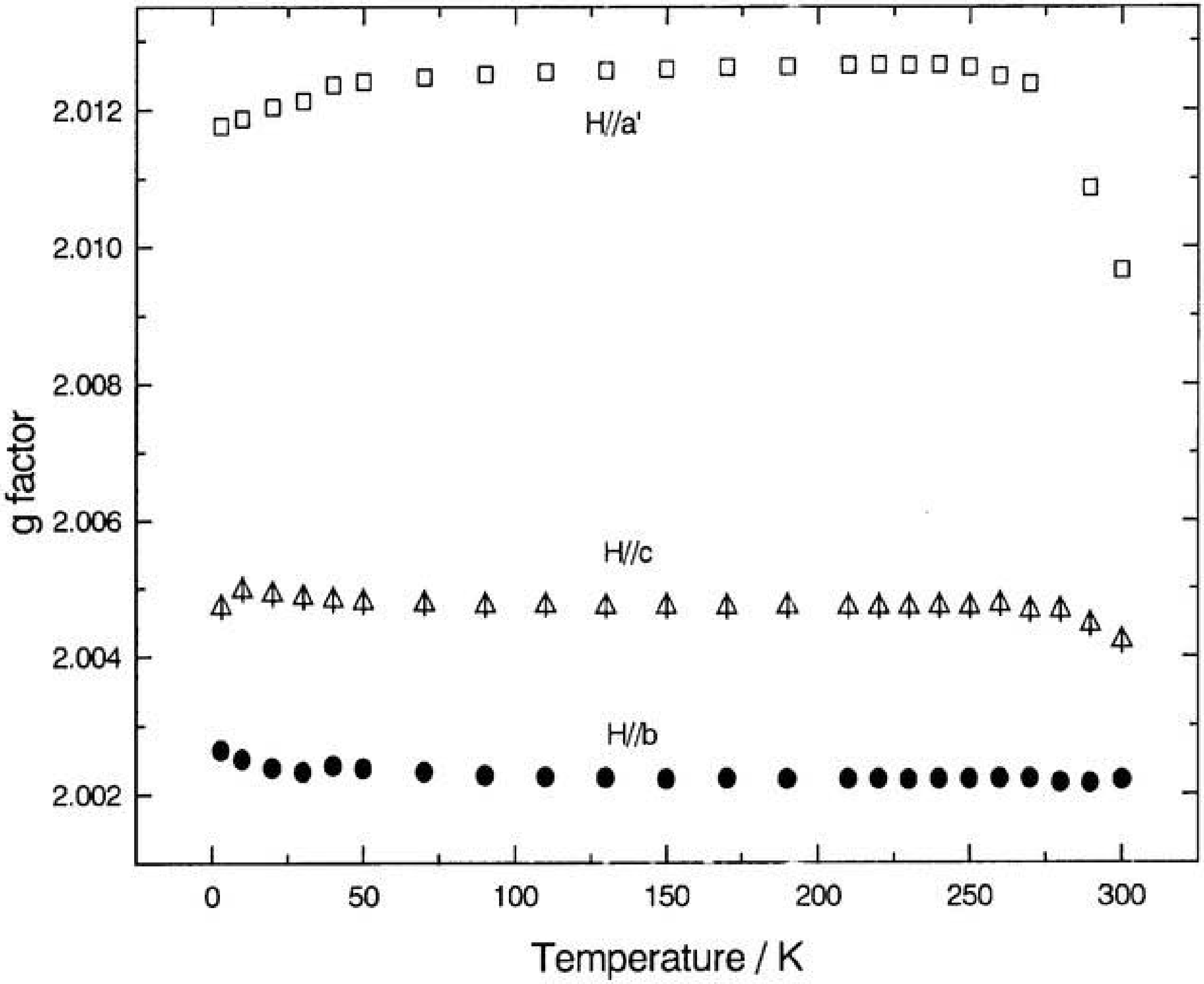

Fig. 18 Temperature dependence of the *g*-factor of θ-$(BDT\text{-}TTP)_2Cu(NCS)_2$.

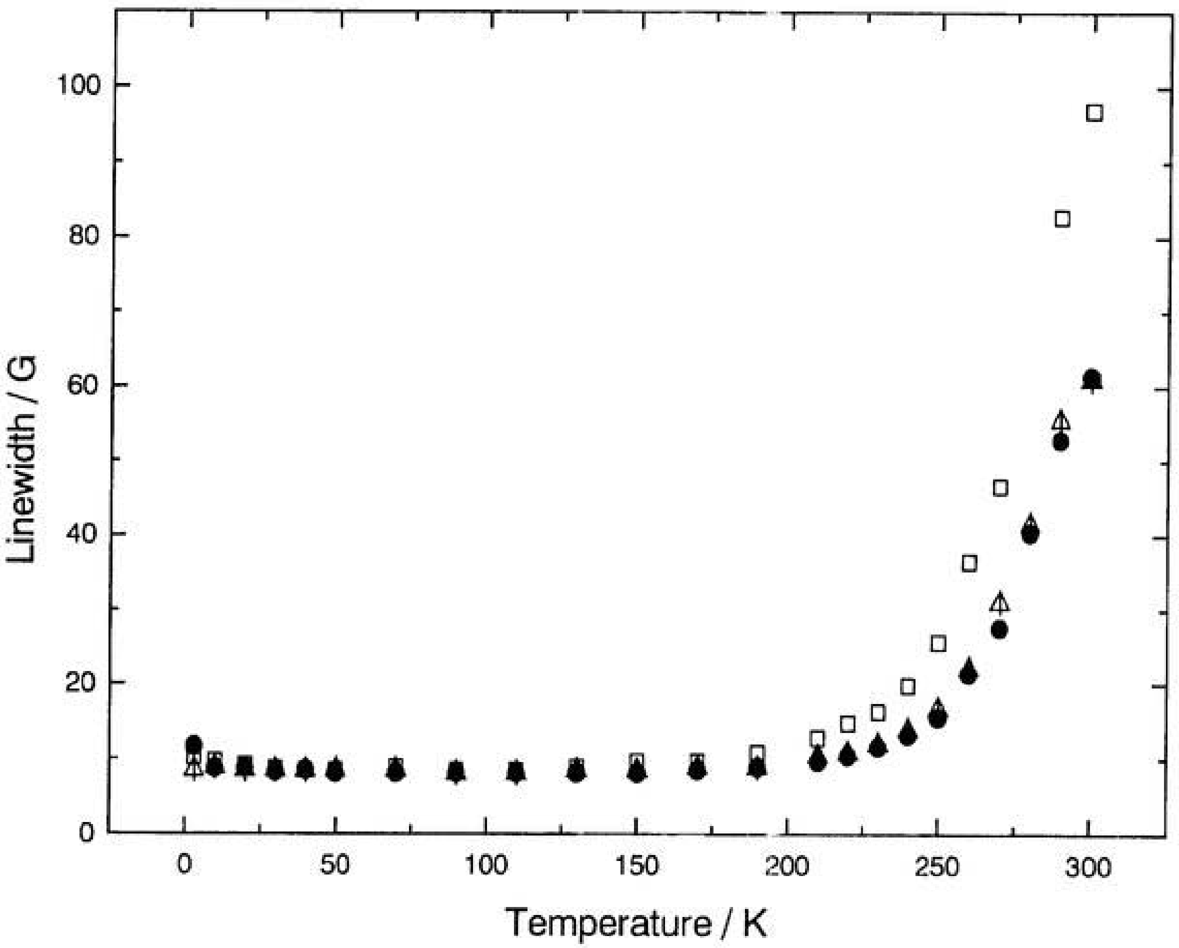

Fig. 19 Temperature dependence of the linewidth of θ-(BDT-TTP)$_2$Cu(NCS)$_2$. The open squares correspond to *H*//*a*', the open triangles to *H*//*c*, and the solid circles to *H*//*b*.

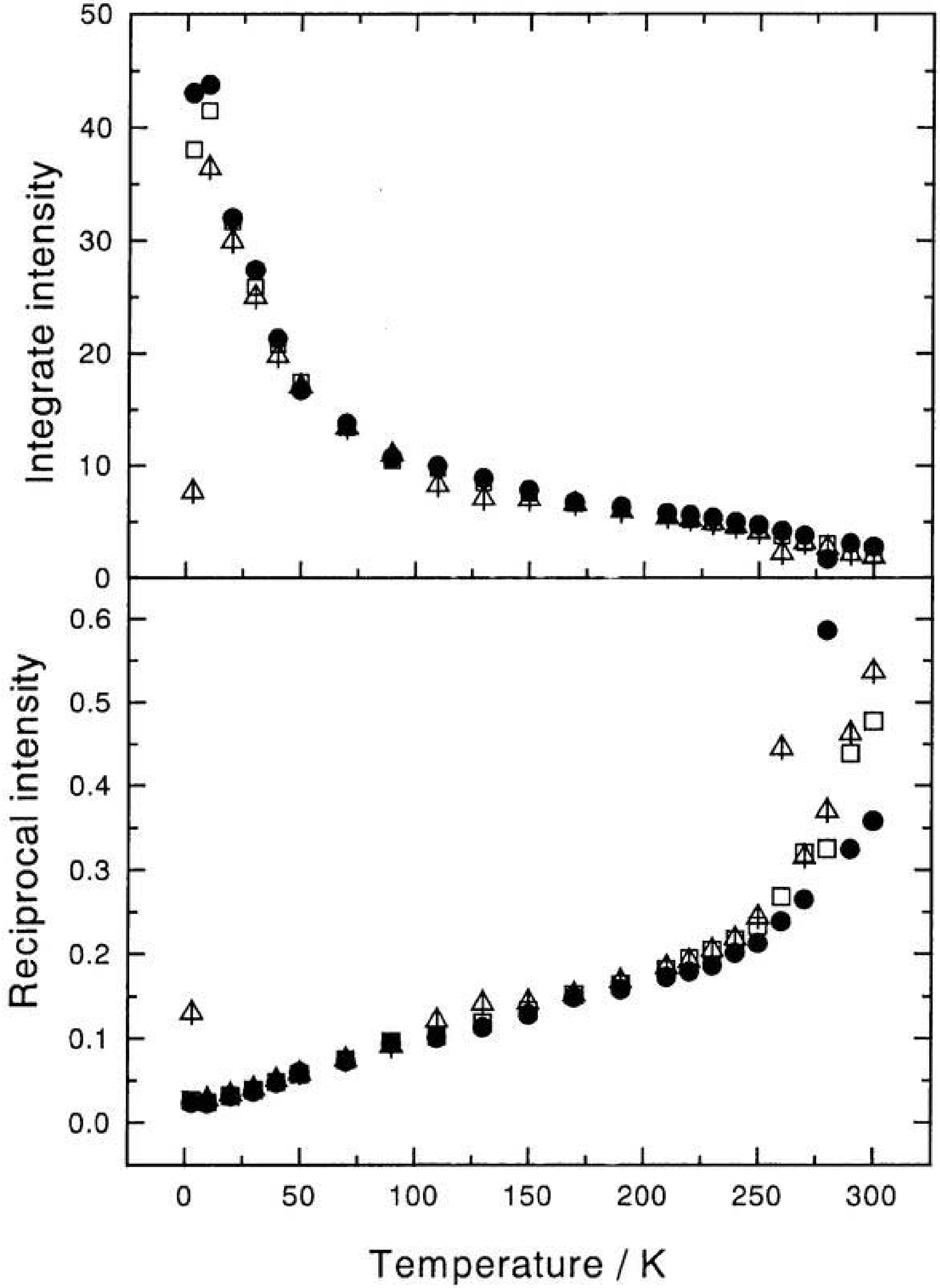

Fig. 20 Temperature dependence of the ESR intensity of θ-(BDT-TTP)$_2$Cu(NCS)$_2$ The open squares correspond to *H*//*a'*, the open triangles to *H*//*c*, and the solid circles to *H*//*b*.

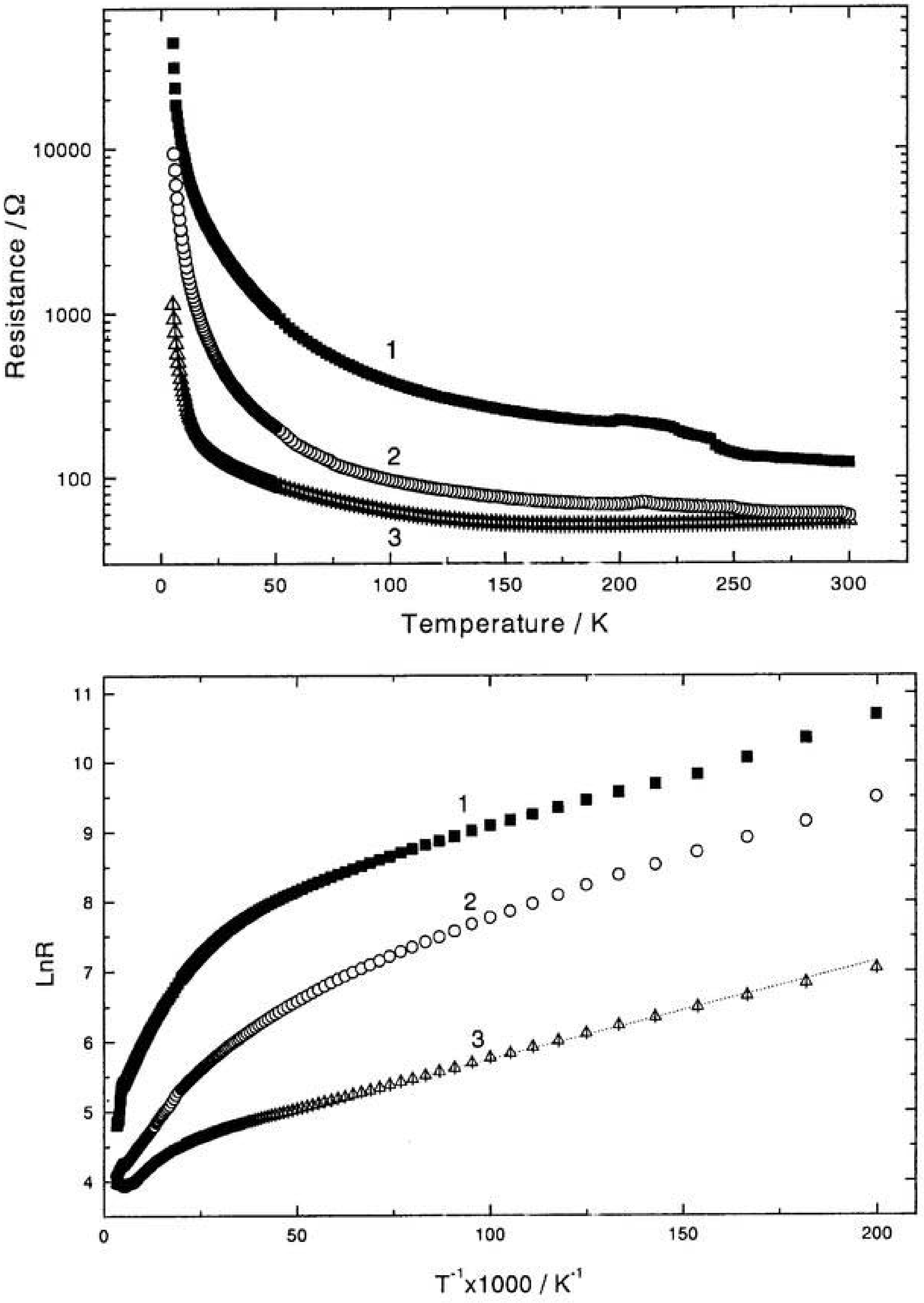

Fig. 21 Temperature dependence of the resistance of θ'-(BDT-TTP)$_2$Cu(NCS)$_2$.

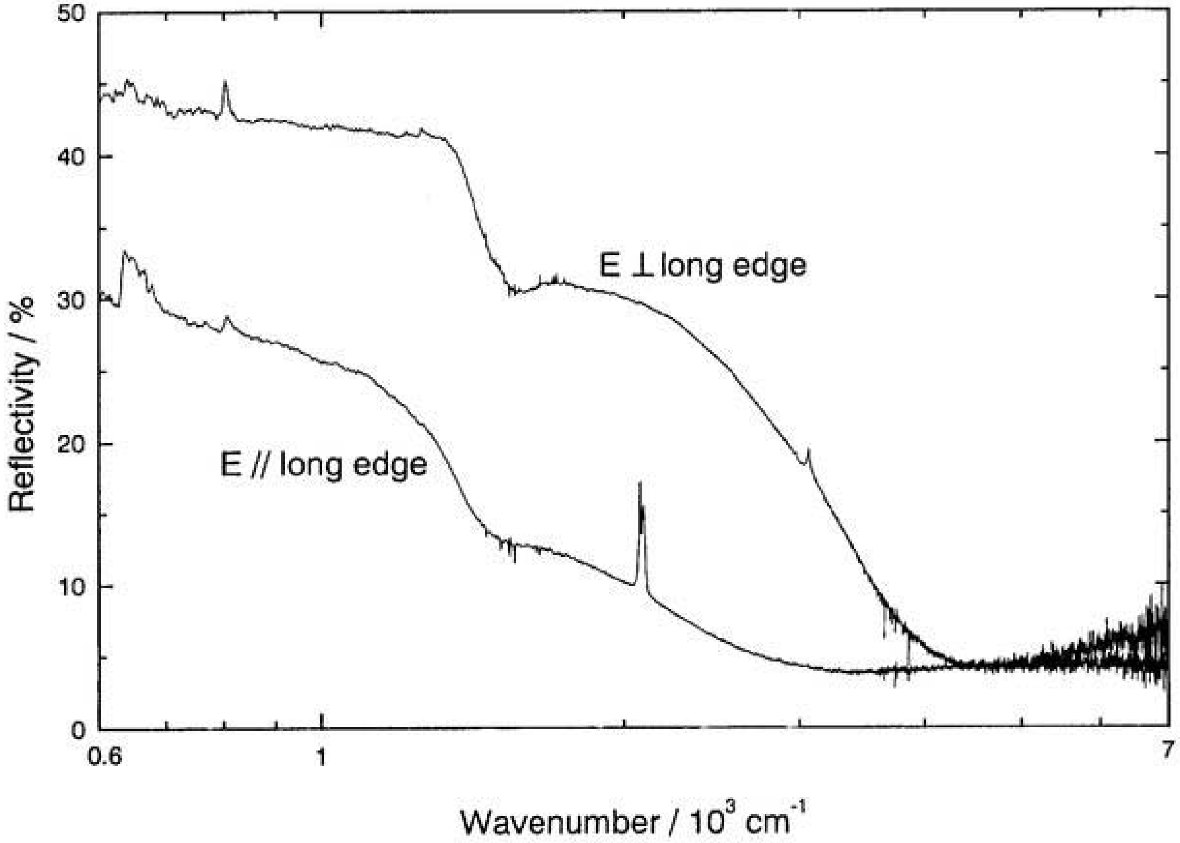

Fig. 22 Polarized reflection spectra of θ'-$(BDT\text{-}TTP)_2Cu(NCS)_2$ at room temperature.

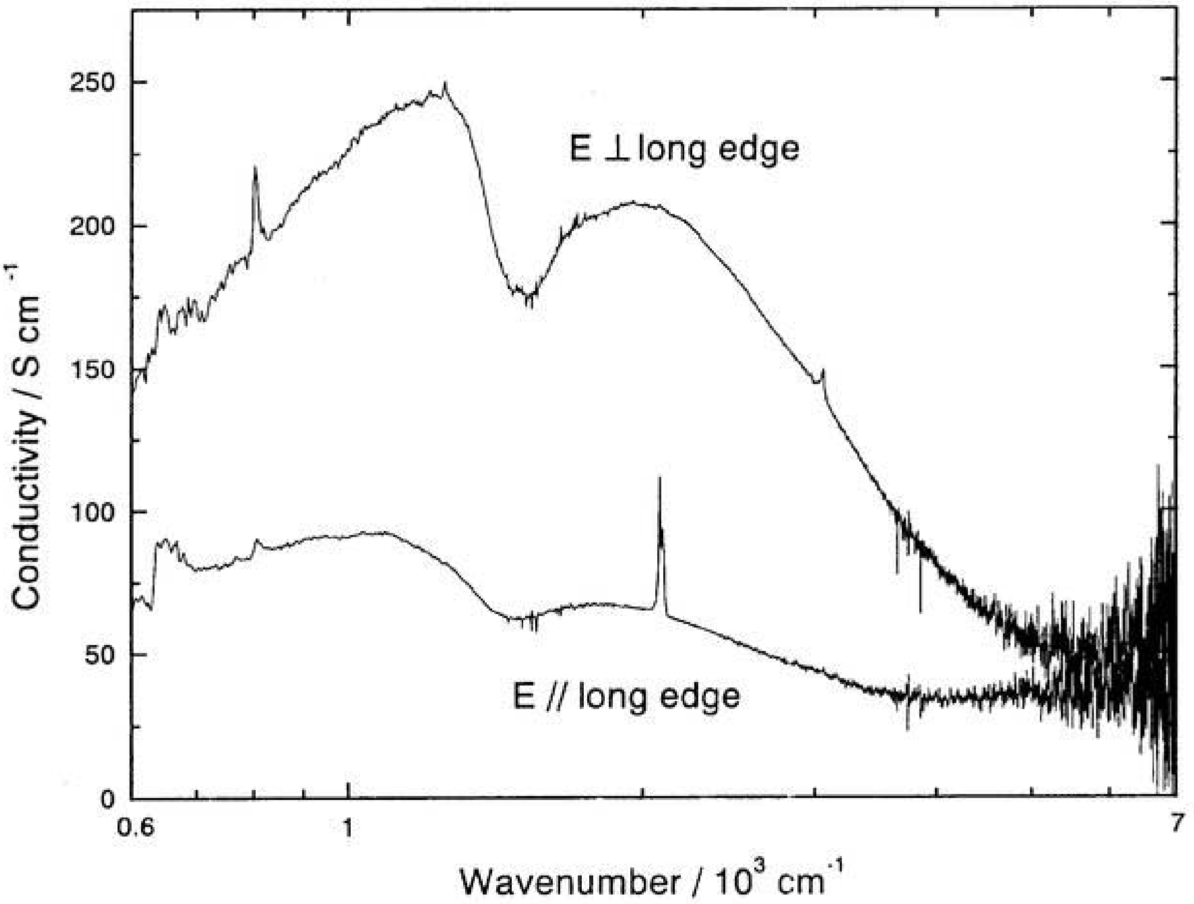

Fig. 23 Conductivity spectra of θ'-(BDT-TTP)$_2$Cu(NCS)$_2$ at room temperature

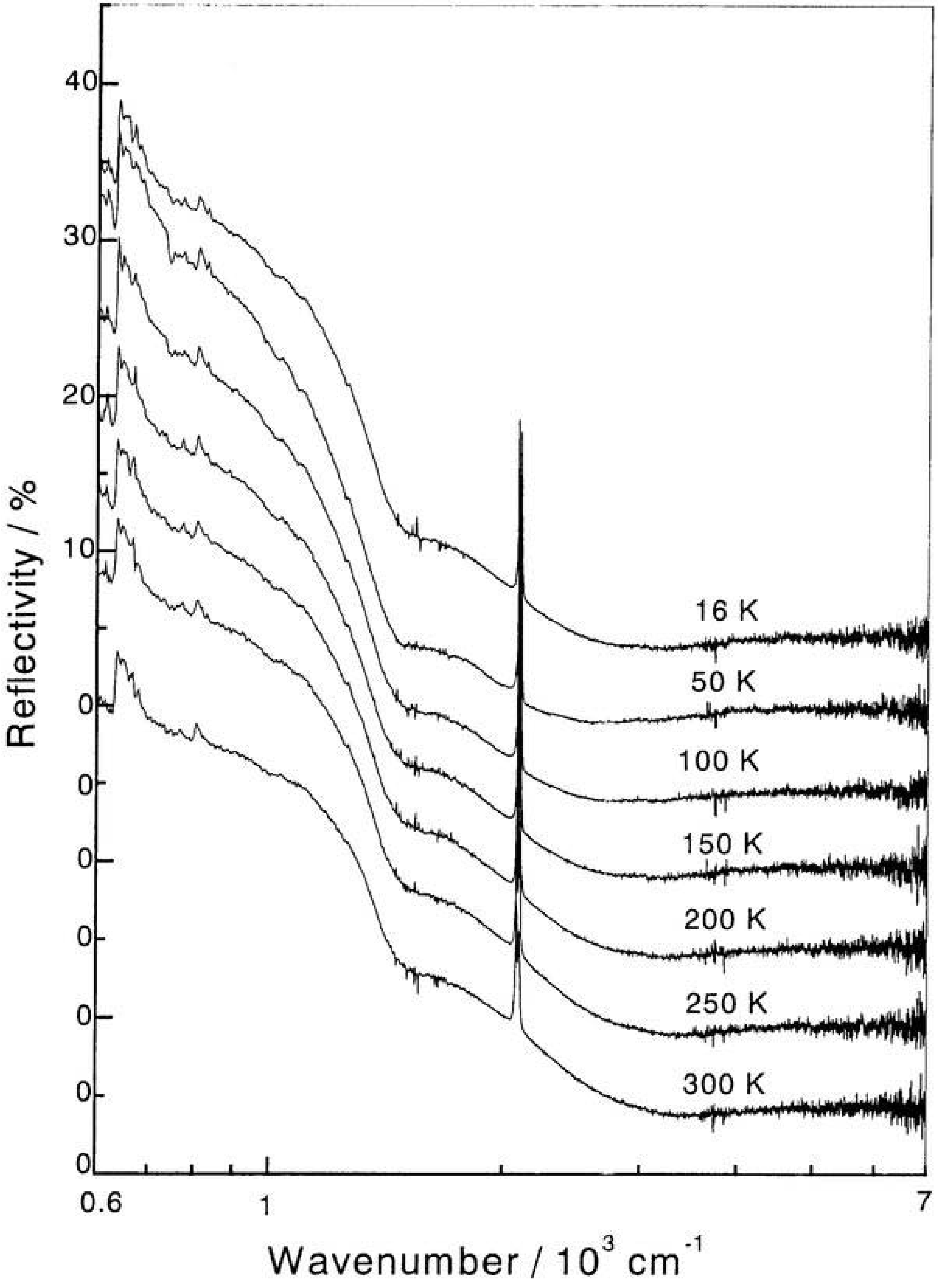

Fig.24 *E* // long edge reflection spectra of θ'-$(BDT\text{-}TTP)_2Cu(NCS)_2$ at various temperatures.

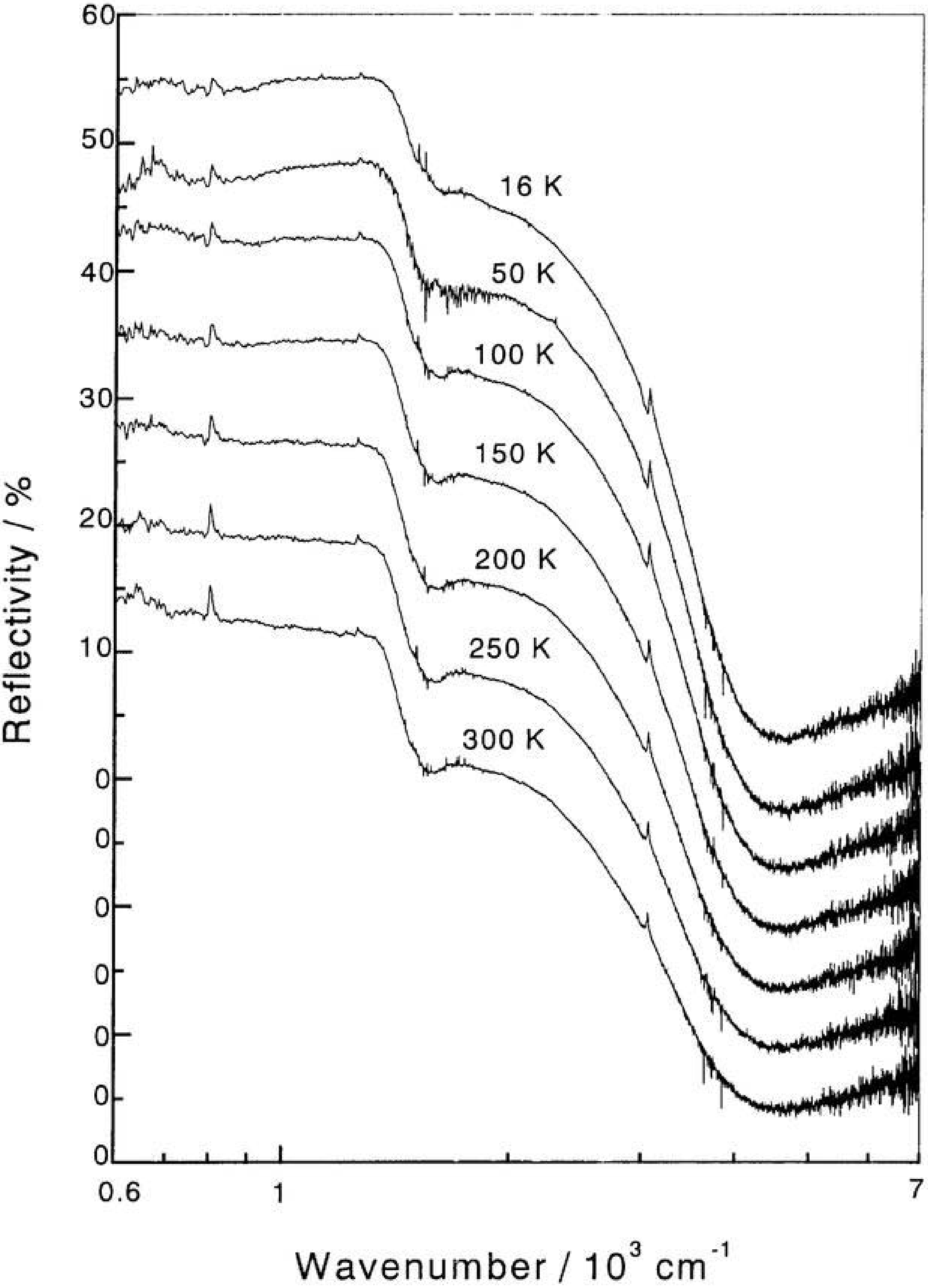

Fig.25 *E* ⊥ long edge reflection spectra of θ'-(BDT-TTP)$_2$Cu(NCS)$_2$.

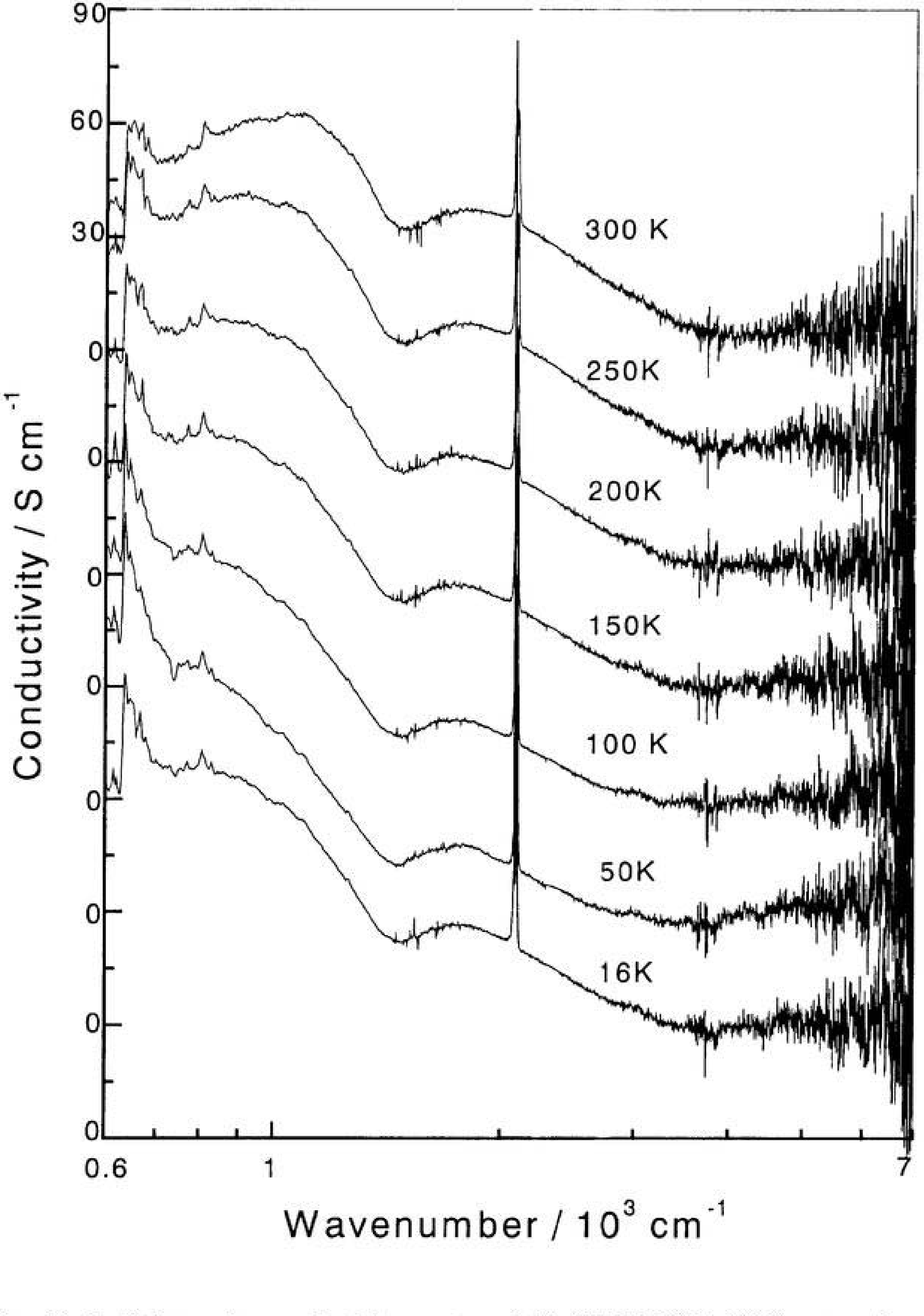

Fig. 26 *E* // long edge conductivity spectra of θ'-(BDT-TTP)$_2$Cu(NCS)$_2$ at various temperatures.

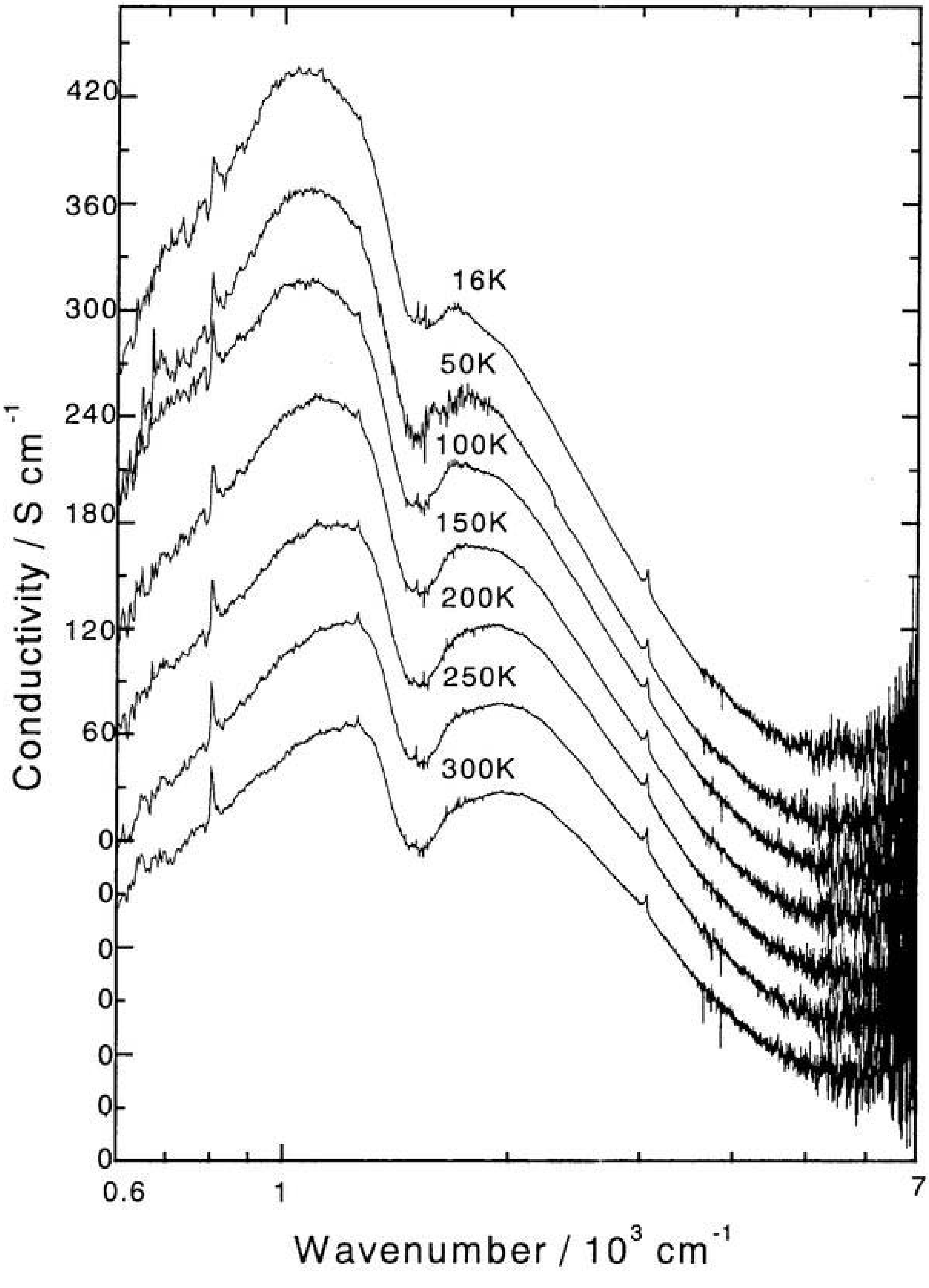

Fig. 27 $E \perp$ long edge conductivity spectra of θ'-(BDT-TTP)$_2$Cu(NCS)$_2$ at various temperatures.

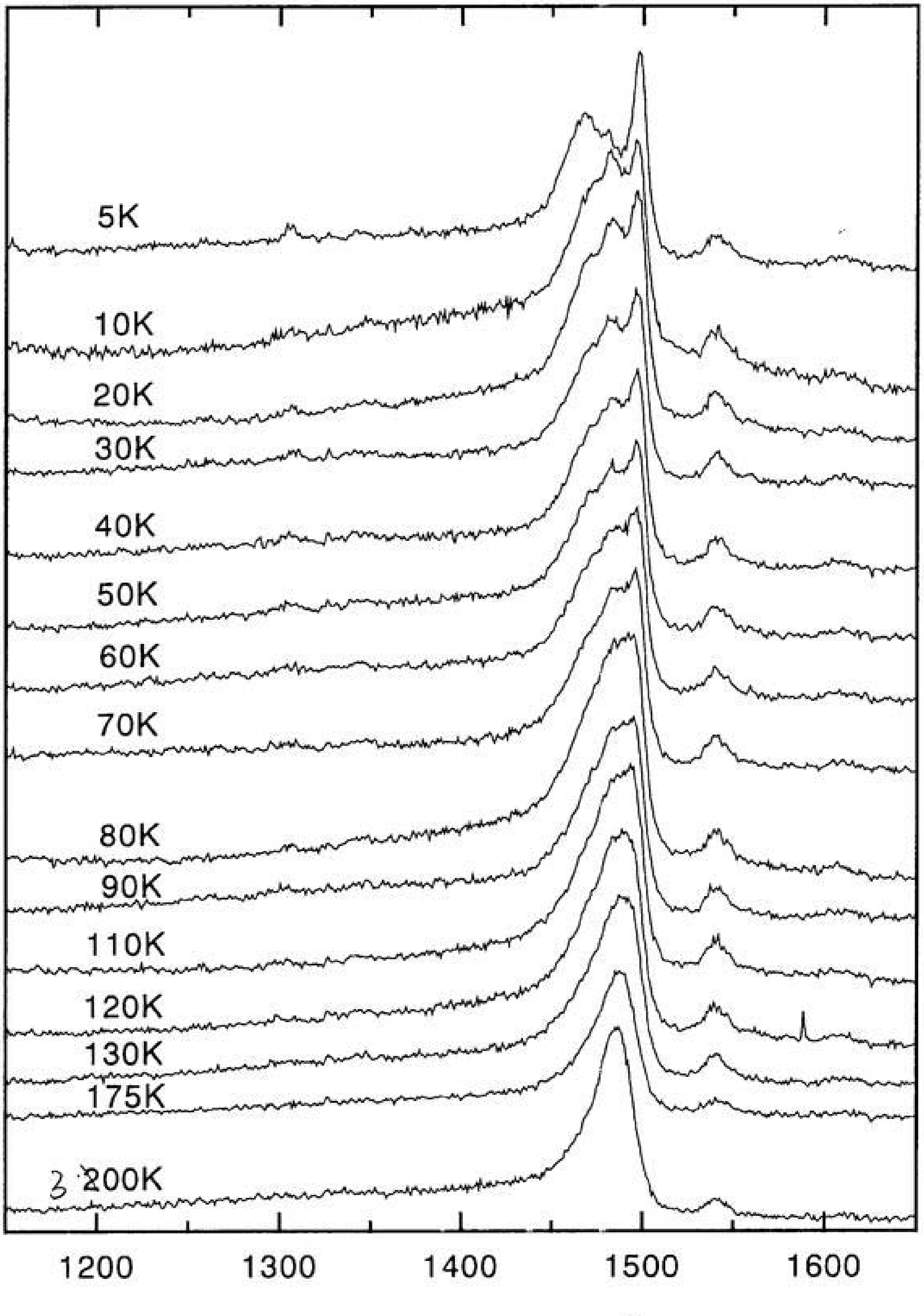

Fig. 28 (a) Raman spectra of θ'-(BDT-TTP)$_2$Cu(NCS)$_2$ at various temperatures.

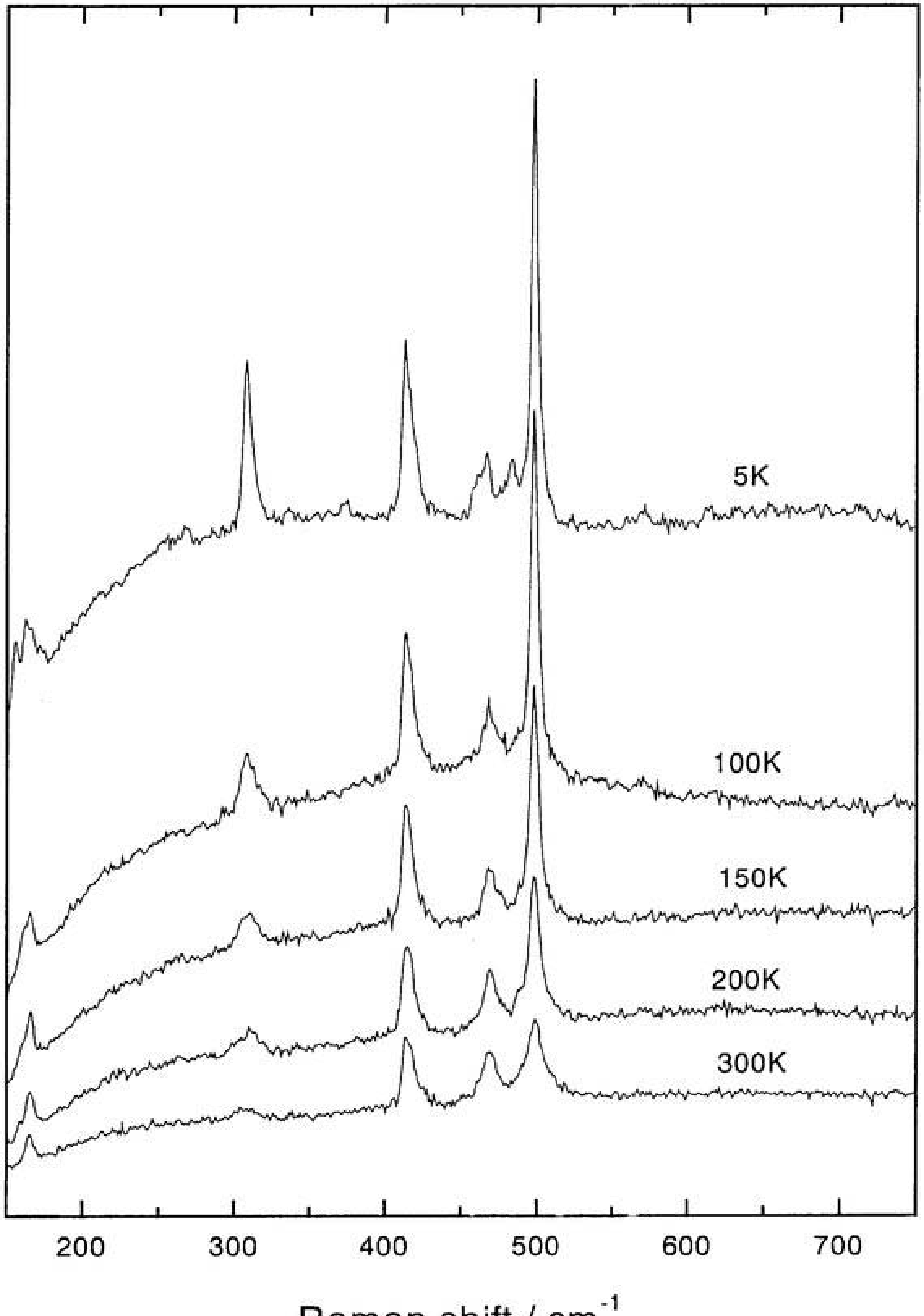

Fig. 28 (b) Raman spectra of θ'-(BDT-TTP)$_2$Cu(NCS)$_2$ at various temperatures.

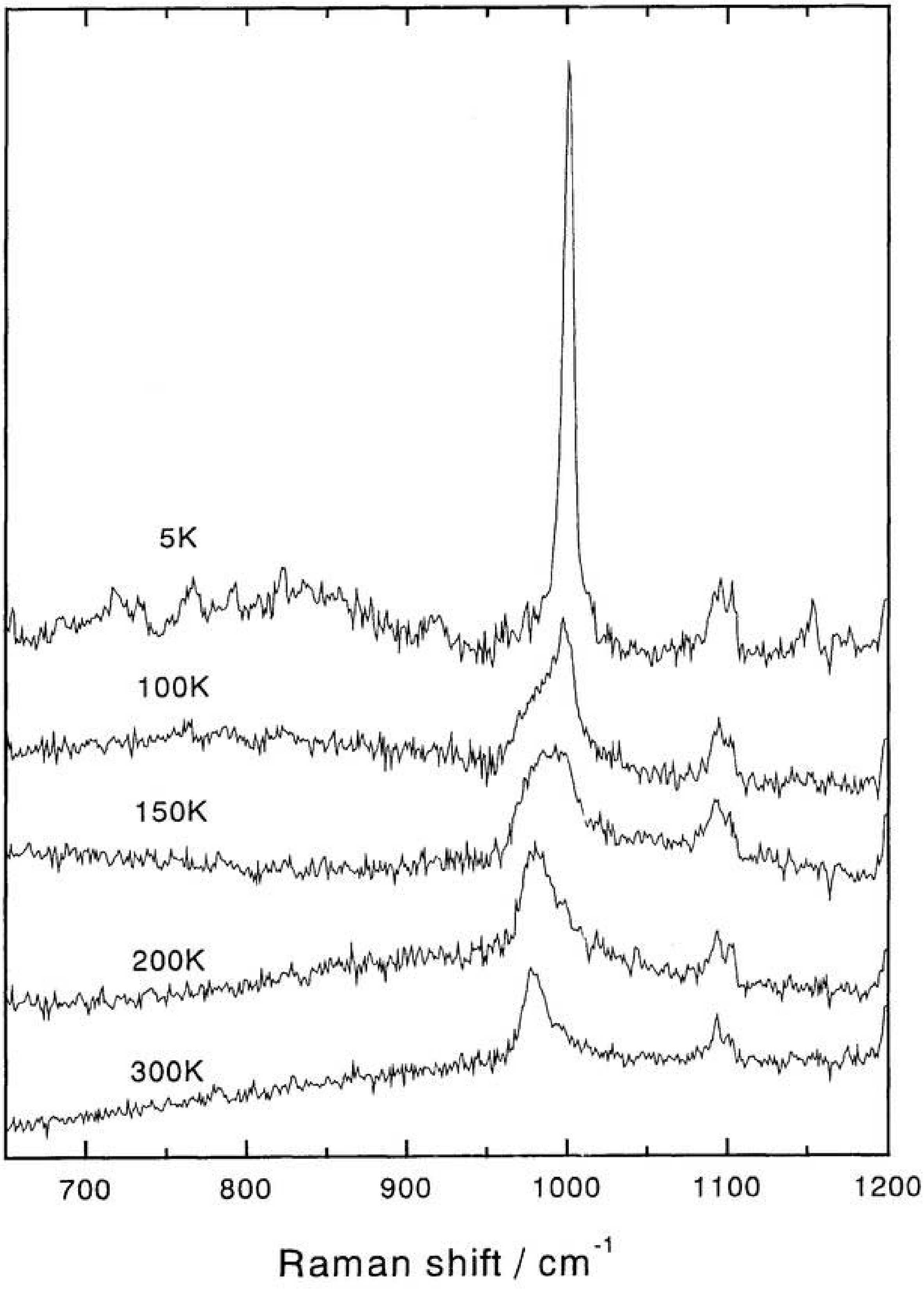

Fig. 28 (c) Raman spectra of θ'-(BDT-TTP)$_2$Cu(NCS)$_2$ at various temperatures.

Chapter 6

Spectroscopic Study of Isostructural Charge-Transfer Salts: Non-metallic DMTTA-BF$_4$ and Metallic DMTSA-BF$_4$

Jianyong Ouyang, Jian Dong, Kyuya Yakushi, Kazuo Takimiya, and Tetsuo Otsubo

Spectroscopic study of the isostructural charge-transfer salts: non-metallic DMTTA-BF$_4$ and metallic DMTSA-BF$_4$

J. Phys. Soc. Jpn., in press

K. Yakushi, J. Dong, J. Ouyang, K. Takimiya, T. Ostubo, and H. Tajima

Metallic properties of 1:1 charge-transfer salt DMTSA-BF$_4$

Synth. Met., 103 (1999) 2208

6.1. Introduction

DMTSA (2,3-dimethyltetraseleno-anthracene) and DMTTA (2,3-dimethyltetrathio-anthracene) are unique organic compounds which make highly conductive 1:1 charge-transfer salts. Takimiya *et al.* reported several highly conductive 1:1 charge-transfer (CT) salts of DMTSA and DMTTA, among which DMTSA-BF_4 and DMTSA-NO_3 showed metal-like temperature dependence of the electrical conductivity in a high-temperature region.$^{1)}$ Later on Kawabata *et al.* reported the metallic properties of DMTSA-BF_4.$^{1)}$ Because of the chemical ratio between DMTTA (and DMTSA) and counter anions, the valence of DMTTA (and DMTSA) was 1+, implying the full oxidation. Thus these CT salts had a half-filled band. Such a system was expected to become a Mott insulator due to the on-site Coulomb energy, which was crucial when the system was one-dimensional. The authors reported the resistivity and thermopower of DMTSA-BF_4, and showed the metallic behavior down to 150K.$^{2)}$ We demonstrated from the temperature-dependent reflection spectrum that the screw-axis symmetry was broken below 150K since a_l vibronic modes of DMTSA were strongly enhanced below this temperature. The paramagnetic susceptibility of DMTSA-BF_4 began to decrease around 150K.$^{3)}$ All these results suggested that DMTSA-BF_4 underwent a Peierls transition around 150K. On the other hand, the isostructural DMTTA-BF_4 has not been studied except the resistivity (1 Ωcm) at room temperature. DMTTA is a sulfur analogue of DMTSA and they resemble the relation between TMTTF and TMTSF in Bechgaard salts. Comparison of non-metallic DMTTA-BF_4 with DMTSA-BF_4 may give an insight for understanding the origin of the metallic properties of DMTSA-BF_4. In this paper we report the temperature dependent properties of resistivity, thermopower, reflection spectrum, and ESR of DMTTA-BF_4 in comparison with DMTSA-BF_4.

6.2. Experimental

The single crystals of DMTTA-BF_4 and DMTSA-ClO_4 were prepared by electrochemical method using 50ml H-tube divided into two compartments by glass filter. The concentration of DMTTA and DMTSA in 1,1,2-trichloroethane was 6×10^{-4} mol/ℓ, and the concentration of $(n\text{-Bu})_4N\text{-}BF_4$ and $(n\text{-Bu})_4N\text{-}ClO_4$ is 1×10^{-2} mol/ℓ. As we reported in the preceding paper, we found another crystal modification DMTSA-$(BF_4)_x$ which was characterized by the X-ray oscillation photograph along the needle axis. Recently we determined the preliminary crystal structure of this modification. The structure is very similar to DMTSA-BF_4 and the molecular stack of DMTSA consists of 6 molecules in the repeating unit along the needle axis. Metallic DMTSA-BF_4 has a metallic luster of reddish copper color, while non-metallic DMTSA-$(BF_4)_x$ is not lustrous. The similar modification was found in DMTSA-ClO_4 and DMTTA-BF_4 as well. DMTTA-BF_4 had a clean metallic luster of copper color, while another is not lustrous. In this experiment we carefully selected lustrous DMTTA-BF_4 crystals for all the experiments.

The dc electrical resistivity was measured by means of a four probe method using the Quantum Design PPMS. The electrical contact to 20μm gold wires was made by a silver paint (Du Pont 4922N). The thermopower was measured along the conducting axis by modifying the method of Chaikin and Kwak.[3)] Both the edges of a single crystal were bonded to the 1μm gold foils attached to boron nitride heat sinks in which carbon heaters were embedded. This apparatus was mounted on a sample puck of PPMS. The voltage between the electrodes was measured on a Keithley 2001 multimeter. The software programs for controlling the heater current and for sampling the voltage were combined with the temperature control system of PPMS. ESR measurement was carried out on a Brucker ESP-300E, equipped with a cryostat of Oxford Instrument ESR900 combined with the temperature controller ITC4. The polarized reflection spectrum in the NIR and visible region was measured on an Atago

Multiviewer spectrometer with multi-channel detection system combined with a SPECTRA TECH IR-Plan microscope. The same microscope was combined with FT-IR, Nicolet Magna 750 for the measurement of NIR and IR regions. The details of the experimental apparatus including cryostat system were described elsewhere.4) The sample size for the low-temperature experiment was *ca.* $1 \times 0.2 \times 0.1 \text{mm}^3$ for DMTSA-BF_4, $0.4 \times 0.1 \times 0.04$ mm^3 for DMTSA-ClO_4, and $0.8 \times 0.12 \times 0.05$ mm^3 for DMTTA-BF_4. The crystal faces were determined by oscillation and Weissenberg photographs. Raman scattering spectrum was measured in back-scattering geometry on a Renishaw Ramascope System-1000 excited by a He-Ne laser with a wavelength of 632.8nm. The laser power was decreased by neutral filter down to 0.1mW and was focused on the 5μmϕ area of the single crystal. The incident light is polarized parallel to the [011] axis of DMTSA-ClO_4 and all polarization was collected for the scattered light. The cryostat Oxford CF1104s was installed under the microscope with a long-working distance (20mm) objective lens, Mitsutoyo M Plan Apo 20×. The silicon diode sensor was attached to the sample holder just below the sample crystal fixed by silicone grease.

6.3. Results and Discussion

6.3.1 Band structure of DMTSA-BF_4 and DMTTA-BF_4

As shown in Fig. 1, the crystal of DMTTA-BF_4 belongs to orthorhombic system with the space group of *Cmcm*, which is isostructural to DMTSA-$BF_4$1) Due to the requirement of the space group symmetry, DMTTA and DMTSA are stacked along the screw axis parallel to the *c*-axis. Since the adjacent molecules along the *c*-axis are connected with a screw axis and glide plane symmetry, the overlap modes in both sides are equivalent to each other in both crystals. If we neglect the inter-stack interaction, this crystal symmetry forms a one-dimensional half-filled band, when we take *c/2* as a repeating unit. Figure 2 (top panel) shows the polarized reflectance spectrum of DMTTA-BF_4 measured on the (100) crystal face, which should be compared with the spectrum of DMTSA-BF_4 measured on the (110) face (see the bottom of Fig. 2). The *E//c* spectra show large dispersions in the infrared region both in DMTTA-BF_4 and DMTSA-BF_4, which are almost completely polarized along the *c*-axis. The low-wavenumber region of the *E//b* spectrum of DMTTA-BF4 is almost flat, whereas the reflectance of *E//[110]* spectrum of DMTSA-BF_4 is gradually increasing toward ω=0. This feature suggests that DMTTA-BF_4 is more one-dimensional than DMTSA-BF_4. The dispersion of the reflectance in the *E//c* spectrum in both compounds is associated with the inter-molecular charge-transfer excitation. The most different point between them is the significantly lower reflectance of DMTTA-BF_4 compared to DMTSA-BF_4. This difference becomes more remarkable in the optical conductivity spectrum obtained by Kramers-Kronig transformation as shown in Fig. 3. In the *E//c* conductivity spectra of DMTTA-BF_4 and DMTSA-BF_4 a single electronic transition shows up in a wide spectral range of 600-20,000 cm^{-1}. From this spectral feature, we consider that only a HOMO band contributes to the Fermi level of the conduction band. If the Fermi level consists of more than two bands, the *E//c* spectrum in this range will have several peaks like $M(dmit)_2$ salts$^{5)}$ or broad like $(DMe\text{-}DCNQI)_2Cu$.$^{6,7)}$ As discussed in the preceding article$^{8)}$, the low-energy absorption bands in the *E⊥c* spectra indicated by arrows are ascribable to the optical transition from the bottom to top of the folded conduction band. The excitation energy thus corresponds to the bandwidth. The lower excitation energy of DMTTA-BF_4 means the narrower bandwidth than that of DMTSA-BF_4. The detailed analysis will be given in the next paragraph. The high-energy interband transitions of both compounds are similar to each other. All these electronic transitions in Fig. 3 are listed in Table I.

The lineshape of the optical conductivity of room-temperature and 10K are shown in Fig. 4 along with the Drude-Lorentz model fitted to the reflectance in the high-frequency region (3×10^3-30×10^3 cm^{-1}). As shown in Fig. 4, $\sigma(\omega)$ is not Drude-like, although it is metallic above 150K. Due to the limited spectral range, it is difficult to discuss the whole spectral feature of this band, but the Drude term is likely to be overlapped in the mid-infrared absorption band. At low temperature, this absorption band is remarkably enhanced with a rich phonon structure. The Drude term will vanish, because the system changes into an insulator at low temperature. So the spectral weight shifts to the mid-infrared region at low temperature. In addition the increase of the transfer integral due to the lattice contraction contributes to the enhancement of this mid-infrared band as well. As shown in Fig. 4 by vertical arrow, the absorption edge in the 10K $\sigma(\omega)$ spectrum looks like to coincide with the gap energy (640cm^{-1}) estimated from the activation energy of the resistivity in the low-temperature phase. As we will discuss more in detail in § 6.3.2 and § 6.3.3, the enhancement of the phonon structure means the structural change. According to this structural change, the conduction band is split and the gap is open at the Fermi level. If we assume the dimerized stack, neglect the correlation effect, and adopt the tight-binding approximation, the upper $E_+(k)$ and lower $E_-(k)$ bands are given by the following equation,

$$E_{\pm}(k) = \pm\sqrt{t_1^2 + t_2^2 + 2t_1t_2\cos(kc)} \tag{6.1}$$

where t_1 and t_2 are the transfer integrals in the dimerized stack. In this model, the band gap is given by $2|t_1\text{-}t_2|$. The low-temperature mid-infrared band is regarded as the optical transition from the lower to upper bands. This optical transition has the highest intensity at the gap energy ($\hbar\omega=2|t_1\text{-}t_2|$) due to the joint density of state and transition probability. The observed shows an asymmetric lineshape with a tail in the high-energy side, although the strong phonon structure disturbs the lineshape of the electronic transition. The plasma frequency of this optical transition is expressed by the following equation,[9)]

$$\omega_p^2 = \frac{e^2}{\varepsilon_0 v_c \hbar^2 \pi}\left\{(c_1^2 - c_2^2)(t_1 - t_2)K\left(\frac{2\sqrt{t_1 t_2}}{t_1 + t_2}\right) + (c_1^2 + c_2^2)(t_1 + t_2)E\left(\frac{2\sqrt{t_1 t_2}}{t_1 + t_2}\right)\right\} \tag{6.2}$$

where, c_1 and c_2 are the inter-molecule distance along the dimerized chain, v_c the volume of the molecular unit DMTSA-BF$_4$, *K(x)* the complete elliptic integral of the first kind, *E(x)* the complete elliptic integral of the second kind. On the other hand, the plasma frequency is experimentally obtained to be 1.22eV carrying out the numerical integration of the optical conductivity using the following equation,

$$\omega_p^2 = \frac{2}{\pi\varepsilon_0}\int_{650}^{8000}\sigma(\omega)d\omega\,. \tag{6.3}$$

If we assume that the band gap is equal to twice the activation energy of the resistivity in semiconductive phase and assume $c_1=c_2=c/2$, t_1 and t_2 are estimated to be 0.25 and 0.21eV. These values are reasonable, when they are compared with the room-temperature value 0.20eV estimated from the Drude fit of the reflectance.[9)] Let us compare with the *E//[110]* spectrum shown in Fig. 5. The excitation energy of this band is determined from the Lorentz fitting of $\sigma(\omega)$ in the range of 3-10×10^3 cm^{-1}. The resonance energies of the Lorentzian are 0.85eV at room temperature and 0.93eV at 10K. We have reported the quantitative interpretation of this low-energy absorption band using the point charge approximation.[9)] If we take $c/2$ as the repeating unit, the system has a half-filled band, but the actual system has 2 molecules in a periodic unit. So the half-filled band is folded at the zone boundary $k=\pi/c$. This absorption band is interpreted as the optical transition at $k=0$ from the bottom of the lower band to the top of the folded band. This optical transition is polarized along the *b*-axis.[10)] As shown in the inset of Fig. 5, the peak energy gives the bandwidth $2|t_1+t_2|$ (0.8eV at RT and 0.92eV at 10K) of the conduction band. These values agree very well with the observed resonant energies at each temperature: 0.85eV at RT and 0.93eV at 10K.

Contrary to metallic DMTSA-BF$_4$, room-temperature $\sigma(\omega)$ of DMTTA-BF$_4$ has a peak at ~2000cm^{-1} and decreases toward $\omega=0$ as shown in Fig. 6. From this spectral feature, we conclude that the optical gap is open at room temperature, thereby DMTTA-BF$_4$ is regarded as a Mott-Hubbard-type insulator. The lineshape is almost symmetric and thus quite different from the asymmetric shape of DMTSA-BF$_4$ which is derived from the divergent nature of the joint density of states at absorption edge in a one-dimensional system. If we interpret this spectrum based on the Hubbard model, this absorption band is interpreted as the optical transition from the lower Hubbard band to upper Hubbard band. Let us analyze the room-temperature conductivity spectrum based on the one-dimensional Hubbard model. According to the exact solution of the one-dimensional Hubbard model, the excitation energy to create the electron-hole pair is given by the following equation,[11]

$$E(k_+,k_-)/4t = u - \frac{1}{2} + \int_0^\infty \frac{J_1(\omega)}{\omega(1+exp(2u\omega))}d\omega + \frac{cos(k_+)+cos(k_-)}{4}$$

$$+\int_0^\infty \frac{J_1(\omega)\{cos(\omega\, sin(k_+) + cos(\omega\, sin(k_-))\}}{\omega(1+exp(2u\omega))}d\omega \qquad (6.4)$$

where k_+ and k_- are the quasi-momenta of electron and hole, $u=U/4t$, $J_1(\omega)$ is the Bessel function of the first kind with order one. As displayed in the inset of Fig. 6, $E(k_+,k_-)$ takes a minimum at $k_+=k_-=\pi$, which corresponds to the absorption edge. The vertical transition ($k_+=k_-$) spans from $E(\pi,\pi)$ to $E(\pi,\pi)+4t$. The analytical solution of the optical spectrum of the one-dimensional Hubbard model has not been obtained so far. Therefore there is an ambiguity to estimate the minimum excitation energy $E(\pi,\pi)$ from such a broad band. The gap is likely to be less than the peak energy (0.3eV) of $\sigma(\omega)$ but larger than the gap energy estimated from the activation energy of the resistivity ($2E_a$=87meV in the range 160-300K). On the other hand, the plasma frequency which is proportional to the integrated intensity of the optical conductivity of the one-dimensional Hubbard model is given by Baeriswyl in the following way,[12)]

$$\frac{\varepsilon_0}{Ne^2d^2}\frac{\hbar^2\omega_p^2}{4t}=\int_0^\infty\left(\frac{1}{\omega(1+exp(2u\omega))}+\frac{u}{1+cosh(2u\omega)}\right)J_0(\omega)J_1(\omega)d\omega \tag{6.5}$$

where N is the density of charge, d the distance between molecules along the c-axis (=$c/2$), ω_p plasma frequency, $u=U/4t$, $Ji(\omega)$ Bessel function of the first kind with order i. The plasma frequency is experimentally obtained as 0.83eV by the numerical integration of $\sigma(\omega)$ from 600cm^{-1} to 8000cm^{-1}. Combining the gap energy and plasma frequency with eqs. (6.4) and (6.5), we estimate (1) U=0.38eV and t=0.12eV for the gap energy of 87meV and (2) U=0.74eV and t=0.15eV for the gap energy of 0.3eV. The actual Hubbard parameters seem to be inbetween. These parameters give the maximum excitation energy $E(\pi,\pi)+4t=0.57eV$ for the case (1) and 0.9eV for the case (2), which corresponds of the energy difference between the bottom of the lower Hubbard band to the top of the upper Hubbard band. From the analogy with the *E//[110]* spectrum of DMTSA-BF$_4$, the 5-6×10^3 cm^{-1} band of DMTTA-BF$_4$ indicated by the arrow in the top panel of Fig. 3 seems to be associated with the optical transition from the bottom of the lower Hubbard band to the top of the upper Hubbard band. The peak energy 5500cm^{-1} (0.68 eV) is located between the corresponding values (0.57eV and 0.9eV) estimated from the analysis of the *E//c* spectrum. At low temperature, the absorption band in the *E//c* spectrum hardly change the spectral shape except the enhancement of the vibronic structure. The integrated intensity again increases by a factor of 1.3.

6.3.2 Phase transitions

The resistivity, thermopower, and spin susceptibility of DMTTA-BF_4 and DMTSA-BF_4 are shown in Fig. 7. The spin susceptibility of DMTTA-BF_4 is obtained from the integrated intensity of the ESR signal. The spin susceptibility of DMTSA-BF_4 is obtained from the static susceptibility subtracting the temperature-independent diamagnetic term. For the estimation of the diamagnetic term, we assume that the paramagnetic susceptibility vanishes in the low-temperature region (2-40K). This assumption is supported by the recent ESR experiment.13) As we have discussed in the previous paper3), DMTSA-BF_4 undergoes a metal-insulator transition at *ca.* 150K, which appears as an upturn in the resistivity and thermopower and downturn in the spin susceptibility. The resistivity of DMTTA-BF_4 is semiconductive with the activation energy of 87meV in the 300-160K range. Below 160K the activation energy continuously increase up to 175meV at70 K without any anomaly. The thermopower of DMTTA-BF_4 decreases continuously down to 100K, below which the data are scattered due to the high resistance. As shown in the spin susceptibility of Fig. 7, DMTTA-BF_4 shows a magnetic phase transition at *ca.* 100K. This phase transition makes no influence on the resistivity. The absolute value of the spin susceptibility of DMTTA-BF_4 is about four times as large as that of DMTSA-BF_4, which is consistent with the high correlation effect in the former compound.

The temperature dependence of the *E//c* optical conductivity are displayed in Fig. 8. The light polarization is exactly perpendicular to the molecular plane of DMTSA and DMTTA. Very strong phonon structures are therefore interpreted from the viewpoint of an electron-molecular vibration coupling model (so-called *e-mv* model) and they are called as vibronic modes14). In this model, the intensity of the optical phonon is borrowed by the electronic polarization between the molecules along the conducting axis. However, these phonons lose the intensity when the both sides of the neighboring molecules are equivalent due to the crystal symmetry, since this electronic polarization is canceled.[15)] In both compounds, these vibronic modes are remarkably enhanced at low temperature. This result strongly suggests the breaking of the screw-axis and glide-plane symmetry at low temperature. However, several vibronic modes are still weakly active above the phase transition temperature and even at room temperature, although the screw-axis and glide-plane symmetry is guaranteed by the space group *Cmcm*. This result suggests the structural fluctuation which is expected to be large in one-dimensional system. The selection rule of the optical transition is determined by the local symmetry around the molecule. So the symmetry breaking in a short range area breaks partly the selection rule, thereby inducing weak vibronic modes. Figure 9 shows the temperature dependence of the intensities of several vibronic modes. In DMTTA-BF_4, the vibronic modes appear as peaks, so several peaks are numerically integrated. The normalized intensity increases monotonously pass over the phase transition temperature (100K) and levels off. However, they appear as dips in DMTSA-BF_4, so the intensity is estimated from the $Re(1/\sigma(\omega))$ vs ω plot.[16)] The intensity increase becomes steep below the phase transition temperature (150K). The way of the enhancement is different between DMTTA-BF_4 and DMTSA-BF_4. Taking the magnetic and electric properties into account, these experimental results suggest the view that the low-temperature states of DMTTA-BF_4 and DMTSA-BF_4 are respectively a spin Peierls and Peierls states. As a matter of fact, the $E\perp c$ polarized phonons are not coupled with the electronic polarization, so the $E//[110]$ infrared spectrum of DMTSA-BF_4 shows no change down to the lowest temperature (see Fig. 5).

6.3.3 Coupling with molecular vibration

The coupling constants of the molecular vibration with the charge-transfer-type excitation are the fundamental quantities of molecules in molecular metals. They contribute to the stabilization of the Peierls state$^{17)}$ and might be related to the superconducting mechanism$^{18)}$ as well. In the preceding article, the conductivity spectrum of DMTSA-BF_4 at 10K are simulated using a dimer model.$^{3)}$ The conductivity spectrum in the dimer model is formulated as the following equation,$^{19)}$

$$\sigma(\omega) = \frac{\omega}{i}\frac{Ne^2d^2}{4}\frac{\chi(\omega)\chi(o)}{\chi(0)-\chi(\omega)D(\omega)} \tag{6.6}$$

$$D(\omega) = \sum\frac{\lambda_\alpha\omega_\alpha^2}{\omega_\alpha^2-\omega^2-i\omega\gamma_\alpha} \tag{6.7}$$

$$\chi(\omega) = \frac{2\omega_{CT}\left|\langle CT|\delta n|G\rangle\right|^2}{\omega_{CT}^2-\omega^2-i\omega\gamma_{CT}} \tag{6.8}$$

where N is the electron density, d the distance between the center of the molecules in the dimer, λ_α the coupling constant of the α-th phonon, ω_α the unperturbed phonon frequency, ω_{CT} the electronic excitation energy in the dimer, γ_α and γ_{CT} the phenomenological linewidth of the phonon and electronic transition. The dip structure is qualitatively reproduced using these equations. In the dimer model, the out-of-phase molecular vibration couples with the charge-transfer excitation and induces the oscillating polarization in the direction connecting the center of molecules in the dimer. On the other hand, in-phase molecular vibration is decoupled with the charge-transfer excitation.$^{20)}$ Due to the decoupling, they are active in Raman and infrared spectra, since the parity selection rule does not work in non-centrosymmetric DMTSA. The unperturbed phonon frequency ω_α obtained by this analysis should coincide with the a_1 phonon appearing in the Raman spectrum and infrared spectrum polarized parallel to the long molecular axis. However, the agreement is not good in DMTSA-BF_4. In the dimerized one-dimensional chain, the polarizations along the opposite sides cancel with each other. So the intensity of a_1 modes depends upon the deviation from the uniform stacking. This seems to be the reason for the above disagreement, since the dimer model neglects the inter-dimer interaction. To analyze $\sigma(\omega)$ of the dimerized one-dimensional chain, Bozio *et al.* presented the model for a dimerized infinite chain.$^{14)}$ However, the information on the dimerized structure at low-temperature and the frequency of the lattice phonon are necessary to analyze the $\sigma(\omega)$ spectrum. To obtain the coupling constants in DMTSA, we analyze the reflection spectrum of DMTSA-ClO_4 single crystal which has a dimerized structure already at room temperature. The description of the crystal structure and reflection spectrum are given in Appendix. The optical conductivity spectrum and the simulation by the dimer model are shown in Fig. 10. In contrast to DMTSA-BF_4, the stacking axis is not perpendicular to the molecular plane, so the infrared active phonon can mix in the $E//a$ spectrum. In this analysis, however, we assume that all the observed phonons are derived from the a_1 vibronic phonons, since the intensity of these phonons is usually stronger than the infrared active decoupled phonons. The obtained parameters are shown in Table II along with the experimentally observed Raman and infrared active modes. The agreement between them is satisfactory in DMTSA-ClO_4. The sum of the coupling constant $\lambda=0.14$ in this spectral region is much smaller than the value 0.34 of TCNQ$^{21)}$ and 0.6 of TTF$^{22)}$. The magnitude of the total coupling constant is connected with the geometrical change from the neutral to ionic state of the molecule. Contrary to TCNQ and TTF, the molecular geometry of DMTSA does not change so much when it is ionized. Takimiya *et al.* claims that Se-Se distance is shortened in DMTSA^{+}.$^{23)}$ The coupling constant of Se-Se stretching mode is not included in λ, since it appears at lower frequency than 600cm^{-1}. The molecular phonon having a large coupling constant often shows a large frequency shift when the molecule is ionized (oxidization or reduction). The comparison of these Raman lines between neutral DMTSA and DMTSA-ClO_4 is listed in Table II as well. All of these Raman lines shows a small shift within 10cm^{-1}

between the neutral and ionic state except the 1170cm^{-1} (11cm^{-1}) and 1387 cm^{-1} (18cm^{-1}) lines in DMTSA-ClO$_4$, which are much smaller than the shift of the charge-sensitive mode in TCNQ[24)] or BEDT-TTF[25)]. As described before, the Se-Se stretching mode is expected to be sensitive to the degree of oxidation from the crystal structure analysis. However, we cannot find such a charge-sensitive Raman active mode in the spectral region of 150-4000cm^{-1}.

6.4 Summary

It is concluded from the optical spectrum that DMTTA-BF$_4$ is a Mott insulator, whereas DMTSA-BF$_4$ looks like a metal in which a one-electron theory can explain the optical transitions very well. The transfer integral along the stack is 0.12-0.15eV in DMTTA-BF$_4$ at room temperature, while in DMTSA-BF$_4$ it is 0.2eV at room temperature and 0.25eV and 0.21eV at 10K. Both compounds undergo phase transitions: Peierls transition for DMTSA-BF$_4$ and spin Peierls transition for DMTTA-BF$_4$. To understand the reason for the metallic nature of DMTSA-BF$_4$, the following points should be considered: (1) strong inter-chain interaction, (2) the contribution of multiple bands to the Fermi level. According to the *E//[110]* spectrum, the inter-chain interaction is much smaller than that of the quasi-one-dimensional metal (TMTSF)$_2$X[26)]. If several bands participate in the Fermi level, the 1:1 charge-transfer salt makes a non-half-filled band. However, this possibility will be small from the *E//c* spectrum in a wide spectral region. The reason why 1:1 charge-transfer salt DMTSA-BF$_4$ is metallic is still not clear.

6.5. Appendix

The crystal structure of DMTSA-ClO$_4$ is analyzed by Takimiya *et al.* and is given in Figs. 5 and 6 of their article[1)]. The crystal belongs to monoclinic system with lattice parameters of *a*=7.166, *b*=11.837, *c*=20.203 Å, β=93.81°, space group *P2₁/c*, *Z*=4. The stacking pattern in the DMTSA column viewed from the short molecular axis is shown in Fig. 11. As shown in this figure, DMTSA is stacked in two different overlapping modes (A and B in Fig. 11). We calculate the overlap integrals between adjacent molecules (A and B) based on extended Huckel approximation, which are -0.022 for mode A and 0.0056 for mode B. The much smaller value of mode B comes not only from the large inter-molecular distance but also the distribution of sign of the atomic orbitals in HOMO. The polarized reflection spectra and optical conductivity spectra parallel and perpendicular to the *a*-axis are shown in Fig. 12. Due to the strong interference in the infrared region, the phonon structure in the *E//[011]* spectrum cannot be obtained. In this spectrum, we cannot observe the optical transition from the bottom of the lower band to the top of the upper band, which shows up in the near-infrared region of DMTSA-BF_4 and DMTTA-BF_4. This optical transition has a finite transition probability, if the center of HOMO in DMTSA forms a zigzag stacking pattern like DMTSA-BF_4. This observation implies the conclusion that the center of HOMO is located near the center of the anthracene skeleton. This result is consistent with the estimation of the center of HOMO based on the quantitative analysis of the optical spectrum of DMTSA-BF_4.

References

1) K. Kawabata, M. Yanai, T. Sambongi, Y. Aso, K. Takimiya, and T. Otsubo, *Mol. Cryst. Liq. Cryst.*, **296** (1997) 197.

2) J. Dong, K. Yakushi, K. Takimiya, and T. Otsubo, J. *Phys. Soc. Jpn.*, **67** (1998) 971.

3) P. M. Chaikin and J. F. Kwak, *Rev. Sci. Instrum.*, **46** (1975) 218.

4) J. Ouyang, K. Yakushi, Y. Misaki, and K. Tanaka, *J. Phys. Soc. Jpn.*, **67** (1998) 3191.

5) H. Tajima, T. Naito, M. Tamura, A. Kobayashi, H. Kuroda, R. Kato, H. Kobayashi, R. A. Clark, and A. E. Underhill, *Solid State Commun.*, **79** (1991) 337. H. Tajima, M. Tamura, T. Naito, A. Kobayashi, H. Kuroda, R. Kato, H. Kobayashi, R. A. clark, and A. E. Underhill, *Mol. Cryst. Liq. Cryst.*, **181** (1990) 233. H. Tajima, T. Naito, M. Tamura, A. Kobayashi, H. Kuroda, R. Kato, H. Kobayashi, R. A. Clark, and A. E. Underhill, *Solid State Commun.*, **79** (1991) 337.

6) K. Yakushi, G. Ojima, A. Ugawa, and H. Kuroda, *Chem. Lett.*, (1988) 95.

7) K. Yakushi, A. Ugawa, G. Ojima, T. Ida, H. Tajima, H. Kuroda, A. Kobayashi, R. Kato, and H. Kobayashi, *Mol. Cryst. Liq. Cryst.*, **181** (1990) 217.

8) J. Ouyang, K. Yakushi, K. Takimiya, and T. Otsubo, *Solid State Commun.*, **110** (1999) 63.

9) H. Tajima: PhD Thesis, University of Tokyo (1989).

10) This polarization comes from the zigzag stack in which DMTSA shifts along the *b*-axis. The details are described in ref. 9.

11) I. A. Musurkin and A. A. Ovchinnikov, *Soviet Physics Solid State*, **12** (1971) 2031.

12) D. Baeriswyl, J. Carmelo, and A. Luther, *Phys. Rev. B*, **33** (1986) 7247.

13) J. Nanba, T. Kanbe, Y. Nogami, K. Oshima, K. Yakushi, J. Dong, K. Takimiya, and T. Otsubo, Spring Meeting of Phys. Soc. Jpn. (1999).

14) M. J. Rice, *Solid State Commun.*, **31** (1979) 93.

15) R. Bozio, M. Meneghetti, and C. Pecile, *Phys. Rev. B*, **36** (1987-II) 7795.

16) V. M. Yartsev and C. S. Jacobsen, *phys. stat. sol.*, (b) **145** (1988) K149.

17) M. J. Rice, V. M. Yartsev, C. S. Jacobsene, *Phys. Rev.* ***B***, 21 (1980) 3437.

18) T. Ishiguro and K. Yamaji, "*Organic Superconductors*" Springer Series in Solid-State Science 88, p187 (1989).

19) A. Painelli and A. Girlando, *J. Chem. Phys.*, 84 (1986) 5655.

20) If the molecular phonon in the dimer is coupled in phase, the polarization of the in-phase a_1 mode is cancelled due to the screw-axis symmetry in DMTSA-BF$_4$. Therefore they are infrared inactive above the phase transition temperature but becomes active below the temperature. However, the infrared active modes of DMTSA-BF$_4$ shows no change below the phase transition temperature (see Fig. 5). This means that the in-phase molecular vibration in the dimer is decoupled with each other.

21) M. J. Rice, N. O. Lipari, and S. Strassler, *Phys. Rev. Lett.*, **39** (1977) 1359.

22) A. Painelli and A. Girlando, *J. Chem. Phys.*, **84** (1986) 5655.

23) This geometrical change is reproduced by the geometrical optimization of PM$_3$ molecular orbital calculation.

24) R.Bozio, A. Cirlando, and C. Pecile, *J. Chem. Soc. Faraday Trans. II*, **71** (1975) 1237.

25) M. E. Kozlov, K. I. Pokhondnia, and A. A. Yurchenko, *Spectrochimica Acta*, **45A** (1989) 437.

26) C. S. Jacobsen, D. B. Tanner, and K. Bechgaard, *Phys. Rev. B*, **28** (1983) 7019.

Table I Electronic absorption bands in DMTTA-BF$_4$ and DMTSA-BF$_4$

DMTTA-BF$_4$		DMTSA-BF$_4$	
$E//c$ (10^3 cm^{-1})	$E\perp c$ (10^3 cm^{-1})	$E//c$ (10^3 cm^{-1})	$E\perp c$ (10_3 cm^{-1})
2.4	-	1.2	-
-	5.6	-	7.0
-	16.8	-	13.4
-	18 (shoulder)	-	16.6

Table II. Analysis of the room-temperature $\sigma(\omega)$ spectrum of DMTSA-ClO$_4$ by dimer model

ω_{CT} (cm^{-1})	$\lvert\langle CT\rvert\delta n\lvert G\rangle\rvert^2$	γ_{CT} (cm^{-1})	$u=U/4t$
2856	1.39	1375	0.32

Ω_α (cm^{-1})[a]	ω_α (cm^{-1})[b]	γ_α	λ_α	DMTSA-ClO$_4$ Raman[c]	DMTSA-BF$_4$ IR ($E\perp c$)[d]	DMTSA Raman[e]
742	745	5	0.003	743	-	-
881	887	6	0.005	-	885	883
947	964	9	0.020	972	958	970
1088	1096	20	0.007	-	1093	-
1159	1165	7	0.002	1170	1161	1159
1242	1265	5	0.010	1266	-	1273
1273	1282	7	0.010	-	1281	-
1313	1340	9	0.026	1340	-	1348
1362	1367	10	0.015	1372	-	1376
1381	1387	8	0.017	1387	1385	1405
1468	1485	17	0.020	1490	-	1486
1525	1532	11	0.009	1535	-	1531

[a] Observed frequency in the $\sigma(\omega)$ spectrum (E//c) of DMTSA-ClO4.

[b] Unperturbed frequency defined by equation (7).

[c] Raman active modes observed in DMTSA-ClO$_4$.

[d] IR active modes observed in the $\sigma(\omega)$ spectrum (E⊥c) of DMTSA-BF$_4$. Because of the strong inteference effect, we utilize the intra-molecular vibration spectrum of DMTSA-BF$_4$ instead of DMTSA-ClO$_4$.

[e] The Raman modes in DMTSA neutral crystal.

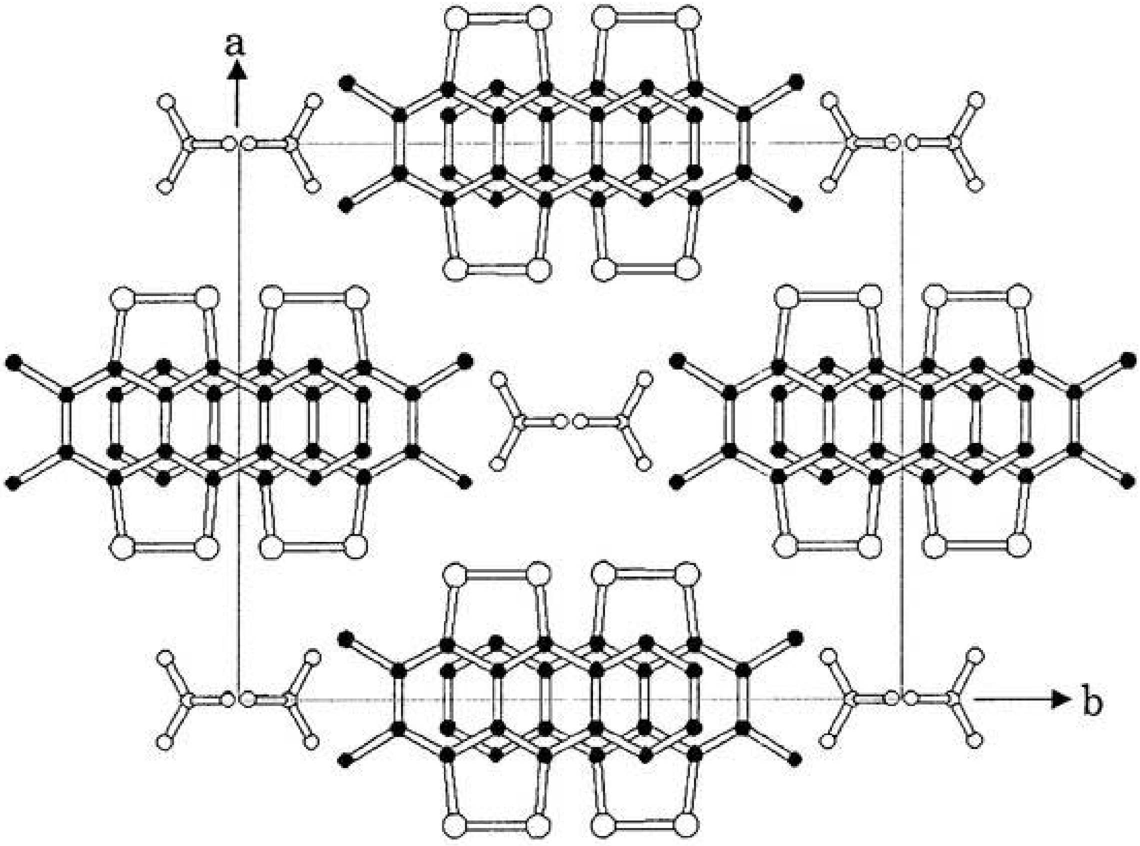

Fig. 1 Crystal structure of DMTTA-BF$_4$. The large and small circles of DMTTA denote the sulfur and carbon atoms, respectively. DMTTA is stacked in a zigzag fashion along the screw axis parallel to the *c*-axis. This crystal structure is isostructural to DMTSA-BF$_4$.

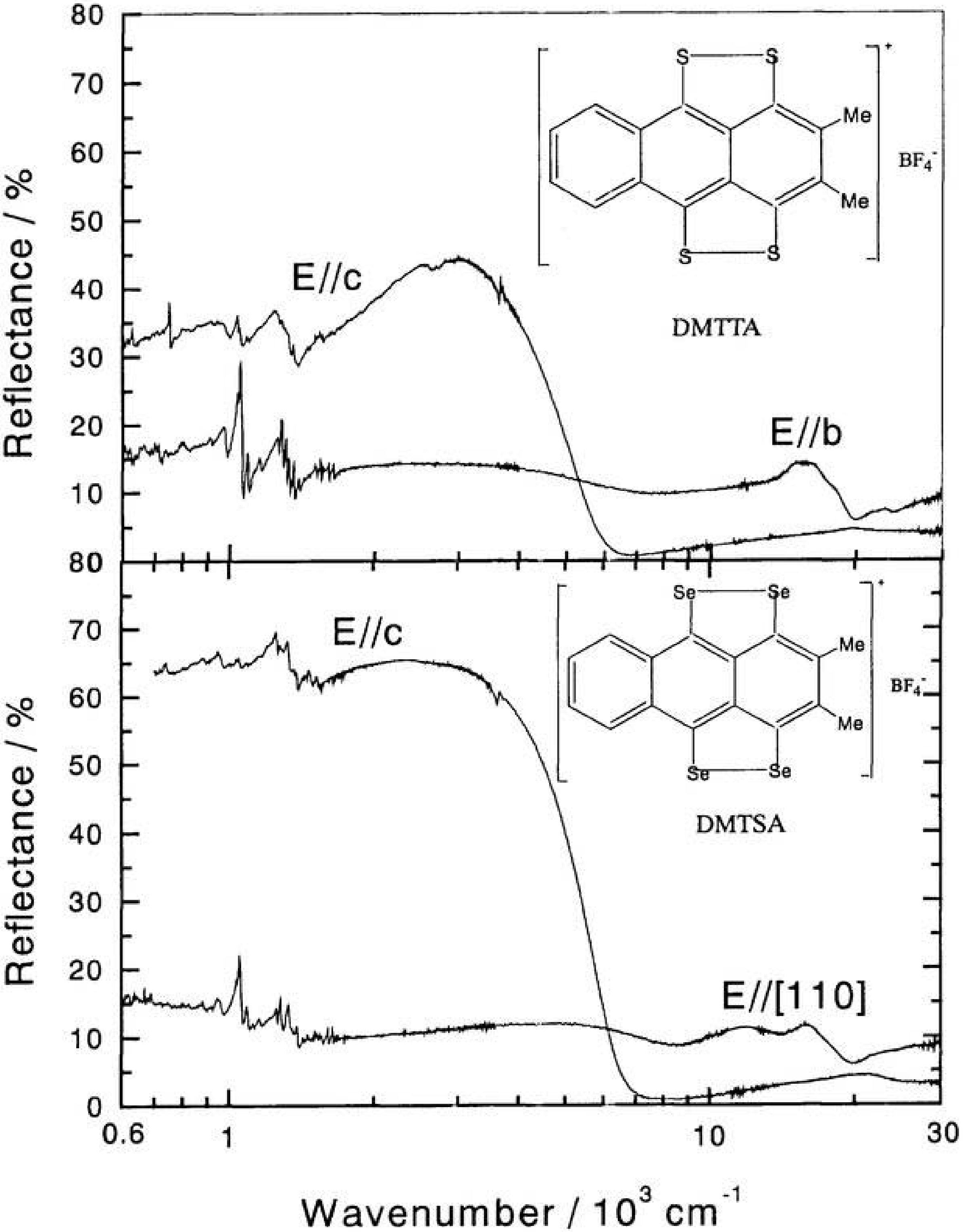

Fig. 2 Reflectance of DMTTA-BF$_4$ (top panel) and DMTSA-BF$_4$ (bottom) plotted against the logarithmic scale of wavenumber. The crystal faces are (100) for DMTTA-BF$_4$ and (110) for DMTSA-BF$_4$. The inset shows the chemical formula of DMTTA-BF$_4$ and DMTSA-BF$_4$.

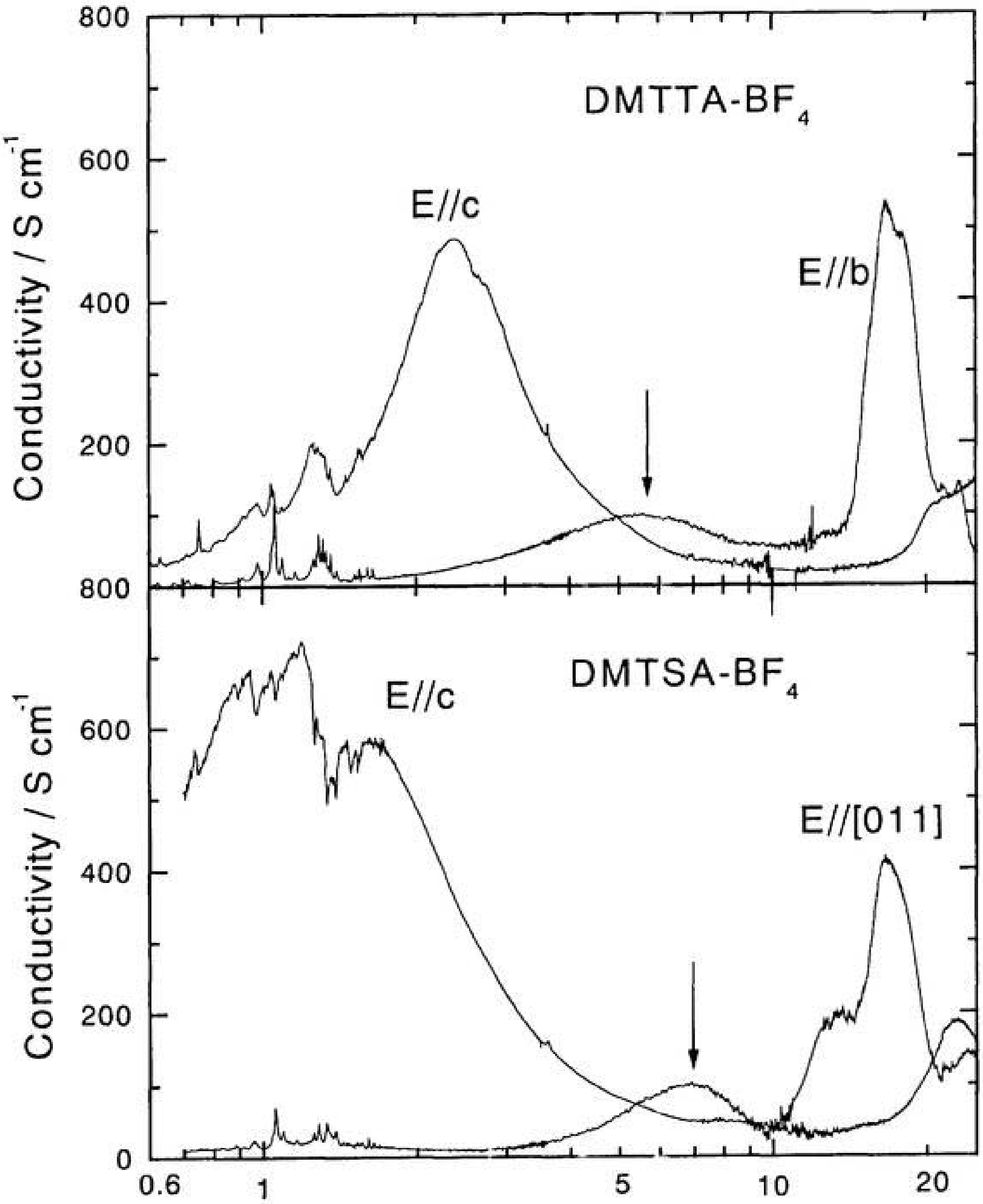

Fig. 3 Optical conductivity of DMTTA-BF$_4$ (top panel) and DMTSA-BF$_4$ (bottom) plotted against the logarithmic scale of the wavenumber. They are obtained from the Krames-Kronig transformation of the reflection spectra in Fig.2.

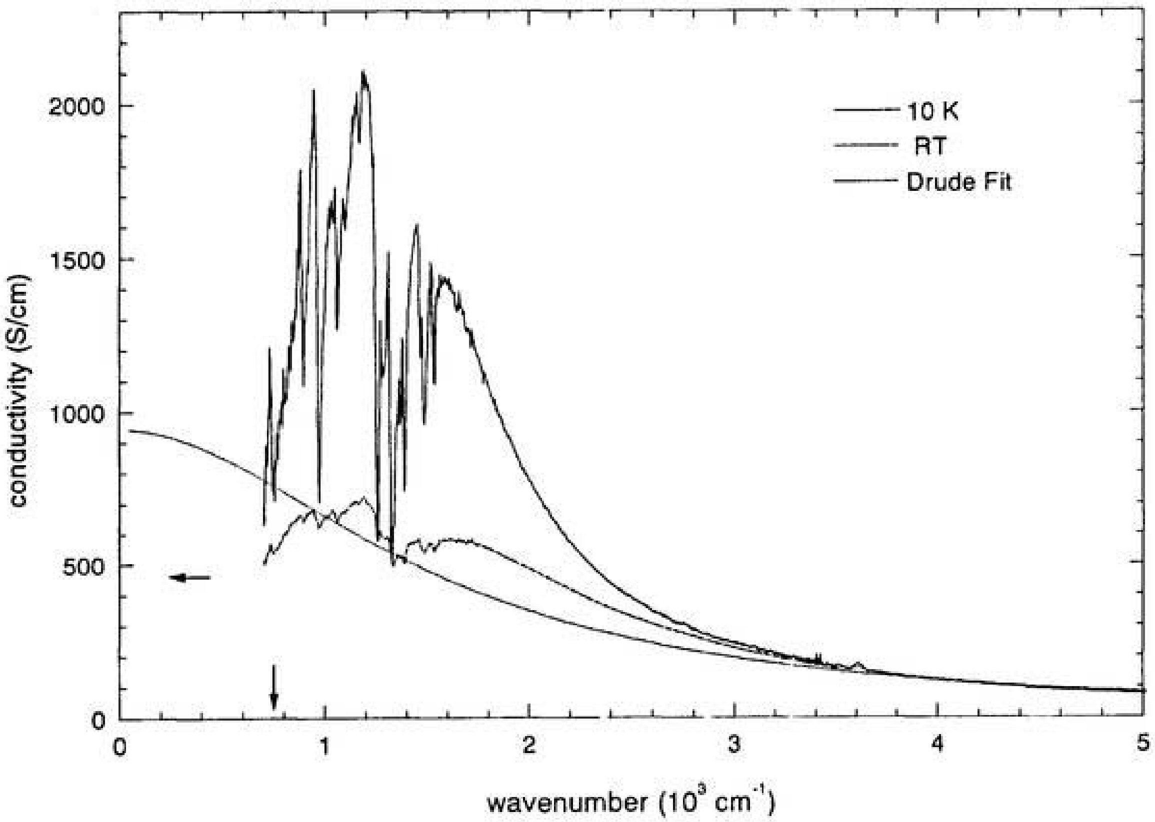

Fig. 4 Room-temperature and 10K optical conductivity spectra (*E*//*c*) of DMTSA-BF$_4$ in the infrared region. The Drude model fitted to the high-wavenumber region of the reflectance is drawn by the dotted line. The horizontal arrow shows the dc conductivity at room temperature. The vertical arrow denotes twice the activation energy of the electrical resistivity below the phase transition temperature.

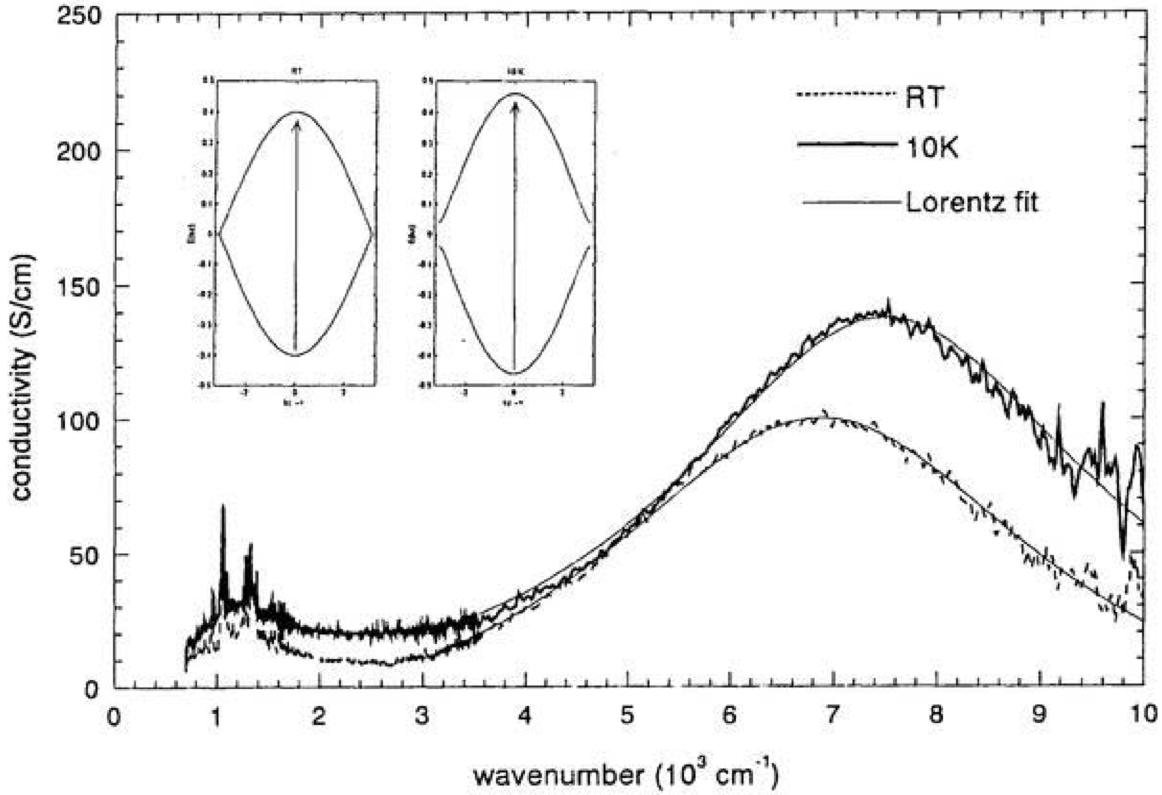

Fig. 5 Room-temperature and 10K *E//[011]* conductivity spectra of DMTSA-BF_4. The thin solid lines are the Lorentz functions fitted to these spectra. The inset shows the one-dimensional tight-binding band at room temperature and 10K.

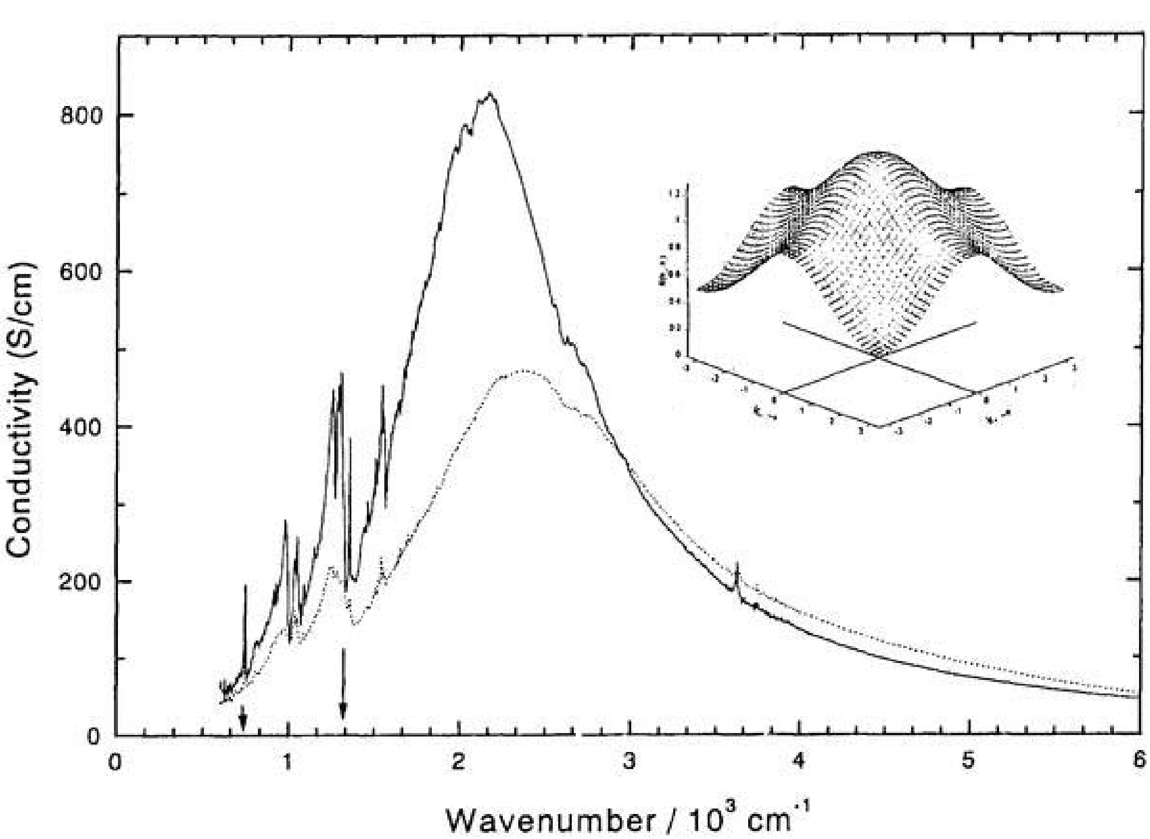

Fig. 6 Room-temperature and 16K conductivity spectra (*E*//*c*) of DMTTA-BF$_4$ in the infrared region. The vertical arrows denote twice the activation energy of the electrical resistivity around room temperature (short one) and 70-80K (long one). The inset shows the excitation energy to create an electron-hole pair in one-dimensional Hubble model when $u=U/4t=1$.

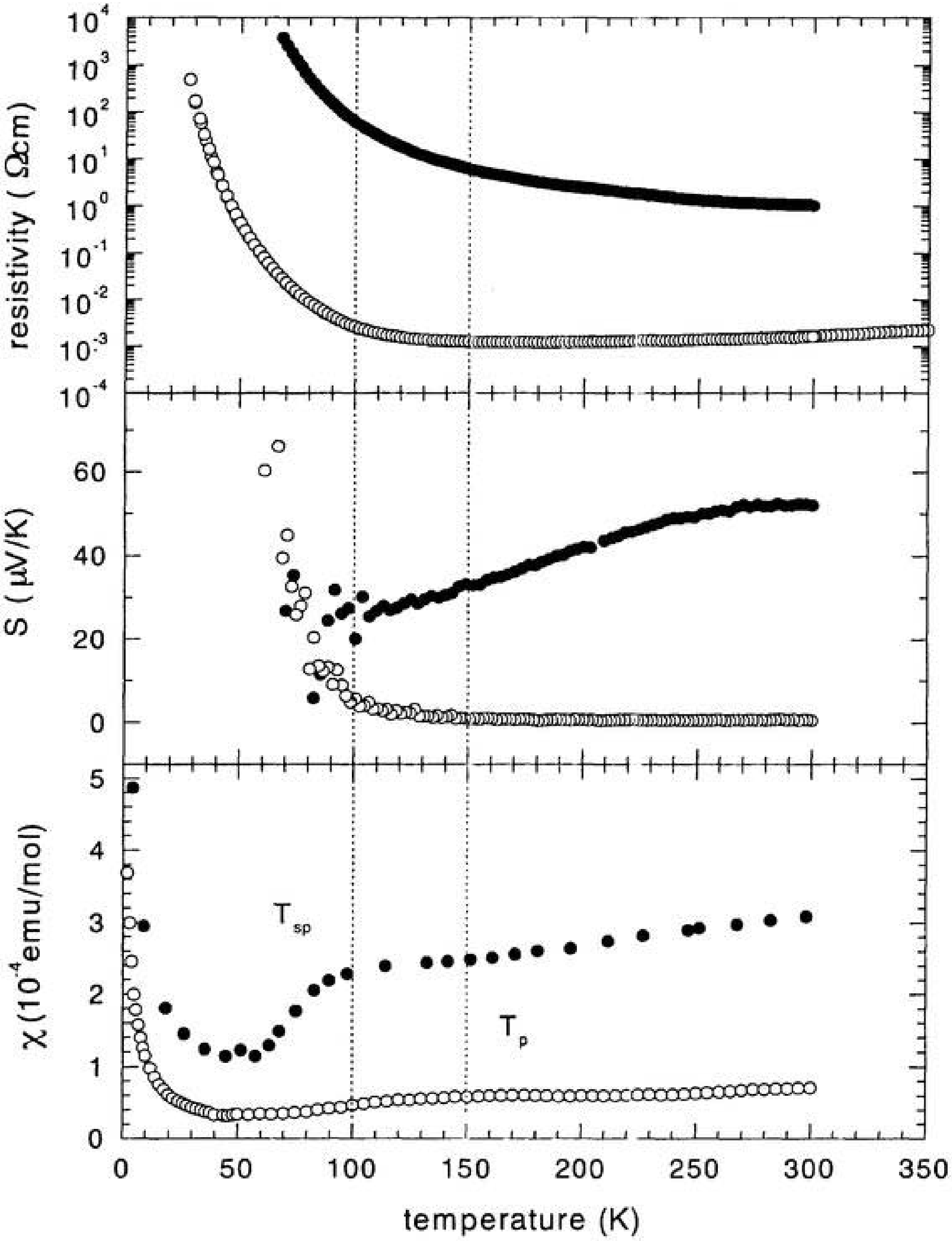

Fig.7 Temperature dependence of the electrical resistivity (top panel), thermopower (middle), and spin susceptibility (bottome) of DMTTA-BF$_4$ (solid circle) ane DMTSA-BF$_4$ (open circle). The vertical dotted lines are the phase transition temperature of DMTTA-BF$_4$ (T$_{sp}$) and DMTSA-BF$_4$ (T$_p$).

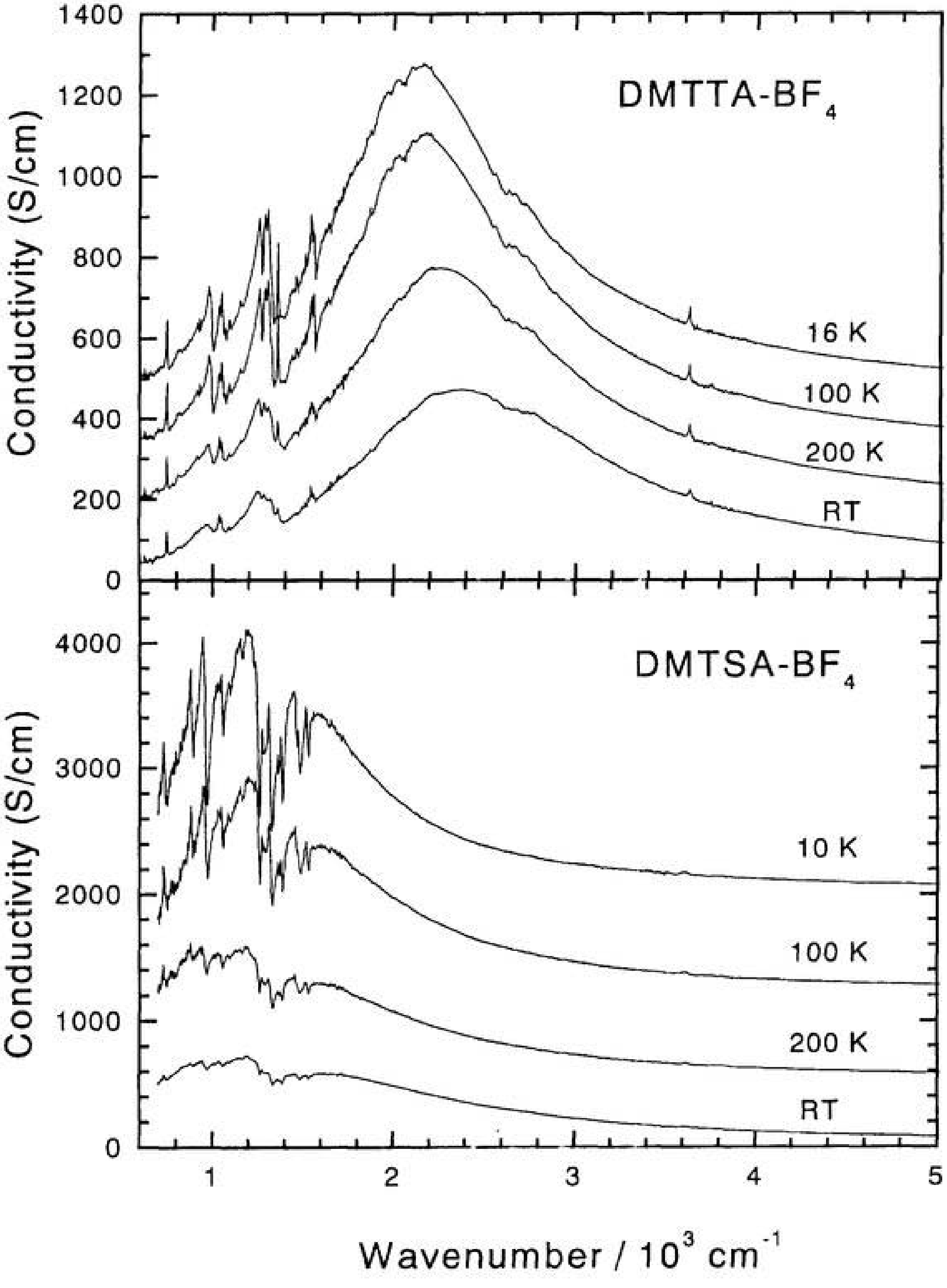

Fig. 8 Temperature dependence of the optical conductivity (*E//c*) of DMTTA-BF$_4$ (top panel) and DMTSA-BF$_4$ (bottom). Note the enhancement of the phonon structure.

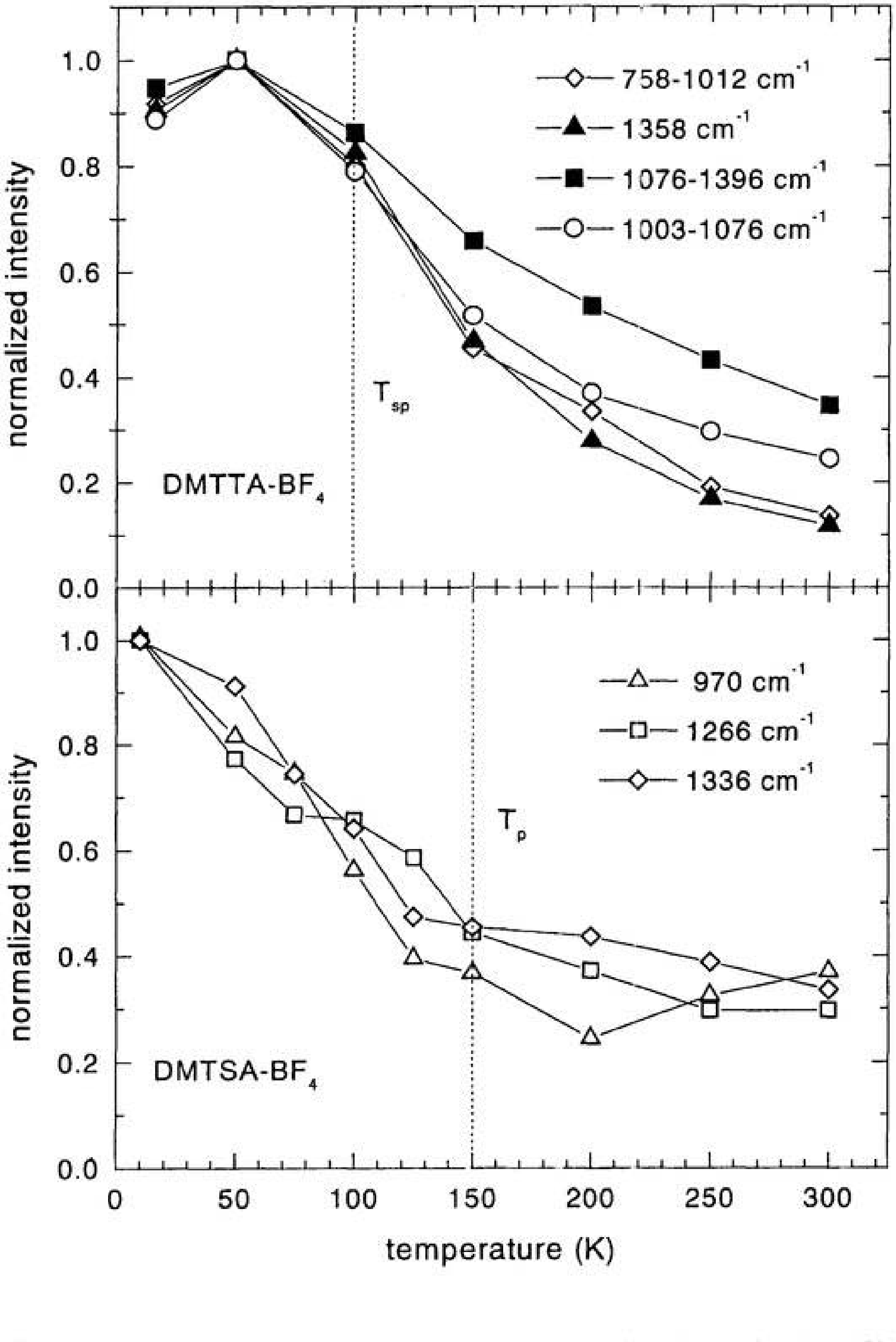

Fig.9 Temperature dependence of the intensity of several vibronic modes DMTTA-BF$_4$ (top panel) and DMTSA-BF$_4$ (bottom).

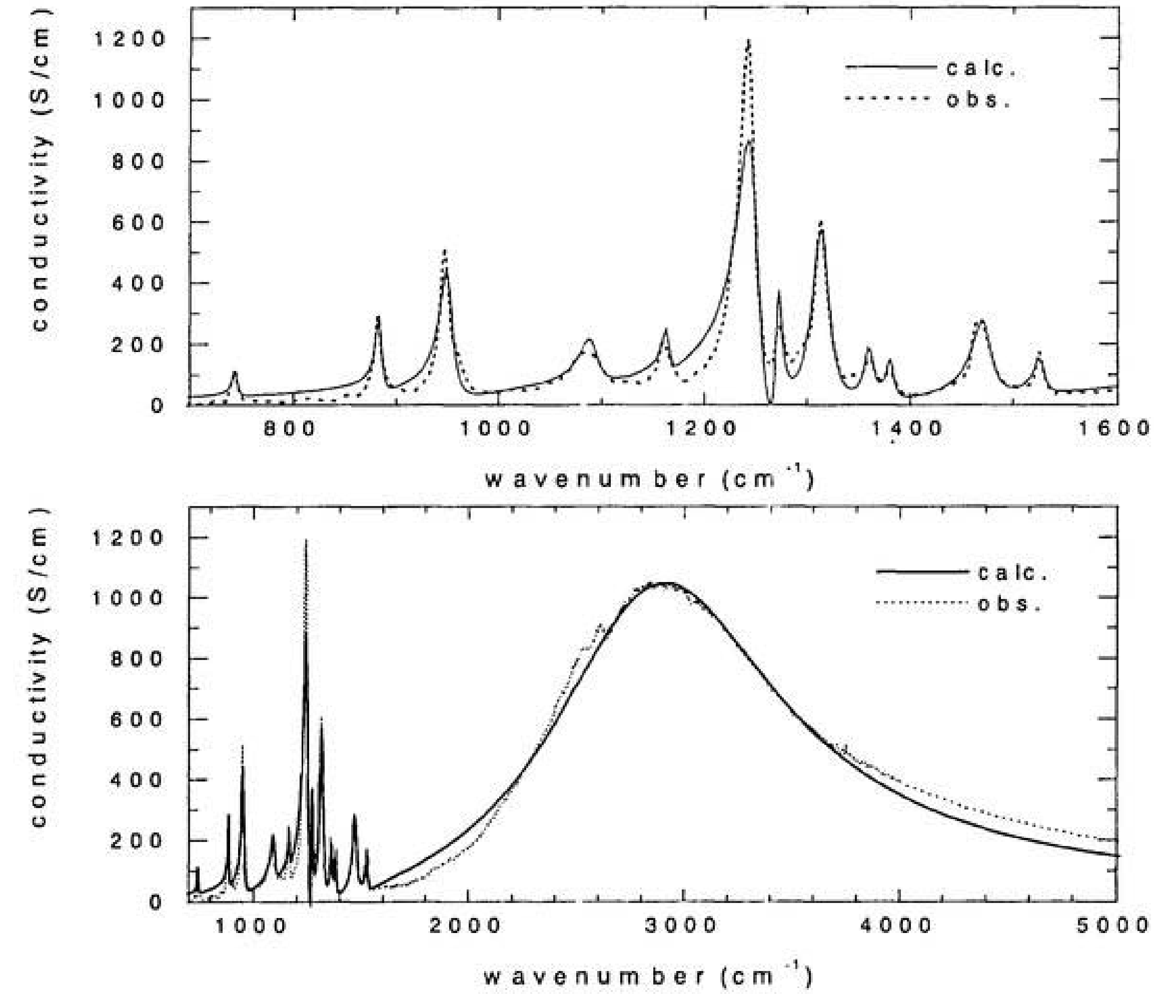

Fig. 10 Optical conductivity spectrum of DMTSA-ClO$_4$ in the infrared region (dotted lines) and the best-fit curve calculated by the dimer model (solid lines; see the text).

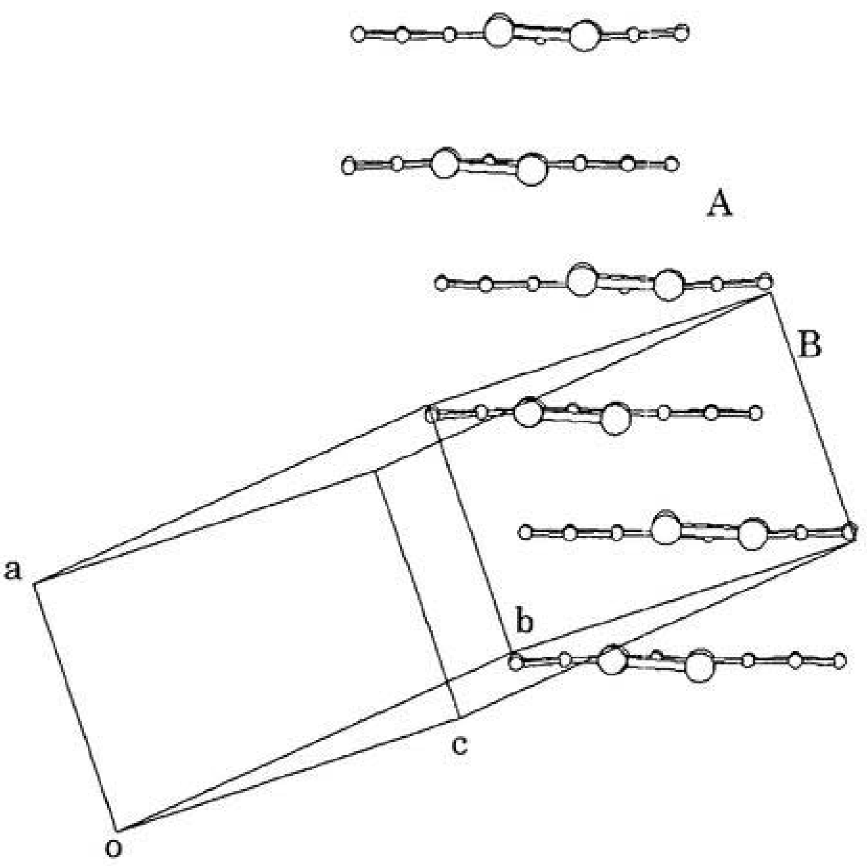

Fig. 11 The stacking pattern of DMTSA in DMTSA-ClO_4 viewed from the short molecular axis. DMTSA is stacked in a dimerized fashion. The inter-molecular distance are (A) 3.32Å and (B) 3.49Å.

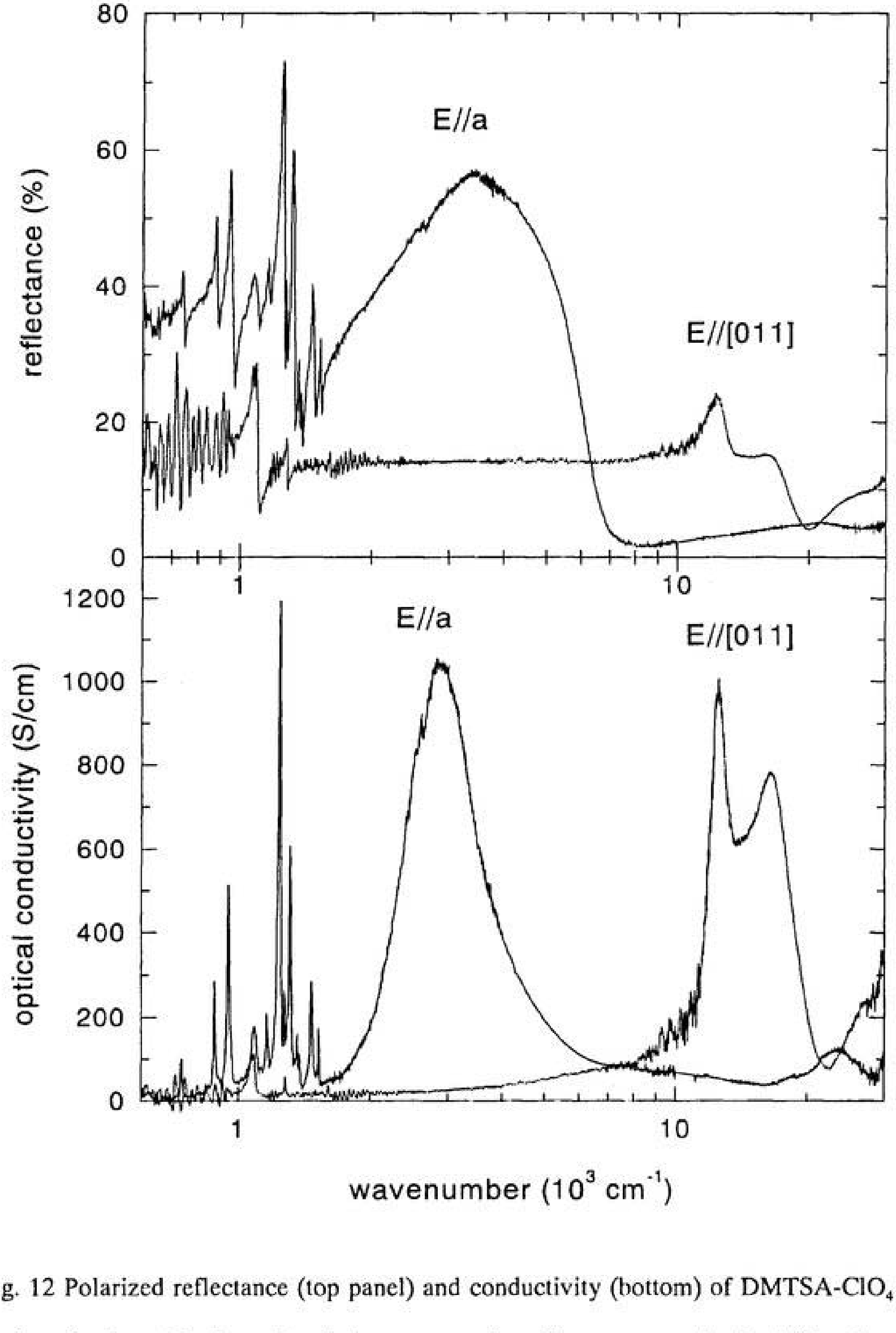

Fig. 12 Polarized reflectance (top panel) and conductivity (bottom) of DMTSA-ClO_4 plotted against the logarithmic scale of the wavenumber. The structure in the infrared region of *E//[011]* spectrum comes from the interference effect at the crystal surface.

Chapter 7

Low-Energy Optical Transitions in Organic Metal DMTSA-BF_4

J. Ouyang, K. Yakushi, K. Takimiya, T. Otsubo, and H. Tajima

Low-energy optical transitions in organic metal DMTSA-BF_4

Solid State Commun., **110** (1999) 63.

7.1. Introduction

In some quasi-one-dimensional organic metals, the repeating unit along the conducting axis consists of more than two molecules. In such a case the HOMO band is folded at the zone boundary and is split into several branches depending upon the number of the molecules and the symmetry relation between these molecules in the repeating unit. It is expected theoretically that the optical transition occurs not only within the partly filled branch but also between these branches. However, only the former optical absorption has been observed so far in quasi-one-dimensional organic metals. This paper reports the first observation of the latter optical transition in the quasi-one-dimensional metal DMTSA-BF_4.

DMTSA was synthesized by Takimiya *et al.* and a high electrical conductivity ($\sigma_{RT} \approx 500$ Scm^{-1}) was found in the charge-transfer salt DMTSA-BF_4[1]. Subsequently Kawabata *et al.* reported metal-like behaviors of DMTSA-BF_4 above 150K, although DMTSA was fully oxidized thereby it was believed to be a Mott insulator[2]. Dong *et al.* showed a quasi-one-dimensional and small-U nature of DMTSA-BF_4 by examining the electrical resistivity, thermopower, magnetic susceptibility, optical spectrum, and band structure calculation[3]. The Hubbard parameter ratio U/W was estimated to be less than 0.8, which was likely to contribute to the metal-like properties of DMTSA-BF_4. These results seemed to guarantee the non-correlated approximation on the electronic structure of this compound.

In this paper we present an interpretation of the low-energy optical transitions polarized parallel and perpendicular to the conducting axis based on the tight-binding band theory. It is well known in the quasi-one-dimensional organic compounds that the Drude-like intra-band optical transition appears in the optical spectrum polarized along the conducting axis. Our attention concerns the optical transition of DMTSA-BF_4 which appears in the near-infrared region and is polarized perpendicular to the conducting axis. The one-dimensional HOMO band is folded at the zone boundary due to the glide-plane symmetry making two branches. We propose this near-infrared band is assigned to the optical transition from the lower to upper branch of the HOMO band, the transition probability of which comes from the zigzag stacking structure of DMTSA molecules in this crystal.

7.2. Experimental

The crystal growth by electrochemical oxidation, existence of the polymorphism, and crystal habit of the metal-like crystal were described before3). A single crystal of 0.25×2×0.1 mm^3 with a smooth surface was selected for the measurement of polarized reflection spectrum in the spectral region of 700-30,000 cm^{-1}. The well-developed crystal face was determined by the oscillation and Weissenberg photographs of X-ray diffraction. The details of the experimental method for the measurement of polarized reflection spectrum were described elsewhere4). For the measurement of solution spectrum of DMTSA molecule, tetrahydrofuran was distilled and then degassed using the technique of freeze pump and thaw. The DMTSA-BF_4 was dissolved in a glove box with Ar atmosphere. The solution spectrum was measured on the UV-VIS spectrophotometer HITACHI U-3500. The molecular orbital of $DMTSA^0$ was calculated using the Extended Hückel method in the HyperChem-R5.1 program system.

7.3. Results and discussion

7.3.1 Crystal structure and polarized reflection spectrum

The crystal of DMTSA-BF_4 belongs to orthorhombic system with the space group of *Cmcm*1). Figure 1a illustrates the top view of the molecular arrangement in crystal. The long molecular axes of all DMTSA are parallel to the *b*-axis. The DMTSA molecules are stacked along the c-axis in a zigzag form as shown in the side view of the single column located at (1/2, 1/2, z) (see Fig. 1b). The two transfer integrals t_c along the conducting c-axis are equivalent to each other due to the glide-plane symmetry. Owing to the zigzag stacking structure, the vector connecting the centers of adjacent molecules has components both in the c- and b-directions. Consequently this structural characteristics suggests that the charge-transfer transition between the neighboring molecules appears both in the c- and b-directions.

The polarized reflection spectra measured on the (110) face of the DMTSA-BF_4 single crystal are shown in Fig. 2. The spectra are recorded with the light polarization parallel and perpendicular to the c-axis in the (110) plane. A well-defined plasma edge appears at 4000-8000cm^{-1} in the $E//c$ reflection spectrum. The high-wavenumber region above 3,000 cm^{-1} of this spectrum can be fitted by Drude-Lorentz model using the following dielectric function:

$$\varepsilon(\omega)=\varepsilon_c-\frac{\omega_p^2}{\omega(\omega+i\gamma)}+\frac{\omega_{0p}^2}{\omega_0^2-\omega^2-i\omega\Gamma}, \tag{7.1}$$

where ε_c stands for the frequency-independent dielectric constant coming from the high-frequency polarization, ω_p and γ are the plasma frequency and the relaxation rate in a Drude model, respectively, ω_{p0}, Γ, and ω_0 are the plasma frequency, the damping constant, and resonant frequency in Lorentz model, respectively. The best-fit parameters are ε_c=2.29, $\omega_p=9.30\times10^3$ cm^{-1}, $\gamma=1.53\times10^3$ cm^{-1}, $\omega_{p0}=6.83\times10^3$ cm^{-1}, $\omega_0=23.28\times10^3$ cm^{-1}, and $\Gamma=5.28\times10^3$ cm^{-1}. The deviation from the Drude model in the low-wavenumber region comes from the effect of the correlation and/or fluctuation of the lattice dimerization. We have discussed this problem in the previous paper$^{3)}$ and will neglect these effects in this paper. In contrast to the $E//c$ spectrum, the dispersion below 1000cm^{-1} in the $E\perp c$ spectrum is small, thereby indicating that DMTSA-BF_4 is a quasi-one-dimensional metal along the c-axis at room temperature. In addition to the dispersion in the infrared region, we can see a broad band at near-infrared region below 10,000cm^{-1} in the $E\perp c$ reflection spectrum. Figure 3 shows the $E//c$ and $E\perp c$ conductivity spectra obtained by Krames-Kronig transformation. In this paper we will discuss the Drude-like electronic transition marked by A and the broad band at 6,900cm^{-1} marked by B. The band A can be undoubtedly assigned to the Drude term in the framework of a one-electron approximation, although the low-wavenumber region is deviated from the typical Drude-like line shape. There are two possible assignments for the band B: one is the inter-band transition from the filled next-HOMO band to the half-filled HOMO band and another is the inter-branch transition within the HOMO band which will be discussed more in detail. The former transition corresponds to the intra-molecular electronic transition of DMTSA$^+$. To examine the former case we dissolved DMTSA-BF_4 in tetrahydrofuran (THF). The solution spectrum of DMTSA-BF_4 is exactly the same as that of DMTSA. The DMTSA$^+$ cation radical may be reduced in the THF solution. Although we purified the solvent and degassed the air and dissolved DMTSA-BF_4 in a glove box, the result is the same. The possibility of this assignment is still remained. Another interpretation is described in the next section and is very consistent with the theoretical prediction.

7.3.2 Optical transitions within the HOMO band

From the polarized reflection spectrum, the one-dimensional model is considered as a good approximation. The two DMTSA molecules along the c-axis repeating unit are connected by the glide-plane symmetry. The energy band is therefore folded at the zone boundary of $k_c=\pi/c$ without opening a gap as shown in Fig. 4. These upper and lower branches of the energy dispersion curve are given by the equation (7.2) using the tight-binding approximation

$$E^{\pm} = \pm\Delta(k) = \pm t_c\sqrt{2+2\cos(k_c c)}\,, \tag{7.2}$$

where + and – represent the upper and lower branches, respectively. Since HOMO of DMTSA^{+} is singly occupied, the HOMO band is half filled, thereby the lower branch is filled and the upper branch is empty. As shown in Fig. 4, there are two kinds of optical transitions: the Drude term (*A*) which is polarized along the *c*-axis and the inter-branch optical transition (*B*) which is proved to be polarized along the *b*-axis.

The Drude term is derived from the Boltzman equation using the extended band $-2\pi/c \le k_c \le 2\pi/c$ 4). The *z*-component of conductivity tensor is given by the following equation,

$$Re\{\sigma_{zz}^{Drude}(\omega)\} = \frac{\varepsilon_0 \omega_p^2 \gamma}{\omega^2 + \gamma^2} \tag{7.3}$$

where ω_p is the plasma frequency, γ the relaxation rate, and ε_0 dielectric constant of vacuum. The conductivity tensor of the inter-branch transition (*B*) shown in Fig. 4 is given by the following equation in the framework of tight-binding approximation 5),

$$\sigma_{jj}^{inter}(\omega) = \frac{2i}{V\hbar^3} \sum_{i,f} \langle i \left[H, P_j\right] f \rangle \langle f \left[H, P_j\right] i \rangle \times \frac{\omega}{\omega_{f,i}(\omega^2 - \omega_{f,i}^2 + i\Gamma\omega)} \tag{7.4}$$

where *j* denotes *x*, *y*, or *z*, *V* is the volume of the crystal, *i* and *f* denote the initial and final states, respectively, ω_{fi} and Γ are the resonant frequency and damping constant, respectively. P_j is the electric dipole moment along the *j*-direction. The formula for the dipole moment $\boldsymbol{P}$ by the point-charge approximation is $\boldsymbol{P} = \sum_l e\boldsymbol{R}_{lm} a_{lm}^{+} a_{lm}$, where $\boldsymbol{R}_{lm}$ is the position vector of the *m*'th molecular site in the *l*'th unit cell 6). Since DMTSA has not center of symmetry, $\boldsymbol{R}_{lm}$ is defined by the center of the density distribution function of HOMO. The tight-binding Hamiltonian *H* is given by the following equation,

$$H = -t_c \sum_{l,l'} \sum_{m,m'} a_{lm}^{+} a_{l'm'} \tag{7.5}$$

where *l* and *l'* denotes the number of the unit cell, *m* and *m'* site number in the unit cell. The equation (7.4) is deduced to the following equation for the *j*-th component of the conductivity tensor:

$$\sigma_{jj}^{inter}(\omega) = \frac{ie^2 t_c^4 \{(R_{l1}^j - R_{l2}^j) + (R_{l+1,1}^j - R_{l2}^j)\}^2}{V\hbar^2} \times$$

$$\sum_{k=-\pi/c}^{\pi/c} \frac{(1+cos(k_c c))^2}{\Delta(k_c)^3} \frac{\omega}{\omega^2 - \omega_{fi}^2 + i\Gamma\omega} \tag{7.6}$$

$\sigma_{xx}(\omega)=0$, because the molecules in site 1 and 2 are located on the same mirror plane perpendicular to the *a*-axis: $R^x{}_{l1}=R^x{}_{l2}$. $\sigma_{zz}(\omega)=0$, since the molecules in site 1 and 2 are connected by the glide-plane symmetry along the *c*-axis, thereby having the same inter-molecular distance: $R^z{}_{l1}-R^z{}_{l2}=-R^z{}_{l+1,1}+R^z{}_{l2}$. However, $\sigma_{yy}(\omega)$ have a finite value, since the molecules are stacked in a zigzag form with a displacement δ: $\delta=|R^y{}_{l1}-R^y{}_{l2}|$. In this experiment, the polarization direction $E\perp c$ is parallel to $[1\bar{1}0]$, which makes an angle θ against the *b*-axis. To calculate the conductivity in this polarization, δ should be replaced by $\delta cos\theta$, thereby the real part of the conductivity is given by

$$Re\{\sigma_{\perp}^{inter}(\omega)\} = \frac{e^2}{v_c} \frac{\sqrt{2}t_c(c/2)\delta^2\cos^2\theta}{\hbar^2\pi} \int_{-\pi/c}^{\pi/c} \frac{\sqrt{1+\cos(k_c c)}\,\omega^2\Gamma}{\left\{\omega^2 - \left(\frac{2\Delta(k_c)}{\hbar}\right)^2\right\}^2 + \Gamma^2\omega^2} dk_c\,, \tag{7.7}$$

where v_c is the unit cell volume. The transfer integral t_c is estimated to be 0.2eV from the plasma frequency of the Drude model best-fitted to the observed $E//c$ reflection spectrum using the following equation[5)]

$$\omega_p^2(//c) = \frac{e^2 Z}{\varepsilon_0 v_c} \frac{c^2 t_c \sin(\pi\rho/2)}{\hbar^2 \pi\rho}, \tag{7.8}$$

where Z (=4) is the number of molecules in a unit cell, ρ (=1) the charge (valence) of the molecule. To estimate the unknown parameter δ in equation (7.7), the plasma frequency of the inter-branch transition B is calculated by the sum rule,

$$\omega_p^2(\perp c) = \frac{2}{\varepsilon_0 \pi}\int_0^{\infty} Re\{\sigma_{\perp}^{inter}(\omega)\} d\omega \cdot \tag{7.9}$$

Inserting $\sigma_{\perp}^{inter}(\omega)$ of the equation (7.7) into the equation (7.9), the following relation is derived

$$\frac{\omega_p^2(//c)}{\omega_p^2(\perp c)} = \frac{(c/2)^2}{(\delta\cos\theta)^2} \tag{7.10}$$

Applying the experimentally obtained values, $\omega_p(//c)$=9.30×10^3 cm^{-1}, $\omega_p(\perp c)$=4.09×10^3 cm^{-1}, and $c/2$=3.385Å, $\delta\cos\theta$ is calculated to be 1.49Å.

Using these parameters and Γ=2.84×10^3 cm^{-1} estimated from the fitting of Lorentz model to the $E\perp c$ reflection spectrum, the conductivity spectra given by equations (7.3) and (7.7) are calculated numerically. The result is shown in Fig. 5 along with the experimental data. The agreement between them is excellent, which strongly supports our interpretation for the band B. Let us briefly discuss about the peak position of the band B, which corresponds to the maximum transition probability of the inter-branch transition (see Fig. 4). The k_c dependence of the transition probability is given by $\frac{t_c^4\delta^2(2+2\cos(k_c c))^2}{\Delta(k_c)^3}$, which has a maximum value at k_c=0 in the Brillouin zone. The energy difference between two branches is 4$|t_c|$, the bandwidth of this HOMO band. The excitation energy of the band B (6.9×10^3 cm^{-1}) agrees well with the transfer integral t_c (=1.6×10^3 cm^{-1}) which is obtained from the plasma frequency of the band A.

7.3.3 Examination of the interpretation for the band B

We will examine the validity of δ obtained by the equation (10) in this section. Since θ is the angle between $[1\bar{1}0]$ and b-axis, δ is calculated to be 1.97Å. We calculate the charge distribution of HOMO of DMTSA^0 using the Extended Hückel method in the HyperChem-

R5.1 program system. The center of the density distribution function of HOMO is approximated by

$$r = \sum_i r_i c_i^2 \Big/ \sum_i c_i^2 \,, \tag{7.11}$$

where the c_i is the coefficient of the p_z atomic orbital of the i-th site in HOMO. Due to the C_{2v} symmetry of DMTSA, the center of HOMO is located on the axis of two-fold rotation. Figure 6 shows c_i^2 at each atomic site and the center of HOMO (marked by ⊕) calculated by equation (11). δ is regarded as the y-component of the vector connecting these marks of the neighboring molecules in the same molecular stack, which is calculated to be 3.27Å. The center of HOMO obtained by the observed spectrum using the equation (7.10) is drawn by ⊗ in Fig. 7. The agreement with the experiment is not quantitatively good, which shows that the point charge approximation seems to be too simple to quantitatively predict the intensity of the optical transition although it is reliable for the qualitative interpretation. A similar quantitative disagreement with the observed spectrum was pointed out in the interpretation of the optical spectra of the charge-transfer salts of BEDT-TTF as well[6)].

Based on our interpretation, the band B appears at $4|t_c|$, thereby it is expected to shift to a high-wavenumber side at low temperature, since the transfer integral along the stacking axis usually increases at low temperature[4,5)]. Actually the band B shifts to the high-wavenumber side by *ca.* 500cm^{-1} at 10K in this compound. DMTSA-BF_4 shows a structural change breaking the glide-plane symmetry below 150K. However, the main change of the band structure occurs at the zone boundary at $k_c=\pi$, whereas the optical transition occurs predominantly at $k_c=0$. Therefore this phase transition does not make a big influence on the optical transition (band B) at $k_c=0$. Let us compare the spectrum of DMTSA-BF_4 with DMTTA-BF_4 which is the sulfur analogue and isostructural to DMTSA-BF_4[1)]. As shown in Fig. 7, a similar broad band was observed in the $E \perp c$ conductivity spectrum of DMTTA-BF_4

but the position of this band (at *ca.* 5,000cm^{-1}) is significantly lower than that of DMTSA-BF$_4$. This suggests the narrower bandwidth of DMTTA-BF$_4$, which is reasonable, since the $4p_z$ selenium atomic orbital is more extended than the $3p_z$ sulfur atomic orbital. In fact it is known that the transfer integral of (TMTSF)$_2$X is larger than that of the sulfur analogue (TMTTF)$_2$X$^{5)}$. Finally we show in Fig. 7 the conductivity spectrum of DMTSA-ClO$_4$ which has a different stacking pattern$^{1)}$ of DMTSA from DMTSA-BF$_4$. This spectrum is measured using the light polarized perpendicular to the stacking direction. In the DMTSA-ClO$_4$ crystal, any polarization cannot be perpendicular to the long molecular axis of DMTSA, because two DMTSA molecules in the unit cell is arranged so as to be perpendicular to each other. As shown in Fig. 7, the corresponding band *B* is not observed in this compound. If the band *B* comes from the intra-molecular electronic transition of DMTSA$^+$ namely the inter-band transition, the band *B* should always appears despite the different stacking pattern.

The same zigzag stacking pattern exists in Bechgaard salts as well$^{5)}$, in which the adjacent molecule is shifted along the long molecular axis, which makes angles 65° with the b'-axis and 25° with the c^*-axis. However, the interpretation of the optical transition like the band *B* has not been claimed yet. Jacobsen *et al.* reports the $E//b'$ and $E//c^*$ reflection spectra of (TMTSF)$_2$SbF$_6$$^{5)}$, where a broad hump is recorded around 5,000-10,000cm^{-1} in the $E//c^*$ spectrum. However, this hump is not so clear since the spectral region is limited down to 5,000cm^{-1}. The clearer hump is observed at 10,000cm^{-1} in the low-temperature $E//b'$ spectrum of (TMTSF)$_2$AsF$_6$$^{11)}$. This position coincides with the bandwidth of this compound. This hump seems to be the same optical transition as the band *B*, although it is assigned to a forbidden transition within the TMTSF cation radical$^{11)}$. To the best of our knowledge, this is the first observation which proves the existence of the optical transition between the split branches of the HOMO band.

References:

1) Takimiya, K., Ohnishi, A., Aso, Y., Otsubo, T., Ogura, F., Kawabata, K., Tanaka, K. and Mizutani, M., *Bull. Chem. Soc. Jpn.,* **67** (1994) 766.

2) Kawabata, K., Yanai, M., Sambongi, T., Aso, Y., Takimiay, K. and Otsubo, T., *Mol. Cryst. Liq. Cryst.,* **296** (1997) 197.

3) Dong, J., Yakushi, K., Takimiya, K. and Otsubo, T., *J. Phys. Soc. Jpn.,* **67** (1998) 971.

4) Ouyang, J., Yakushi, K., Misaki, Y. and Tanaka, K., *J. Phys. Soc. Jpn.*, **67** (1998) 3191.

5) M. Tamura, *Thesis*, University of Tokyo, 1994.

6) Tajima, H., Yakushi, K., and Kuroda, H., *Solid State Commun.,* **56** (1985) 159. Tajima, H., Yakushi, K. and Kuroda, H., *Solid State Commun.,* **56** (1985) 251. Kuroda, H., Yakushi, K. and Tajima, H., *Mol. Cryst. Liq. Cryst.,* **125** (1985) 135. Kuroda, H., Yakushi, K., Tajima, H., Ugawa, A., Tamura, M., Okawa, Y., Kobayashi, A., Kato, R., Kobayashi, H. and Saito, G., *Synth. Met.,* **27** (1988) A491.

7) J. B. Torrance, B. A. Scott, B. Welber, F. B. Kaufman, and P. E. Seiden, *Phys. Rev. B*, **19** (1979) 730.

8) J.Dong, K.Yakushi, Y.Yamashita, K.Imaeda, and H.Inokuchi, *phys. stat. sol. (b)* **195** (1996) 611.

9) L. Ducasse, M. Abderrabba, J. Hoarau, M. Pesquert, B. Gallois, and J. Gaultier, *J. Phys. C: Solid State Phys.*, **19** (1986) 3805.

10) G. Rindorf, H. Soling, and N. Thorup, *Acta Cryst. B*, **38** (1982) 2805.

11) C. S. Jacobsen, D. B. Tanner, and K. Bechgaard, *Phys. Rev. B*, **28** (1983) 7019

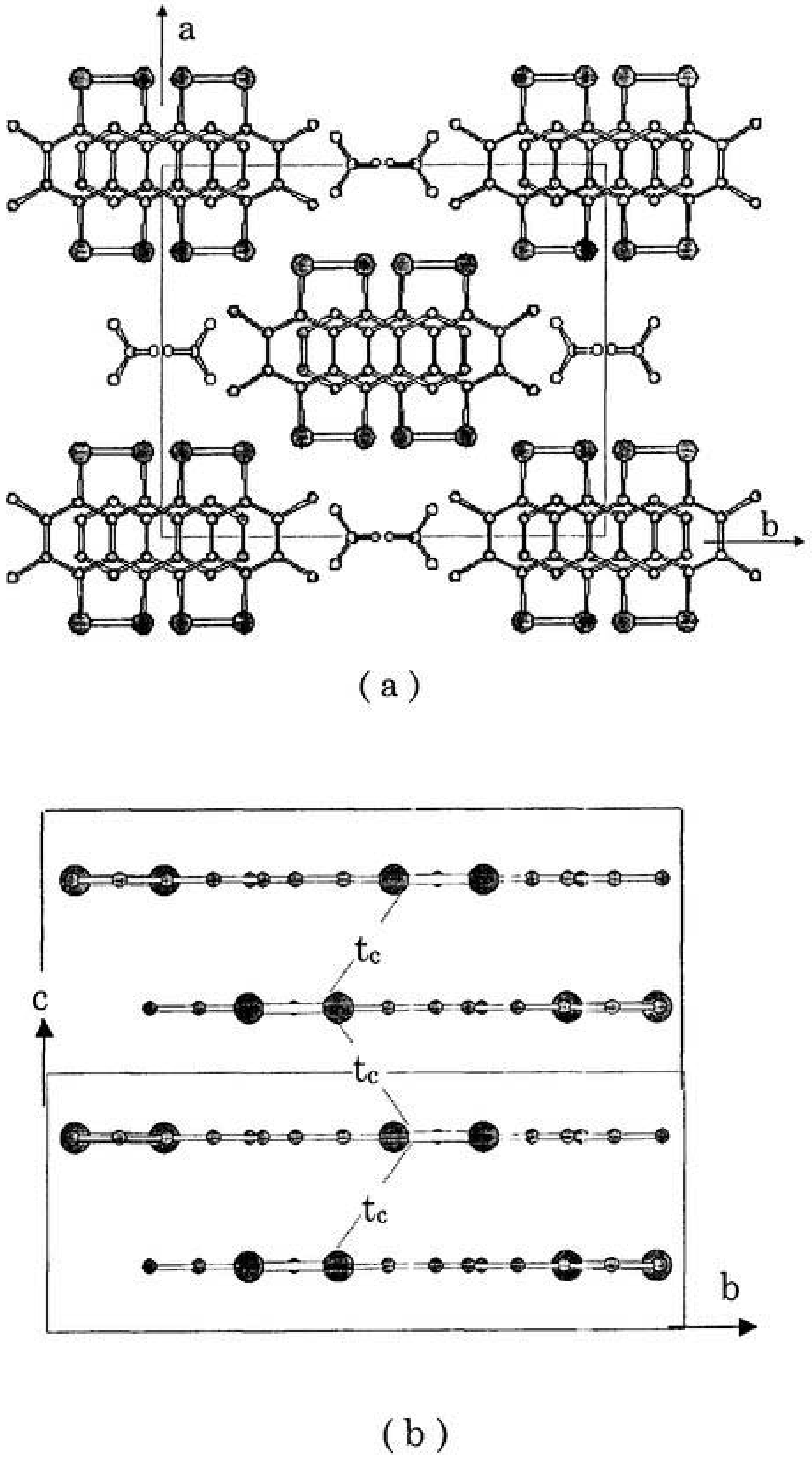

Fig. 1 (a) Crystal structure of DMTSA-BF$_4$ single crystal viewed from the *a*-axis. (b) Stacking pattern of DMTSA in the column located on (0,0,z) in the unit cell.

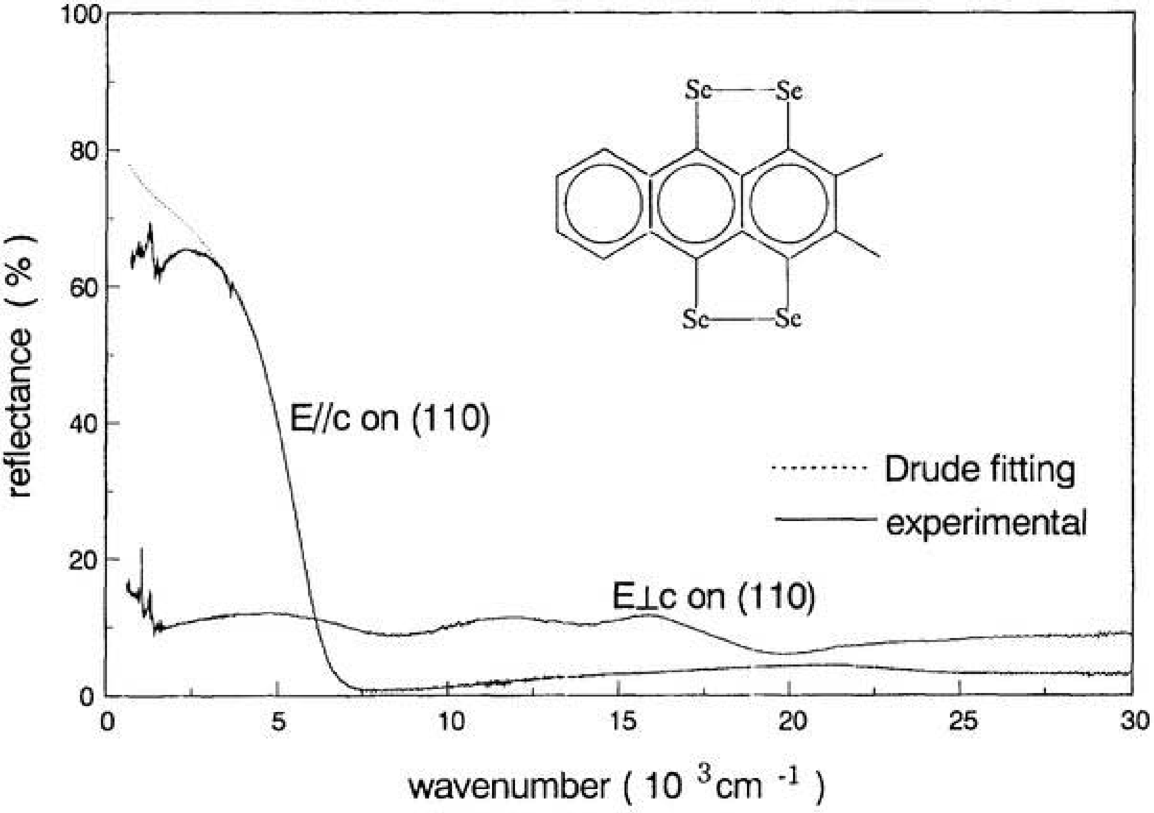

Fig.2 Polarized reflection spectra of DMTSA-BF_4 single crystal on the (110) crystal face. The inset shows the structure formula of DMTSA.

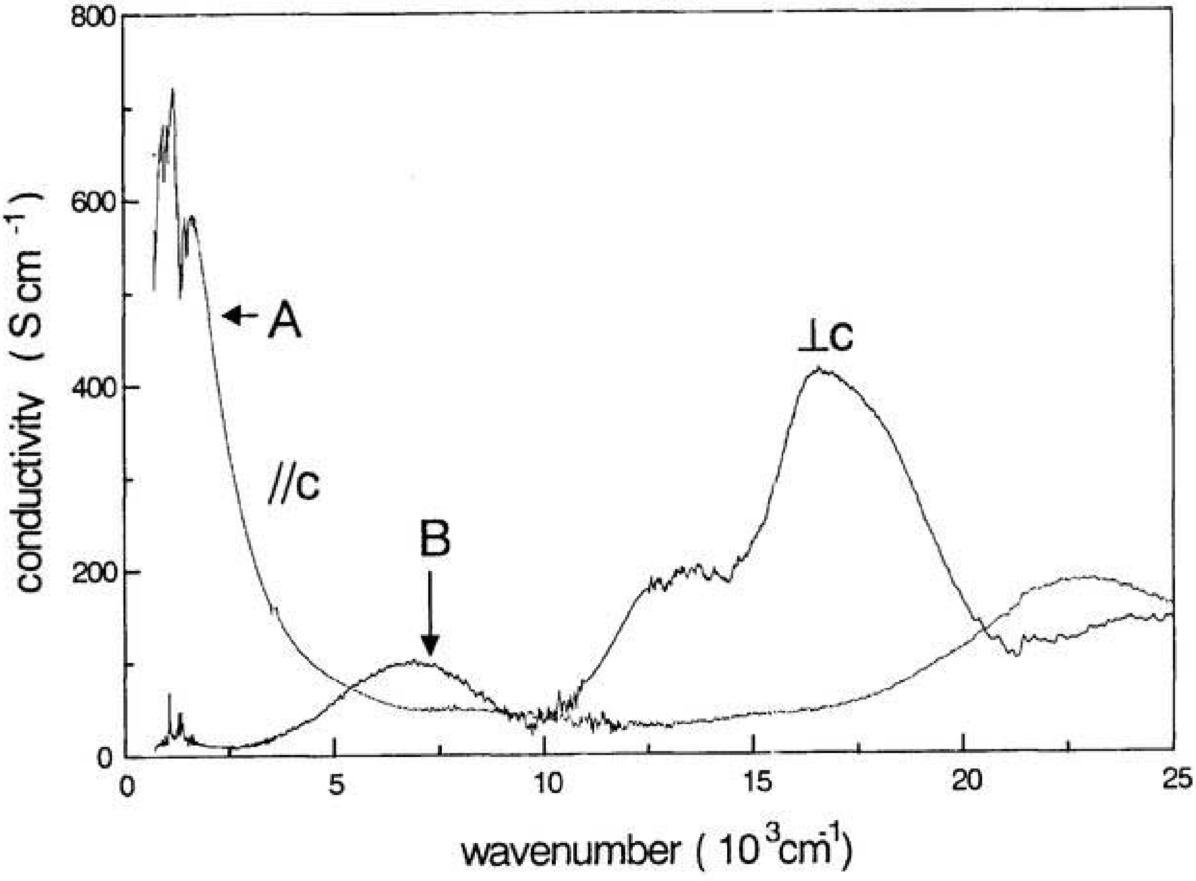

Fig. 3 Optical conductivity spectra of DMTSA-BF_4 crystal

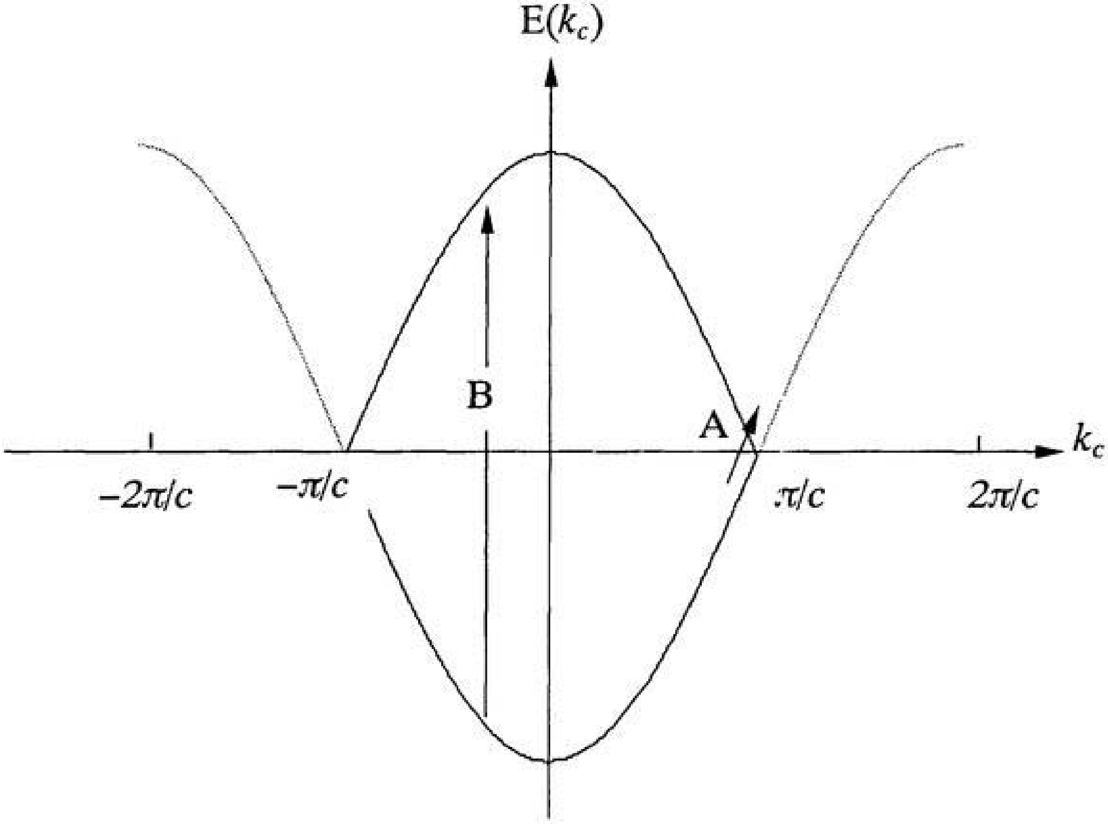

Fig. 4 One-dimensional energy band of DMTSA-BF$_4$ crystal. The extended scheme of the upper half branch is drawn by the broken line. The lower half is filled and the upper half is empty. *A* and *B* indicate the intra-band and inter-branch transitions, respectively.

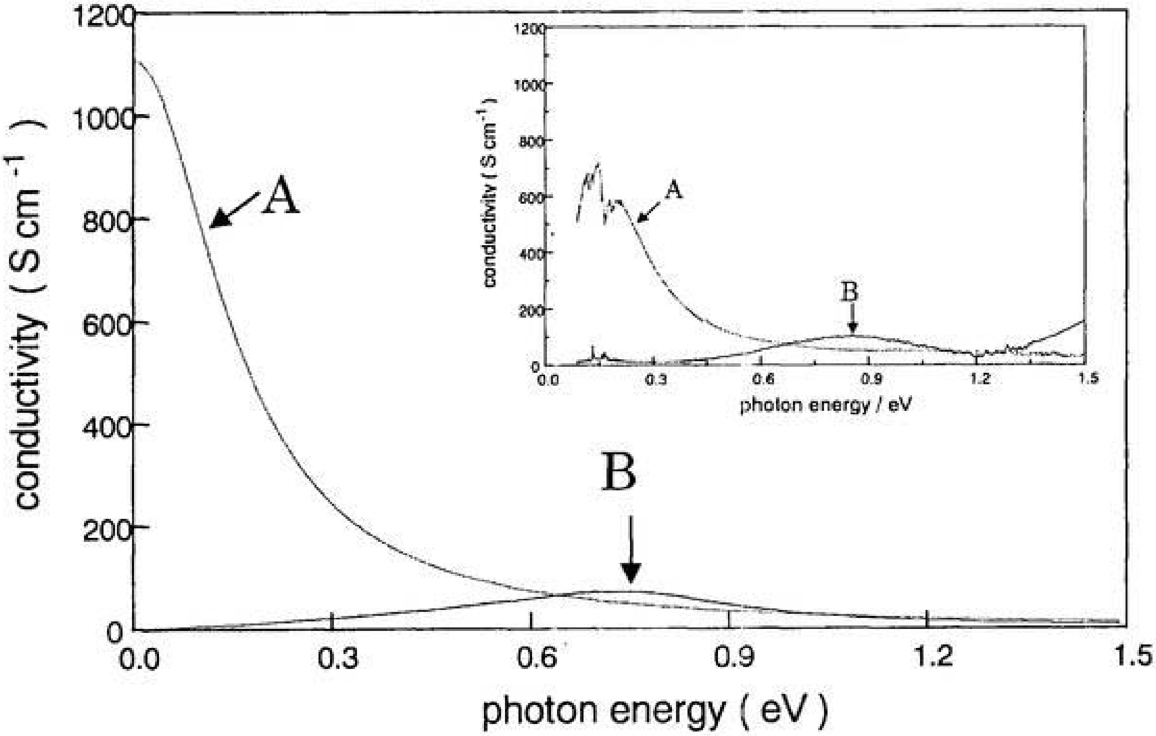

Fig.5 Calculated curve of the conductivity spectra of the band *A* (*E*//*c*) and the band *B* (*E*⊥*c*). The inset shows the observed spectra.

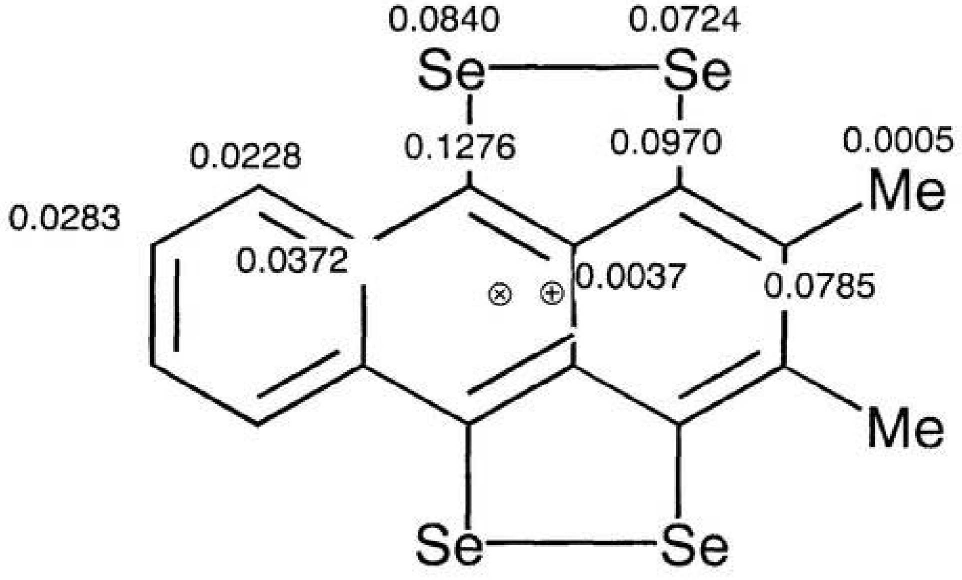

Fig. 6 The square of the coefficient of the p_z atomic orbital in HOMO. The geometry of molecules is taken from the crystal structure analysis. The coordinates of the hydrogen atoms are calculated according to the bond length and the bond angle. The symbols ⊕ and ⊗ denote the center of HOMO predicted by calculation and determined by experiment, respectively.

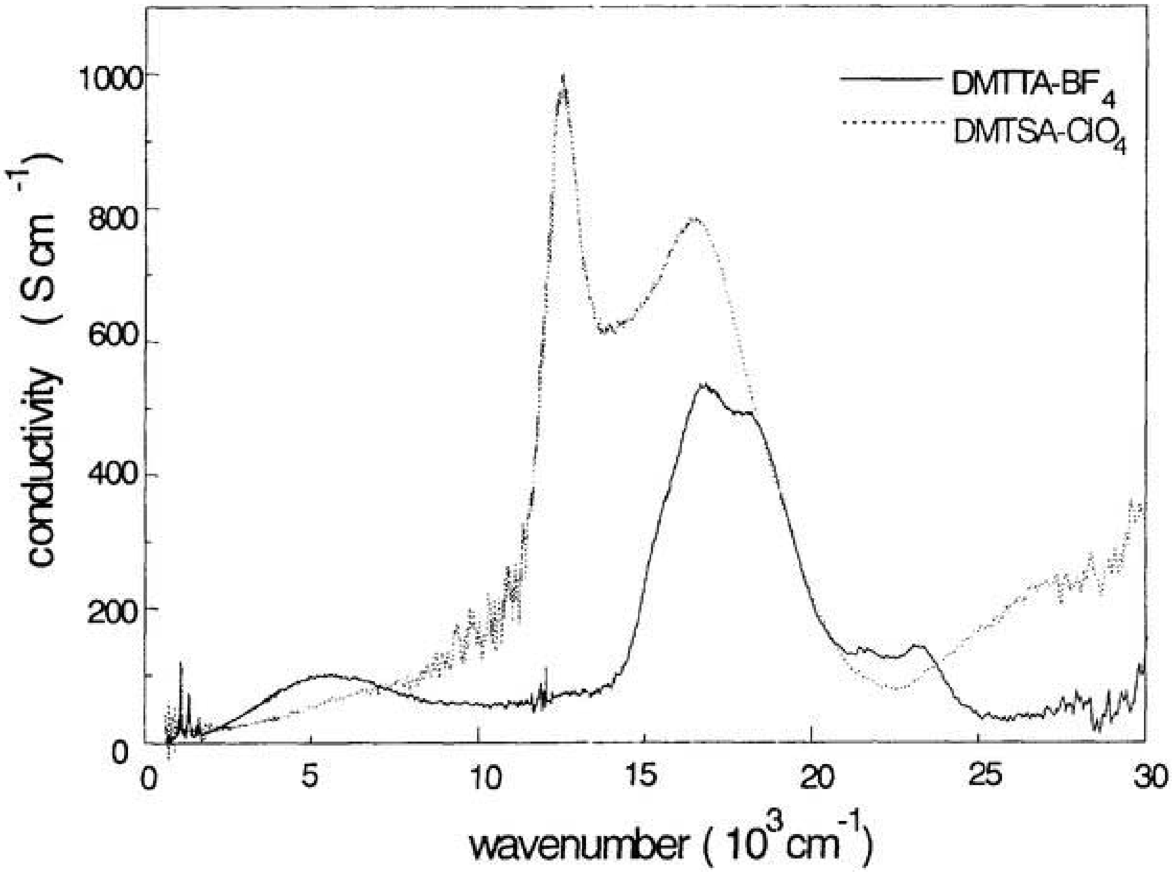

Fig. 7 Conductivity spectra of *E*//*b* on the (100) crystal face of DMTTA-BF$_4$ and *E*⊥*c* on the (110) face of DMTSA-ClO$_4$.

General Conclusion

The following is the summary of our study on the organic conductors, charge-transfer salts of BDT-TTP, DMTSA and their analogues, primarily by the polarized reflection spectroscopy, Raman scattering, ESR and electrical resistance measurement at the present stage.

(1) **$(BDT\text{-}TTP)_2X$ (X=SbF_6, AsF_6).** $(BDT\text{-}TTP)_2X$ (X=SbF_6, AsF_6) has β-type crystal structure. Strong dispersion with a significant anisotropy appears in the infrared region of $E//a$ and $E\perp a$ spectra. The plasma edges in both directions can be fitted by Drude model very well. These indicate a two-dimensional electronic structure with significant anisotropy in the crystals. The transfer integrals estimated from the plasma frequencies are t_a=-0.259 and t_p=-0.048eV for $(BDT\text{-}TTP)_2SbF_6$. The estimated t_a is comparable with the calculated by the extended Hückel method, while the estimated t_p is almost half of the calculated. The Fremi surfaces of both compounds are open in the first Brillouin zone, in contrast to the closed Fermi surface of $(BDT\text{-}TTP)_2SbF_6$ proposed by the theoretical prediction. The anisotropy of the Fermi surface increases at low temperature. The CH stretching mode strongly appears at 3084cm^{-1} in $E\perp a$ spectrum, suggesting that the conjugated HOMO electrons even extend to the hydrogen atoms.

(2) **$(ST\text{-}TTP)_2AsF_6$ and $(BDS\text{-}TTP)_2AsF_6$.** The crystal structure of BDT-TTP analogue salts $(ST\text{-}TTP)_2AsF_6$ and $(BDS\text{-}TTP)_2AsF_6$ (ST-TTP: 2-(1,3-diselenol-2-ylidene)-5-(1,3-dithiol-2-ylidene)-1,3,4,6-tetrathiopentalene, BDS-TTP: 2,5-bis(1,3-diselenol-2-ylidene)-1,3,4,6-tetrathiapentalene)) are iso-structural to $(BDT\text{-}TTP)_2X$ (X=SbF_6, AsF_6). The IR polarized reflection spectra resemble those of $(BDT\text{-}TTP)_2X$ (X=SbF_6, AsF_6). The estimated transfer integrals are t_a=-0.241, t_p=-0.042eV for $(ST\text{-}TTP)_2AsF_6$ and t_a=-0.255, t_p=-0.044eV for $(BDS\text{-}TTP)_2AsF_6$, which are smaller than BDT-TTP salts in spite of the introduction of the selenium atoms. The Fermi surfaces of both compounds are open as well. The inter-band electronic transition and the charge sensitive vibrational mode in the Raman spectrum shift to

lower energy region on increasing selenium atoms in the donor molecule, while the Raman shift between the neutral molecule and the 2:1 salts does not vary.

(3) (BDT-TTP)$_2$Y (Y=ClO$_4$, ReO$_4$). The BDT-TTP molecules stack uniformly in (BDT-TTP)$_2$Y (Y=ClO$_4$, ReO$_4$) crystal. The chemical ratio of BDT-TTP to ReO$_4$ was expected not to be 1:0.5 but 1:0.36. However, the most charge sensitive vibrational mode of both compounds appears at 1480 cm^{-1} in the Raman spectrum, the same position as (BDT-TTP)$_2$X (X =SbF$_6$, AsF$_6$), thereby indicating that the ratio of BDT-TTP to the anions is 2:1 in both compounds. The polarized reflection spectra resemble those of (BDT-TTP)$_2$X (X=SbF$_6$, AsF$_6$). The Fermi surfaces of (BDT-TTP)$_2$Y (Y =ClO$_4$, ReO$_4$) are open as well. The weak band at 8420cm^{-1} of *E//c* spectrum is assigned to the inter-band transition of BDT-TTP$^+$ monocation radical.

(4) θ-(BDT-TTP)$_2$Cu(NCS)$_2$. Different from (BDT-TTP)$_2$X (X=SbF$_6$, AsF$_6$, ClO$_4$ and ReO$_4$) which are metallic down to liquid helium temperature, θ-(BDT-TTP)$_2$Cu(NCS)$_2$ is a semiconductor, although it is expected to be a two-dimensional metal from the calculation of the band structure. The phase transition is observed at *ca.* 250K in the electrical resistance measurement. The activation energy changes from 30-40meV before the phase transition to 100meV. The polarized reflection spectra suggest two dimensional electronic structure and larger inter-stack transfer integral than the intra-stack transfer integral. The spectroscopic weight of the CT band shifts to higher energy region below the phase transition temperature. The onset energy of the *E//c* CT band at 16K is comparable with the energy gap estimated from the resistance measurement. The charge-sensitive mode in the Raman spectrum splits into several modes at low temperature, suggesting the charge disproportionation through the phase transition. The spin susceptibility increases on lowering temperature down to 10K, conforming the Curie-Weiss law with the magnetic moment of 0.62μ_B. The variations of the *g*-value and the linewidth of ESR signal with the temperature confirm the phase transition. All of these results show that θ-$(BDT\text{-}TTP)_2Cu(NCS)_2$ is a Mott insulator. Another modified $(BDT\text{-}TTP)_2Cu(NCS)_2$ crystal was found, which exhibits different physical properties from θ-$(BDT\text{-}TTP)_2Cu(NCS)_2$.

(5) DMTSA-BF_4 and DMTTA-BF_4. The polarized reflection spectra of DMTSA-BF_4 and DMTTA-BF_4 demonstrate that both compounds have a quasi-1D electronic structure. 1D metal DMTSA-BF_4 shows a metal-insulator transition at *ca.* 150K. DMTTA-BF_4 is a Mott insulator with $U/4t\sim0.8\text{-}1.2$, and a magnetic phase transition takes place at *ca.* 100K by the ESR experiment. The low-temperature reflection spectra of both compounds strongly suggest the breaking of screw-axis symmetry along the conducting axis. The phase transitions are regarded as the spin Peierls transition for DMTTA-BF_4 and Peierls transition for DMTSA-BF_4. Assuming a dimerized stack structure, the transfer integrals t_1 and t_2 are estimated as 0.25 and 0.21eV from the 10K spectrum of DMTSA-BF_4.

(6) DMTSA-BF_4. An interpretation is given to the broad absorption band at *ca.* 6900cm^{-1} in the $E\perp c$ spectrum of DMTSA-BF_4 single crystal. It is assigned to the inter-branch transition from the lower to the upper branch produced by folding the HOMO band at the zone boundary. According to the formulation of this optical transition, the transition probability originates from the zigzag stacking structure of DMTSA molecules in the crystal. The numerical calculation of the conductivity spectra of this transition agrees well with the observed conductivity spectrum.